MULTIVARIABLE CONTROL OF A TWIN LIFT HELICOPTER SYSTEM (TLHS) USING THE LQG/LTR DESIGN METHODOLOGY

by

ARMANDO ANTONIO RODRIGUEZ

B.S.E.E., Polytechnic Institute of New York (1983)

SUBMITTED IN PARTIAL FULFILLMENT OF THE REQUIREMENT FOR THE DEGREE OF

MASTER OF SCIENCE

at the

MASSACHUSETTS INSTITUTE OF TECHNOLOGY

May 1987

Signature of Author..... Signature redacted

Department of Electrical Engineering and Computer Science, May 1987

Certified by..... Signature redacted

Professor M. Athans
Thesis Supervisor

Accepted by..... Signature redacted

Professsor A.C. Smith, Chairman,
Department Graduate Committee

MULTIVARIABLE CONTROL OF A TWIN LIFT HELICOPTER SYSTEM USING THE LQG/LTR DESIGN METHODOLOGY

by

ARMANDO ANTONIO RODRIGUEZ

Submitted to the Department of Electrical Engineering
on May 15, 1987 in partial fulfillment of the requirements for the degree of
Master of Science in Electrical Engineering

ABSTRACT

This multivariable control study investigates the feasibility of a high performance (high bandwidth) automatic flight control system (AFCS) for a Twin Lift Helicopter System (TLHS). Two system configurations are considered in order to see if one has any advantages over the other. Each TLHS configuration consists of two Sikorsky UH-60A Blackhawk helicopters, jointly lifting a heavy payload. The payload is suspended from the ends of a rigid bar. The endpoints of the bar are attached, via tethers, below the helicopter c.g.'s. For one configuration the tether lengths are equal (Equal Tether Configuration) and for the other they are unequal (Unequal Tether Configuration). In each case we regulate the horizontal separation (between the helicopter c.g.'s) and the load motion, while horizontal and vertical velocities are commanded.

It is concluded that a high performance design is feasible for each configuration provided that model uncertainty is sufficiently low. If model uncertainty is high, the designs become unfeasible. This is because, in such a case, the large robustness requirement forces the helicopters to undergo

---

THESIS SUPERVISOR: Michael Athans
Professor of Systems Science and Engineering.

substantial pitching and oscillations in the vertical plane in order to regulate the horizontal separation and load motion when horizontal and vertical velocities are commanded. Moreover, if model uncertainty is high then only low bandwidth designs become feasible. This is due to the fact that a trade-off must be made between performance and stability robustness and that this trade-off is exacerbated by the high bandwidth objective. It is also concluded that besides providing a larger tip-to-tip rotor clearance, unequal tethered flight offers no significant advantages over equal tethered flight. To reach these conclusions three steps are taken.

First, guidelines are presented which can be used to systematically develop a "real world" multi-input multi-output (MIMO) AFCS for even highly-coupled high-order Twin Lift models. These guidelines are based on singular value ideas and the well established LQG/LTR design procedure. Secondly, the guidelines are applied to the Equal and Unequal Tether Configurations. Finally, the designs for each configuration are compared and the conclusions are made.

ACKNOWLEDGEMENTS

First and foremost, I would like to express my deepest appreciation to Professor Michael Athans. His infinite support, steadfast guidance, and everlasting patience have been very much appreciated. I feel extremely fortunate to have had him as a professor and as my thesis supervisor. His exciting style of lecturing, as well as his highly respected status in the field, has given me much to which I can aspire. I look forward to working with him in the future.

Secondly, I would like to than Professor Curtiss of Princeton University, Frank Warburton and Ted Carter of Sikorsky Aircraft. Their work introduced me to the Twin Lift Control Problem. I found the problem fascinating to say the least.

This acknowledgement would be far from complete without thanking my colleagues at M.I.T. They not only have provided technical support and unending hours of pleasurable arguing, but also a unique friendship which I shall treasure forever. Specifically, I would like to thank Dr. Daniel Grunberg, Petros Kapasouris, Ioannis Kyratzoglou, Dr. Richard LaMaire, David Milich, Jason Papastavrou, Wilma Quinn, Brett Ridgely, Jeff Shamma, Petros Voulgaris, Jim Walton, and Elaine Wagner.

I would like to thank Fifa Monserrate for helping me type this very long document. Her patience has been very much appreciated.

The artwork in this thesis was done by Arthur Giordani, the labs' draftsman. His work has given the thesis a professional look. This look, hopefully, will make the thesis more "appetizing" to those that read it.

I would also like to thank A.T. & T. Bell Labs for their most generous fellowship. I would specifically like to thank my mentor at the labs, Dr. Sid Ahuja, for his unending support.

Finally, I would like to thank my father for the love, encouragement, and support that he has given me over the years. When my mother died, thirteen years ago, he stayed with me and my two young brothers. He taught us the differences between right and wrong. He taught us to seek affluence but to remember the poor. Finally, he taught us the value of an education. For teaching me these values I shall always love him. I do not dedicate this thesis to him only because

it is my doctoral thesis which I wish to dedicate to him.

I dedicate this thesis to my wisest and oldest friend, Ted Hernandez. He's lived through both World Wars, the best of times, and the worst. I remember him helping me with my first science project (a diorama of our solar system). He took me to my first baseball game and bought me my first dictionary. I don't think I could ever repay him enough for all that he has done for me. I wish him health, happiness, and strength for the next hundred years.

This research was carried out at the M.I.T Laboratory for Information and Decision Systems (L.I.D.S.) with support from the NASA Ames and Langley Research Centers under grant NASA/NAG-2-297.

To my life long friend

Theodore Hugh Warfield Hernandez

TABLE OF CONTENTS

CHAPTER 4: AFCS DESIGN FOR TLHS EQUAL TETHER CONFIGURATION

CHAPTER 5: ANALYSIS OF TLHS UNEQUAL TETHER MODEL

CHAPTER 6: AFCS DESIGN FOR UNEQUAL TETHER CONFIGURATION

LIST OF FIGURES (By Chapter)

CHAPTER 2

CHAPTER 3

CHAPTER 4

CHAPTER 5

CHAPTER 6

APPENDICES

LIST OF TABLES (By Chapter)

CHAPTER 2

CHAPTER 3

CHAPTER 4

CHAPTER 5

CHAPTER 6

LIST OF ACRONYMS, ABBREVIATIONS, AND NOTATION

The following acronyms, abbreviations, and notation are used throughout the thesis:

AFCS :	Automatic Flight Control System
TLHS :	Twin Lift Helicopter System
ETP :	Equal Tether Plant
UTP :	Unequal Tether Plant
AVM:	Average Vertical Motion
SM :	Symmetric Motion
ASM :	Anti-Symmetric Motion
SASM :	Symmetric-Anti-Symmetric Motion
SISO :	single-input single-output
TITO :	two-input two-output
tfm :	transfer function matrix
tf:	transfer function
LQG/LTR:	Linear Quadratic Gaussian with Loop Transfer Recovery
KFFDE :	Kalman Filter Frequency Domain Equality
KF:	Kalman Filter
LQ:	Linear Quadratic
FOL:	Filter Open Loop
FARE:	Filter Algebraic Riccati Equation
CARE:	Control Algebraic Riccati Equation
↑GM:	Upward gain margin
↓GM:	Downward gain margin
PM:	Phase margin
ω_g:	Gain crossover frequency
ω_p:	Phase crossover frequency
ω_{CL}:	Closed loop gain crossover frequency (bandwidth)
MOID:	Maximum-output input-direction
MOOD:	Maximum-output output-direction
SVD:	Singular value decomposition
c.g.:	Center of gravity
$\mathrm{Re}(\cdot)$:	Real part of a complex number, vector, matrix, or signal

$\mathrm{Im}(\cdot)$:	Imaginary part of a complex number, vector, matrix, or signal
$(\cdot)^T$:	Transpose of a vector or matrix
$(\cdot)^H$:	Conjugate-transpose of a vector or matrix
$\|\cdot\|_2$:	Euclidean two-norm
$\mathbf{R}^n$ ($\mathbf{C}^n$):	Space of n-dimensional real (complex) vectors
(A_p,B_p,C_p):	State space representation for plant (TLHS)
(A,B,C):	State space representation for design plant
$G_p(s)$:	Plant (TLHS) transfer function matrix
G(s):	Design plant transfer function matrix
$\sigma_i[\, G(j\omega)\,]$:	i^{th} singular value of the matrix $G(j\omega)$
$G_{KF}(s)$:	Target loop (Kalmanf filter) transfer function matrix
μ:	Target loop bandwidth parameter
L:	Matrix design parameter
H_μ:	Filter gain matrix
ρ:	Target loop transfer function matrix recovery parameter
G_ρ:	Control gain matrix
K(s):	Recovered compensator transfer function matrix
$G_L(s)$:	Recovered loop transfer function matrix (loop broken at error)
S(s):	Recovered sensitivity transfer function matrix
T(s):	Recovered closed loop transfer function matrix
ft.:	feet
fps.:	feet / second
deg.:	degree
rad.:	radian
lb.:	pound
sec.:	second
dec.:	decade
db.:	decibel
oct.:	octave
fig.:	figure
eq.:	equation

CHAPTER 1: INTRODUCTION AND OVERVIEW

1.1 Motivation for Research

Ever since its birth in 1939, the helicopter has found itself playing a major role in areas such as agriculture, industry, public service, and the armed forces. The helicopter has been used to spray crops, assist construction engineers, obtain traffic reports, and to perform vital military operations.

As the years have passed, and the technology improved, the applications of the helicopter have increased. The need for bigger, more powerful helicopters has also grown. During the past few years, however, a leveling off of heavy lift helicopter production has occured (NASA, [16]). The high development costs for a new heavy lift helicopter have become difficult for users to justify, especially when there are much more economical alternatives. An appropriate question to ask would be: "Does such an alternative exist at the present time and state of helicopter technology?" The answer, of course, is affirmative. The Twin Lift Helicopter System (TLHS) is such an alternative.

Twin Lift allows us to use already existing helicopters to demonstrate its performance for only a fraction of the cost required to develop a new heavy lift helicopter. Twin Lift is not only highly cost-effective, but it provides the only immediate method for achieving a significant increase in payloads beyond the 16 tons currently managable in the Western World.

In addition to being an economical solution to the heavy lift problem, Twin Lift represents an extremely challenging design problem for control engineers. As will become apparent in the chapters which follow, the TLHS is an inherently unstable multivariable system with "highly coupled" dynamics. In order to systematically develop a high performance multivariable centralized automatic flight control system (AFCS) for the TLHS, a design methodology is needed which trivializes the stabilization problem and possesses enough degrees of freedom to address the following key feedback design issues:

(1) low frequency command following,

(2) low frequency disturbance rejection,

(3) Insensitivity to low frequency parameter uncertainty,

(4) stability robustness to high frequency unmodeled dynamics,

(5) attenuation of high frequency sensor noise,

(6) saturation of actuators.

An appropriate question to ask would be: "Does such a multivariable design methodology exist?" The answer, of course, is again affirmative. The Linear Quadratic Guassian with Loop Transfer Recovery (LQG/LTR) design methodology, when coupled with singular value ideas, constitutes such a methodology (Doyle, Stein, Athans, Lehtomaki [5], [6], [7], [8]).

This thesis shows how the LQG/LTR design methodology, coupled with singular value ideas, can be used to develop a high performance multivariable centralized AFCS for a TLHS.

Having given industrial and academic motivations for Twin Lift control research, the section is concluded with a quote:

> "The practical advantages of harnessing two helicopters to the same payload have long been recognized, but as with all technologies a full understanding of the factors governing its use are required before it is universally accepted." (Curtiss, Warburton [1])

1.2 Prior Research

The dynamics of a single hovering helicopter have been understood for many years (Bramwell, [3]). In the early 1960's, engineers at Kaman Aircraft showed how tethered helicopters differed from their free flying counterparts (Kaufman, Schultz [2]). Much work on helicopters carrying sling loads has also been done (Dukes, [4]).

During the 1960's, multilift investigations were sponsored by the Department of Defense, but no major advances were made. In 1968 Sikorsky Aircraft was funded to explore twin lift techniques. These studies culminated in a 1970 Sikorsky demonstration of a 20-ton twin lift configuration using CH-54B crane helicopters with rear viewing cockpits [1]. That twin lift experience resulted in the development of a master-slave automatic control concept in which a command pilot, in the master helicopter, flies the desired formation by manipulating his helicopter

while the slave is automatically controlled to maintain horizontal separation as well as spreader bar orientation. The 1970 demonstration showed that twin lift air taxi operations for short distances, at low speeds, were definitely feasible. Because of high pilot workload, however, high speed demonstrations were deemed unsafe. Sikorsky engineers concluded that a better understanding of twin lift dynamics was required [1].

In order to develop such an understanding Professor Curtiss, of Princeton University, in collaboration with Sikorsky engineer, Frank Warburton, developed a seven degree of freedon linear model for the longitudinal dynamics of a TLHS near hover. In a joint paper [1] they analyzed the system and used root locus techniques to identify the key parameters affecting nominal stability. They showed that the TLHS dynamics could essentially be thought of as those of a tethered helicopter [2] with those of a helicopter carrying a sling load [4]. The paper indicated how separation and attitude feedback could be used to achieve nominal stability. Other practical issues were also addressed.

The above discussion clearly indicates a steady trend toward understanding twin lift helicopter dynamics. There are key issues, however, which have not yet been addressed in the literature. This thesis will carefully delineate some of those issues in an effort to understand them, quantify them, and in the end, provide a sound design process for developing a multivariable centralized AFCS for TLHS's.

1.3 Contributions of Research

Because of the inherent coupling in TLHS's, single-input single-output (SISO) design techniques can not easily be used to systematically develop a centralized AFCS.

The paramount contribution of this thesis is the delineation of well defined guidelines for designing a "real world" multi-input multi-output (MIMO) AFCS for TLHS's. These guidelines combine state space analysis methods and singular value ideas with the well established LQG/LTR design methodology. Furthermore, the guidelines are just as easily applicable to highly coupled 16 degree of freedom Twin Lift models as to relatively weakly coupled 7 degree of freedom models.

More specifically, it is shown how singular value ideas can be used to formulate frequency

domain performance and stability robustness specifications for MIMO Twin Lift controllers in a manner which closely parallels classical SISO feedback control problem formulations. Furhermore, it is shown that the LQG/LTR procedure not only trivializes the Twin Lift stabilization problem, but also possesses enough degrees of freedom to meet pre-defined frequency domain performance and robustness specifications.

In addition, it is shown how singular vector information can be used to understand the input/output directionality properties of a TLHS under full automatic control. In order to help visualize this information the notion of MOID and MOOD plots is introduced.

Another contribution of the thesis is that it provides two complete case studies of a TLHS under full automatic control. One is for the Equal Tether Configuration and the other for the Unequal Tether Configuration. The studies show fundamental trade-offs that must be made in designing an AFCS (equal tethers or unequal). In particular, it will be shown that Twin Lift control engineers must trade-off desired performance (bandwidth) versus model simplicity. More specifically, as model simplicity (uncertainty) increases engineers must settle for less demanding performance specifications. Moreover, this will be shown to be true whether the tether lengths are equal or unequal.

The comparison between equal tethered flight and unequal tethered flight is another contribution since it shows that besides providing a larger tip-to-tip rotor clearance, unequal tethered flight offers no significant advantages over equal tethered flight when a high performance design is the objective.

Finally, the fact that we address the TLHS high performance (high bandwidth) design problem marks still another contribution. By addressing this challenging problem one obtains an indication of how much can realistically be expected from TLHS's under full automatic control. This information is crucial for Twin Lift engineers developing specifications for future "real world" TLHS's.

1.4 Outline of Thesis

The main body of the thesis is organized as follows:

Chapter 2 describes the TLHS to be studied and develops the mathematical model which will be used throughout the thesis.

Chapter 3 is the first analysis chapter. In this chapter the model developed in Chapter 2 is analyzed assuming the tether lengths are equal ("Equal Tether Problem"). The chapter describes the three basic motions associated with any TLHS [1]. In this chapter the natural modes of the TLHS "Equal Tether Configuration" are identified and discussed. The variables to be controlled (i.e. outputs to be commanded by pilot) are selected and design specifications are presented using singular value ideas. Classical-like arguments are given to understand the difficulties associated with the development of a high performance design.

Chapter 4 is the first design chapter. In this chapter the LQG/LTR design process is described and applied to the Equal Tether Problem. A high bandwidth LQG/LTR AFCS is obtained and evaluated. Fundamental trade-offs regarding performance and model uncertainty are presented. To help visualize the directionality properties of the resulting LQG/LTR-based design, we introduce the notions of MOID and MOOD plots. These plots are entirely based on information provided by singular vectors. The chapter shows that a high performance Equal Tether AFCS is feasible only if model uncertainty is "sufficiently" low. It is also shown that if model uncertainty is high then only a low bandwidth design becomes feasible. This is because, in such a case, the large robustness requirement forces the helicopters to undergo substantial pitching and oscillations in the vertical plane in order to regulate the horizontal separation and load motion when horizontal and vertical velocities are commanded.

Chapter 5 is the second analysis chapter. This chapter addresses the problem in which the tether lengths are unequal ("Unequal Tether Problem"). The chapter essentially parallels chapter 3, but emphasis is placed on the coupling between two of the three basic motions when the tether lengths are unequal ("Unequal Tether Configuration"). Comparisons are made between the Unequal and Equal Teher Configurations.

Chapter 6 is the second design chapter. In this chapter the LQG/LTR design methodology is

applied to the Unequal Tether Problem. A high bandwidth design is obtained and evaluated. Again, emphasis is placed on the coupling which occurs when the tether lengths are unequal. Comparisons are made with the Equal Tether AFCS. The chapter shows that the trade-offs that a designer must make when the tether lengths are equal remain when unequal tether lengths are used. It is also shown that unequal tethered flight offers no significant advantages over equal tethered flight when a high performance design is the objective.

Chapter 7 summarizes the thesis and gives suggestions for future research.

CHAPTER 2: MODELING A TWIN LIFT HELICOPTER SYSTEM (TLHS)

2.1 Introduction

In this chapter the Twin Lift Helicopter System (TLHS) configuration to be studied is described. The helicopter controls which shall enter the final control law are identified and discussed. Finally, a seven degree of freedom linear model is developed for the longitudinal dynamics of a TLHS near hover [1]. This model shall be used throughout the thesis.

2.2 Description of TLHS; Longitudinal Configuration

The basic configuration to be studied in this thesis is shown in Fig. 2.2.1. It consists of two helicopters, two tethers, a "spreader" bar, two load cables, and a payload.

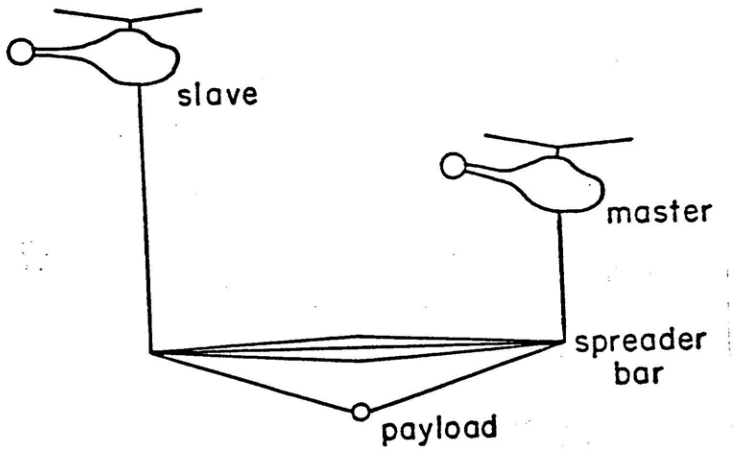

Fig. 2.2.1: TLHS; Longitudinal Configuration.

This configuration is referred to as the longitudinal configuration* because the spreader bar is parallel to the longitudinal axes of the helicopters. In studying the longitudinal configuration it is assumed that the lateral dynamics of the helicopters and load-bar assembly decouple from the planar

*The lateral configuration is obtained by rotating the helicopters ninety degrees so that their longitudinal axes are perpendicular to the spreader bar.

(longitudinal) dynamics of interest. This, of course, implies that the system motion is restricted to the vertical (longitudinal) plane and hence only vertical translation, horizontal translation, and pitching are allowed.

The helicopters being modeled are Sikorsky UH-60A Blackhawks. They are assumed to be identical and to have no on-board autopilots or stabilization avionics. The lead helicopter shall be referred to as the master helicopter and the trail helicopter as the slave. Each tether is assumed to have a fixed length .* The helicopter-tether attachment points are assumed to be a fixed distance, h, below the center of gravities (c.g.'s) of the helicopters. Each tether is attached to one end of the spreader bar. The spreader bar is assumed to be rigid and to have a fixed length, L. It provides horizontal separation for the helicopters, helps distribute the load more evenly between the helicopters, and helps vertical following of the master by the slave [1]. The payload is suspended a fixed distance, Z, below the spreader bar c.g. via two fixed length load cables. For simplicity the tethers, as well as the load cables, are assumed to have no compliance and to always be in tension.

2.3 Description of Helicopter Controls

Controlling the longitudinal dynamics of a TLHS near hover is the problem being addressed in this thesis. In order to develop a control law, the pertinent control inputs must be identified and understood. Because the thesis restricts the system motion to the longitudinal plane, only four helicopter controls (two per helicopter) are relevant. These are the collective pitch controls and the cyclic pitch controls [3] (Fig. 2.3.1).**

The collective pitch controls essentially control the vertical (up / down) motions of the helicopters. A pilot ordinarily *** manipulates his collective to control the lifting power of his

---

* Real time tether length variations will not be used to control the system.

** The tail rotor pedals (directional controls) are not relevant to our study since no yawing is allowed. The throttle control is not considered since engine dynamics are assumed to be negligible in our study.

*** We say ordinarily since in our study it is assumed that there is only one pilot which shall eventually issue only reference commands to an AFCS which will dynamically coordinate the controls of each helicopter so as to achieve the desired response.

helicopter. Pulling back on the collective pitch stick causes an increase in the angle (pitch) with which the main rotor blades cut through the air (angle of attack), thus increasing the lift. The name collective pitch control stems from the fact that the blades pitch simultaneously (collectively) when the pilot issues collective pitch commands.

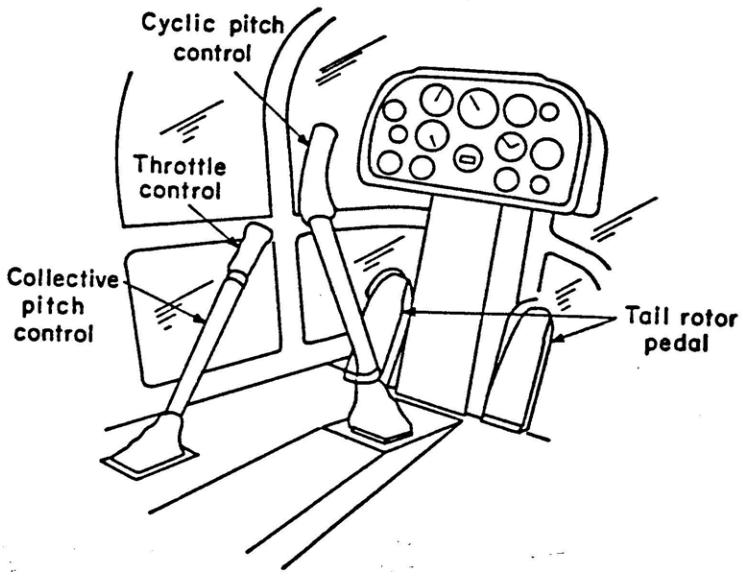

Fig. 2.3.1: Helicopter Cockpit.

The cyclic pitch controls* essentially control the horizontal (fore / aft) and pitching motions of the helicopters. A pilot ordinarily manipulates his cyclic pitch stick to control that point in the rotation of the main rotor at which maximum blade pitching occurs. By doing so the pilot, in effect, tilts the lift vector in the direction of desired motion thus providing more thrust in that direction, causing his helicopter to pitch downward and accelerate forward. The name cyclic pitch control stems from the fact that the point in the main rotor cycle at which maximum blade pitching occurs is altered when the pilot issues cyclic pitch commands.

In actuality, the collectives also affect the horizontal and pitching motions of the helicopters while the cyclics affect their vertical motions. Throughout the thesis, however, it is assumed that these couplings are negligibly small.

* The cyclic control shall not be used to control roll and lateral motions since these motions are not considered in this thesis.

2.4 Development of Linear Model

In this section a seven degree of freedom linear model is developed for the longitudinal dynamics of the TLHS near hover [1]. A more detailed derivation appears in Appendix 2. All designs presented in this thesis shall be based on this model.

The following seven variables (degrees of freedom) can be used to describe the TLHS longitudinal dynamics:*

(1) x_s - Horizontal coordinate of slave helicopter c.g. with respect to hover point (ft.),

(2) z_s - Vertical coordinate of slave helicopter c.g. with respect to hover point (ft.),

(3) θ_s - Pitch attitude of slave helicopter (rads.),

(4) θ_m - Pitch attitude of master helicopter (rads.),

(5) ε_s - Angle that slave tether makes with vertical (rads.),

(6) ε_m - Angle that master tether makes with vertical (rads.),

(7) ε_B - Angle that spreader bar makes with horizontal (rads.).

where all counter-clockwise angles are assumed to be positive angles.

These seven degrees of freedom capture the vertical, horizontal, and pitching motions of each helicopter (3 degrees of freedom per helicopter) as well as the pendular motion of the load-bar assembly (1 degree of freedom for load-bar assembly).

Some very important (time invariant) TLHS parameters are:**

W_H - Weight of master and slave helicopters (lbs.),

I_y - Moment of inertia of master and slave helicopters about their pitch axes (slug ft.^{2}),

---

* Appendix 1 is a glossary. It provides definitions for all Twin Lift variables and parameters. It also contains the numerical values of all relevant TLHS parameters.

** Their values, and all other relevant Twin Lift parameter values, are provided in Appendix 1.

h - Distance from helicopter c.g.'s to helicopter-tether attachment points (ft.),

H_m - Length of master helicopter tether (ft.),

H_s - Length of slave helicopter tether (ft.),

L - Length of spreader bar (ft.),

W_B - Weight of spreader bar (lbs.),

I_B - Moment of inertia of spreader bar about its c.g. (slug ft.^{2}),

Z - Distance that payload hangs below spreader bar c.g. during unperturbed hover (ft.),

W_L - Weight of payload (lbs.).

The seven degrees of freedom and the parameters described above can be visualized as shown in Fig. 2.4.1.

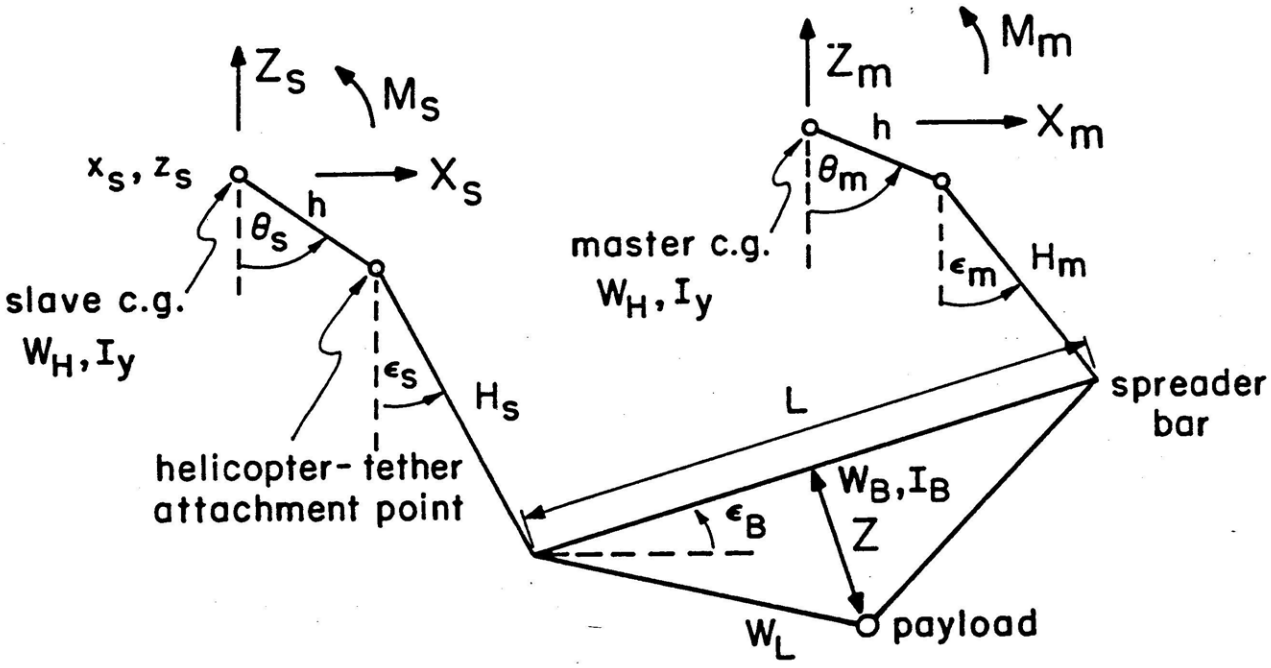

Fig: 2.4.1: Initial Seven Degrees of Freedom for TLHS

Longitudinal Dynamics Near Hover.

To develop the model, it is assumed that the following aerodynamic forces and moments act on the helicopters:

X_m, X_s - Horizontal aerodynamic forces acting on master and slave helicopter c.g.'s (lbs.),

Z_m, Z_s - Vertical aerodynamic forces acting on master and slave helicopter c.g.'s (lbs.),

M_m, M_s - Aerodynamic moments about master and slave helicopter pitch axes (ft. lbs.).

It should be noted that the aerodynamic moments on the spreader bar are assumed to be negligible in comparison with the other forces and moments acting on the system.

Using the aforementioned variables, parameters, aerodynamic forces and moments, a nonlinear model can be developed using Lagrangian methods. Doing so gives a set of seven second order nonlinear ordinary differential equations written in terms of the aerodynamic forces and moments discussed above (see Appendices 2.1 and 2.2 for more details).

To obtain a linear model about hovering trim, with the tethers vertical and the spreader bar horizontal, it is necessary to determine the equilibrium (trim) value of all variables, aerodynamic forces and moments under these conditions. These values are:

$$\dot{x}_{so} = \dot{z}_{so} = 0 \qquad \text{(Helicopters hovering)}$$

$$\varepsilon_{so} = \varepsilon_{mo} = \varepsilon_{Bo} = 0 \qquad \text{(Tethers vertical and spreader bar horizontal)}$$

$$X_{mo} = X_{so} = 0 \qquad \text{(Horizontal equilibrium)}$$

$$Z_{mo} = Z_{so} = W_H + 0.5\,[W_B + W_L] \qquad \text{(Vertical equilibrium)}$$

$$\theta_{mo} = \theta_{so} = M_{mo} = M_{so} = 0$$

where the subsrcipts "o" are used to denote equilibrium (large signal) values. It should be noted that the last condition assumes that the helicopter main rotor shafts pass through their c.g.'s when at hover.

Next, each variable, aerodynamic force and moment, is written as a sum of an equilibrium (large signal) component and an incremental (small signal) component (small perturbation from equilibrium value). The following example illustrates how this is done.

Ex:	Z_m	=	Z_{mo}	+	ΔZ_m	(For aerodynamic forces)
	M_m	=	M_{mo}	+	ΔM_m	(For aerodynamic moments)
	ε_B	=	ε_{Bo}	+	$\delta\varepsilon_B$	(For position and angular variables)
	↑		↑		↑	
	"true" quantities		"equilibrium" quantities		"incremental" quantities	

Assuming that all variable perturbations (incremental components), $\delta(\cdot)$, are small and neglecting products and squares of variables gives us a set of seven second order linear ordinary differential equations in terms of the incremental variables and the incremental aerodynamic forces and moments acting on the helicopters; namely $(\Delta X_m, \Delta Z_m, \Delta M_m)$ and $(\Delta X_s, \Delta Z_s, \Delta M_s)$. For notational economy we drop the δ's on the motion variables.* This concludes the linearization of the nonlinear equations near hovering trim with the tethers vertical and spreader bar horizontal (see Appendices 2.3 and 2.4 for more detail).

In order to exploit the "natural" symmetry of the TLHS, it is convenient to introduce the following "natural" seven degrees of freedom [1]:

3 Average Variables:

$\Sigma x \equiv [x_m + x_s] / 2$: Average horizontal helicopter coordinate (ft.), (2.1)

$\Sigma z \equiv [z_m + z_s] / 2$: Average vertical helicopter coordinate (ft.), (2.2)

$\Sigma\theta \equiv [\theta_m + \theta_s] / 2$: Average helicopter pitch attitude (rads.). (2.3)

3 Difference Variables:

$\Delta x \equiv [x_m - x_s]$: Horizontal separation between helicopter c.g.'s (ft.), (2.4)

$\Delta z \equiv [z_m - z_s]$: Vertical separation between helicopter c.g.'s (ft.), (2.5)

$\Delta\theta \equiv [\theta_m - \theta_s]$: Differential pitch attitude (rads.). (2.6)

1 Generalized Load Coordinate:

$x_L' \equiv x_L - \Sigma x - (h + H_s)\,\Sigma\theta - (Z / L)\,\Delta z$ (ft.). (2.7)

where x_L is the horizontal coordinate of the payload with respect to the hover point.

---

* Note that only incremental (small signal) quantities shall appear in the final linear model.

The above seven degrees of freedom are independent and hence sufficient to describe the longitudinal dynamics of the TLHS near hover. It should be noted, however, that the following incremental expressions are very useful:

$$\Delta x = -\left[h\,\Delta\theta + H_m\,\varepsilon_m - H_s\,\varepsilon_s \right] \tag{2.8a}$$

$$= \left[h\,\theta_s + H_s\,\varepsilon_s\right] - \left[h\,\theta_m + H_m\,\varepsilon_m\right] \tag{2.8b}$$

$$\Delta z = L\,\varepsilon_B \tag{2.9}$$

$$x_L' = 0.5\left[H_m\,\varepsilon_m + H_s\,\varepsilon_s\right] - H_s\,\Sigma\theta \tag{2.10a}$$

$$= 0.5\left[H_m\,(\varepsilon_m - \theta_m) + H_s\,(\varepsilon_s - \theta_s)\right] + 0.5\left[H_m - H_s\right]\theta_m \tag{2.10b}$$

$$\varepsilon_m = \left\{ 2\left[x_L' + H_s\,\Sigma\theta\right] - \left[\Delta x + h\,\Delta\theta\right] \right\} / 2\,H_m \tag{2.11}$$

$$\varepsilon_s = \left\{ 2\left[x_L' + H_s\,\Sigma\theta\right] + \left[\Delta x + h\,\Delta\theta\right] \right\} / 2\,H_s \tag{2.12}$$

In a manner analogous to eqs. (2.1) - (2.6), we define an average tether angle and a differential tether angle:

$$\Sigma\varepsilon \equiv \left[\varepsilon_m + \varepsilon_s\right] / 2 \tag{2.13}$$

$$\Delta\varepsilon \equiv \left[\varepsilon_m - \varepsilon_s\right] \tag{2.14}$$

The proof of eqs. (2.8) and (2.10) are given in Appendix 2.5. Equation (2.9) is, of course, based on the small angle assumption for the spreader bar angle, ε_B. Equations (2.11) and (2.12) follow from eqs. (2.8) and (2.10).

The interpretation of the 4 average variables (Σx, Σz, $\Sigma\theta$, $\Sigma\varepsilon$) and the 4 difference variables (Δx, Δz, $\Delta\theta$, $\Delta\varepsilon$) should be apparent from eqs. (2.1) - (2.6), (2.13), (2.14), and the fact that the variables are incremental (small signal) quantities. Nevertheless, we shall comment on Δx and Δz which may be a bit confusing to some.

It should be emphasized that $\Delta x = 0$ implies that the actual horizontal separation between the

helicopter c.g.'s is L; the spreader bar length. From eq. (2.8) we see that this can occur if and only if $h\,\theta_m + H_m\,\varepsilon_m = h\,\theta_s + H_s\,\varepsilon_s$. This makes sense since the left and right sides of this equation are merely the horizontal (incremental) distances from the spreader bar endpoints to the master and slave helicopter c.g.'s, respectively. To better visualize this condition it helps to interpret eq. (2.8) as indicated by Fig. 2.4.2. Note that eq. (2.8) does not capture the effect that the spreader bar rotation has on horizontal separation. Namely, when the spreader bar rotates by an

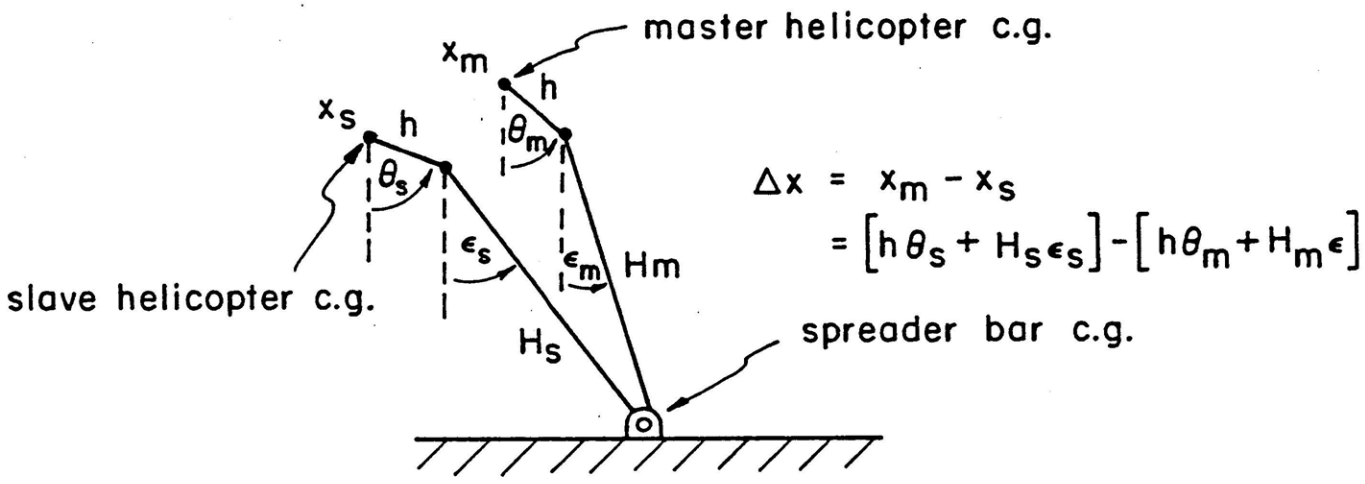

Fig. 2.4.2: Visualization of (Incremental) Horizontal Separation.

angle ε_B, the horizontal separation should decrease by an amount $L\,(1 - \cos\varepsilon_B)$. This nonlinear effect is not captured since ε_B is assumed to be small.

It should also be emphasized that $\Delta z = 0$ implies that the actual vertical separation between the helicopter c.g.'s is $H_m - H_s$; the difference between the master and slave tether lengths. From eq. (2.9) we see that this can occur if and only if $\varepsilon_B = 0$; i.e. when the spreader bar is horizontal. To help visualize this condition, it helps to interpret eq. (2.9) as indicated in Fig. 2.4.3. Note that eq. (2.9) does not capture the effect that helicopter pitching and tether rotation has on vertical separation. Namely, when the helicopters pitch and the tethers rotate, the vertical separation decreases by an amount $[H_m - H_s] - [H_m \cos\varepsilon_m - H_s \cos\varepsilon_s] - h\,[\cos\theta_m - \cos\theta_s]$. This nonlinear

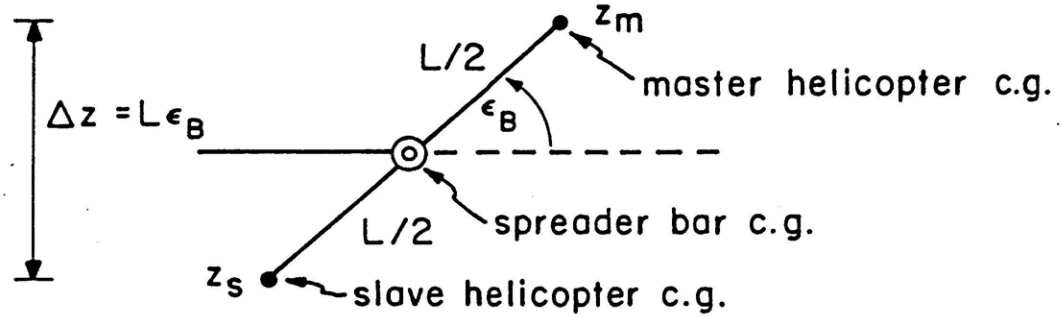

Fig. 2.4.3: Visualization of (Incremental) Vertical Separation.

effect is not captured since θ_m, θ_s, ε_m, and ε_s are assumed to be small.

An interpretation for x_L' follows from eq. (2.10). This equation shows that when the tether lengths are equal ($H_m = H_s = H$), then

$$x_L' = 0.5\, H\, [\, (\varepsilon_m - \theta_m) + (\varepsilon_s - \theta_s)] \qquad (2.15a)$$

$$= H\, [\Sigma\varepsilon - \Sigma\theta] \qquad (2.15b)$$

In such a case x_L' represents the average displacement of the spreader bar end points from the helicopter-tether attachment points, measured parallel to the longitudinal axes of the helicopters. This is shown if Fig. 2.4.4.

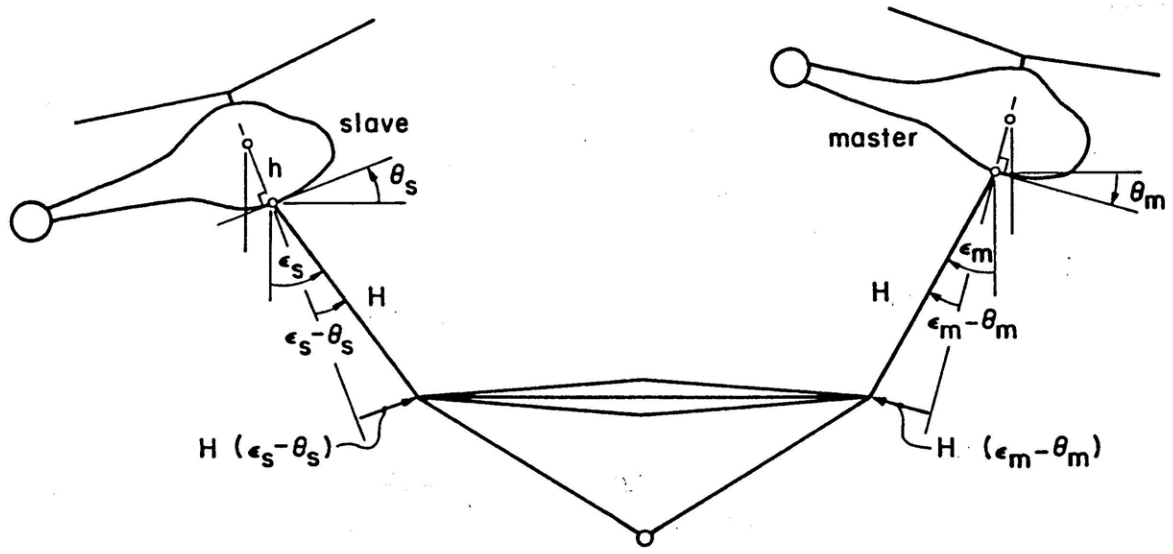

Fig. 2.4.4: Interpretation of Generalized Load Coordinate ($H_m = H_s = H$).

When the tether lengths are not equal ($H_m \neq H_s$), then x_L' is given by eq. (2.10). To interpret x_L' in this case we rewrite eq. (2.7) in its more useful form:

$$\boxed{x_L - \Sigma x = (h + H_s)\,\Sigma\theta + (Z / L)\,\Delta z + x_L'} \tag{2.16}$$

The quantity $x_L - \Sigma x$ shall henceforth be referred to as the load deviation from center. The quantity Σx shall be referred to as the center. It follows from eq. (2.16) that x_L' should simply be interpreted as that quantity which must be added to $(h + H_s)\,\Sigma\theta + (Z / L)\,\Delta z$ to get $x_L - \Sigma x$. Substituting eqs. (2.9) - (2.10) into eq. (2.16) gives us:

$$x_L - \Sigma x = h\,\Sigma\theta + (Z / L)\,\Delta z + 0.5\,[H_m\,\varepsilon_m + H_s\,\varepsilon_s] \tag{2.17a}$$

$$= h\,\Sigma\theta + Z\,\varepsilon_B + 0.5\,[H_m\,\varepsilon_m + H_s\,\varepsilon_s] \tag{2.17b}$$

$$= 0.5\,\{\,[h\,\theta_m + H_m\,\varepsilon_m] + [h\,\theta_s + H_s\,\varepsilon_s]\,\} + Z\,\varepsilon_B \tag{2.17c}$$

This can be concisely written as follows:

$$\boxed{x_L - \Sigma x = \Sigma x_{HB} + x_{BL}} \tag{2.18}$$

where

$$\Sigma x_{HB} \equiv [x_{MB} + x_{SB}] / 2 \tag{2.19}$$

$$x_{MB} \equiv [h\,\theta_m + H_m\,\varepsilon_m] \tag{2.20}$$

$$x_{SB} \equiv [h\,\theta_s + H_s\,\varepsilon_s] \tag{2.21}$$

$$x_{BL} \equiv Z\,\varepsilon_B \tag{2.22}$$

The quantities x_{MB} and x_{SB} are the (incremental) horizontal distances from the master and slave helicopter c.g.'s to their respective spreader bar endpoints. The quantity x_{BL} is simply the

(incremental) horizontal distance from the spreader bars' c.g. to the load. x_{MB}, x_{SB}, x_{BL}, and x_L - Σx can be visualized as in Fig. 2.4.5.

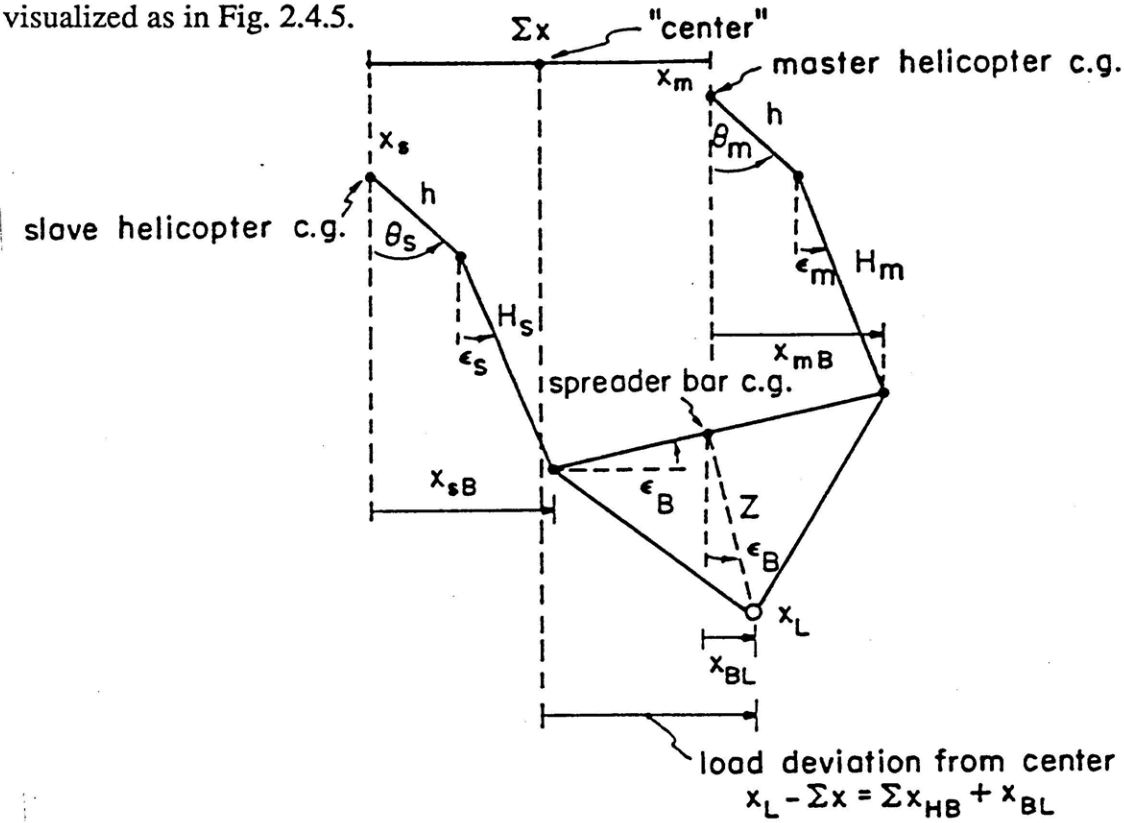

Fig. 2.4.5: Visualization of Load Deviation from Center.

Equations (2.16) - (2.22) and Fig. 2.4.5 show that the load deviation from center depends on the pitch attitudes of the helicopters, their vertical separation, and their respective tether angles. They also show that $x_L - \Sigma x = 0$ if and only if $\Sigma x_{HB} = - x_{BL}$. Physically, we see from Fig. 2.4.5, this means that the average horizontal (incremental) distance from the helicopter c.g.'s to their respective spreader bar endpoint must be equal and opposite to the horizontal load displacement (incremental) resulting from spreader bar inclination. The load deviation from center, as the name implies, shall play an important role in regulating the load motion.

After introducing the seven incremental variables (Σx, $\Sigma\theta$, Σz, Δx, $\Delta\theta$, Δz, x_L'), manipulating the equations, and defining new parameters to simplify them (Appendix 2.6), we develop the aerodynamic forces and moments on the helicopters by making use of the Blackhawk

helicopter control and aerodynamic derivatives near hover (Appendix 1).

Control derivatives are constants of proportionality that allow us to introduce the four helicopter incremental controls into the linear model. The four helicopter contols can be written as follows:

Θ_{cm}, Θ_{cs} - "True" master and slave helicopter collective pitch controls,

B_{lcm}, B_{lcs} - "True" master and slave helicopter cyclic pitch controls,

where $\Theta_{cm} = \Theta_{cmo} + \delta\Theta_{cm}$, $\Theta_{cs} = \Theta_{cso} + \delta\Theta_{cs}$, (2.23)

and $B_{lcm} = B_{lcmo} + \delta B_{lcm}$, $B_{lcs} = B_{lcso} + \delta B_{lcs}$. (2.24)

Θ_{cmo} and Θ_{cso} denote the master and slave equilibrium (large signal) components of collective. They provide the vertical aerodynamic forces, $Z_{mo} = Z_{so} = W_H + 0.5\,[W_B + W_L]$, which maintain the TLHS in vertical equilibrium. B_{lcmo} and B_{lcso} denote the master and slave equilibrium (large signal) components of cyclic. They are both zero since $X_{mo} = X_{so} = M_{mo} = M_{so} = 0$.

$\delta\Theta_{cm}$ and $\delta\Theta_{cs}$ denote the master and slave incremental (small signal) components of collective. They are to be generated by an AFCS (not a pilot). δB_{lcm} and δB_{lcs} denote the master and slave incremental (small signal) components of cyclic. They too are to be generated by an AFCS (not a pilot).

It is assumed throughout the thesis that the incremental collectives and cyclics must always satisfy:

$$|\delta\Theta_c| < 10 \text{ degrees} \quad \text{and} \quad |\delta B_{lc}| < 15 \text{ degrees.} \tag{2.25}$$

Again, for notational economy we shall suppress the δ's.

In an analogous manner to the average and difference variables defined earlier, we define the following four controls:

2 Average Controls:

$\Sigma\Theta_c \equiv [\Theta_{cm} + \Theta_{cs}] / 2$: Average collective control (rads.), (2.26)

$\Sigma B_{lc} \equiv [B_{lcm} + B_{lcs}] / 2$: Average cyclic control (rads.), (2.27)

2 Difference Controls:

$\Delta\Theta_c \equiv [\Theta_{cm} - \Theta_{cs}]$: Differential collective control (rads.), (2.28)

$\Delta B_{lc} \equiv [B_{lcm} - B_{lcs}]$: Differential cyclic control (rads.). (2.29)

Aerodynamic derivatives are constants of proportionality which allow us to express the incremental aerodynamic forces and moments acting on the helicopters in terms of the aforementioned incremental variables. Appendix 2.7 contains the incremental aerodynamic forces and moments acting on the TLHS.

Substituting the incremental aerodynamic forces and moments of Appendix 2.7 into the simpified incremental equations of Appendix 2.6 gives the final seven linear second order ordinary differential equations describing the the longitudinal dynamics of the TLHS near hover. These equations appear in Appendix 2.8. The equations in Appendix 2.8 can then be rearranged to obtain the following 12^{th} order state space model:

$$\dot{\underline{x}}_p = A_p \underline{x}_p + B_p \underline{u}_p ; \qquad \underline{x}_p \in \mathbf{R^{12}}, \quad \underline{u}_p \in \mathbf{R^4} \tag{2.30}$$

$$\underline{x}_p \equiv [\, \Sigma\dot{z} \parallel \Delta x \;\; \Delta\theta \;\; \Delta\dot{x} \;\; \Delta\dot{\theta} \parallel \Sigma\theta \;\; \Delta z \;\; x_L' \;\; \Sigma\dot{x} \;\; \Sigma\dot{\theta} \;\; \Delta\dot{z} \;\; \dot{x}_L' \,] \tag{2.31}$$

$$\underline{u}_p \equiv [\, \Sigma\Theta_c \parallel \Delta B_{lc} \parallel \Delta\Theta_c \;\; \Sigma B_{lc} \,]^T. \tag{2.32}$$

where the symbol $\parallel$ is used to partition the state and control vectors.

The matrices A_p and B_p are given in Table 2.4.1a and 2.4.1b, respectively. TLHS parameter values are provided in Table 2.4.2 as well as in Appendix 1. Table 2.4.3 summarizes the important Twin Lift geometrical relationships discussed in this chapter. It is emphasized that all state and control variables in the linear model are, by definition, incremental (small signal) quantities and thus represent small perturbations from their equilibrium (large signal) counterparts. This model shall be used to develop the two AFCS designs presented in this thesis. One AFCS is for the Equal Tether Configuration ($H_m = H_s$) and the other for the Unequal Tether Configuration ($H_m \neq H_s$).

Table 2.4.1a Linear Model For Longitudinal Dynamics of TLHS Near Hover

$$A_p =$$

$\frac{Z_w}{1+\mu}$											
			1								
				1							
	$-\mu w_A^2$	$-[g(1+\mu)+\mu w_A^2 h]$	X_u		$-2\mu w_A^2 S H_s$		$-2\mu w_A^2 S$				
	$-\epsilon\mu w_A^2$	$-\epsilon\mu w_A^2 (h+H_A)$	M_u	M_q	$-2\mu\epsilon w_A^2 S H_s$		$-2\mu\epsilon w_A^2 S$				
									1		
										1	
											1
	$\frac{\mu}{2} w_A^2 S$	$\frac{\mu}{2} w_A^2 Sh$			$-g\left[1+\mu S\frac{H_s}{H_A}\right]$		μw_A^2	X_u			
	$\frac{\mu}{2}\epsilon w_A^2 S$	$\frac{\mu}{2}\epsilon w_A^2 Sh$			$-\epsilon\mu w_A^2 S H_s$		$\epsilon\mu w_A^2$	M_u	M_q		
	ZTS	$ZTSh$			$4TH_s$	$-4T\hat{H}_A$	$4T$			$Z_w TJ$	
	$-\left[\frac{\mu}{2} w_A^2 S\right] V$	$-\left[\frac{\mu}{2} w_A^2 S\right] Vh$			$g\left[1+\mu S\frac{H_s}{H_A}\right]+F$	$4T\delta_L \hat{Z}\hat{H}_A$	D	E	$-M_q(h+H_s)$	$-Z_w TJ\delta_L \hat{Z}$	

Definitions: $\Psi \equiv 1 + e_b + 4\mu \hat{Z}^2 \delta_L (1 - \delta_L)$

$D \equiv -\omega_A{}^2 [1 + \mu + (h + H_s)\mu\epsilon + (4 T \delta_L \hat{Z} / \omega_A{}^2)]$

$E \equiv -[X_u + M_u (h + H_s)]$

$F \equiv (h + H_s)\epsilon\mu\omega_A{}^2 S H_s - \omega_A{}^2 H_s - 4 T \delta_L \hat{Z} H_s$

$J \equiv [\mu \delta_L \hat{Z} \omega_A{}^2]^{-1}$

$T \equiv [J \Psi]^{-1}$

$V \equiv 1 + (h + H_s)\epsilon + (1/\mu) + (4 \delta_L{}^2 \hat{Z}^2 / \Psi)$

Notes:
1. Places where no entry appears implies a zero entry.
2. This model can also be used to study the lateral dynamics. All that is needed is a simple transformation of coordinates.

Units: radians, feet, radians/second, feet/second, pounds

Table 2.4.1b Linear Model For Longitudinal Dynamics of TLHS Near Hover

$$B_p = \begin{bmatrix} \frac{Z_{\theta c}}{1+\mu} & & & \\ & & & \\ & & & \\ & X_{Blc} & & \\ & M_{Blc} & & \\ & & & \\ & & & \\ & & & \\ & & & X_{Blc} \\ & & & M_{Blc} \\ & & Z_{\theta c}{}^{TJ} & \\ & & -Z_{\theta c}{}^{TJ}\delta_L \hat{Z} & -[X_{Blc}+M_{Blc}(h+H_s)] \end{bmatrix}$$

TLHS Parameters:

$\mu \equiv [\, M_L + M_B \,] / 2\, M_H$ $\qquad$ $\delta_L \equiv M_L / [\, M_L + M_B \,]$ $\qquad$ $\omega_A{}^2 \equiv (\, g / H_A \,)$

$H_A \equiv 2\, H_s\, H_m / [\, H_s + H_m \,]$ $\qquad$ $\hat{H}_A \equiv H_A / L$ $\qquad$ $S \equiv [\, H_m - H_s \,] / [\, H_s + H_m \,]$

$\varepsilon \equiv M_H\, h / I_y$ $\qquad$ $\hat{Z} \equiv Z / L$ $\qquad$ $e_b \equiv 2\, I_B / M_H\, L^2$

$I_B \equiv (\, 1 / 12 \,)\, M_B\, L^2$

Notes: 1. Refer to Appendix 1 or Table 2.4.2 for parameter values.

2. Although the above model assumes angles to be measured in radians, most discussions throughout the thesis assumes angles to be measured in degrees. Displacements and velocities are assumed to be measured in feet and feet/second, respectively. Forces (weights) are assumed to be measured in pounds.

Table 2.4.2: TLHS Nominal Parameter Values

UH-60A Blackhawk Helicopter Helicopter Parameters

W_H = 14000 lbs. - Helicopter weight.

M_H = 434.78 slugs - Helicopter mass.

I_y = 5700 slug ft^2 - Helicopter moment of inertia about pitch axis.

h = 3.6 ft.- Distance from helicopter c.g. to helicopter-tether attachment point.

UH-60A Control Derivatives Near Hover

X_{Blc} = 27.4 ft / $radsec^2$ - Horizontal acceleration per radian of cyclic.

$Z_{\Theta c}$ = 340.9 ft / rad sec^2 - Vertical acceleration per radian of collective.

M_{Blc} = - 47.24 rad / rad sec^2 - Angular acceleration per radian of cyclic.

UH-60A Aerodynamic Derivatives Near Hover

X_u = - 0.06 ft sec^{-2} / ft sec^{-1} - Used to characterize horizontal drag forces due to horizontal motion.

Z_w = - 0.346 ft sec^{-2} / ft sec^{-1} - Used to characterize vertical drag forces due to vertical motion.

M_u = 0.041 rad sec^{-2} / rad sec^{-1} - Used to characterize pitching moments due to forward motion.

M_q = - 3.1 rad sec^{-2} / rad sec^{-1} - Used to characterize rotational damping due to pitching.

Tether Lengths

$H_m = H$ = 13.25 ft. - Master helicopter tether length.

H_s - Slave helicopter tether length; $H_s = 2H_m$ in Chapters 3 and 4 (Equal Tether Problem).

$H_s = 2H_m$ in Chapters 5 and 6 (Unequal Tether Problem).

Spreader Bar and Load Parameters

L = 69 ft.

W_B = 644 lbs - Spreader bar weight.

M_B = 20 slugs - Spreader bar mass.

I_B = 7935 slug ft^2 - Spreader bar moment of inertia about its c.g.

Z = 34.5 ft. - Distance that load is suspended below spreader bar c.g.

W_L = 12000 lbs. - Weight of load.

M_L = 372.67 slugs - Mass of load.

g = 32.2 ft / sec^2 - acceleration due to gravity.

Table 2.4.3: Important Twin Lift Geometric Relationships

$$\Delta x = - [h \Delta\theta + H_m \varepsilon_m - H_s \varepsilon_s]$$

$$= [h \theta_s + H_s \varepsilon_s] - [h \theta_m + H_m \varepsilon_m]$$

$$\Delta z = L \varepsilon_B$$

$$x_L' = 0.5 [H_m \varepsilon_m + H_s \varepsilon_s] - H_s \Sigma\theta$$

$$= 0.5 [H_m (\varepsilon_m - \theta_m) + H_s (\varepsilon_s - \theta_s)] + 0.5 [H_m - H_s] \theta_m$$

$$\varepsilon_m = \{ 2 [x_L' + H_s \Sigma\theta] - [\Delta x + h \Delta\theta] \} / 2 H_m$$

$$\varepsilon_s = \{ 2 [x_L' + H_s \Sigma\theta] + [\Delta x + h \Delta\theta] \} / 2 H_s$$

$$x_L - \Sigma x = (h + H_s) \Sigma\theta + \hat{Z} \Delta z + x_L'$$

2.5 Classical Derivation of Linear Model

In the previous section a linear model was developed for the longitudinal dynamics of a TLHS near hovering trim. The development was rigorous and based on Lagrangian methods. Although rigorous and correct, the Lagrangian method provides little incite into the physics of Twin Lift. This is because the method relies on energy concepts which, for complicated systems, provide limited incite. In order to provide incite into the physics of Twin LIft, we shall derive the same linear model using the classical Newtonian approach. In doing so expressions are obtained for important quantities such as the tensions in the tethers and load cables. For simplicity, small angle assumptions shall be made from the very beginning. First, we shall consider the helicopters and then the load-bar assembly.

2.5.1 Helicopter Equations

Consider the free-body diagram for the master helicopter shown in Fig. 2.5.1. The figure shows all external forces and moments which act on the master helicopter. These include aerodynamic forces and moments, the force of gravity, the force due to the tension in the master tether, and the equilibrium (large signal) component of rotor thrust. A similar free-body diagram can be drawn for the slave helicopter.

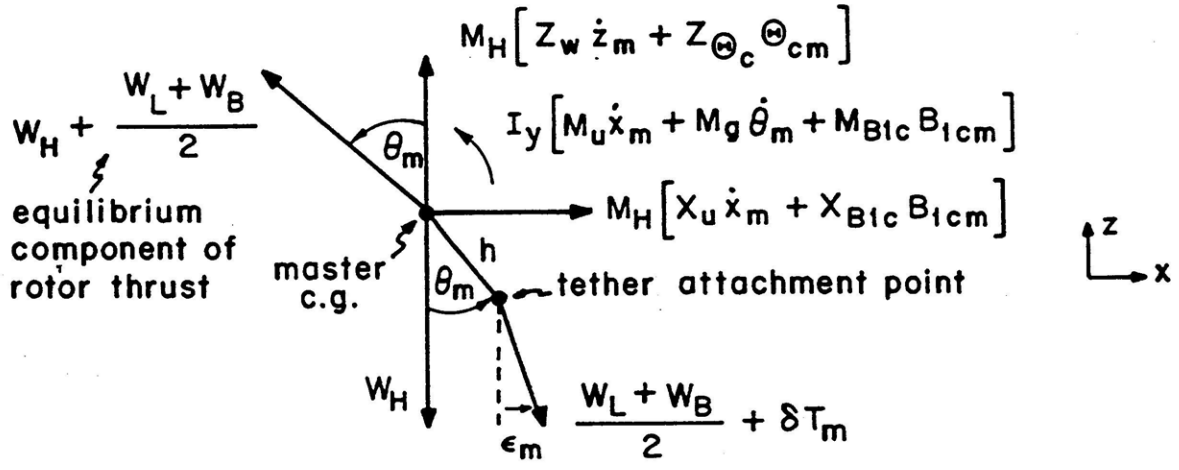

Fig. 2.5.1.1: Free Body Diagram For Master Helicopter.

To obtain the equations of motion for the master and slave helicopters we apply Newton's second law of motion.

First, we use small angle assumptions to resolve the rotor and tether forces into vertical and horizontal components. This is shown in Fig. 2.5.1.2.

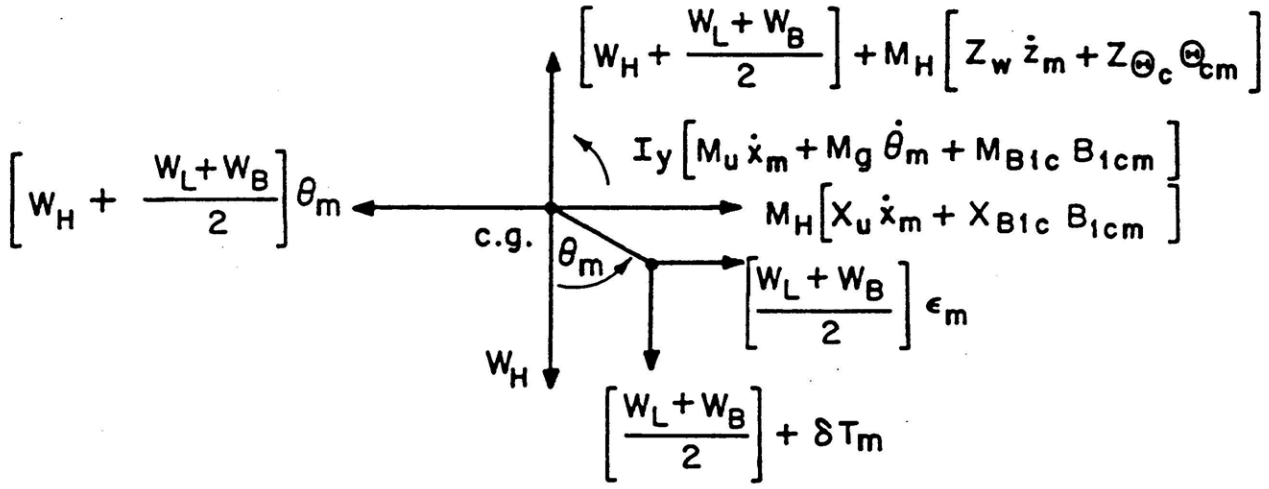

Fig. 2.5.1.2: Free Body Diagram for Master Helicopter.

Summing forces in the z and x directions gives us the following equations for the master and slave helicopters.

$$M_H \ddot{z}_m = M_H[Z_w \dot{z}_m + Z_{\Theta c} \Theta_{cm}] - \delta T_m \quad (2.33)$$

$$M_H \ddot{z}_s = M_H[Z_w \dot{z}_s + Z_{\Theta c} \Theta_{cs}] - \delta T_s \quad (2.34)$$

$$M_H \ddot{x}_m = 0.5[W_L + W_B]\,\varepsilon_m - [W_H + 0.5(W_L + W_B)]\,\theta_m + M_H[X_u \dot{x}_m + X_{Blc} B_{lcm}] \quad (2.35)$$

$$M_H \ddot{x}_s = 0.5[W_L + W_B]\,\varepsilon_s - [W_H + 0.5(W_L + W_B)]\,\theta_s + M_H[X_u \dot{x}_s + X_{Blc} B_{lcs}] \quad (2.36)$$

Taking moments about the helicopter c.g.'s gives us the following equations:

$$I_y \ddot{\theta}_m = 0.5[W_L+W_B]\,h\,\varepsilon_m - 0.5[W_L+W_B]\,h\,\theta_m + I_y[M_u \dot{x}_m + M_q \dot{\theta}_m + M_{Blc} B_{lcm}] \quad (2.37)$$

$$I_y \ddot{\theta}_s = 0.5[W_L+W_B]\,h\,\varepsilon_s - 0.5[W_L+W_B]\,h\,\theta_s + I_y[M_u \dot{x}_s + M_q \dot{\theta}_s + M_{Blc} B_{lcs}] \quad (2.38)$$

Taking the average and difference of each pair of equations gives us the following set of equations:

$$M_H \Sigma\ddot{z} = M_H[Z_w \ \Sigma\dot{z} + Z_{\Theta c} \Sigma\Theta_c] - 0.5[\delta T_m + \delta T_s] \tag{2.39}$$

$$M_H \Delta\ddot{z} = M_H[Z_w \ \Delta\dot{z} + Z_{\Theta c} \Delta\Theta_c] - [\delta T_m - \delta T_s] \tag{2.40}$$

$$M_H \Sigma\ddot{x} = 0.5[W_L + W_B] \Sigma\varepsilon - [W_H + 0.5(W_L + W_B)] \Sigma\theta + M_H[X_u \Sigma\dot{x} + X_{Blc} \Sigma B_{lc}] \tag{2.41}$$

$$M_H \Delta\ddot{x} = 0.5[W_L + W_B] \Delta\varepsilon - [W_H + 0.5(W_L + W_B)] \Delta\theta + M_H[X_u \Delta\dot{x} + X_{Blc} \Delta B_{lc}] \tag{2.42}$$

$$I_y \Sigma\ddot{\theta} = 0.5[W_L+W_B] \, h \, \Sigma\varepsilon - 0.5[W_L+W_B] \, h \, \Sigma\theta + I_y[M_u \Sigma\dot{x} + M_q \Sigma\dot{\theta} + M_{Blc} \Sigma B_{lc}] \tag{2.43}$$

$$I_y \Delta\ddot{\theta} = 0.5[W_L+W_B] \, h \, \Delta\varepsilon - 0.5[W_L+W_B] \, h \, \Delta\theta + I_y[M_u \Delta\dot{x} + M_q \Delta\dot{\theta} + M_{Blc} \Delta B_{lc}] \tag{2.44}$$

Defining the parameters:

$$\mu \equiv 0.5 \, [M_L + M_B] / M_H \tag{2.45}$$

$$\varepsilon \equiv M_H \, h / I_y \tag{2.46}$$

we can rewrite eqs. (2.39) - (2.44) as follows:

$$\Sigma\ddot{z} = Z_w \ \Sigma\dot{z} + Z_{\Theta c} \Sigma\Theta_c - 0.5[\delta T_m + \delta T_s] / M_H \tag{2.47}$$

$$\Delta\ddot{z} = Z_w \ \Delta\dot{z} + Z_{\Theta c} \Delta\Theta_c - [\delta T_m - \delta T_s] / M_H \tag{2.48}$$

$$\Sigma\ddot{x} = \mu g \, \Sigma\varepsilon - [1 + \mu] \, g \, \Sigma\theta + X_u \Sigma\dot{x} + X_{Blc} \Sigma B_{lc} \tag{2.49}$$

$$\Delta\ddot{x} = \mu g \, \Delta\varepsilon - [1 + \mu] \, g \, \Delta\theta + X_u \Delta\dot{x} + X_{Blc} \Delta B_{lc} \tag{2.50}$$

$$\Sigma\ddot{\theta} = \varepsilon\mu g \, \Sigma\varepsilon - \varepsilon\mu g \, \Sigma\theta + M_u \Sigma\dot{x} + M_q \Sigma\dot{\theta} + M_{Blc} \Sigma B_{lc} \tag{2.51}$$

$$\Delta\ddot{\theta} = \varepsilon\mu g \, \Delta\varepsilon - \varepsilon\mu g \, \Delta\theta + M_u \Delta\dot{x} + M_q \Delta\dot{\theta} + M_{Blc} \Delta B_{lc} \tag{2.52}$$

The quantities δT_m and δT_s represent the incremental (small signal) components of tension in the master and slave tethers. They shall be computed shortly.

In Table 2.4.3 expressions were given for ε_m and ε_s. From these expressions it follows that

$$\Sigma\varepsilon = \{ \, S \, [\Delta x + h \, \Delta\theta] + 2[x_L' + H_s \, \Sigma\theta] \, \} / 2 \, H_A \tag{2.53}$$

$$\Delta\varepsilon = -\{ [\Delta x + h\,\Delta\theta] + 2S[x_L' + H_s\,\Sigma\theta] \} / 2\,H_A \tag{2.54}$$

where

$$H_A \equiv 2H_s\,H_m / [H_s + H_m] \tag{2.55}$$

$$S \equiv [H_m - H_s] / [H_s + H_m] \tag{2.56}$$

Substituting eqs. (2.53) - (2.56) into eqs. (2.49) - (2.52) gives us the desired expressions for $\Delta\ddot{x}$, $\Delta\ddot{\theta}$, $\Sigma\ddot{x}$, and $\Sigma\ddot{\theta}$. After finding expressions for δT_m and δT_s we can obtain the desired $\Sigma\ddot{z}$ and $\Delta\ddot{z}$ equations from eqs. (2.47) - (2.48). By desired we mean the equations in Table 2.4.1.

It should be noted that eqs. (2.47) - (2.52) are valid for both the Equal Tether ($H_m = H_s$) and Unequal Tether ($H_m \neq H_s$) Configurations. In fact, the only place that the tether lengths enter is via $\Sigma\varepsilon$ and $\Delta\varepsilon$. The incite that the above relationships provide should be apparent.

2.5.2 Spreader Bar Equations

To compute the tensions δT_m and δT_s we require a free-body diagram for the spreader bar. Such a diagram appears in Fig. 2.5.2.1. The figure contains all external forces which act on the

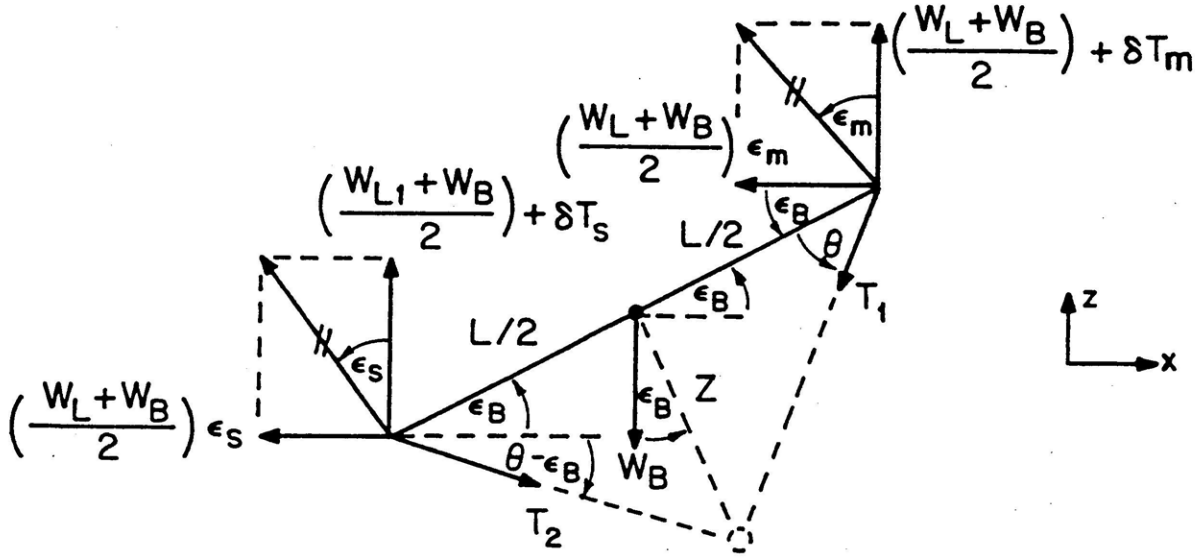

Fig. 2.5.2.1: Free Body Diagram For Spreader Bar.

spreader bar. These include gravity, the tether tension forces, and the load-cable tension forces. Again we note that it is assumed that the aerodynamic forces and moments which act on the spreader bar are negligible in comparison with the forces and moments shown in Fig. 2.5.2.1.

Summing forces in the z and x directions gives us the following equations:

$$M_B \ddot{z}_B = W_L + [\delta T_m + \delta T_s] - [T_1 \sin(\theta + \varepsilon_B) + T_2 \sin(\theta - \varepsilon_B)] \tag{2.57}$$

$$M_B \ddot{x}_B = - [W_L + W_B] \Sigma\varepsilon - [T_1 \cos(\theta + \varepsilon_B) + T_2 \cos(\theta - \varepsilon_B)] \tag{2.58}$$

where

$$z_B = z_L + Z \tag{2.59}$$

$$x_B = x_L - Z \varepsilon_B \tag{2.60}$$

Substituting the first order Taylor series expansions:

$$\sin(\theta \pm \varepsilon_B) \approx \sin\theta \pm \cos\theta \, \varepsilon_B \tag{2.61}$$

$$\cos(\theta \pm \varepsilon_B) \approx \cos\theta \mp \sin\theta \, \varepsilon_B \tag{2.62}$$

into eqs. (2.57) - (2.58) gives us

$$M_B \ddot{z}_B = W_L + [\delta T_m + \delta T_s] - T_1 [\sin\theta + \cos\theta \, \varepsilon_B] - T_2 [\sin\theta - \cos\theta \, \varepsilon_B] \tag{2.63}$$

$$M_B \ddot{x}_B = - (W_L + W_B) \Sigma\varepsilon - T_1 [\cos\theta - \sin\theta \, \varepsilon_B] + T_2 [\cos\theta + \sin\theta \, \varepsilon_B] \tag{2.64}$$

Taking moments about the spreader bar c.g. gives us the following expression:

$$I_B \ddot{\varepsilon}_B = 0.5 [\delta T_m - \delta T_s] L - 0.5 [T_1 - T_2] L \sin\theta \tag{2.65}$$

where

$$I_B = 2 (M_B / L) \int_0^{L/2} x^2 \, dx = (1 / 12) M_B L^2 \tag{2.66}$$

It thus follows from eqs. (2.63) and (2.65) that

$$\delta T_m + \delta T_s = M_B \ddot{z}_B - W_L + [T_1 + T_2] \sin\theta + [T_1 - T_2] \cos\theta \, \varepsilon_B \tag{2.67}$$

$$\delta T_m - \delta T_s = 2 (I_B / L) \ddot{\varepsilon}_B + [T_1 - T_2] \sin\theta \tag{2.68}$$

From these equations we see that δT_m and δT_s can be found if the load-cable tensions, T_1 and T_2, were known. We now compute expressions for them.

2.5.3 Load-Cable Tensions

The free body diagram for the load when the system is in equilibrium is given in Fig. 2.5.3.1.

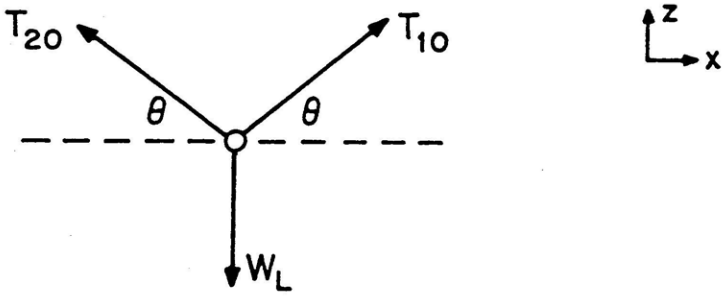

Fig. 2.5.3.1: Free Body Diagram For Payload when System is in Equilibrium.

From the diagram it can easily be shown that

$$T_{10} = T_{20} = T = 0.5\ (W_L / \sin\theta) \tag{2.69}$$

Now suppose the system is not in equilibrium. In such a case we let

$$T_1 = T + \delta T_1 \tag{2.70}$$

$$T_2 = T + \delta T_2 \tag{2.71}$$

and the free body diagram for the load becomes that shown in Fig. 2.5.3.2.

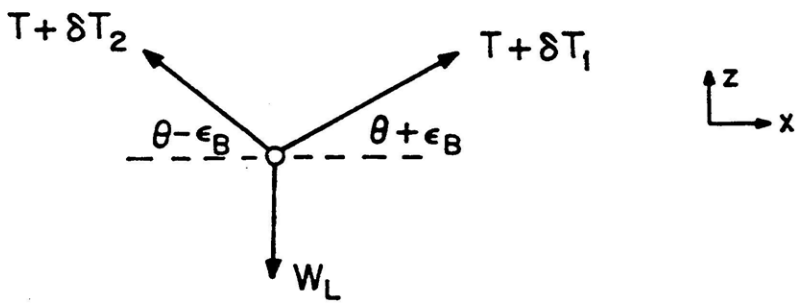

Fig. 2.5.3.2: Free Body Diagram for Payload.

Summing forces in the z and x directions and using the Taylor expansions in eqs. (2.61) - (2.62) gives us the following equations:

$$M_L \ddot{z}_L = [T + \delta T_1] [\sin\theta + \cos\theta \, \varepsilon_B] + [T + \delta T_2] [\sin\theta - \cos\theta \, \varepsilon_B] - W_L \quad (2.72)$$

$$M_L \ddot{x}_L = [T + \delta T_1] [\cos\theta - \sin\theta \, \varepsilon_B] - [T + \delta T_2] [\cos\theta + \sin\theta \, \varepsilon_B] \quad (2.73)$$

Rearranging these equations and neglecting products of small terms gives us the followingg equations:

$$M_L \ddot{z}_L = [2T \sin\theta - W_L] + [\delta T_1 + \delta T_2] \sin\theta \quad (2.74)$$

$$M_L \ddot{x}_L = - 2T\sin\theta \, \varepsilon_B + [\delta T_1 - \delta T_2] \cos\theta \quad (2.75)$$

Using the fact that $2T \sin\theta = W_L$ then gives us

$$\delta T_1 + \delta T_2 = M_L \ddot{z}_L / \sin\theta \quad (2.76)$$

$$\delta T_1 - \delta T_2 = M_L [\ddot{x}_L + g \, \varepsilon_B] / \cos\theta \quad (2.77)$$

From eqs. (2.76) - (2.77) we then get

$$\delta T_1 = 0.5 [M_L \ddot{z}_L / \sin\theta + M_L [\ddot{x}_L + g \, \varepsilon_B] / \cos\theta] \quad (2.78)$$

$$\delta T_2 = 0.5 [M_L \ddot{z}_L / \sin\theta - M_L [\ddot{x}_L + g \, \varepsilon_B] / \cos\theta] \quad (2.79)$$

With these expressions we can now compute the individual tether tensions, δT_m and δT_s.

2.5.4 Tether Tensions

Substituting eqs. (2.70) - (2.71) into eqs. (2.67) - (2.68), and using the fact that $2T \sin\theta = W_L$, gives us

$$\delta T_m + \delta T_s = M_B \ddot{z}_B + [\delta T_1 + \delta T_2] \sin\theta + [\delta T_1 - \delta T_2] \cos\theta \, \varepsilon_B \quad (2.80)$$

$$\delta T_m - \delta T_s = 2 (I_B / L) \ddot{\varepsilon}_B + [\delta T_1 - \delta T_2] \sin\theta \quad (2.81)$$

Sustituting eqs. (2.76) - (2.77) into these, and neglecting products of small terms, gives us

$$\delta T_m + \delta T_s = M_B \ddot{z}_B + M_L \ddot{z}_L \tag{2.82}$$

$$\delta T_m - \delta T_s = 2 (I_B / L) \ddot{\varepsilon}_B + M_L [\ddot{x}_L + g \varepsilon_B] \tan\theta \tag{2.83}$$

where $\tan\theta = 2 (Z / L) = 2 \hat{Z}$.

We now note that z_B may be written as follows:

$$z_B = z_L + Z \tag{2.84}$$

$$= z_s - [h + H_s - 0.5 \ L \varepsilon_B] \tag{2.85}$$

$$= z_m - [h + H_s + 0.5 \ L \varepsilon_B] \tag{2.86}$$

$$= \Sigma z - [h + 0.5 (H_m + H_s)] \tag{2.87}$$

These imply that

$$\ddot{z}_B = \ddot{z}_L = \Sigma \ddot{z} \tag{2.88}$$

Using this fact and noting that $\tan\theta = 2 (Z / L) = 2 \hat{Z}$ and $\varepsilon_B = \Delta z / L$ we can rewrite eqs. (2.82) - (2.83) as follows:

$$\delta T_m + \delta T_s = (M_L + M_B) \Sigma \ddot{z} \tag{2.89}$$

$$\delta T_m - \delta T_s = M_H e_b \Delta \ddot{z} + 2 \hat{Z} \ M_L [\ddot{x}_L + \omega_A{}^2 \hat{H}_A \Delta z] \tag{2.90}$$

where

$$e_b \equiv 2 I_B / M_H L^2 \tag{2.91}$$

$$\omega_A{}^2 \equiv g / H_A \tag{2.92}$$

$$\hat{H}_A \equiv H_A / L \tag{2.93}$$

From eqs. (2.89) - (2.90) it thus follows that

$$\delta T_m = 0.5 [(M_L + M_B) \Sigma \ddot{z} + M_H e_b \Delta \ddot{z} + 2 \hat{Z} \ M_L (\ddot{x}_L + \omega_A{}^2 \hat{H}_A \ \Delta z)] \tag{2.94}$$

$$\delta T_s = 0.5 [(M_L + M_B) \Sigma \ddot{z} - M_H e_b \Delta \ddot{z} + 2 \hat{Z} \ M_L (\ddot{x}_L - \omega_A{}^2 \hat{H}_A \Delta z)] \tag{2.95}$$

With these the equations for $\Sigma\ddot{z}$ and $\Delta\ddot{z}$, eqs. (2.47) - (2.48) become

$$\Sigma\ddot{z} = Z_w \Sigma\dot{z} + Z_{\Theta c} \Sigma\Theta_c - \mu \Sigma\ddot{z} \tag{2.96}$$

$$\Delta\ddot{z} = Z_w \Delta\dot{z} + Z_{\Theta c} \Delta\Theta_c - [e_b \Delta\ddot{z} + 2 \hat{Z} (M_L / M_H) (\ddot{x}_L + \omega_A{}^2 \hat{H}_A \Delta z)] \tag{2.97}$$

or

$$\Sigma\ddot{z} = [1 / (1 + \mu)] [Z_w \Sigma\dot{z} + Z_{\Theta c} \Sigma\Theta_c] \tag{2.98}$$

$$[1 + e_b] \Delta\ddot{z} = Z_w \Delta\dot{z} + Z_{\Theta c} \Delta\Theta_c - 4 \mu \delta_L \hat{Z} (\ddot{x}_L + \omega_A{}^2 \hat{H}_A \Delta z) \tag{2.99}$$

where

$$\delta_L \equiv M_L / (M_L + M_B) \tag{2.100}$$

We note that eq. (2.98) is exactly the equation for $\Sigma\ddot{z}$ in Table 2.4.1. To get the expressions for $\Delta\ddot{z}$ and $\ddot{x}_L'$, given in Table 2.4.1, we first need an expression for $\ddot{x}_L$.

2.5.5 Load Equation

To obtain an expression for $\ddot{x}_L$ we consider thee load-bar assembly. A free body diagram for the load-bar assembly is given in Fig. 2.5.5.1.

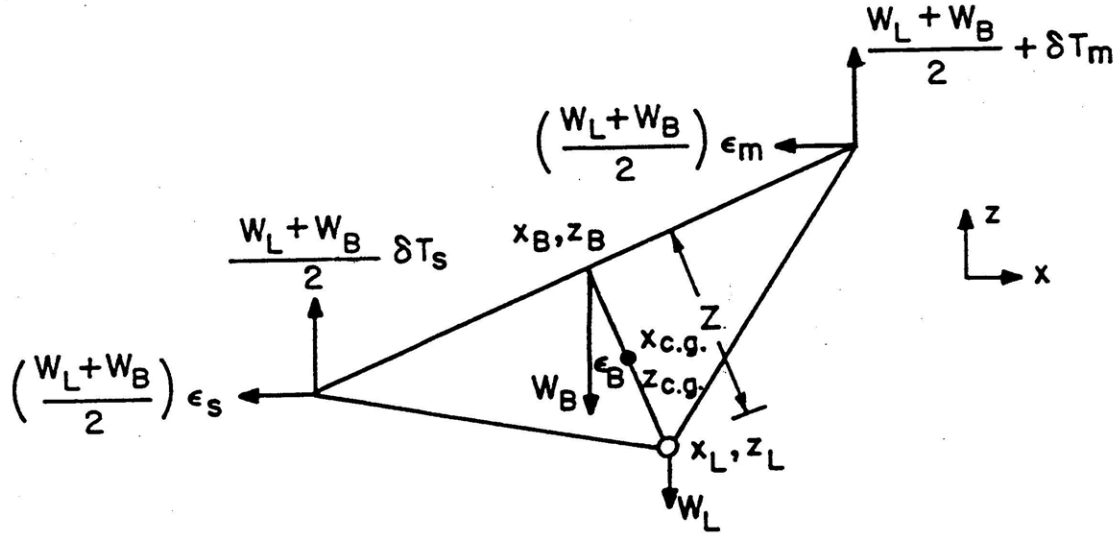

Fig. 2.5.5.1: Free Body Diagram for Load-Bar Assembly.

We want to apply Newton's law at the center of gravity of the load-bar assembly. Suppose that the load-bar assembly has c.g. at $(x_{c.g.}, z_{c.g.})$. By definition $x_{c.g.}$ and $z_{c.g.}$ must satisfy:

$$(M_L + M_B)\, z_{c.g.} = M_L\, z_L + M_B\, z_B \tag{2.101}$$

$$(M_L + M_B)\, x_{c.g.} = M_L\, x_L + M_B\, x_B \tag{2.102}$$

Recalling that $z_B = z_L + Z$ znd $x_B = x_L - Z\,\varepsilon_B$ we then have

$$z_{c.g.} = z_L + M_B\, Z / (M_L + M_B) \tag{2.103}$$

$$x_{c.g.} = x_L - M_B\, \hat{Z}\, \Delta z \;/ (M_L + M_B) \tag{2.104}$$

Applying Newton's law at $(x_{c.g.}, z_{c.g.})$ gives us

$$(M_L + M_B)\, \ddot{x}_{c.g.} + (W_L + W_B)\, \Sigma\varepsilon = 0 \tag{2.105}$$

Substituting eq. (2.104) into this gives us

$$(M_L + M_B)\, \ddot{x}_L - M_B\, Z\, \Delta z + (W_L + W_B)\, \Sigma\varepsilon = 0 \tag{2.106}$$

or

$$\ddot{x}_L = (1 - \delta_L)\, \hat{Z}\, \Delta\ddot{z} - g\, \Sigma\varepsilon \tag{2.107}$$

It should be noted that this equation can also be obtained from eqs. (2.60), (2.64), (2.69) - (2.71), and (2.76) - (2.77). Substituting this equation into eq. (2.99) gives us the desired equation for $\Delta\ddot{z}$; i.e. the one in Table 2.4.1. To get the desired equation for $\ddot{x}_L'$ we recall that

$$x_L' = x_L - [\Sigma x + (h + H_s)\, \Sigma\theta + \hat{Z}\, \Delta z] \tag{2.108}$$

Using this relationship together with eq. (2.107) and the equations for $\Delta\ddot{x}$, $\Delta\ddot{\theta}$, $\Sigma\ddot{x}$, $\Sigma\ddot{\theta}$, $\Delta\ddot{z}$ gives us the desired equation for $\ddot{x}_L'$.

Table 2.5.5.1 summarizes the classical derivation. Table 2.5.5.2 gives the Twin Lift equations written in terms of $\Sigma\varepsilon$ and $\Delta\varepsilon$. With the exception of the $\ddot{x}_L$' equation, the equations in Table 2.5.5.2 show no explicit dependence on the tether lengths.

2.6 Summary

In this section the TLHS longitudinal configuration was described. The relevant controls for controlling this configuration were identified and discussed. A seven degree of freedom linear model was then developed for the longitudinal rigid body dynamics of the TLHS near hover. This model shall serve as the basis for developing the two AFCS's presented in this thesis. The model assumes that both helicopters are identical. Other, more subtle, properties of the model shall be disclosed in Chapters 3 and 5 where the "Equal Tether" and "Unequal Tether" configurations are analyzed.

Table 2.5.5.1: Summary of Classical Derivation.

Helicopters

$$M_H \Sigma\ddot{z} = M_H[Z_w \ \Sigma\dot{z} + Z_{\Theta c} \Sigma\Theta_{cm}] - 0.5[\delta T_m + \delta T_s]$$

$$M_H \Delta\ddot{z} = M_H[Z_w \ \Delta\dot{z} + Z_{\Theta c} \Delta\Theta_{cm}] - [\delta T_m - \delta T_s]$$

$$M_H \Sigma\ddot{x} = 0.5[W_L + W_B] \Sigma\varepsilon - [W_H + 0.5(W_L + W_B)] \Sigma\dot{\theta} + M_H[X_u \Sigma\dot{x} + X_{Blc} \Sigma B_{lc}]$$

$$M_H \Delta\ddot{x} = 0.5[W_L + W_B] \Delta\varepsilon - [W_H + 0.5(W_L + W_B)] \Delta\dot{\theta} + M_H[X_u \Delta\dot{x} + X_{Blc} \Delta B_{lc}]$$

$$I_y \Sigma\ddot{\theta} = 0.5[W_L + W_B] \, h \, \Sigma\varepsilon - 0.5[W_L + W_B] \, h \, \Sigma\theta + I_y[M_u \Sigma\dot{x} + M_q \Sigma\dot{\theta} + M_{Blc} \Sigma B_{lc}]$$

$$I_y \Delta\ddot{\theta} = 0.5[W_L + W_B] \, h \, \Delta\varepsilon - 0.5[W_L + W_B] \, h \, \Delta\theta + I_y[M_u \Delta\dot{x} + M_q \Delta\dot{\theta} + M_{Blc} \Delta B_{lc}]$$

Spreader Bar

$$M_B \ddot{z}_B = [\delta T_m + \delta T_s] - [\delta T_1 + \delta T_2] \sin\theta \ , \ \ddot{z}_B = \Sigma\ddot{z}$$

$$M_B \ddot{x}_B = - [W_L + W_B] \Sigma\varepsilon - [\delta T_1 - \delta T_2] \cos\theta + W_L \varepsilon_B$$

$$I_B \ddot{\varepsilon}_B = 0.5 [\delta T_m - \delta T_s] L - 0.5 [\delta T_1 - \delta T_2] L \sin\theta \ , \ \varepsilon_B = \Delta z / L$$

Load-Cable Tensions

$$M_L \ddot{z}_L = [\delta T_1 + \delta T_2] \sin\theta \qquad \delta T_1 + \delta T_2 = M_L \ddot{z}_L / \sin\theta$$

$$M_L \ddot{x}_L = - 2W_L \varepsilon_B + [\delta T_1 - dT_2] \cos\theta \qquad \delta T_1 - \delta T_2 = M_L [\ddot{x}_L + g \varepsilon_B] / \cos\theta$$

Load-Bar Assembly

$$(M_L + M_B) \ddot{x}_{c.g.} + (W_L + W_B) \Sigma\varepsilon = 0$$

$$x_{c.g.} = x_L - M_B \hat{Z} \Delta z \ / (M_L + M_B) \qquad \ddot{x}_L = (1 - \delta_L) \hat{Z} \Delta\ddot{z} - g \Sigma\varepsilon$$

Tether Tensions

$$\delta T_m + \delta T_s = M_B \ddot{z}_B + [\delta T_1 + \delta T_2] \sin\theta = (M_B + M_L) \Sigma\ddot{z}$$

$$\delta T_m - \delta T_s = 2 (I_B / L) \ddot{\varepsilon}_B + [\delta T_1 - \delta T_2] \sin\theta = 2 (I_B / L^2) \Delta\ddot{z} + M_L[\ddot{x}_L + g \varepsilon_B] \tan\theta$$

$$\Sigma\varepsilon = \{S[\Delta x + h \Delta\theta] + 2[x_L' + H_s \Sigma\theta]\}/2H_A \quad \Delta\varepsilon = - \{[\Delta x + h \Delta\theta] + 2S[x_L' + H_s \Sigma\theta]\}/2H_A$$

Table 2.5.5.2 : Twin Lift Equations Written in Terms of $\Sigma\varepsilon$ and $\Delta\varepsilon$

$$\Sigma\ddot{z} = [1 / (1 + \mu)] [Z_w \ \Sigma\dot{z} + Z_{\Theta c} \Sigma\Theta_c]$$

$$\Delta\ddot{x} = \mu g \Delta\varepsilon - [1 + \mu] g \Delta\theta + X_u \Delta\dot{x} + X_{Blc} \Delta B_{lc}$$

$$\Delta\ddot{\theta} = \varepsilon \mu g \Delta\varepsilon - \varepsilon \mu g \Delta\theta + M_u \Delta\dot{x} + M_q \Delta\dot{\theta} + M_{Blc} \Delta B_{lc}$$

$$\Sigma\ddot{x} = \mu g \Sigma\varepsilon - [1 + \mu] g \Sigma\theta + X_u \Sigma\dot{x} + X_{Blc} \Sigma B_{lc}$$

$$\Sigma\ddot{\theta} = \varepsilon \mu g \Sigma\varepsilon - \varepsilon \mu g \Sigma\theta + M_u \Sigma\dot{x} + M_q \Sigma\dot{\theta} + M_{Blc} \Sigma B_{lc}$$

$$\Psi\Delta\ddot{z} = 4\mu\delta_L \hat{Z} g [\Sigma\varepsilon - (g / L) \Delta z] + Z_w \ \Delta\dot{z} + Z_{\Theta c} \Delta\Theta_c$$

$$\ddot{x}_L' = - [\Sigma\ddot{x} + (h + H_s) \Sigma\ddot{\theta} + \hat{Z} \Delta\ddot{z}] + \ddot{x}_L$$

$$= - [\Sigma\ddot{x} + (h + H_s) \Sigma\ddot{\theta} + \hat{Z} \Delta\ddot{z}] + [(1 - \delta_L) \hat{Z} \Delta\ddot{z} - g \Sigma\varepsilon]$$

Note: With the exception of the $\ddot{x}_L'$ equation, the above equations depend on the tether lengths only through $\Sigma\varepsilon$ and $\Delta\varepsilon$.

CHAPTER 3: ANALYSIS OF TLHS EQUAL TETHER MODEL

3.1 Introduction

In this chapter the linear model developed in Chapter 2 shall be analyzed using the nominal parameter values given in Table 2.4.2. In particular, the chapter will focus on the "Equal Tether Problem"; i.e. the case in which the master and slave tether lengths are equal ($H_m = H_s = H$). The chapter discusses the decoupling of the "Equal Tether Model" into three sets of differential equations which describe "3 Basic Motions" [1]. The natural modes of the Equal Tether Configuration are identified and discussed. Outputs are selected and performance and stability robustness specifications are presented using singular value ideas in the frequency domain. The purpose of the chapter is to provide a thorough understanding of the Equal Tether Model so that a high performance (high bandwidth) centralized AFCS can be developed in the next chapter.

3.2 The 3 Basic Motions

A seven degree of freedom linear model was developed in the previous chapter. This model characterizes the longitudinal rigid body dynamics of a TLHS near hover. When the helicopters are assumed to be identical and the tether lengths are assumed to be equal (Fig. 3.2.1), the 12^{th} order model decouples into three systems of differential equations. These three systems describe the "3 Basic Motions" of a TLHS. These three basic motions shall be referred to as the Average Vertical Motion, Symmetric Motion, and the Anti-Symmetric Motion. Their associated states and controls are listed in Table 3.2.1.

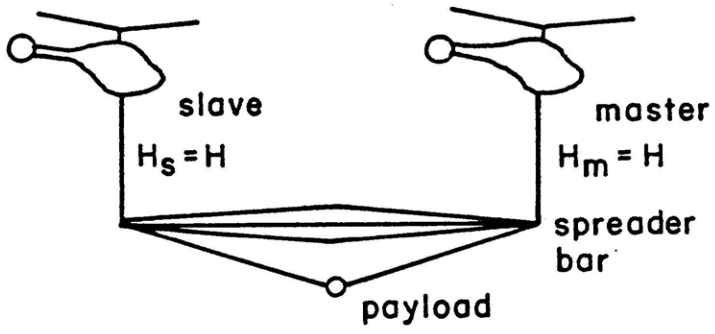

Fig. 3.2.1: Visualization of Equal Tether Configuration.

The Average Vertical Motion (AVM) refers simply to the average vertical velocity of the helicopters ($\Sigma\dot{z}$). This motion is controlled by issuing average collective commands ($\Sigma\Theta_c$). The AVM is similar to the vertical motion of a single hovering helicopter (Appendix 3). This motion is always decoupled from the Symmetric and Anti-Symmetric Motions; i.e. even if the tether lengths are unequal (Chapters 5 & 6). Fig. 3.2.2 shows a block diagram for the AVM.

Table 3.2.1: The 3 Basic Motions*

1. Average Vertical Motion (AVM) - 1 degree of freedom state: $\Sigma\dot{z}$ control: $\Sigma\Theta_c$
2. Symmetric Motion (SM) - 2 degrees of freedom states: Δx, $\Delta\theta$, $\Delta\dot{x}$, $\Delta\dot{\theta}$ control: ΔB_{lc}
3. Anti-Symmetric Motion (ASM) - 4 degrees of freedom states: $\Sigma\theta$, Δz, x_L', $\Sigma\dot{x}$, $\Sigma\dot{\theta}$, $\Delta\dot{z}$, $\dot{x}_L'$ controls: $\Delta\Theta_c$, ΣB_{lc}

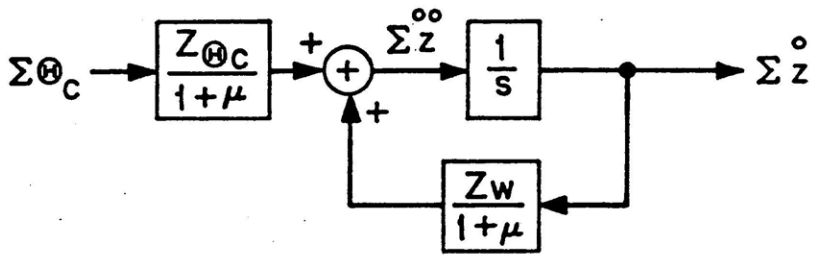

Fig. 3.2.2: Block Diagram for TLHS Average Vertical Motion (AVM).

* From now on all variables and controls are incremental (small signal) quantities and the adjective incremental (small signal) shall usually be suppressed.

The Symmetric Motion (SM), Fig. 3.2.3, refers to that portion of the TLHS motion which is symmetric about the equilibrium configuration (tethers vertical and spreader bar horizontal). The SM involves the Δx, $\Delta\theta$ degrees of freedom and is controlled by issuing differential cyclic commands (ΔB_{lc}). The SM is similar to that of a single hovering helicopter tethered to a fixed point in space [2].

The Anti-Symmetric Motion (ASM), Fig. 3.2.4, refers to that portion of the TLHS motion which is not symmetric with respect to the equilibrium configuration. The ASM involves the $\Sigma\dot{x}$, $\Sigma\theta$, Δz, x_L' degrees of freedom and is controlled by issuing differential collective ($\Delta\Theta_c$) and average cyclic commands (ΣB_{lc}). It can be shown that when the payload and spreader bar c.g.'s coincide ($Z = 0$), the ASM is similar to that of a hovering helicopter carrying a sling load [1].

The block diagrams for the SM and ASM are given in Fig. 3.2.5 and 3.2.6, respectively.

It is strongly emphasized that although the equations are decoupled in terms of the defined variables, they remain coupled in certain quantities such as the individual helicopter controls, velocities, and pitch attitudes. An important consequence of this is that although the AVM, SM, and ASM's may be treated separately to obtain incite about the Twin Lift control problem, they must subsequently be evaluated simultaneously, along with their corresponding controllers, so that important quantities can be untangled using the following relationships:

$$x_m = \Sigma x + 0.5\,\Delta x \qquad x_s = \Sigma x - 0.5\,\Delta x, \tag{3.1}$$

$$z_m = \Sigma z + 0.5\,\Delta z \qquad z_s = \Sigma z - 0.5\,\Delta z, \tag{3.2}$$

$$\theta_m = \Sigma\theta + 0.5\,\Delta\theta \qquad \theta_s = \Sigma\theta - 0.5\,\Delta\theta, \tag{3.3}$$

$$\Theta_{cm} = \Sigma\Theta_c + 0.5\,\Delta\Theta_c \qquad \Theta_{cs} = \Sigma\Theta_c - 0.5\,\Delta\Theta_c, \tag{3.4}$$

$$B_{lcm} = \Sigma B_{lc} + 0.5\,\Delta B_{lc} \qquad B_{lcs} = \Sigma B_{lc} - 0.5\,\Delta B_{lc}. \tag{3.5}$$

These relationships follow trivially from eqs. (2.1) - (2.7). They are needed for evaluating the response of the Equal Tether (and Unequal Tether) AFCS to exogenous signals; i.e. pilot commands, disturbances, and sensor noise.

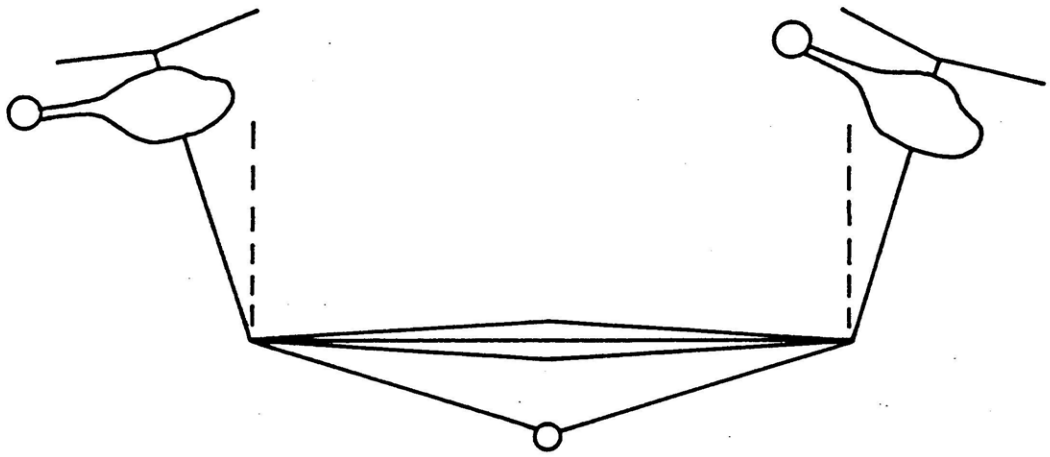

Fig. 3.2.3: Visualization of TLHS Symmetric Motion (SM).

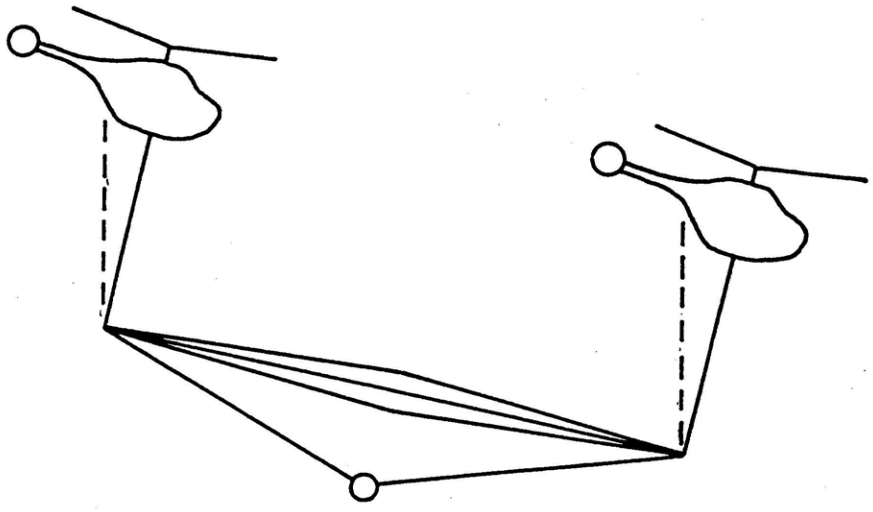

Fig. 3.2.4: Visualization of TLHS Anti-Symmetric Motion (ASM).

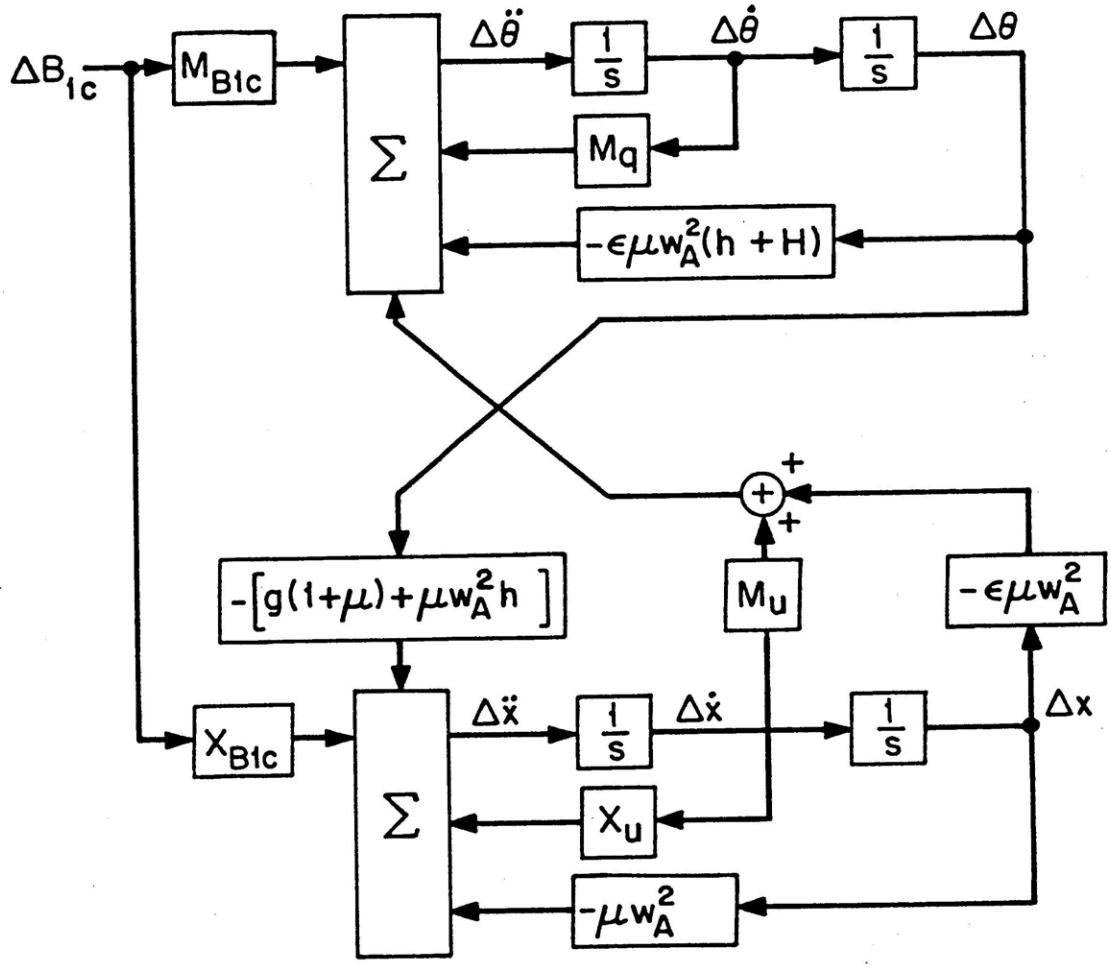

Fig. 3.2.5: Block Diagram for TLHS Symmetric Motion (SM).

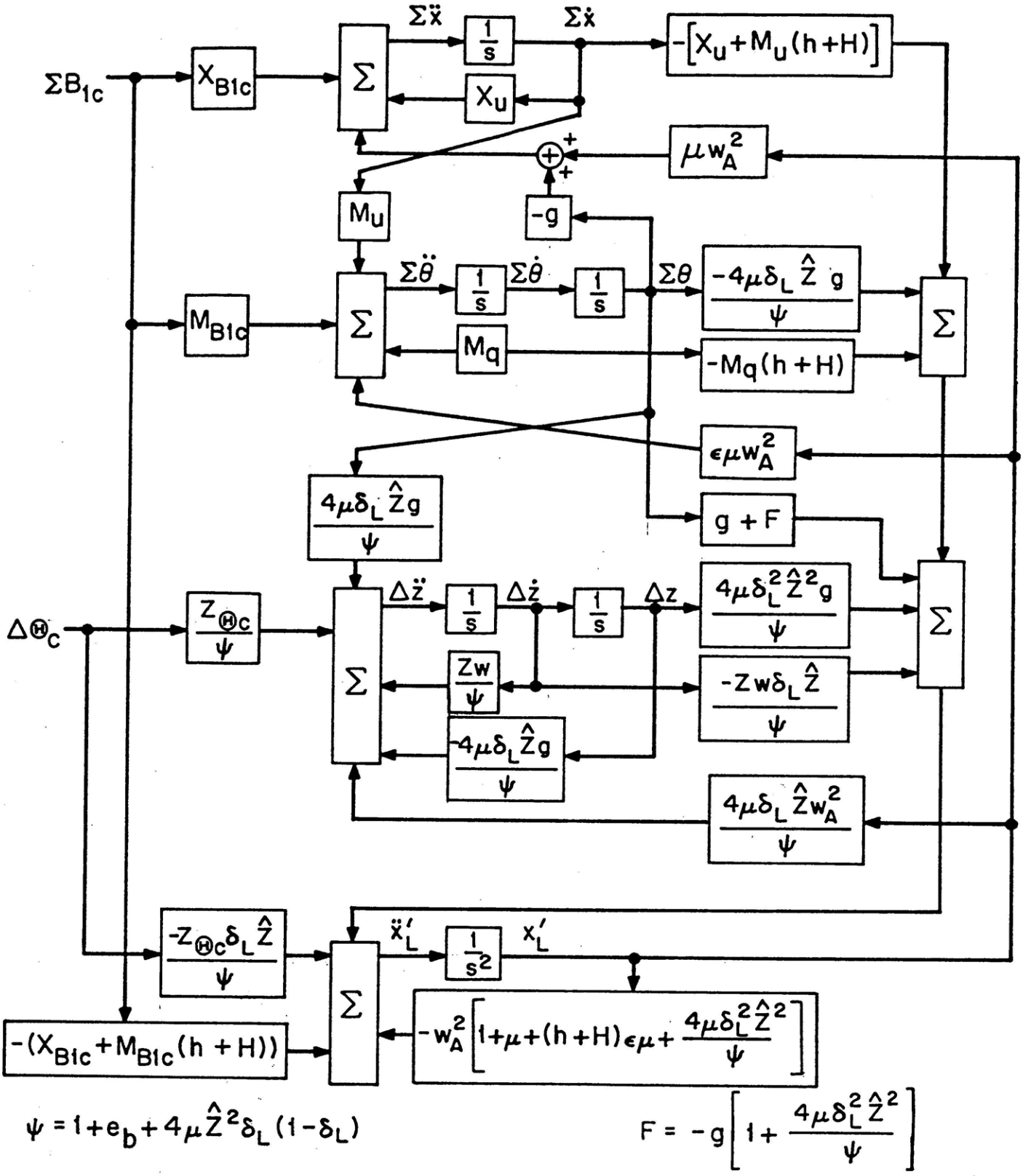

Fig. 3.2.6: Block Diagram for TLHS Anti-Symmetric Motion (ASM).

Other useful expressions, which follow from those in Table 2.4.3, are given in Table 3.2.2.

Table 3.2.2: Important Equal Tether Geometric Relationships

$$\Delta x = -\,[h\,\Delta\theta + H\,\Delta\varepsilon]$$

$$\Delta z = L\,\varepsilon_B$$

$$x_L' = H\,[\Sigma\varepsilon - \Sigma\theta]$$

$$\varepsilon_m = \{\, 2\,[x_L' + H\,\Sigma\theta] - [\Delta x + h\,\Delta\theta]\,\} \,/\, 2H$$

$$\varepsilon_s = \{\, 2\,[x_L' + H\,\Sigma\theta] + [\Delta x + h\,\Delta\theta]\,\} \,/\, 2H$$

$$x_L - \Sigma x = (h + H)\,\Sigma\theta + \hat{Z}\,\Delta z + x_L'$$

$$= h\,\Sigma\theta + \hat{Z}\,\Delta z + H\,\Sigma\varepsilon$$

$$\Sigma\varepsilon = [x_L' + H\,\Sigma\theta] \,/\, H$$

$$\Delta\varepsilon = -\,[\Delta x + h\,\Delta\theta] \,/\, H$$

3.3 Modal Analysis of TLHS Equal Tether Configuration

3.3.1 Introduction

In this section the natural modes of the Equal Tether Configuration ($H_s = H_m = H$) are identified and discussed. These modes are found by solving the 12^{th} order ordinary eigenvalue problem associated with the homogeneous system ($\underline{u}_p = \underline{0}$):

$$\dot{\underline{x}}_p(t) = A_p\,\underline{x}(t), \qquad \underline{x}(0) = \underline{x}_0 \in \mathbf{R}^{12} \tag{3.6}$$

where A_p is given in Table 3.3.3.1 (Kailaith, Strang [11], [12]). In doing so, the solution to the eq. (3.6) may be written as follows:

$$\underline{x}(t) = e^{A_p t}\,\underline{x}_0 = \sum_{i=1}^{12} (\underline{w}_i^H\,\underline{x}_0)\,e^{\lambda_i t}\,\underline{v}_i \tag{3.7}$$

Table 3.3.1.1: A_p Matrix for Equal Tether Configuration

$$A_p = \begin{bmatrix}
-0.2384 & 0. & 0. & 0. & 0. & 0. & 0. & 0. & 0. & 0. & 0. & 0. \\
0. & 0. & 0. & 1.0000 & 0. & 0. & 0. & 0. & 0. & 0. & 0. & 0. \\
0. & 0. & 0. & 0. & 1.0000 & 0. & 0. & 0. & 0. & 0. & 0. & 0. \\
0. & -1.0975 & -0.8847 & -0.0600 & 0. & 0. & 0. & 0. & 0. & 0. & 0. & 0. \\
0. & -17.2670 & -5.0777 & 2.3493 & -3.1000 & 0. & 0. & 0. & 0. & 0. & 0. & 0. \\
0. & 0. & 0. & 0. & 0. & 0. & 0. & 0. & 0. & 1.0000 & 0. & 0. \\
0. & 0. & 0. & 0. & 0. & 0. & 0. & 0. & 0. & 0. & 1.0000 & 0. \\
0. & 0. & 0. & 0. & 0. & 0. & 0. & 0. & 0. & 0. & 0. & 1.0000 \\
0. & 0. & 0. & 0. & 0. & -0.5620 & 0. & 1.0975 & -0.0600 & 0. & 0. & 0. \\
0. & 0. & 0. & 0. & 0. & 0. & 0. & 17.2670 & 2.3493 & -3.1000 & 0. & 0. \\
0. & 0. & 0. & 0. & 0. & 0.4679 & -0.3885 & 2.0233 & 0. & 0. & -0.3361 & 0. \\
0. & 0. & 0. & 0. & 0. & -0.2220 & 0.1844 & -9.5654 & -0.6308 & 0.9116 & 0.1595 & 0.
\end{bmatrix}$$

Units: degs, ft, deg / sec, ft / sec, lbs

where $A_p \underline{v}_i = \lambda_i \underline{v}_i \qquad i = 1, 2, ..., 12 \qquad (3.8)$

$\underline{w}_j^H A_p = \underline{w}_j^H \lambda_j \qquad j = 1, 2, ..., 12 \qquad (3.9)$

$$\underline{w}_i^H \underline{v}_j = \delta_{ij} = \begin{cases} 1 & \text{if } i = j \\ 0 & \text{if } i \neq j \end{cases} \qquad (3.10)$$

and the subscript "H" is used to denote a conjugate transpose (hermitian) operation. The λ_i are the eigenvalues of A_p. The $\underline{v}_i$ and $\underline{w}_i$ are the right and left eigenvectors of A_p corresponding to the λ_i.

From eqs. (3.6) and (3.10) it is seen that the prescription for studying real exponential modes is as follows:

$$\underline{x}_0 = \underline{v}_i \quad \Rightarrow \quad \underline{x}(t) = e^{\lambda_i t} \underline{v}_i \text{ for any real mode } (\lambda_i, \underline{v}_i, \underline{w}_i). \qquad (3.11)$$

What is the prescription for studying complex (exponential-sinusoidal) modes? Suppose $\underline{v}_{i,\,i+1} = \underline{a} \pm j\underline{b}$ are complex conjugate right eigenvectors corresponding to the complex conjugate eigenvalues $\lambda_{i,\,i+1} = \sigma \pm j\omega$, respectively. It can then be shown that

If $\underline{x}_0 = k_1 \underline{a} + k_2 \underline{b}$ where $k_1, k_2 \in \mathbf{R^1}$

$$\Rightarrow \underline{x}(t) = (k_1^2 + k_2^2)^{0.5} e^{\sigma t} [\underline{a} \cos(\omega t - \tan^{-1}(k_2 / k_1)) - \underline{b} \sin(\omega t - \tan^{-1}(k_2 / k_1))] \qquad (3.12)$$

Eqs. (3.11) and (3.12) provide mathematical formulae for studying the natural modes of the Equal Tether Configuration (or any other dynamical system).

The modes of the Equal Tether Configuration are those of the three subsystems discussed in the previous section. These modes are given in Table 3.3.1.2 and are plotted in Fig. 3.3.1.1. The λ_i and corresponding $\underline{v}_i$, for the Equal Tether Configuration, are given in Table 3.3.1.3. For convenience the polar form of the Equal Tether Model's complex eigenvectors have been provided in Table 3.3.1.4.

Table 3.3.1.2: Natural Modes of TLHS Equal Tether Configuration.*

AVM:	Vertical Damping Mode: $\lambda_1 = -0.2384$, $\tau = 4.2$ sec.
SM:	Tethered Helicopter Mode: $\lambda_2 = 0.7561$. Horizontal Spring Mode: $\lambda_{3,4} = -0.8122 \pm j\,2.2228$, $\zeta = 0.34$, $\omega_n = 2.37$ rad/sec, $\tau = 1.23$sec. Symmetric Damping Mode: $\lambda_5 = -2.2919$, $\tau = 0.44$ sec.
ASM:	Backflapping Mode: $\lambda_{6,7} = 0.0402 \pm j\,0.4785$, $\zeta = 0.084$, $\omega_n = 0.48$ rad/sec. Vertical Spring Mode: $\lambda_{8,9} = -0.1976 \pm j\,0.7364$, $\zeta = 0.26$, $\omega_n = 0.76$ rad/sec, $\tau = 5.06$ sec. Pendular Mode: $\lambda_{10,11} = -0.5314 \pm j\,2.6245$, $\zeta = 0.2$, $\omega_n = 2.7$ rad/sec, $\tau = 1.88$ sec. Anti-Symmetric Damping Mode: $\lambda_{12} = -2.1187$, $\tau = 0.47$ sec.

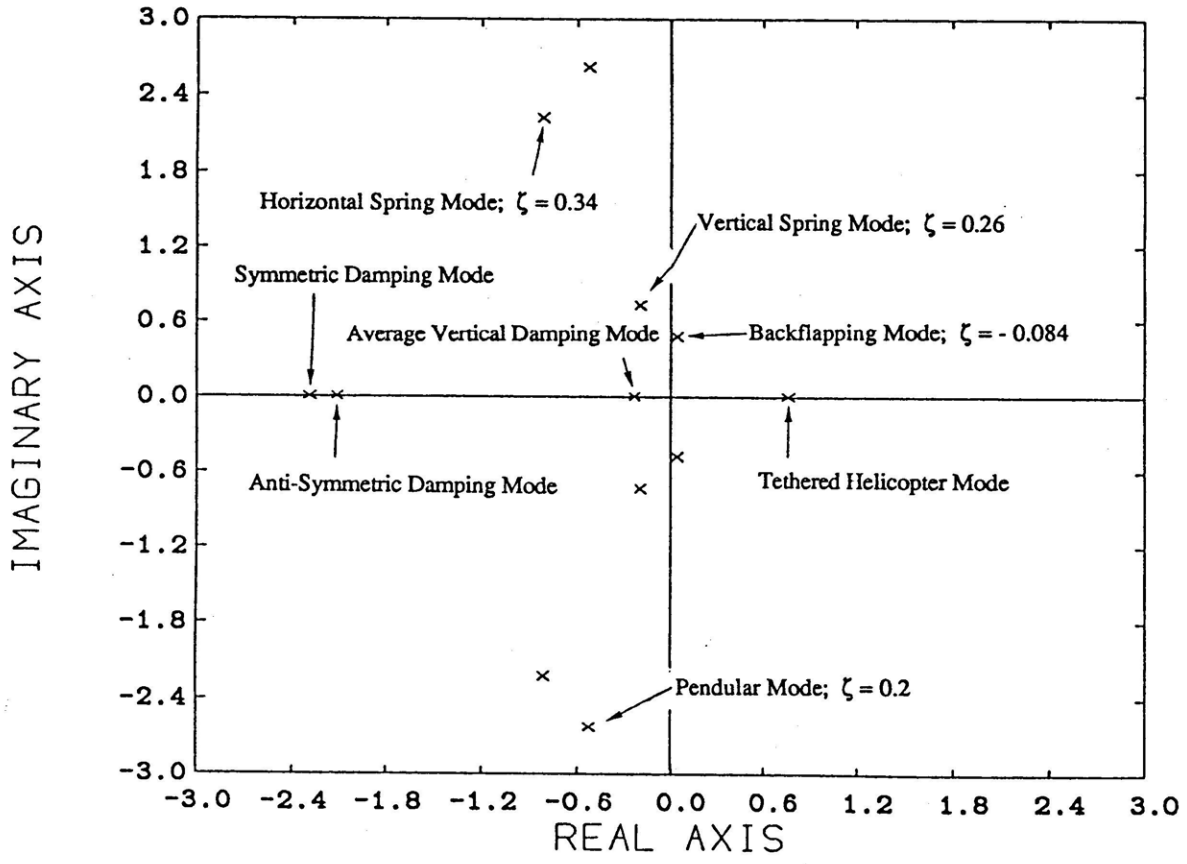

Fig. 3.3.1.1: Poles of TLHS Equal Tether Configuration.

* ζ - damping factor ω_n - undamped natural frequency τ - time constant

Table 3.3.1.3: Eigenvalues and Right Eigenvectors For Equal Tether Model

AVM: Average Vertical Damping

$\lambda_1 = -0.2384$

$$\underline{v}_1 = \begin{matrix} -1.0000 \\ 0. \\ 0. \\ 0. \\ 0. \\ 0. \\ 0. \\ 0. \\ 0. \\ 0. \\ 0. \\ 0. \end{matrix}$$

SM: Tethered Helicopter

$\lambda_2 = 0.7561$

$$\underline{v}_2 = \begin{matrix} 0. \\ 0.3658 \\ -0.7089 \\ 0.2766 \\ -0.5360 \\ 0.0000 \\ 0.0000 \\ 0.0000 \\ 0.0000 \\ 0.0000 \\ -0.0000 \\ 0.0000 \end{matrix}$$

Horizontal Spring

$\lambda_{3,4} = -0.8122 \pm j\ 2.2228$

$$\underline{v}_3 = \begin{matrix} 0. + 0.\ i \\ 0.0613 - 0.0365i \\ 0.3673 + 0.1073i \\ 0.0314 + 0.1658i \\ -0.5368 + 0.7292i \\ -0.0000 + 0.0000i \\ -0.0000 + 0.0000i \\ 0.0000 - 0.0000i \\ -0.0000 + 0.0000i \\ 0.0000 - 0.0000i \\ 0.0000 + 0.0000i \\ 0.0000 + 0.0000i \end{matrix}$$

Symmetric Damping

$\lambda_5 = -2.2919$

$$\underline{v}_5 = \begin{matrix} 0. \\ 0.0564 \\ -0.3959 \\ -0.1292 \\ 0.9074 \\ 0.0000 \\ -0.0000 \\ -0.0000 \\ 0.0000 \\ -0.0000 \\ -0.0000 \\ 0.0000 \end{matrix}$$

ASM: Backflapping

$\lambda_{6,7} = 0.0402 \pm j\ 0.4785$

$$\underline{v}_6 = \begin{matrix} 0. + 0.\ i \\ -0.0000 - 0.0000i \\ 0.0000 - 0.0000i \\ 0.0000 - 0.0000i \\ 0.0000 + 0.0000i \\ 0.1789 + 0.3106i \\ 0.7512 + 0.0100i \\ 0.0225 + 0.0030i \\ -0.3746 + 0.0800i \\ -0.1414 + 0.0981i \\ 0.0254 + 0.3598i \\ -0.0005 + 0.0109i \end{matrix}$$

Vertical

$\lambda_{8,9} = -0.1976 \pm j\ 0.7364$

$$\underline{v}_8 = \begin{matrix} 0. + 0.\ i \\ -0.0000 + 0.0000i \\ -0.0000 + 0.0000i \\ -0.0000 - 0.0000i \\ 0.0000 - 0.0000i \\ 0.3172 + 0.2415i \\ -0.5786 - 0.2456i \\ -0.0269 - 0.0214i \\ -0.1580 + 0.3116i \\ -0.2405 + 0.1858i \\ 0.2952 - 0.3775i \\ 0.0211 - 0.0155i \end{matrix}$$

Pendular

$\lambda_{10,11} = -0.5314 \pm j\ 2.6245$

$$\underline{v}_{10} = \begin{matrix} 0. + 0.\ i \\ -0.0000 + 0.0000i \\ -0.0000 + 0.0000i \\ -0.0000 - 0.0000i \\ -0.0000 - 0.0000i \\ 0.2093 + 0.2160i \\ 0.0330 - 0.0083i \\ -0.1604 - 0.0548i \\ -0.0475 + 0.1205i \\ -0.6780 + 0.4345i \\ 0.0043 + 0.0909i \\ 0.2290 - 0.3919i \end{matrix}$$

Anti-Symmetric Damping

$\lambda_{12} = -2.1187$

$$\underline{v}_{12} = \begin{matrix} 0. \\ 0.0000 \\ -0.0000 \\ -0.0000 \\ 0.0000 \\ -0.4158 \\ -0.0124 \\ 0.0706 \\ -0.1511 \\ 0.8809 \\ 0.0263 \\ -0.1496 \end{matrix}$$

Table 3.3.1.4: Polar Form of Equal Tether Complex Eigenvectors

SM: Horizontal Spring

MAG	PHAS
0.07134	- 30.8°
0.3827	16.29°
0.1687	79.3°
0.9044	126.4°

ASM:

Backflapping		Vertical Spring		Pendular	
MAG	PHAS	MAG	PHAS	MAG	PHAS
0.3584	60°	0.3987	37.3°	0.301	45.9°
0.7512	1°	0.6286	- 157°	0.034	- 14.1°
0.0227	7.6°	0.0344	- 141.5°	0.1695	- 161.2°
0.383	168°	0.3494	117°	0.1295	112°
0.1721	145.3°	0.3039	142.3°	0.8053	147.4°
0.3607	86°	0.4792	- 51.98	0.091	87.3°
0.0109	92.6°	0.0262	- 36.3	0.4539	- 59.7°

MAG ≡ magnitude PHAS ≡ phase

In discussing the modes of the Equal Tether Configuration it is, of course, assumed that all four incremental inputs (collectives and cyclics) are zero; i.e. only equilibrium values are applied. Although the discussion shall be based on the right eigenvectors in Table 3.3.1.3, reference shall be made to single helicopters, tethered helicopters, and helicopters carrying sling loads in order to provide incite into the difficulty of controlling the Equal Tether Configuration being studied.

3.3.2 Discussion of AVM Modes

The AVM possesses one natural modes; an Average Vertical Damping Mode. This mode only affect the $\Sigma\dot{z}$ degree of freedom and can be described as follows.

The Average Vertical Damping Mode characterizes the effect of vertical aerodynamic drag forces on the TLHS during average vertical climbs ($\Sigma\dot{z}$). More specifically, if the TLHS is given an initial average velocity, $\Sigma\dot{z}_0$, then this average velocity will decay exponentially to zero with a time constant of 4.2 seconds. This mode is similar to that experienced by a single hovering helicopter but has a larger time constant due to the extra mass in TLHS's. This is apparent fromthe AVM differential equation:

$$\Sigma\ddot{z} = [1 / (1 + \mu)] [Z_w \Sigma\dot{z} + Z_{\Theta c} \Sigma\Theta_c] \quad (3.13)$$

$$= - 0.2384 \Sigma\dot{z} + 4.0985 \Sigma\Theta_c \quad (3.14)$$

where $\Sigma\dot{z}$ is measured in feet / second and $\Sigma\Theta_c$ in degrees. The vertical damping mode for a single helicopter has time constant $1 / | Z_w | = 2.89$ seconds.

3.3.3 Discussion of SM Modes

The SM possesses three natural modes; a Tethered Helicopter Mode, a Horizontal Spring Mode, and a Symmetric Damping Mode. These modes only affect the Δx, $\Delta\theta$ degrees of freedom. Because of this, the modes are symmetric with respect to the equilibrium configuration (tethers vertical and spreader bar horizontal). The SM modes can thus be studied by assuming each helicopter to be tethered to a fixed point in space (Fig. 3.3.3.1).

The Tethered Helicopter Mode is an unstable exponential mode. This mode is not present in free flying helicopters or in helicopters carrying sling loads. The mode, however, is present in helicopters which are tethered to a fixed point in space [2]. The instability is due to the tension in the tethers and the fact that the helicopter-tether attachment points are below the helicopter c.g.'s.

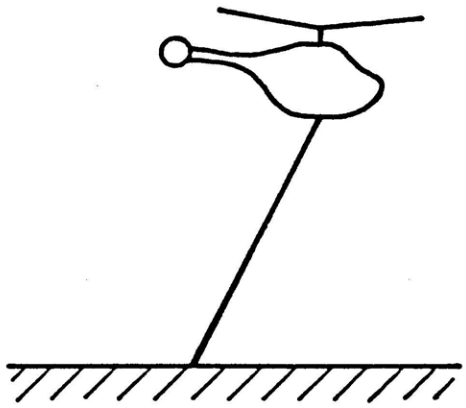

Fig. 3.3.3.1: Helicopter Tethered to a Fixed Point in Space

Given the proper initial conditions (eq. (3.11)), the helicopters experience a divergence in their relative pitch attitudes ($\Delta\theta$) as well as in their relative positions (Δx). More specifically, suppose the master helicopter experiences a horizontal velocity disturbance. Because the helicopter-tether attachment point is below the helicopter c.g., a nose-down pitching moment is induced about the helicopter c.g. As a result, a nose-down pitch attitude begins to develop. The downward pitching causes the helicopter's forward component of rotor thrust to increase. This, in turn, causes the helicopter to accelerate and pitch divergently. Since the slave exhibits a similar response (only with signs reversed), we see a divergence in the relative pitch attitudes and positions of the helicopters. Because of the nature of this instability; i.e because the helicopters tend to topple over, the mode is sometimes referred to as the inverted pendular mode [2]. It should be noted that as the helicopter-tether attachment points approach the helicopter c.g.'s (i.e. as $h \rightarrow 0$), the mode approaches a horizontal equilibrium mode (a natural integrator). Throughout the thesis, however, the attachment points remain a fixed distance, $h = 3.6$ ft., below the helicopter c.g.'s. As a consequence, a minimum gain will be required to just stabilize the SM.

The Horizontal Spring Mode is a stable, moderately damped, sinusoidal mode. This high frequency pitching mode is due to the stabilizing effect of the tethers attached below the helicopter c.g.'s; i.e. given the proper initial conditions (eq. (3.12)), the helicopters will pitch and translate

back to their equilibrium positions just as if a horizontal spring were present. More specifically, suppose that the master helicopter experiences a small forward velocity disturbance while pitching upward. The relative airspeed causes the rotor to tilt backwards thus exerting a nose-up pitching moment about the helicopter c.g. The nose-up pitching continues until it is arrested by the restoring moment due to the tether. Because of the nose-up pitch attitude, the backward component of rotor thrust decelerates the helicopter until its forward motion is arrested. At this point backward motion begins. The relative airspeed causes the rotor to tilt forwards thus exerting a nose-down pitching moment. The cycle is then repeated. Because of the symmetry associated with the symmetric modes, the slave exhibits a similar behavior (only with sign reversed). This mode resembles the anti-symmetric backflapping mode (characteristic of a hovering helicopter) to be described subsequently, but is stable because of the restoring moment provided by the tethers. It should be noted that as $h \rightarrow 0$ the horizontal spring mode becomes unstable [1]; i.e. the stabilizing horizontal spring effect due to the tethers is lossed. As a matter of fact, the mode becomes identical to the unstable Backflapping Mode (to be described subsequently), but only at a much higher frequency due to the extra load-bar mass in the TLHS.

The Symmetric Damping Mode is a stable exponential mode which characterizes the effect of horizontal aerodynamic drag forces on the TLHS during symmetric translations ($\Delta\dot{x}$). More specifically, if the TLHS is given the proper initial condition (eq. (3.11)), including an initial differential horizontal velocity, $\Delta\dot{x}$, then this initial velocity will decay to zero with a time constant of 0.44 sec. This mode is similar to that experienced by a single hovering helocopter (Appendix 3) but has a larger time constant which can be attributed to the extra load-bar mass. The extra load-bar mass requires a larger component of thrust to keep the system in vertical equilibrium. It is this larger component of thrust that results in the larger time constant.

To gain incite into the nature of the SM modes it is instructive to see the effect of varying the load-bar weight ($\mu = [M_L+M_B] / 2M_H$) and the distance from the helicopter-tether attachment point to the helicopter c.g.'s (h). Fig. 3.3.3.2 shows the effects of varying the parameter μ on the SM modal characterisics. Fig. 3.3.3.3 shows the effects of varying h [1].

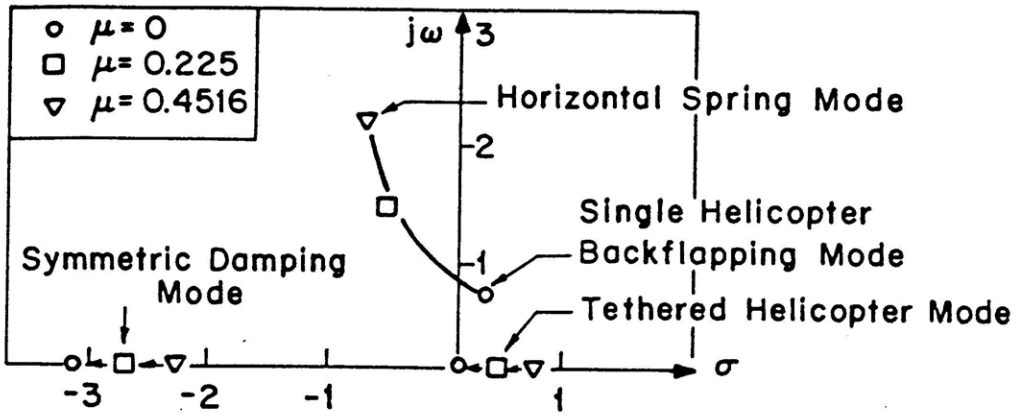

Fig. 3.3.3.2: Influence of Varying $\mu \equiv [M_L + M_B] / 2M_H$ on SM Modal Characteristics.

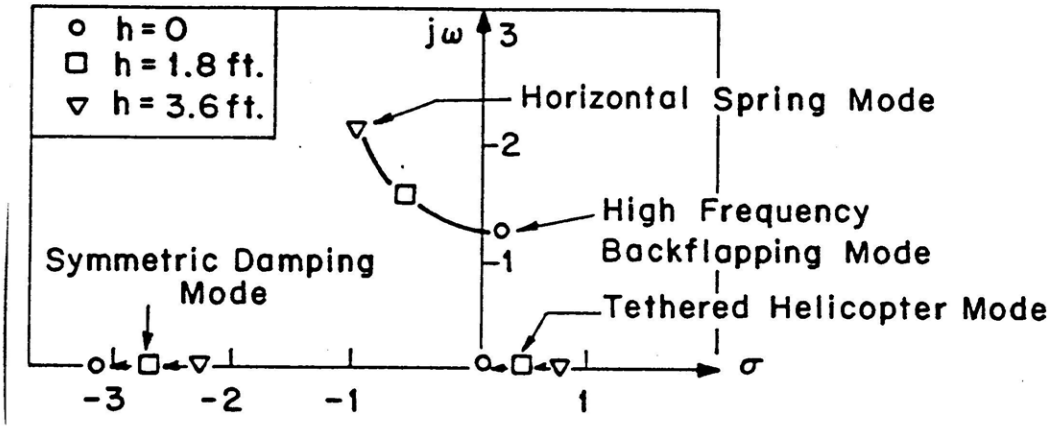

Fig. 3.3.3.3: Influence of Varying h on SM Modal Characteristics.

Fig. 3.3.3.2 shows that for a small load-bar weight (small μ), the Tethered Helicopter Mode approaches the origin; i.e. a natural integrator. This horizontal separation equilibrium mode is due to the fact that for $\mu = 0$, any initial helicopter separation will be maintained if no collective or cyclic commands are issued. Similarly, for small μ, the Horizontal Spring Mode approaches a mode which is identical to the Backflapping Mode of a single hovering Blackhawk helicopter. This is because for $\mu = 0$ the SM equations become

$$\begin{bmatrix} \Delta\dot{x} \\ \Delta\dot{\theta} \\ \Delta\ddot{x} \\ \Delta\ddot{\theta} \end{bmatrix} = \begin{bmatrix} 0 & 0 & 1 & 0 \\ 0 & 0 & 0 & 1 \\ 0 & -g & X_u & 0 \\ 0 & 0 & M_u & M_q \end{bmatrix} \begin{bmatrix} \Delta x \\ \Delta\theta \\ \Delta\dot{x} \\ \Delta\dot{\theta} \end{bmatrix} + \begin{bmatrix} 0 \\ 0 \\ X_{Blc} \\ M_{Blc} \end{bmatrix} \Delta B_{lc} \quad (3.22a)$$

$$= \begin{bmatrix} 0 & 0 & 1 & 0 \\ 0 & 0 & 0 & 1 \\ 0 & -0.562 & -0.06 & 0 \\ 0 & 0 & 2.3493 & -3.1 \end{bmatrix} \begin{bmatrix} \Delta x \\ \Delta\theta \\ \Delta\dot{x} \\ \Delta\dot{\theta} \end{bmatrix} + \begin{bmatrix} 0 \\ 0 \\ 0.4782 \\ -47.24 \end{bmatrix} \Delta B_{lc} \qquad (3.22b)$$

when Δx is measured in ft., $\Delta\dot{x}$ in ft./sec., $\Delta\theta$ in degs., and $\Delta\dot{\theta}$ in degs./sec.. These equations are identical to those for a single hovering Blackhawk helicopter (Appendix 3). Because of this, we also see that as $\mu \to 0$, the Symmetric Damping Mode approaches the Horizontal Damping Mode of a single Blackhawk near hover. It is emphasized that $\mu = 0.4516$ shall be used to develop the Equal Tether AFCS (Chapter 3) and the Unequal Tether AFCS (Chapter 6).

3.3.4 Discussion of ASM Modes

The ASM possesses four natural modes; a Backflapping Mode, a Vertical Spring Mode, a Pendular Mode, and an Anti-Symmetric Damping Mode. These modes only affect the $\Sigma\dot{x}$, $\Sigma\theta$, Δz, x_L' degrees of freedom. Consequently, in studying the ASM modes it is reasonable to assume that $\Delta x = \Delta\theta = 0$.

The Backflapping Mode (Fig. 3.3.4.1) is a low frequency unstable exponential-sinusoidal mode. This mode is due to the backflapping of the main rotor with forward motion and is characteristic of a hovering helicopter (Appendix 3). More specifically, suppose that the master helicopter experiences a small horizontal velocity disturbance (Fig. 3.3.4.1a). The relative airspeed

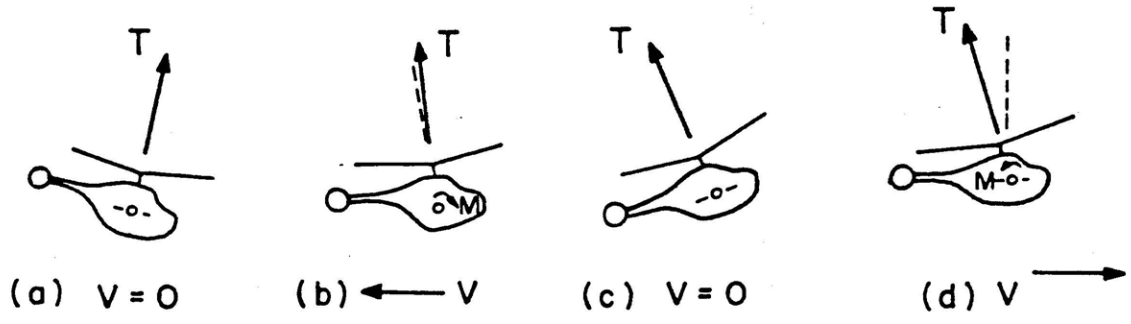

Fig. 3.3.4.1: Visualization of Backflapping Mode.

causes the rotor to tilt backwards and exert a nose-up pitching moment about the helicopter's c.g. A nose-up pitch attitude then begins to develop and the backward component of rotor thrust decelerates the helicopter until its forward motion is arrested. At this point (Fig. 3.3.4.1c) the disc tilt and rotor moment vanish but the nose-up pitch attitude remains so that backward motion begins. This causes the rotor to tilt forward and exert a nose-down pitching moment (Fig. 3.3.4.1b). Following this, a nose-down pitch attitude develops (Fig. 3.3.4.1a) which accelerates the helicopter forward and returns it to the situation in Fig. 3.3.4.1d. The cycle then begins again. The amplitude of the oscillations increase steadily because of the helicopter inertia. Since the slave exhibits an identical response its motion need not be discussed. In addition, it should be noted that because this mode is largely associated with $\Sigma\theta$, and hence $\Sigma\dot{x}$, we expect a relatively large impact on x_L. However when x_L is strongly affected we expect significant Δz motion. This is confirmed by the magnitude of the Δz component of the Backflapping Modes' eigenvectors (Table 3.3.1.4). Finally, because this mode is unstable, the AFCS will require a minimum gain just to stabilize the ASM.

The Vertical Spring Mode is a stable, low frequency, lightly damped sinusoidal mode. This mode is associated, primarily, with the Δz degree of freedom and is due to the fact that the payload is suspended a fixed distance, Z, below the spreader bar c.g. More specifically, suppose that the slave helicopter experiences an upward velocity perturbation and the master helicopter a downward velocity perturbation. This causes the spreader bar to rotate clockwise about it's c.g. This, in turn results in the load swinging to the left of the center ($x_L - \Sigma x \approx \hat{Z}\,\Delta z \approx Z\,\varepsilon_B < 0$). Consequently, the tension in the slave tether increases and the tension in the master tether decreases, causing the slave and master to decelerate. This continues until the slave and master motions are arrested. The load then swings to the right and the bar rotates counter-clockwise about it's c.g. This results in the slave moving downward and the master upward. The cycle then repeats itself every 8.5 seconds and the motion decays with a time constant of 5.06 seconds. To better understand the origin of this mode, it is important to note that as $Z \rightarrow 0$, this mode approaches two real modes. One being

similar to the natural vertical damping mode of a helicopter but less damped ($s = Z_w / (1+e_b) = -0.3434$)*, the other a natural vertical equilibrium mode ($s = 0$). This clearly shows that the Vertical Spring Mode is due to the fact that the load is suspended below the spreader bar c.g. We note that when $Z = 0$, the ASM is identical to that of a single helicopter carrying a sling load [1] [4].

The Pendular Mode is a stable, high frequency, lightly damped, sinusoidal mode. This mode characterizes the natural tendency of the load to sway. The mode is predominantly associated with $\Sigma\varepsilon$, but because the tethers are attached below the helicopter c.g.'s, it has a relatively large impact on $\Sigma\dot{\theta}$. This is confirmed by the magnitude of the $\Sigma\dot{\theta}$ component in the Pendular Modes' eigenvectors (Table 3.3.1.4). This mode has a period of 2.4 seconds and decays with a time constant of 1.88 seconds. It should be noted that this mode has a frequency of oscillation ($\omega_n = 2.7$ rad/sec) which is considerably larger than the uncoupled pendulous frequency, $\omega_A = \sqrt{g / H_A}$ = 1.56 rad/sec. Finally, it should also be noted that this mode decays because of aerodynamic damping on the helicopters; not on the load-bar assembly.

The Anti-Symmetric Damping Mode is a stable exponential mode which, as the Symmetric Damping Mode, essentially characterizes the effect of horizontal aerodynamic forces and moments on the TLHS during horizontal translation ($\Sigma\dot{x}$). More specifically, suppose that the load is initially to the right of the center and that both helicopters experience forward velocity perturbations. Their velocities will decay to zero exponentially with a time constant of 0.47 second. This is larger than the Symmetric Damping time constant (0.44 seconds) as well as the 0.31 second time constant of a single Blackhawk helicopter near hovering trim (Appendix 3).

To gain incite into the nature of the ASM modes, it is instructive to see the effect of varying the load-bar weight and the distance that the load is suspended below the spreader bar c.g., Z. The effects of varying h on the ASM modal characteristics are shown to be of secondary importance in [1].

---

* Z_w is an aerodynamic derivative and $e_b \equiv (2\, I_B)/(M_H L^2) = W_B / (6\, W_H)$.

For $M_L = M_B = 0$ ($\mu = 0$) the ASM equations become

$$\Delta\ddot{z} = Z_w \Delta\dot{z} + Z_{\Theta_c} \Delta\Theta_c \quad (3.23a)$$

$$= -0.346 \Delta\dot{z} + 5.9494 \Delta\Theta_c \quad (3.23b)$$

$$\begin{bmatrix} \Sigma\dot{\theta} \\ \Sigma\ddot{x} \\ \Sigma\ddot{\theta} \end{bmatrix} = \begin{bmatrix} 0 & 0 & 1 \\ -g & X_u & 0 \\ 0 & M_u & M_q \end{bmatrix} \begin{bmatrix} \Sigma\theta \\ \Sigma\dot{x} \\ \Sigma\dot{\theta} \end{bmatrix} + \begin{bmatrix} 0 \\ X_{Blc} \\ M_{Blc} \end{bmatrix} \Sigma B_{lc} \quad (3.24a)$$

$$= \begin{bmatrix} 0 & 0 & 1 \\ -0.562 & -0.06 & 0 \\ 0 & 2.3493 & -3.1 \end{bmatrix} \begin{bmatrix} \Sigma\theta \\ \Sigma\dot{x} \\ \Sigma\dot{\theta} \end{bmatrix} + \begin{bmatrix} 0 \\ 0.4782 \\ -47.24 \end{bmatrix} \Sigma B_{lc} \quad (3.24b)$$

where Δz is measured in ft., $\Sigma\theta$ in degs., $\Sigma\dot{x}$ in ft. / sec., and $\Delta\Theta_c$ and ΣB_{lc} in degs.. These equations are identical to those for a single hovering Blackhawk helicopter (Appendix 3). Notice that for $M_L = M_B = 0$ we have no equation for $\ddot{x}_L'$. For "small" M_L and M_B (not both zero) one can show that the equation for $\ddot{x}_L'$ becomes:

$$\ddot{x}_L' = -(g / H)\, x_L' - [X_u + (h + H)\, M_u]\, \Sigma\dot{x} - M_q (h + H)\, \Sigma\dot{\theta} - [X_{Blc} + (h + H)\, M_{Blc}]\, \Sigma B_{lc} \quad (3.25)$$

These facts are in agreement with Fig. 3.3.4.2 which shows that as $\mu \rightarrow 0$ the Vertical Spring Mode, a damped sinusoidal mode, approaches an integrator and the vertical damping mode of a single hovering helicopter. Similarly, as $\mu \rightarrow 0$, the Backflapping and Anti-Symmetric Modes approach the backflapping and horizontal damping modes of a single hovering helicopter. As $\mu \rightarrow 0$, the Pendular Mode approaches the uncoupled pendular mode. This mode is an undamped sinusoidal mode with frequency $\omega_A = \sqrt{g / H} = 1.56$ rad / sec.

Again, we emphasize that $\mu = 0.4516$ shall be used to develop the Equal Tether AFCS (Chapter 4) and the Unequal Tether AFCS (Chapter 6).

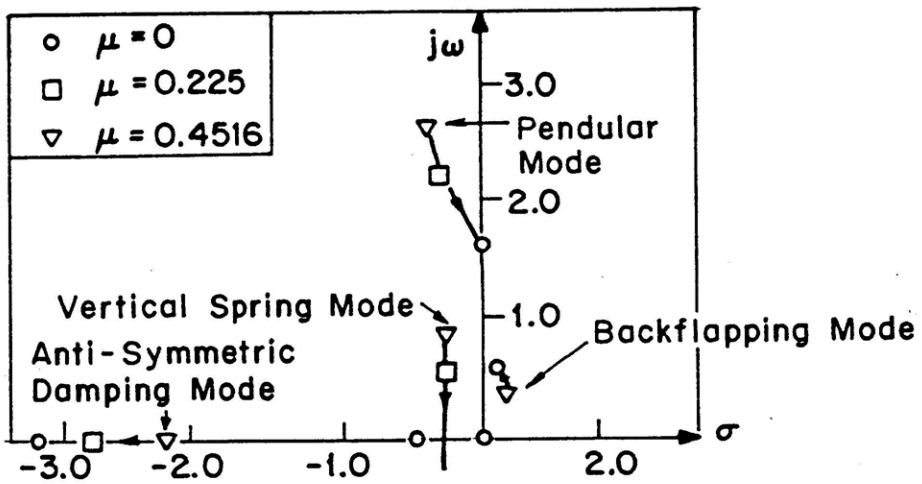

Fig. 3.3.4.2: Influence of Varying $\mu \equiv [M_L + M_B] / 2M_H$ on ASM Modal Characteristics.

Fig. 3.3.4.3 shows the effects of varying $\hat{Z} \equiv Z / L$, the normalized distance from the spreader bar c.g. to the load, on the ASM modal characteristics [1]. We see that as $\hat{Z} \rightarrow 0$, the Vertical Spring Mode approaches two real modes (s = 0 and $s = Z_w / (1 + e_b) = - 0.3434$). The Backflapping and Anti-Symmetric Damping Mode characteristics, however, do not change much as $\hat{Z} \rightarrow 0$. Finally, as $\hat{Z} \rightarrow 0$ the Pendular Mode increases in frequency and becomes more lightly damped. It is emphasized that $\hat{Z} = 0.5$ shall be used throughout the thesis.

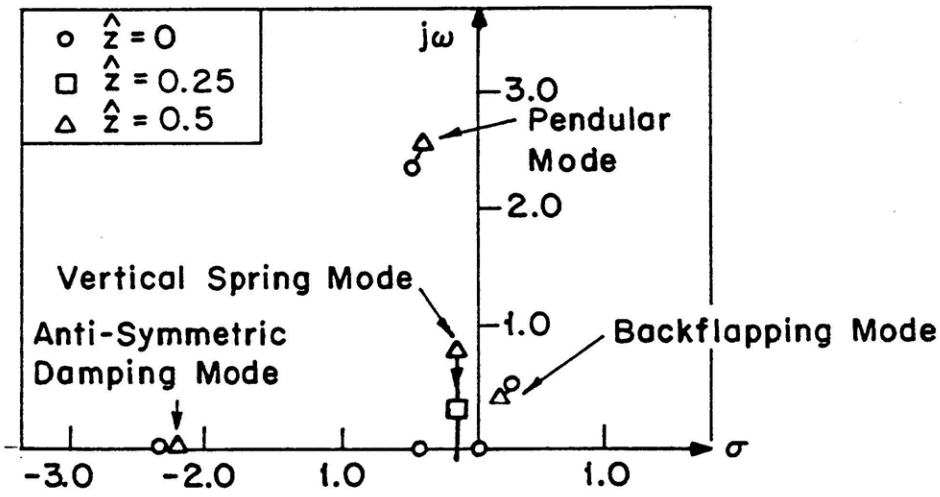

Fig. 3.3.4.3: Influence of Varying $\hat{Z} \equiv Z / L$ on ASM Modal Characteristics.

3.4 Selection of Outputs for TLHS Equal Tether Problem

To emphasize the decoupling of the Equal Tther Model into 3 subsystems we rewrite our Equal Tether Model as follows:

$$\dot{\underline{x}}_p = A_p \underline{x}_p + B_p \underline{u}_p; \quad \underline{x}_p \in \mathbf{R}^{12}, \underline{u}_p \in \mathbf{R}^4 \tag{3.26}$$

$$\underline{x}_p \equiv [\ \Sigma\dot{z} \ \| \ \Delta x \ \ \Delta\theta \ \ \Delta\dot{x} \ \ \Delta\dot{\theta} \ \| \ \Sigma\theta \ \ \Delta z \ \ x_L' \ \ \Sigma\dot{x} \ \ \Sigma\dot{\theta} \ \ \Delta\dot{z} \ \ \dot{x}_L' \ ]^T \tag{3.27}$$

$$\underline{u}_p \equiv [\ \Sigma\Theta_c \ \| \ \Delta B_{lc} \ \| \ \Delta\Theta_c \ \ \Sigma B_{lc} \ ]^T \tag{3.28}$$

where $$A_p \equiv \text{diag}\,(A_{p1}, A_{p2}, A_{p3}) \tag{3.29}$$

$$B_p \equiv \text{diag}\,(B_{p1}, B_{p2}, B_{p3}) \tag{3.30}$$

and the pairs (A_{pi}, B_{pi}), i = 1, 2, 3, describe the AVM, SM, and ASM, respectively.

In order to formulate the Twin Lift control problem we must choose outputs (quantities to control). The number of outputs must equal the number of inputs. Since the TLHS dynamics decouples into 3 subsystems, it only makes sense to select outputs for each of the subsystems.

3.4.1 Selection of Outputs for AVM Subsystem: The AVM Plant

The pair (A_{p1}, B_{p1}) describes the TLHS's AVM, involves the $\Sigma\dot{z}$ degree of freedom, and is conrolled by issuing average collective commands ($\Sigma\Theta_c$). This subsystem has only one input which can be used to control at most one output, the average vertical velocity: $\Sigma\dot{z}$. The AVM thus has the following state space representation:

$$\dot{x}_{p1} = A_{p1} x_{p1} + B_{p1} u_{p1}; \qquad x_{p1} \in \mathbf{R}^1 \tag{3.31}$$

$$y_{p1} = C_{p1} x_{p1}; \qquad u_{p1}, y_{p1} \in \mathbf{R}^1 \tag{3.32}$$

where $u_{p1} \equiv \Sigma\Theta_c$, $x_{p1} \equiv \Sigma\dot{z}$, $C_{p1} \in \mathbf{R}$, and $y_{p1} \equiv \Sigma\dot{z}$. When $\Sigma\dot{z}$ is measured in ft./sec. and $\Sigma\Theta_c$ in degs., we have

$$A_{p1} = Z_w / (1 + \mu) = -0.2384 \tag{3.33}$$

$$B_{p1} = Z_{\Theta c} / (1 + \mu) = 4.0985 \tag{3.34}$$

$$C_{p1} = 1 \tag{3.35}$$

This SISO (single-input single-output) system has transfer function given by:

$$G_{p1}(s) = C_{p1}\,(sI - A_{p1})^{-1}\,B_{p1}. \tag{3.36a}$$

$$= [\,Z_{\Theta c} / (1+\mu)\,] / [\,s - (Z_w / (1+\mu))\,] \tag{3.36b}$$

$$= 4.0985 / [s + 0.2384] \tag{3.36c}$$

It is very easy to show that the state space triple (A_{p1}, B_{p1}, C_{p1}) is controllable and observable. It thus follows that the state space and transfer function representations are equivalent minimal representations [11]. From now on the state space representation given by eqs. (3.27) - (3.28), and the equivalent I/O representation given by eq. (3.29), shall be referred to as the AVM Plant.

For convenience all AVM Plant parameter values are provided in Table 3.4.1.1.

Table 3.4.1.1: AVM Plant Parameters

$W_H = 14000$ lbs., $M_H = 434.78$ slugs

$W_B = 644$ lbs., $M_B = 20$ slugs

$W_L = 12000$ lbs., $M_L = 372.67$ slugs

$\mu = [M_L + M_B] / 2M_H = 0.4516$

$Z_w = -\,0.346$ ft. sec^{-2} / ft. sec^{-1}

$Z_{\Theta c} = 340.9$ ft. / rad. $sec^2 = 5.949$ ft. / deg. sec^2

It should be noted from eq. (3.36) that the AVM plant pole is simply the single root of the characteristic polynomial:

$$\det (sI - A_{p1}) = s + 0.2384 \tag{3.37}$$

This pole has already been interpreted in the modal discussion of section 3.3.1. In that section we described the pole as the Average Vertical Damping Mode; a mode which characterizes the effects of vertical aerodynamic deag forces on the TLHS during average vertical translations, $\Sigma\dot{z}$.

It should also be noted from eq. (3.36) that the AVM Plant has no zeros.

3.4.2 Selection of Outputs for SM Subsystem: The SM Plant

The pair (A_{p2}, B_{p2}) describes the TLHS's SM, involves the Δx, $\Delta\theta$ degrees of freedom, and is conrolled by issuing differential cyclic commands (ΔB_{lc}). This subsystem has only one control input which can be used to control at most one output. Since the horizontal separation, Δx, is much more critical than $\Delta\theta$, we select Δx as the output to be controlled. Typically Δx will be commanded to zero. With input and output clearly defined, the SM thus has the following state space representation:

$$\dot{\underline{x}}_{p2} = A_{p2}\,\underline{x}_{p2} + B_{p2}\,u_{p2}; \qquad \underline{x}_{p2} \in \mathbf{R^4} \tag{3.38}$$

$$y_{p2} = C_{p2}\,\underline{x}_{p2}; \qquad u_{p2}, y_{p2} \in \mathbf{R^1} \tag{3.39}$$

where $u_{p2} \equiv \Delta B_{lc}$, $\underline{x}_{p2} \equiv [\,\Delta x \;\; \Delta\theta \;\; \Delta\dot{x} \;\; \Delta\dot{\theta}\,]^T$, $C_{p2} \in \mathbf{R^{1x4}}$, and $y_{p2} \equiv \Delta x$. When Δx is measured in ft., $\Delta\dot{x}$ in ft./sec., $\Delta\theta$ in degs., and $\Delta\dot{\theta}$ in degs./sec., and ΔB_{lc} in degs., we have

$$A_{p2} = \begin{bmatrix} 0 & 0 & 1 & 0 \\ 0 & 0 & 0 & 1 \\ -\mu\omega_A{}^2 & -[g(1+\mu)+\mu\omega_A{}^2 h] & X_u & 0 \\ -\varepsilon\mu\omega_A{}^2 & -\varepsilon\mu\omega_A{}^2(h+H) & M_u & M_q \end{bmatrix} \tag{3.40a}$$

$$= \begin{bmatrix} 0 & 0 & 1 & 0 \\ 0 & 0 & 0 & 1 \\ -1.09748 & -0.88468 & -0.06 & 0 \\ -17.267 & -5.0777 & 2.3493 & -3.1 \end{bmatrix} \tag{3.40b}$$

$$B_{p2} = \begin{bmatrix} 0 \\ 0 \\ X_{Blc} \\ M_{Blc} \end{bmatrix} = \begin{bmatrix} 0 \\ 0 \\ 0.478185 \\ -47.24 \end{bmatrix} \tag{3.41}$$

$$C_{p2} = [\,1 \;\; 0 \;\; 0 \;\; 0\,]^T \tag{3.42}$$

This SISO system has transfer function given by:

$$G_{p2}(s) = C_{p2}\,(sI - A_{p2})^{-1}\,B_{p2}. \tag{3.43a}$$

$$= k_2\,[s^2 + b_1 s + b_0] \,/\, [s^4 + a_3 s^3 + a_2 s^2 + a_1 s + a_0] \tag{3.43b}$$

$$= 0.4782\,[s^2 + 3.1s + 92.475] \,/\, [s^4 + 3.16s^3 + 6.361s^2 + 5.785s - 9.703] \tag{3.43c}$$

where

$$k_2 \equiv X_{Blc} \tag{3.44}$$

$$b_1 \equiv - M_q \tag{3.45}$$

$$b_0 \equiv \varepsilon\mu\omega_A{}^2\,(h + H) - M_{Blc}\,[\,\mu\omega_A{}^2 h + g\,(1 + \mu)\,] \,/\, X_{Blc} \tag{3.46}$$

$$a_3 \equiv - [\,M_q + X_u\,] \tag{3.47}$$

$$a_2 \equiv M_q\,X_u + \mu\omega_A{}^2[\,1 + \varepsilon\,(h + H)\,] \tag{3.48}$$

$$a_1 \equiv M_u\,[\,\mu\omega_A{}^2 h + g\,(1 + \mu)] - M_q\,\mu\omega_A{}^2 - X_u\,\varepsilon\mu\omega_A{}^2\,(h + H) \tag{3.49}$$

$$a_0 \equiv - \varepsilon\mu\omega_A{}^2\,g. \tag{3.50}$$

It can be shown that the state space triple (A_{p2}, B_{p2}, C_{p2}) is controllable and observable. It thus follows that the state space and transfer function representations are equivalent minimal representations. From now on the state space representation given by eqs. (3.31) - (3.32), and the equivalent I/O representation given by eq. (3.33), shall be referred to as the SM Plant.

For convenience all SM Plant parameter values are given in Table 3.4.2.1. Appendix 1 contains all TLHS parameter values.

From our discussion it follows that the poles of the SM Plant are simply the roots of the characteristic polynomial:

$$\det\,(sI - A_{p2}) = s^4 + 3.16s^3 + 6.361s^2 + 5.785s - 9.703 \tag{3.51}$$

These poles have already been interpreted in the modal discussion of section 3.3.2 which was based on the right eigenvectors of A_{p2}. In that section we referred to these poles as the Tethered

Table 3.4.2.1: SM Plant Parameters

$W_H = 14000$ lbs.	$M_H = 434.78$ slugs	$W_B = 644$ lbs.
$M_B = 20$ slugs	$W_L = 12000$ lbs.	$M_L = 372.67$ slugs
$\mu \equiv [M_L + M_B] / 2M_H = 0.4516$	$h = 3.6$ ft.	$H = 13.25$ ft.
$g = 32.2$ ft/sec^2	$\omega_A{}^2 = g / H = 2.43\ 1 /$ sec^2	$I_y = 5700$ slug ft^2
$\varepsilon \equiv M_H h / I_y = 0.2746$ ft^{-1}		
$X_u = -0.06$ ft sec^{-2} / ft sec^{-1}	$M_u = 0.041$ rad sec^{-2} / ft sec^{-1}	$M_q = -3.1$ rad sec^{-2}/rad sec^{-1}
$X_{Blc} = 27.4$ ft / rad sec^2	$M_{Blc} = -47.24$ rad / rad sec^2	

Helicopter Mode, the Horizontal Spring Mode, and the Symmetric Damping Mode. The Tethered Helicopter Mode was described as an unstable exponential mode associated with helicopters which are tethered to a fixed point in space. The instability is due to the fact that the helicopter-tether attachment points are located below the c.g.'s of the helicopters. The Horizontal Spring Mode was described as a stable, moderately damped, sinusoidal mode. This mode is associated with the stabilizing effect of the tethers when attached below the c.g.'s of the helicopters. The Symmetric Damping Mode was described as characterizing the effects of horizontal translations (Δx).

Note that unlike the natural modes of the SM Plant, which are independent of the output selected, the zeros are functions of the output chosen. This follows from the fact that the zeros are given by the roots of the polynomial:

$$\det \begin{bmatrix} sI - A_{p2} & -B_{p2} \\ C_{p2} & 0 \end{bmatrix} = \det (sI - A_{p2}) \det [G_{p2}(s)] \qquad (3.52a)$$

$$= 0.4782 \, [s^2 + 3.1\ s + 92.475] \qquad (3.52b)$$

This clearly shows a dependence on the output matrix $C_{p2} \in \mathbf{R^{1x4}}$ which selects the output, $y_{p2} \equiv \Delta x$. The roots of this polynomial are $s = -1.55 \pm j\ 9.4906$ ($\tau = 2 / M_q = 0.65$ sec., $\zeta = 0.16$, ω_n

= 9.62 rad./sec.). For reasons to be given these zeros shall be referred to as the SM Helicopter PItching Zeros. The pole-zero structure for the SM Plant is given in Fig. 3.4.2.1.

Since we intend to base our SM AFCS design on the SM Plant linear model it is important to understand the nature of its lightly damped, high frequency, zeros. To do this it is necessary to recall the definition of a tansmission zero for a state space triple (A, B, C) [7].

A state space triple (A, B, C) has a transmission zero at $s = z_0$ if there exists an initial condition, $\underline{x}_0$, and an initial input direction, $\underline{u}_0$, such that when $\underline{x}(0) = x_0$ is the initial state and $\underline{u}(t) = e^{z_0 t}\underline{u}_0$ the applied control then the state and output trajectories are given by $\underline{x}(t) = e^{z_0 t}\underline{x}_0$ and $\underline{y}(t) = \underline{0}$, respectively, for all $t \geq 0$.

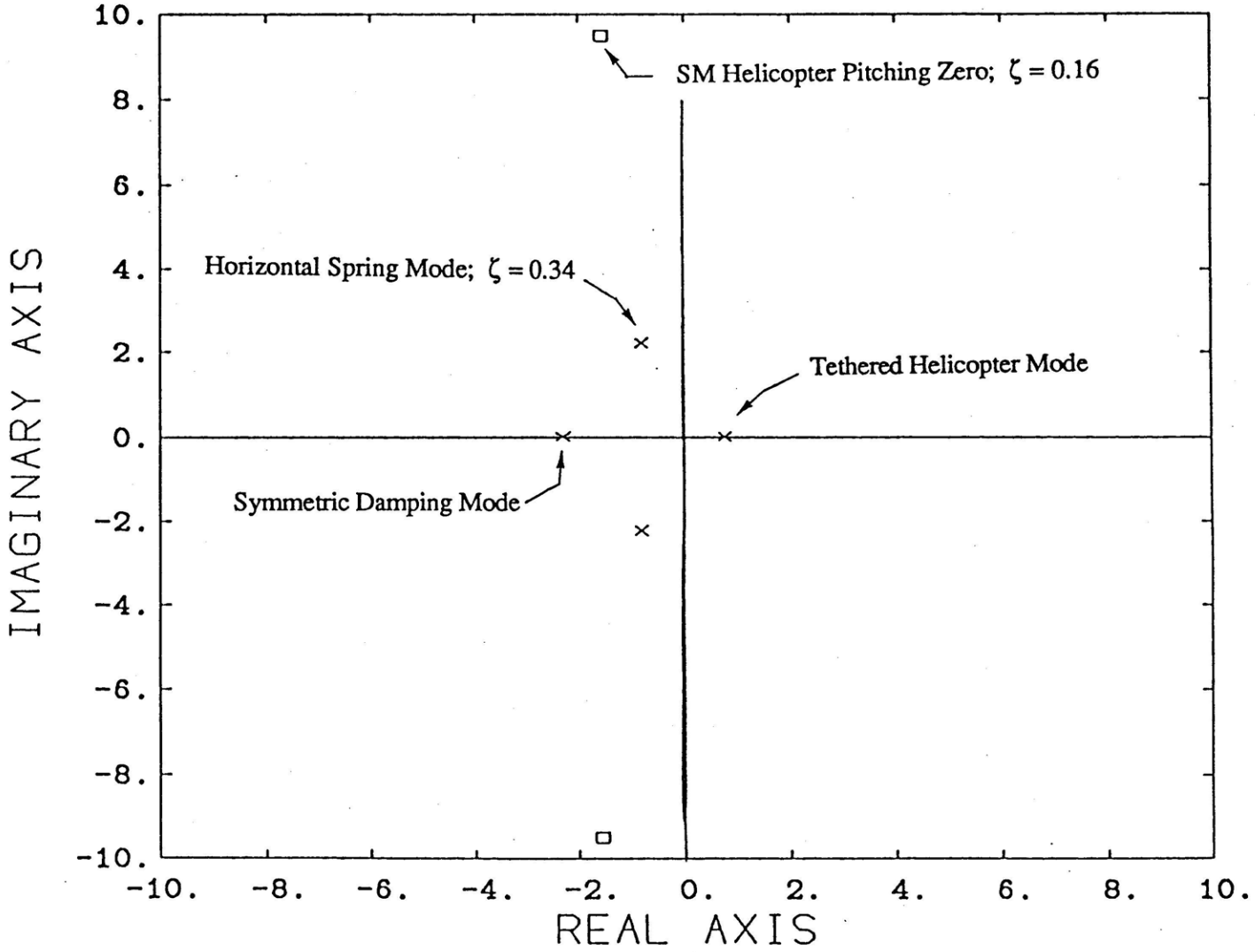

Fig. 3.4.2.1: Pole-Zero Diagram for SM Plant.

The zero, z_0, the right zero direction, $\underline{x}_0$, and the input direction, $\underline{u}_0$, can be found by solving the following system of linear algebraic equations:

$$\begin{bmatrix} z_0 I - A & -B \\ C & 0 \end{bmatrix} \begin{bmatrix} \underline{x}_0 \\ \underline{u}_0 \end{bmatrix} = \begin{bmatrix} \underline{0} \\ \underline{0} \end{bmatrix} \tag{3.53a}$$

or equivalently, by solving the following right generalized eigenvalue problem:

$$\begin{bmatrix} A & B \\ C & 0 \end{bmatrix} \begin{bmatrix} \underline{x}_0 \\ \underline{u}_0 \end{bmatrix} = z_0 \begin{bmatrix} I & 0 \\ 0 & 0 \end{bmatrix} \begin{bmatrix} \underline{x}_0 \\ \underline{u}_0 \end{bmatrix} \tag{3.53b}$$

Doing so for the SM Plant ($A = A_{p2}$, $B = B_{p2}$, $C = C_{p2}$) gives us the following for one zero:

$$z_0 = -1.55 + j\,9.4906 \tag{3.54}$$

$$\underline{x}_0 = [0 \quad -j0.1351 \quad 0 \quad 1.2825 + j\,0.2095]^T \tag{3.55a}$$

$$= [0 \quad 0.1351e^{-j90^\circ} \quad 0 \quad 1.299e^{j9.28^\circ}]^T \tag{3.55b}$$

$$\underline{u}_0 = -j\,0.25 = 0.25\,e^{-j90^\circ} \tag{3.56}$$

and (z_0^*, $\underline{x}_0^*$, $\underline{u}_0^*$) for the other complex conjugate zero. To interpret these complex zeros and directions we provide the following general result.

Suppose that (z_0, $\underline{x}_0$, $\underline{u}_0$) and (z_0^*, $\underline{x}_0^*$, $\underline{u}_0^*$) define a pair of complex conjugate zeros in the s-plane; one at $s = z_0 = \sigma + j\omega$ and the other at $s = z_0^* = \sigma - j\omega$. Suppose further that we define

$$\underline{x}_{0r} \equiv \text{Re}\{\,\underline{x}_0\,\} \qquad \underline{x}_{0i} \equiv \text{Im}\{\,\underline{x}_0\,\} \tag{3.57}$$

$$\underline{u}_r(t) \equiv \text{Re}\{e^{z_0 t}\underline{u}_0\} \qquad \underline{u}_i(t) \equiv \text{Im}\{e^{z_0 t}\underline{u}_0\} \tag{3.58}$$

$$\underline{x}_r(t) \equiv \text{Re}\{e^{z_0 t}\underline{x}_0\} \qquad \underline{x}_i(t) \equiv \text{Im}\{e^{z_0 t}\underline{x}_0\} \tag{3.59}$$

where Re $\{\cdot\}$ and Im $\{\cdot\}$ imply that the real parts and imaginary parts must be taken one component at a time. With these definitions it can be shown that for all a, $b \in \mathbf{R}$, if

$$\underline{x}_0(0) = a\,\underline{x}_{0r} + b\,\underline{x}_{0i} \tag{3.60}$$

and

$$\underline{u}(t) = a\,\underline{u}_r(t) + b\,\underline{u}_i(t) \tag{3.61}$$

then

$$\underline{x}(t) = a\,\underline{x}_r(t) + b\,\underline{x}_i(t) \tag{3.62}$$

and

$$\underline{y}(t) = \underline{0} \tag{3.63}$$

for all $t \geq 0$. The implications of this can be stated as follows:

> To study a complex conjugate pair of zeros we can apply any linear combination of the state-control vectors
>
> $$\text{Re}\begin{bmatrix} \underline{x}_0 \\ e^{z_0 t}\underline{u}_0 \end{bmatrix} \quad \text{and} \quad \text{Im}\begin{bmatrix} \underline{x}_0 \\ e^{z_0 t}\underline{u}_0 \end{bmatrix} \tag{3.64}$$
>
> Doing so gives us the same linear combination of $\text{Re}\{ e^{z_0 t}\underline{u}_0 \}$ and $\text{Im}\{ e^{z_0 t}\underline{u}_0 \}$, respectively.

Applying the above genereal result to the SM Plant gives us the following:

$$z_0 = \sigma + j\omega = -1.55 + j\,9.4906 \tag{3.65}$$

$$\underline{x}_0 = [\,0 \quad -j\,0.1351 \quad 0 \quad 1.2825 + j\,0.2095\,]^T \tag{3.66}$$

$$\underline{x}_{0r} = \text{Re}\{\underline{x}_0\} = [\,0 \quad 0 \quad 0 \quad 1.2825\,]^T \tag{3.67a}$$

$$\underline{x}_{0i} = \text{Im}\{\underline{x}_0\} = [\,0 \quad -0.1351 \quad 0 \quad 0.2095\,]^T \tag{3.67b}$$

$$u_0 = 0.25\,e^{-j\,90^\circ} \tag{3.68}$$

$$e^{z_0 t}u_0 = e^{(\sigma + j\,\omega)\,t}\,0.25\,e^{-j\,90^\circ} = 0.25\,e^{\sigma t}\,e^{j(\omega t - 90^\circ)} \tag{3.69a}$$

$$= 0.25\,e^{\sigma t}\,[\,\cos(\omega t - 90^\circ) + j\sin(\omega t - 90^\circ)\,] \tag{3.69b}$$

$$= [\,0.25\,e^{\sigma t}\sin\omega t\,] + j\,[\,-0.25\,e^{\sigma t}\cos\omega t\,] \tag{3.69c}$$

$$u_r(t) \equiv \text{Re}\{ e^{z_0 t}u_0 \} = 0.25\,e^{\sigma t}\sin\omega t \tag{3.70a}$$

$$u_i(t) \equiv \text{Im}\{ e^{z_0 t}u_0 \} = -0.25\,e^{\sigma t}\cos\omega t \tag{3.70b}$$

$$e^{z_0 t}\underline{x}_0 = e^{(\sigma + j\omega)\,t}\,[\,0 \quad 0.1351\,e^{-j90^\circ} \quad 0 \quad 1.299 e^{j9.28^\circ}\,]^T \tag{3.71a}$$

$$= e^{\sigma t}\,[\,0 \quad 0.1351\,e^{j\,(\omega t - 90^\circ)} \quad 0 \quad 1.299\,e^{j\,(\omega t + 9.28^\circ)}\,]^T \tag{3.71b}$$

$$= [\,0 \quad 0.1351e^{\sigma t}\sin\omega t \quad 0 \quad 1.299e^{\sigma t}\cos(\omega t + 9.28^\circ)\,]^T$$

$$+ j\,[\,0 \quad -0.1351e^{\sigma t}\cos\omega t \quad 0 \quad 1.299\,e^{\sigma t}\sin(\omega t + 9.28^\circ)\,]^T \tag{3.71c}$$

$$\underline{x}_r(t) \equiv \mathrm{Re}\,\{\,e^{Z_0 t}\underline{x}_0\,\} = [\,0 \;\; 0.1351e^{\sigma t}\sin\omega t \;\; 0 \;\; 1.299\,e^{\sigma t}\cos(\omega t + 9.28^\circ)]^T \tag{3.72a}$$

$$\underline{x}_i(t) \equiv \mathrm{Im}\,\{\,e^{Z_0 t}\underline{x}_0\,\} = [\,0 \;\; -0.1351e^{\sigma t}\cos\omega t \;\; 0 \;\; 1.299\,e^{\sigma t}\sin(\omega t + 9.28^\circ)]^T \tag{3.72b}$$

From these it follows that for all a, b $\in$ **R**, if

$$\underline{x}_{p2}(0) = a\,\underline{x}_{or} + b\,\underline{x}_{oi} \tag{3.73a}$$

$$= a\,[\,0 \;\; 0 \;\; 0 \;\; 1.2825]^T + b\,[\,0 \;\; -0.1351 \;\; 0 \;\; 0.2095\,]^T \tag{3.73b}$$

and

$$u_{p2}(t) = a\,u_r(t) + b\,u_i(t) \tag{3.74a}$$

$$= a\,[\,0.25\;e^{\sigma t}\sin\omega t] + b\,[-0.25\,e^{\sigma t}\cos\omega t] \tag{3.74b}$$

then

$$\underline{x}_{p2}(t) = a\,\underline{x}_r(t) + b\,\underline{x}_i(t) \tag{3.75a}$$

$$= a\,[0 \quad 0.135\,e^{\sigma t}\sin\omega t \quad 0 \quad 1.299\,e^{\sigma t}\cos(\omega t + 9.28^\circ)\,]^T \tag{3.75b}$$

$$+ b\,[0 \;\; -0.135\,e^{\sigma t}\cos\omega t \;\; 0 \;\; 1.299\,e^{\sigma t}\sin(\omega t + 9.28^\circ)\,]^T \tag{3.75c}$$

and

$$y_{p2}(t) = 0 \tag{3.76}$$

for all $t \geq 0$. With these relationships, and the fact that $\underline{x}_{p2} = [\,\Delta x \;\Delta\theta \;\Delta\dot{x} \;\Delta\dot{\theta}]^T$, we have a complete characterization of the SM Plant zeros. These zeros characterize the fact that if initially $\Delta x = \Delta\dot{x} = 0$ and the helicopters are given the appropriate initial relative pitch and pitch rate (eq. (3.73)) and if the differential cyclic, $u_{p2} \equiv \Delta B_{lc}$, is properly manipulated (eq. (3.74)), then the helicopters will pitch in accordance with eq. (3.75) maintaining $y_{p2} \equiv \Delta x = 0$ for all time. Since $\Delta x = -\,[h\,\Delta\theta + H\,\Delta\varepsilon] = 0$, this means that

$$\Delta\theta = -\,(H / h)\,\Delta\varepsilon = -\,3.681\,\Delta\varepsilon \tag{3.77}$$

for all time. This implies that if $\Sigma\theta = \Sigma\varepsilon = 0$, then $\theta_m = -(H/h)\,\varepsilon_m$, $\theta_s = -\theta_m$, and $\varepsilon_s = -\varepsilon_m$. In such a case we can have the situation depicted in fig. 3.4.2.1 which assumes (a = 0, b = 1) in eqs. (3.73) - (3.75).

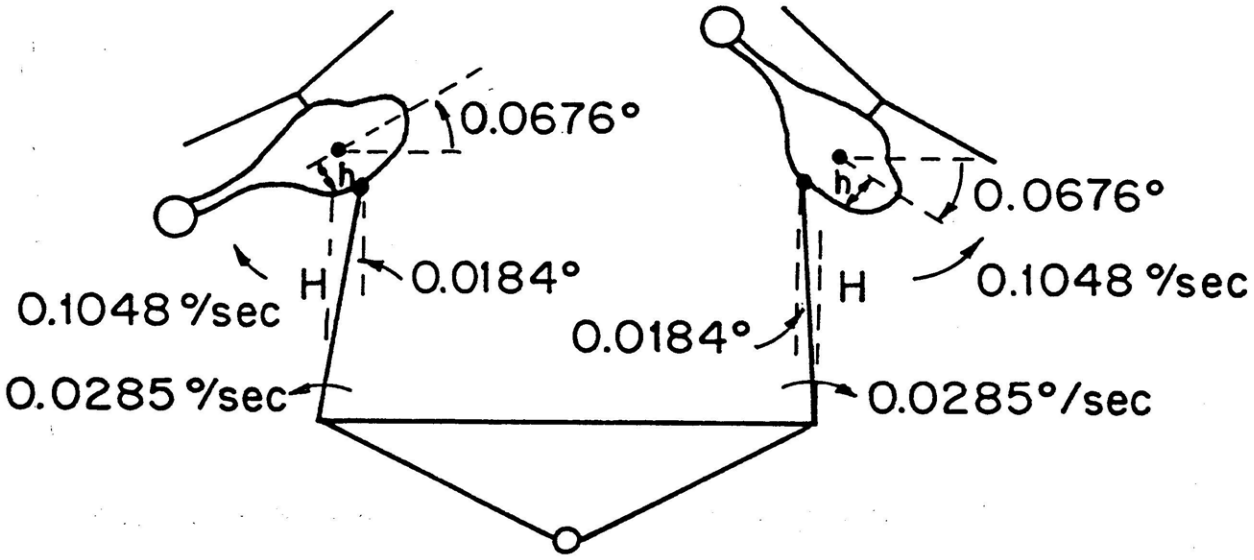

Fig. 3.4.2.1: Visualization of an Initial Condition to Interpret the SM Helicopter Zeros (a = 0, b = 1).

Physically, the SM Plant zeros are due to the fact that each helicopter can pitch without undergoing translation provided that they are given appropriate initial conditions and that their cyclics are properly adjusted. This fact shall be discussed in more detail later in the section. For now we shall shed light on the above "numerical" analysis by providing "symbolic" relationships which show the exact dependence of the zeros and their directions on the SM Plant parameters.

Given the definition of a transmission zero we know that if the SM Plant is properly excited $(z_0, \underline{x}_0, u_0)$ then $\Delta x = 0$ for all time. It thus follows that $\Delta x(0) = \Delta\dot{x}(0) = 0$. Substituting $\Delta x = 0$ into the differential equations describing the SM:

$$M_H \Delta\ddot{x} = 0.5(W_L + W_B)\Delta\varepsilon - (W_H + 0.5(W_L+W_B))\Delta\theta + M_H X_u \Delta\dot{x} + M_H X_{Blc}\Delta B_{lc} \quad (3.78a)$$

$$I_y \Delta\ddot{\theta} = 0.5(W_L+W_B)h\Delta\varepsilon - 0.5(W_L+W_B)h\Delta\theta + I_y M_u \Delta\dot{x} + I_y M_q \Delta\dot{\theta} + I_y M_{Blc}\Delta B_{lc} \quad (3.78b)$$

$$\Delta\varepsilon = -[\Delta x + h\,\Delta\theta] / H \quad (3.78c)$$

gives us the equation

$$\Delta\theta(t) = \frac{M_H X_{Blc}}{W_H + 0.5(W_L + W_B)(1 + h/H)} \Delta B_{lc}(t) \tag{3.79a}$$

$$= 0.5405\ \Delta B_{lc}(t) \tag{3.79b}$$

This equation completely specifies the right zero direction, $\underline{x}_0$. More specifically the equation shows that if $\Delta B_{lc} = 0.25\ e^{\sigma t} \cos\omega t$ then $\Delta\theta = 0.1351 e^{\sigma t} \sin\omega t$ and $\Delta\theta = 1.299 e^{\sigma t} \cos(\omega t + 9.28°)$. Also if $\Delta B_{lc} = -0.25 e^{\sigma t} \cos\omega t$ then $\Delta\theta = -0.1351 e^{\sigma t} \cos\omega t$ and $\Delta\theta = 1.299 e^{\sigma t} \sin(\omega t + 9.28°)$. These, of course, are in agreement with eqs. (3.73) - (3.74).

Substituting $\Delta x = 0$ and $\Delta\theta = \Delta\theta_0 e^{z_0 t}$ into the SM equations and using eq. (3.79) gives us the following quadratic in z_0:

$$\boxed{z_0^2 + |M_q| z_0 + 0.5(W_L + W_B)(1 + h/H)[h/I_y + |M_{Blc}| / M_H X_{Blc}] + |M_{Blc}| g / X_{Blc} = 0} \tag{3.80}$$

where $|\ |$ is used to denote the absolute value of an otherwise negative quantity. This quadratic shows that for $\mu \equiv [M_L + M_B] / 2M_H = 0$ (i.e. $W_L = W_B = 0$), the quadratic becomes identical to that for a single hovering helicopter with velocity as an output (Appendix 3). This fact shall be further addressed later in the section. For now, it suffices to note that the discriminant of eq. (3.80) for the single hovering helicopter ($\mu = 0$) is negative; i.e.

$$|M_q|^2 - 4 |M_{Blc}| g / X_{Blc} < 0 \tag{3.81}$$

This, of course, implies that the quadratic

$$z_0^2 + |M_q| z_0 + |M_{Blc}| g / X_{Blc} = 0 \tag{3.82}$$

(for a single hovering helicopter with horizontal velocity as an output) always has complex

conjugate zeros. Furthermore, since $0.5\,(W_L + W_B)\,(1 + h/H)\,[h/I_y + |M_{Blc}|/M_H X_{Blc}]$ is always nonnegative, it follows that the zeros for the SM Plant (with output Δx) also occur in complex conjugate pairs. In addition these zeros always have real part at $s = -|M_q|/2 = -1.55$, radial frequency greater than or equal to $|M_{Blc}|\,g/X_{Blc}\,]^{0.5} = 7.45$, and damping ratio less than 0.2. Of course, for our fixed parameter SM Plant it has already been shown that $z_0 = -1.55 \pm j\,9.4906$ ($\omega_n = 9.62$, $\zeta = 0.16$).

To terminate the section we note that the SM Plants' zeros (associated with the output Δx) might have been anticipated from our knowledge of a single hovering helicopter with horizontal velocity as an output (Appendix 3).

As mentioned throughout the section, the SM equations reduce to those of a single helicopter when $\mu = 0$. Setting $\mu = 0$ gives us $b_0 = -g\,MB_{lc}/X_{Blc} = 55.52$ and $b_1 = -M_q = 3.1$ for which the zeros become $z_0 = -1.55 \pm j\,7.29$ ($\omega_n = 7.45$, $\zeta = 0.2$). These lightly damped, high frequency, zeros characterize the fact that a hovering helicopter can pitch without undergoing translation, provided the helicopter (initially at rest) is given an appropriate initial pitch, pitch rate (determined by $\Delta\theta = (X_{Blc}/g)\,\Delta B_{lc} = 0.851\,\Delta B_{lc}$), and that its cyclic control is properly manipulated. Based on this fact alone one might anticipate the lightly damped zeros of the SM Plant where Δx is an output.

The implications of the SM Plants' modes and zeros on the Twin Lift Equal Tether Control Problem shall be discussed in a later section. Now we shall select outputs for the ASM subsystem, define an ASM Plant, and study its zeros.

3.4.3 Selection of Outputs for ASM Subsystem: The ASM Plant

The pair (A_{p3}, B_{p3}) describes the TLHS's ASM, involves the $\Sigma\dot{x}$, $\Sigma\theta$, Δz, x_L' degrees of freedom, and is conrolled by issuing differential collective commands ($\Delta\Theta_c$) and average cyclic commands (ΣB_{lc}). This subsystem has only two control inputs which can be used to control at

most two outputs. The load deviation from center, x_L-Σx, shall be selected as an output because it will allow the pilot to directly control the load motion in a "very natural manner"; i.e. by controlling the vertical separation between the helicopters (eq. (3.11)). Typically x_L-Σx will be commanded to zero. The average horizontal velocity, $\Sigma\dot{x}$, shall also be selected as an output since the regulation of pilot commanded velocities is essential. The ASM thus has the following state space representation:

$$\dot{\underline{x}}_{p3} = A_{p3}\,\underline{x}_{p3} + B_{p2}\,\underline{u}_{p3}; \qquad \underline{x}_{p3} \in \mathbf{R}^7 \tag{3.83}$$

$$\underline{y}_{p3} = C_{p3}\,\underline{x}_{p3}; \qquad \underline{u}_{p3},\, \underline{y}_{p3} \in \mathbf{R}^2 \tag{3.84}$$

where $\underline{u}_{p3} \equiv [\,\Delta\Theta_c \;\; \Sigma B_{lc}\,]^T$, $\underline{x}_{p2} \equiv [\,\Sigma\theta \;\; \Delta z \;\; x_L' \;\; \Sigma\dot{x} \;\; \Sigma\dot{\theta} \;\; \Delta\dot{z} \;\; \dot{x}_L'\,]^T$, $C_{p3} \in \mathbf{R}^{2x7}$, and $\underline{y}_{p3} = [\, x_L\text{-}\Sigma x \;\; \Sigma\dot{x}]^T$. When $\Delta\Theta_c$, ΣB_{lc}, $\Sigma\theta$ are measured in degs., $\Sigma\dot{\theta}$ in degs./sec., Δz, x_L', $x_L - \Sigma x$ in ft., and $\Sigma\dot{x}$, $\Delta\dot{z}$, $\dot{x}_L'$ in ft./sec., we have

$$A_{p3} = \begin{bmatrix} 0 & 0 & 0 & 0 & 1 & 0 & 0 \\ 0 & 0 & 0 & 0 & 0 & 1 & 0 \\ 0 & 0 & 0 & 0 & 0 & 0 & 1 \\ -g & 0 & \mu\omega_A{}^2 & X_u & 0 & 0 & 0 \\ 0 & 0 & \varepsilon\mu\omega_A{}^2 & M_u & M_q & 0 & 0 \\ 4TH & -4T\hat{H} & 4T & 0 & 0 & Z_w TJ & 0 \\ -4T\delta_L\hat{Z}H & 4T\delta_L\hat{Z}H & D & E & -M_q(h+H) & -Z_w TJ\delta_L\hat{Z} & 0 \end{bmatrix} \tag{3.85a}$$

$$= \begin{bmatrix} 0 & 0 & 0 & 0 & 1 & 0 & 0 \\ 0 & 0 & 0 & 0 & 0 & 1 & 0 \\ 0 & 0 & 0 & 0 & 0 & 0 & 1 \\ -0.56195 & 0 & 1.0975 & -0.06 & 0 & 0 & 0 \\ 0 & 0 & 17.267 & -2.3493 & -3.1 & 0 & 0 \\ 0.4679 & -0.3885 & 2.0233 & 0 & 0 & -0.3361 & 0 \\ -0.2220 & 0.1844 & -9.5654 & -0.6309 & 0.91161 & 0.1595 & 0 \end{bmatrix} \tag{3.85b}$$

$$B_{p3} = \begin{bmatrix} 0 & 0 \\ 0 & 0 \\ 0 & 0 \\ 0 & X_{Blc} \\ 0 & M_{Blc} \\ Z_{\Theta_c} TJ & 0 \\ -Z_{\Theta_c} TJ\delta_L\hat{Z} & -[X_{Blc} + M_{Blc}(h+H)] \end{bmatrix} = \begin{bmatrix} 0 & 0 \\ 0 & 0 \\ 0 & 0 \\ 0 & 0.4782 \\ 0 & -47.24 \\ 5.7789 & 0 \\ -2.7423 & 13.4136 \end{bmatrix} \tag{3.86}$$

$$C_{p3} = \begin{bmatrix} (h+H) & Z & 1 & 0 & 0 & 0 & 0 \\ 0 & 0 & 0 & 1 & 0 & 0 & 0 \end{bmatrix} \quad (3.87a)$$

$$= \begin{bmatrix} 0.2836 & 0.5 & 1 & 0 & 0 & 0 & 0 \\ 0 & 0 & 0 & 1 & 0 & 0 & 0 \end{bmatrix} \quad (3.87b)$$

This TITO (two-input two-output) system has transfer function matrix given by:

$$G_{p3}(s) = C_{p3}\,(sI - A_{p3})^{-1}\,B_{p3}. \quad (3.88a)$$

$$= \begin{bmatrix} g_{11}(s) & g_{12}(s) \\ g_{21}(s) & g_{22}(s) \end{bmatrix} \quad (3.88b)$$

where $g_{ij}(s) \equiv n_{ij}(s) / d(s) \qquad i, j = 1, 2 \quad (3.88c)$

and

$$n_{11}(s) = 0.147\,s^5 + 0.465\,s^4 + 10.969\,s^3 + 32.371\,s^2 + 1.305\,s + 15.142 \quad (3.89a)$$

$$n_{12}(s) = -0.478\,s^5 - 1.641\,s^4 - 52.445\,s^3 - 19.611\,s^2 - 60.985\,s - 0.097 \quad (3.89b)$$

$$n_{21}(s) = -3.009\,s^4 - 9.329\,s^3 + 26.612\,s^2 + 0.0004\,s - 0.0024 \quad (3.89c)$$

$$n_{22}(s) = 0.478\,s^6 + 1.643\,s^5 + 46.528\,s^4 + 20.858\,s^3 + 155.97\,s^2 + 34.435\,s + 38.1 \quad (3.89d)$$

$$d(s) \equiv \det(sI - A_{p3}) \quad (3.89e)$$

$$= s^7 + 3.496\,s^6 + 11.203\,s^5 + 20.681\,s^4 + 12.404\,s^3 + 12.694\,s^2 + 1.936\,s + 2.0356 \quad (3.89f)$$

The roots of these polynomials are as follows:

$$\text{Roots}(n_{11}) = -0.099 \pm j\,8.592,\ 0.055 \pm j\,0.072,\ -3.071 \quad (3.90a)$$

$$\text{Roots}(n_{12}) = -1.544 \pm j\,10.254,\ -0.173 \pm j\,1.076,\ -0.002 \quad (3.90b)$$

$$\text{Roots}(n_{21}) = -4.903,\ 18.034,\ -0.0095,\ 0.0095 \quad (3.90c)$$

$$\text{Roots}(n_{22}) = -1.545 \pm j\,9.506,\ -0.061 \pm j\,1.784,\ -0.112 \pm j\,0.508 \quad (3.90d)$$

$$\text{Roots}(d) = \text{eigenvalues of } A_{p3} \quad (3.90e)$$

$$= 0.0402 \pm j\,0.4785,\ -0.1976 \pm j\,0.7364,\ -0.5314 \pm j\,2.6245,\ -2.1187 \quad (3.90f)$$

It can be shown that the state space triple (A_{p3}, B_{p3}, C_{p3}) is controllable and observable. It thus follows that the state space and transfer function matrix representations are equivalent minimal representations. From now on the state space representation given by eqs. (3.83) - (3.87) and the equivalent I/O representation given by eqs. (3.88) - (3.90) shall be referred to as the ASM Plant.

For convenience all ASM Plant parameter values are given in Table 3.4.3.1.

From our discussion it follows that the poles of the ASM Plant are simply the roots of the characteristic polynomial:

$$\det (sI - A_{p3}) = s^7 + 3.496\, s^6 + 11.203\, s^5 + 20.681\, s^4 + 12.404\, s^3 + 12.694\, s^2 + 1.936\, s + 2.0356 \quad (3.91)$$

These poles have already been interpreted in the modal discussion of section 3.3.3, which was based on the right eigenvectors of A_{p3}. In that section we referred to these poles as the Backflapping Mode, the Vertical Spring Mode, the Pendular Mode, and Anti-Symmetric Damping Mode. The Backflapping Mode was described as a low frequency unstable exponential-sinusoidal mode characteristic of hovering helicopters. The instability is due to the backflapping of the main rotor with forward motion. The Vertical Spring Mode was described as a stable, low frequency, lightly damped, sinusoidal mode. This mode is associated with the fact that the load is suspended a distance Z below the c.g. of the spreader bar. The Pendular Mode was described as a stable, high frequency, lightly damped, sinusoidal mode. This mode characterizes the natural tendency of the load to sway. The Anti- Symmetric Damping Mode was described as a stable exponential mode. This mode characterizes the effect of horizontal aerodynamic drag forces on the TLHS during horizontal translation ($\Sigma\dot{x}$).

Note that unlike the natural modes of the ASM Plant, which are independent of the outputs selected, the zeros are a function of the outputs chosen. This follows from the fact that the zeros

Table 3.4.3.1: ASM Plant Parameters

$W_H = 14000$ lbs.	$M_H = 434.78$ slugs	$W_B = 644$ lbs.	$M_B = 20$ slugs
$W_L = 12000$ lbs.	$M_L = 372.67$ slugs	$I_y = 5700$ slug ft^2	$h = 3.6$ ft.
$H_s = H$	$H_m = H$	$H = 13.25$ ft.	$Z = 34.5$ ft.
$L = 69$ ft.			

$\mu \equiv [M_L + M_B] / 2M_H = 0.4516$

$\delta_L \equiv M_L / [M_L + M_B] = 0.9491$

$g = 32.2$ ft / sec^2

$\omega_A{}^2 = g / H = 2.43$

$\varepsilon \equiv M_H h / Iy = 0.2746$ ft^{-1}

$I_B = (1 / 12) M_B L^2 = 7935$ slug ft^2

$e_b \equiv 2 I_B / M_H L^2 = M_B / 6 M_H = 0.0077$

$\hat{H} \equiv H / L = 0.192$

$\hat{Z} \equiv Z / L = 0.5$

$\Psi \equiv 1 + e_b + 4 \mu \hat{Z}^2 \delta_L (1 - \delta_L) = 1.0295$

$D \equiv - \omega_A{}^2 [1 + \mu + (h + H_s) \mu \varepsilon + 4 T \delta_L \hat{Z} / \omega_A{}^2] = - 3.9363$ ft sec^{-2} / ft

$E \equiv - [X_u + M_u (h + H_s)] = - 0.63085$ ft sec^{-2} / ft sec^{-1}

$J \equiv [\mu \delta_L \hat{Z} \omega_A{}^2]^{-1} = 1.9203$ sec^2

$T \equiv \mu \delta_L \hat{Z} \omega_A{}^2 / \Psi = 0.50584$ sec^{-2}

$X_u = - 0.06$ ft sec^{-2} / ft sec^{-1}

$X_{Blc} = 27.4$ ft sec^{-2} / rad

$M_u = 0.041$ rad sec^{-2} / ft sec^{-1}

$M_{Blc} = -47.24$ rad sec^{-2} / rad

$M_q = - 3.1$ rad sec^{-2} / rad sec^{-1}

$Z_w = - 0.346$ ft sec^{-2} / ft sec^{-1}

$Z_{\Theta c} = 340.9$ ft sec^{-2} / rad

are given by the roots of the polynomial:

$$\det \begin{bmatrix} sI - A_{p3} & -B_{p3} \\ C_{p3} & 0 \end{bmatrix} = \det [\, sI - A_{p3}] \ \det [\, G_{p3}(s) \,] \tag{3.92}$$

This clearly shows a dependenceon the output matrix $C_{p3} \in \mathbf{R}^{2x7}$.

Note that unlike the poles of the ASM Plant, which are independent of the outputs selected, $y_{p3} \equiv [x_L - \Sigma x \ \Sigma \dot{x}]^T$. The roots of this polynomial can be shown to be $z_{1,2} = -0.179 \pm j\, 6.41$ ($\tau =$ 5.56 sec., $\zeta = 0.028$, $\omega_n = 6.42$ rad/sec) and $z_{3,4} = -1.37 \pm j\, 9.81$ ($\tau = 0.73$ sec, $\zeta = 0.138$, ω_n = 9.9 rad/sec). For reasons to be given subsequently, $z_{1,2}$ shall be referred to as the ASM Load Motion Zero and $z_{3,4}$ as the ASM Helicopter Pitching Zero. It should be emphasized that the zeros $z_{1,2,3,4}$, of the ASM Plant $G_{p3}(s)$, are not zeros of the individual transfer functions within $G_{p3}(s)$ (eqs. (3.89) - (3.90)). This fact is true for most MIMO systems with coupled dynamics [7]. The pole-zero structure for the ASM Plant is given in Fig. 3.4.3.1.

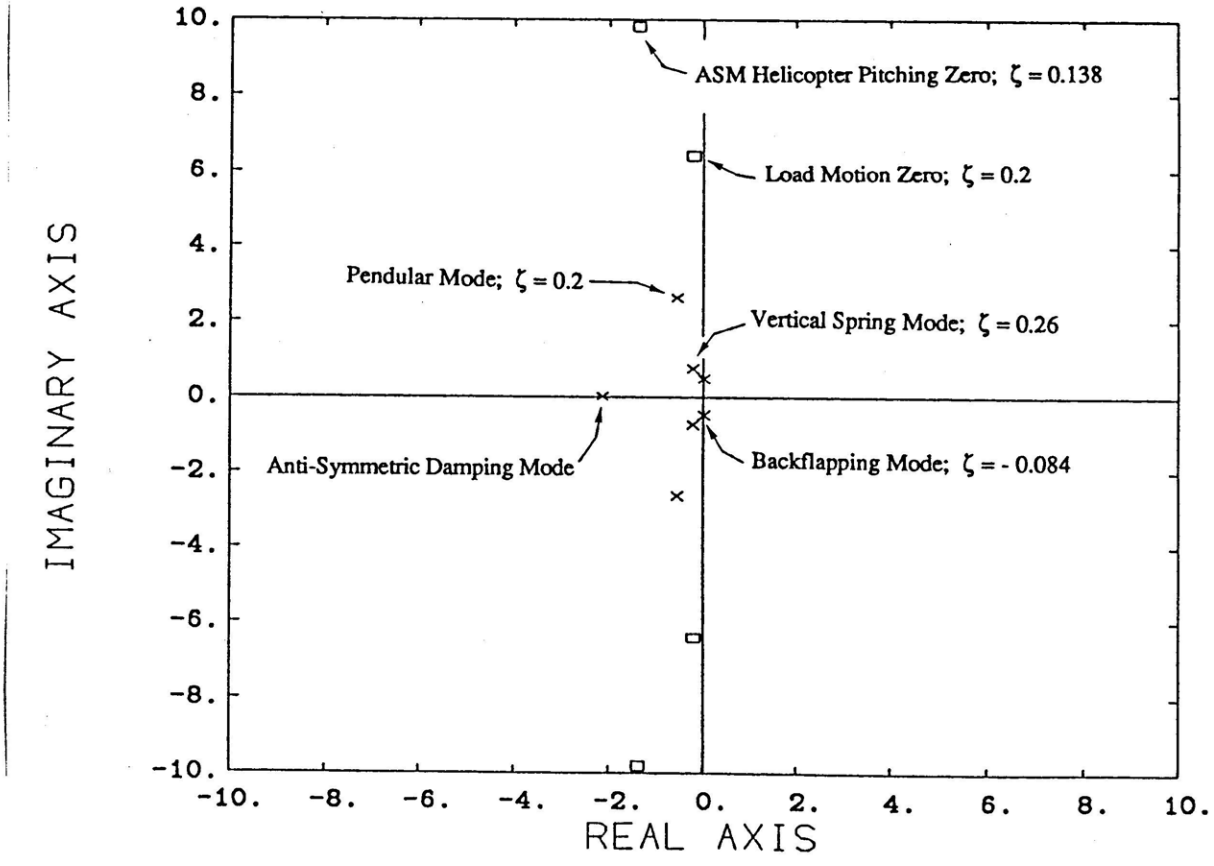

Fig. 3.4.3.1: Pole-Zero Diagram for ASM Plant.

To interpret these zeros we solve the following right generalized eigenvalue problem:

$$\begin{bmatrix} A_p & B_p \\ C_p & 0 \end{bmatrix} \begin{bmatrix} \underline{x}_0 \\ \underline{u}_0 \end{bmatrix} = z \begin{bmatrix} I & 0 \\ 0 & 0 \end{bmatrix} \begin{bmatrix} \underline{x}_0 \\ \underline{u}_0 \end{bmatrix} \quad i = 1, 2, 3, 4 \qquad (3.93)$$

for the input directions, $\underline{u}_i$, and the right zero directions, $\underline{x}_i$. Doing so gives us the following:

ASM Load Motion Zeros:

$$z_{1,2} = -0.179 \pm j\,6.41 = \sigma_{1,2} \pm j\,\omega_{1,2} \qquad (3.94a)$$

$$\underline{x}_{1,2} = [0.9823 \;\; -0.6349 \;\; 0.0286 \;\; 0 \;\; -3.8326 \;\; 4.8345 \;\; -1.2902]^T \qquad (3.94b)$$
$$\pm j\,[0.5703 \;\; -0.7362 \;\; 0.204 \;\; 0 \;\; 6.1973 \;\; -3.9398 \;\; 0.1475]^T$$
$$= [1.14e^{\pm j30.1^\circ} \;\; 0.972e^{\mp j130.8^\circ} \;\; 0.21e^{\pm j82^\circ} \;\; 0 \;\; 7.29e^{\pm j121.7^\circ} \;\; 6.24\,e^{\mp j39.2^\circ} \;\; 1.3e^{\pm j174^\circ}]^T \qquad (3.94c)$$

$$\underline{u}_{1,2} = [\,4.3715 \;\; 1.0888]^T \pm j\,[\,5.0917 \;\; 2.1028]^T \qquad (3.94d)$$
$$= [\,6.71\,e^{\pm j49.4^\circ} \;\; 2.37\,e^{\pm j62.6^\circ}]^T \qquad (3.94e)$$

ASM Helicopter Pitching Zeros:

$$z_{3,4} = -1.37 \pm j\,9.81 = \sigma_{3,4} \pm j\,\omega_{3,4} \qquad (3.95a)$$

$$\underline{x}_{3,4} = [\,0.1464 \;\; -0.0031 \;\; -0.0415 \;\; 0 \;\; 2.8309 \;\; 0.377 \;\; -1.2021]^T \qquad (3.95b)$$
$$\pm j\,[-0.3092 \;\; -0.038 \;\; 0.11 \;\; 0 \;\; 1.86 \;\; 0.0217 \;\; -0.5578]^T$$
$$= [\,0.34e^{\,j64.7^\circ} \;\; 0.038e^{\mp j94.7^\circ} \;\; 0.12e^{\pm j110.7^\circ} \;\; 0 \;\; 3.39e^{\pm j33.3^\circ} \;\; 0.38e^{\pm j3.3^\circ} \;\; 1.2e^{\mp j151^\circ}]^T \qquad (3.95c)$$

$$\underline{u}_{3,4} = [-0.1019 \;\; 0.2673]^T \pm j\,[0.6198 \;\; -0.6156]^T \qquad (3.95d)$$
$$= [\,0.63\,e^{\pm j99.3^\circ} \;\; 0.671e^{\mp j66.5^\circ}]^T \qquad (3.95e)$$

The relations in (3.94) can be used to interpret the ASM Load Motion Zeros. From these equations it follows that for all a, b $\in$ **R**, if

$$\underline{x}_{p3}(0) = a\,\mathrm{Re}\{\,\underline{x}_1\} + b\,\mathrm{Im}\,\{\,\underline{x}_1\,\} \qquad (3.96a)$$

$$= a\,[0.9823 \;\; -0.6349 \;\; 0.0286 \;\; 0 \;\; -3.8326 \;\; 4.8345 \;\; -1.2902]^T$$
$$+ b\,[0.5703 \;\; -0.7362 \;\; 0.204 \;\; 0 \;\; 6.1973 \;\; -3.9398 \;\; 0.1475]^T \qquad (3.96b)$$

$$\underline{u}_{p3}(t) = a\,\mathrm{Re}\,\{\,\underline{u}_1 e^{z_1 t}\,\} + b\,\mathrm{Im}\,\{\,\underline{u}_1 e^{z_1 t}\,\} \qquad (3.97a)$$

$$= a\,[\,6.71 \;\; e^{\sigma_1 t}\cos(\omega_1 t + 49.4°) \;\; 2.37 e^{\sigma_1 t}\cos(\omega_1 t + 62.6°)\,]^T$$

$$+ b\,[\,6.71 \;\; e^{\sigma_1 t}\sin(\omega_1 t + 49.4°) \;\; 2.37 e^{\sigma_1 t}\sin(\omega_1 t + 62.6°)\,]^T \qquad (3.97b)$$

$$\underline{x}_{p3}(t) = a\,\mathrm{Re}\,\{\,\underline{x}_1 e^{z_1 t}\,\} + b\,\mathrm{Im}\,\{\,\underline{x}_1 e^{z_1 t}\,\} \qquad (3.98a)$$

$$= a\,e^{\sigma_1 t}[1.14\cos(\omega_1 t + 30.1°) \;\; 0.972\cos(\omega_1 t - 130.8°) \;\; 0.21\cos(\omega_1 t + 82°) \;\; 0$$

$$7.29\cos(\omega_1 t + 121.7°) \;\; 6.24\cos(\omega_1 t - 39.2°) \;\; 1.3\cos(\omega_1 t + 174°)]^T$$

$$+ b\,e^{\sigma_1 t}[1.14\sin(\omega_1 t + 30.1°) \;\; 0.972\sin(\omega_1 t - 130.8°) \;\; 0.21\sin(\omega_1 t + 82°) \;\; 0$$

$$7.29\sin(\omega_1 t + 121.7°) \;\; 6.24\sin(\omega_1 t - 39.2°) \;\; 1.3\sin(\omega_1 t + 174°)]^T$$

(3.98b)

and

$$\underline{y}_{p3}(t) = \underline{0} \qquad (3.99)$$

for all $t \geq 0$. Considering only the real part of eq. (3.96) with ($a = -1$, $b = 0$) gives

$$\underline{x}_{p3}(0) = [\,-0.9823 \;\; 0.6349 \;\; -0.0286 \;\; 0 \;\; 3.8326 \;\; -4.8345 \;\; 1.2902]^T \qquad (3.100)$$

Using the Equal Tether ($H_s = H_m = H$) relationships for x_L' and $x_L - \Sigma x$, given in Table 3.2.2, the initial condition in eq. (3.100) can be visualized as indicated in Fig. 3.4.3.2.

Here the collectives and cyclics are coordinated so that $\Delta\Theta_c$ leads ΣB_{lc} by 13.2° (eq. (3.97)). This results in Δz leading $\Sigma\varepsilon$ and $\Sigma\varepsilon$ leading $\Sigma\theta$. This in turn results in $x_L - \Sigma x = 0$ and $\Sigma\dot{x} = 0$. Because these zeros, relatively speaking, are primarily associated with the Δz and $\Sigma\varepsilon$ degrees of freedom ($\Delta\dot{z}(0) = -4.84$ ft./sec., $\Sigma\dot{\varepsilon}(0) = 9.41$ deg./sec.) we refer to them as the ASM Load Motion Zeros.

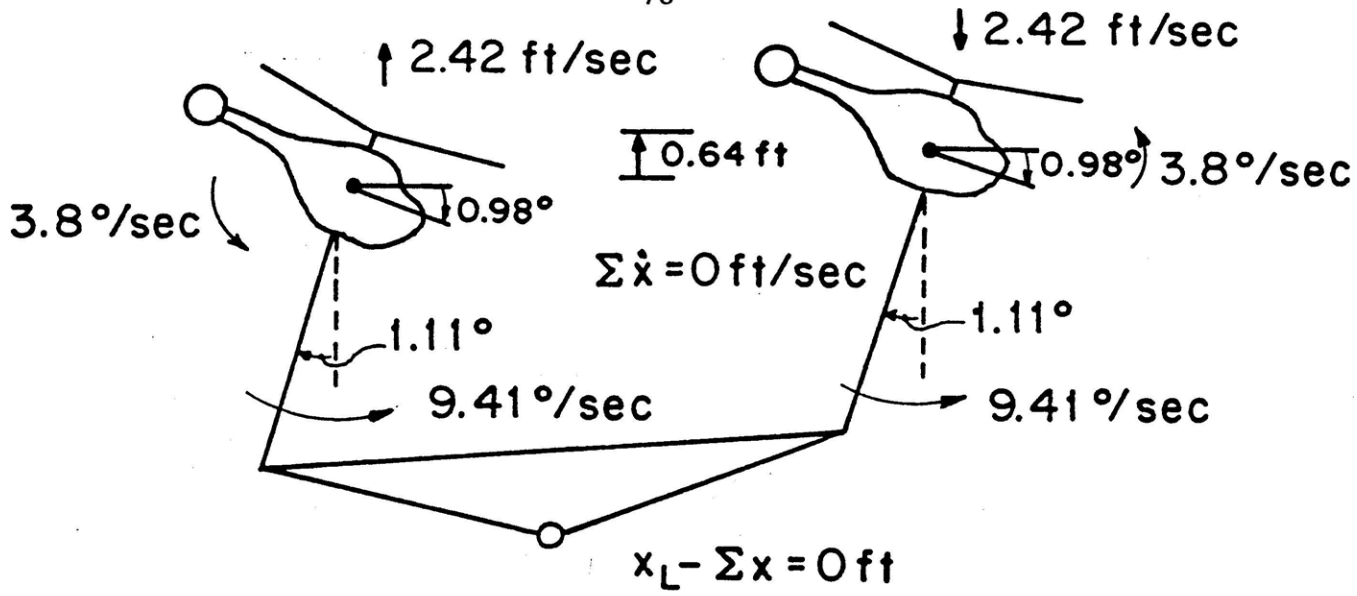

Fig. 3.4.3.2: Visualization of Initial Condition to Interpret ASM Load Motion Zeros (a = -1 , b = 0).

The relationships in (3.95) can be used to interpret the ASM Helicopter Pitching Zeros.

From these equations it follows that for all a, b ∈ **R**, if

$$\underline{x}_{p3}(0) = a\,\mathrm{Re}\{\,\underline{x}_3\,\} + b\,\mathrm{Im}\,\{\,\underline{x}_3\,\} \tag{3.101a}$$

$$= a\,[\;0.1464\;\;-0.0031\;\;-0.0415\;\;0\;\;2.8309\;\;0.371\;\;-1.021\;]^T$$

$$+ b\,[-0.3092\;\;-0.038\;\;0.11\;\;0\;\;1.86\;\;0.0217\;\;-0.5578]^T \tag{3.101a}$$

$$\underline{u}_{p3}(t) = a\,\mathrm{Re}\,\{\,\underline{u}_3\,e^{z_3 t}\,\} + b\,\mathrm{Im}\,\{\,\underline{u}_3\,e^{z_3 t}\,\} \tag{3.102a}$$

$$= a\,[\;0.63\,e^{\sigma_3 t}\cos(\omega_3 t + 99.3°)\;\;0.671 e^{\sigma_3 t}\cos(\omega_3 t - 66.5°)\;]^T$$

$$+ b\,[\;0.63\;\;e^{\sigma_1 t}\sin(\omega_3 t + 99.3°)\;\;0.671 e^{\sigma_3 t}\sin(\omega_3 t - 66.5°)\;]^T \tag{3.102b}$$

$$\underline{x}_{p3}(t) = a\,\mathrm{Re}\,\{\,\underline{x}_3\,e^{z_3 t}\,\} + b\,\mathrm{Im}\,\{\,\underline{x}_3\,e^{z_3 t}\,\} \tag{3.103a}$$

$$= a\,e^{\sigma_3 t}\,[0.34\cos(\omega_1 t - 64.7°)\;\;\;0.038\cos(\omega_3 t - 94.7°)\;\;\;0.12\cos(\omega_3 t + 110.7°)$$

$$0\;\;\;3.39\cos(\omega_3 t + 33.3°)\;\;0.38\cos(\omega_3 t + 3.3°)\;\;1.2\cos(\omega_3 t - 151°)]^T$$

$$+ b\,e^{\sigma_3 t}\,[0.34\sin(\omega_3 t - 64.7°)\;\;\;0.038\sin(\omega_3 t - 94.7°)\;\;\;0.12\sin(\omega_3 t + 110.7°)$$

$$0\;\;\;3.39\sin(\omega_3 t + 33.3°)\;\;0.38\,\sin(\omega_3 t + 3.3°)\;\;1.2\sin(\omega_3 t - 151°)]^T$$

(3.103b)

and

$$\underline{y}_{p3}(t) = \underline{0} \tag{3.104}$$

for all $t \geq 0$. Considering only the real part of eq. (3.101) with (a = -1, b = 0) gives

$$x_{p3}(0) = [-0.1464 \quad 0.0031 \quad 0.0415 \quad 0 \quad -2.8309 \quad -0.371 \quad 1.021]^T \tag{3.105}$$

Using the Equal Tether relationships for x_L' and $x_L - \Sigma x$ once again, the initial condition in eq. (3.105) can be visualized as indicated in Fig. 3.4.3.3.

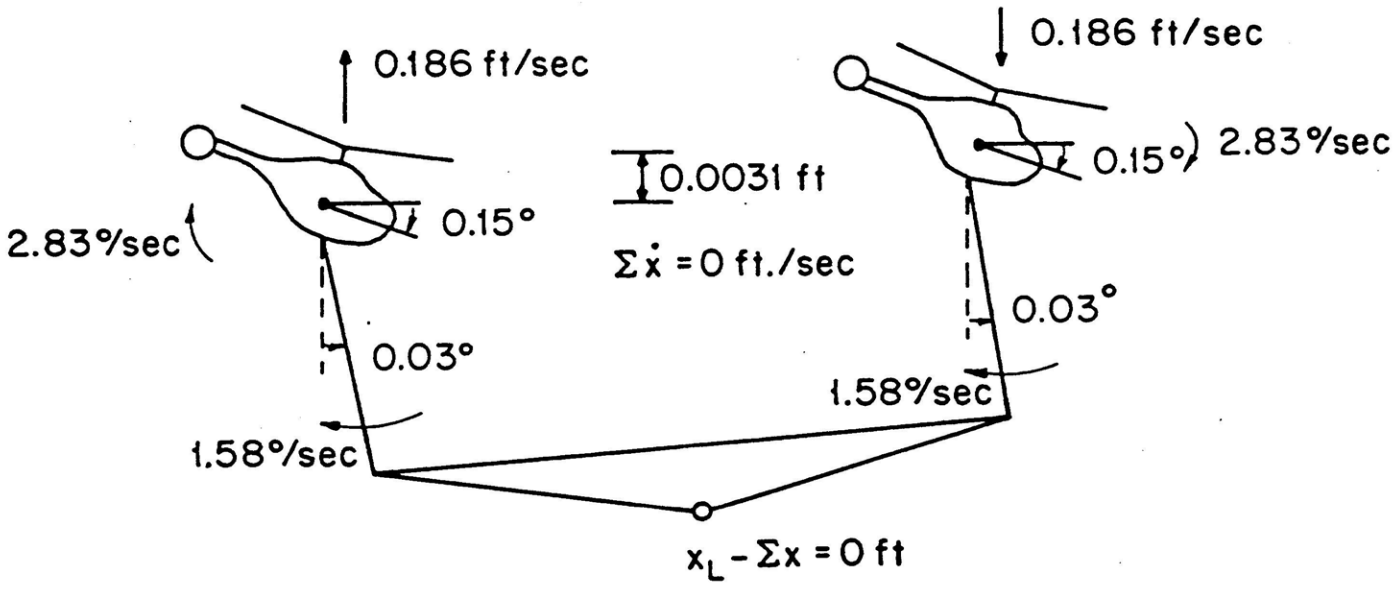

Fig. 3.4.3.3: Visualization of Initial Condition to Interpret ASM Helicopter Pitching Zeros (a = -1, b = 0).

Here the collectives and cyclics are coordinated so that $\Delta\Theta_c$ lead ΣB_{lc} by 165.8°. Doing so results in $\Sigma\Theta$ leading Δz and Δz leading $\Sigma\varepsilon$. This in turn results in $x_L - \Sigma x = 0$ and $\Sigma\dot{x} = 0$. These high frequency, lightly damped, zeros are characteristic of a single hovering helicopter. For this reason we refer to them as the ASM Helicopter Pitching Zeros. Note that, relatively speaking, they primarily involve the $\Sigma\theta$ degree of freedom ($\Sigma\dot{\theta}(0) = 2.83$ deg/sec).

The implications of the ASM Plants' modes and lightly damped zeros on the Twin Lift Equal Tether Control Problem shall be discussed subsequently. Now we shall combine the AVM, SM, and ASM Plants to form an "Equal Tether Plant", $G_p(s)$.

3.4.4 TLHS Equal Tether Configuration: The Equal Tether Plant

The previous 3 sections can be summarized by simply specifying the complete state space representation for the TLHS Equal Tether Configuration:

$$\dot{\underline{x}}_p = A_p \underline{x}_p + B_p \underline{u}_p; \qquad \underline{x}_p \in \mathbf{R}^{12} \tag{3.106}$$

$$\underline{y}_p = C_p \underline{x}_p; \qquad \underline{u}_p, \underline{y}_p \in \mathbf{R}^4 \tag{3.107}$$

$$\underline{x}_p \equiv [\, \Sigma\dot{z} \;\|\; \Delta x \;\; \Delta\theta \;\; \Delta\dot{x} \;\; \Delta\dot{\theta} \;\|\; \Sigma\theta \;\; \Delta z \;\; x_L' \;\; \Sigma\dot{x} \;\; \Sigma\dot{\theta} \;\; \Delta\dot{z} \;\; \dot{x}_L' \,]^T \tag{3.108}$$

$$\underline{u}_p \equiv [\, \Sigma\Theta_c \;\|\; \Delta B_{lc} \;\|\; \Delta\Theta_c \;\; \Sigma B_{lc} \,]^T \tag{3.109}$$

$$y_p \equiv [\, \Sigma\dot{z} \;\|\; \Delta x \;\|\; x_L - \Sigma x \;\; \Sigma\dot{x} \,]^T \tag{3.110}$$

where $A_p \equiv \text{diag}\,(A_{p1}, A_{p2}, A_{p3})$ (3.111)

$$B_p \equiv \text{diag}\,(B_{p1}, B_{p2}, B_{p3}) \tag{3.112}$$

$$C_p \equiv \text{diag}\,(C_{p1}, C_{p2}, C_{p3}) \tag{3.113}$$

and the state space triple (A_{pi}, B_{pi}, C_{pi}), i = 1, 2, 3, refer to the AVM, SM, and ASM plants, respectively. The transfer function matrix for our plant (Equal Tether Configuration of TLHS) is then given by:

$$G_p(s) \equiv C_p\,(sI - A_p)^{-1} B_p \tag{3.114a}$$

$$= \text{diag}\,(G_{p1}(s), G_{p2}(s), G_{p3}(s)) \tag{3.114b}$$

where the

$$G_{pi}(s) \equiv C_{pi}\,(sI - A_{pi})^{-1} B_{pi}; \qquad i = 1, 2, 3 \tag{3.115}$$

refer to the AVM, SM, and ASM plants respectively.

From now on when we refer to the "Equal Tether Plant", $G_p(s)$, we are referring to eqs. (3.49) - (3.59). The matrices (A_p, B_p, C_p) are given in Table 3.4.4.1 for convenience. An input/output visualization of the TLHS is provided in Fig. 3.4.4.1. When the tether lengths are equal this visualization can be redrawn as in Fig. 3.4.4.2 which shows the individual AVM, SM, and ASM Plants.

Table 3.4.4.1: State Space Reresentation for Equal Tether Plant

$A_p =$

-0.2384	0.	0.	0.	0.	0.	0.	0.	0.	0.	0.	0.
0.	0.	0.	1.0000	0.	0.	0.	0.	0.	0.	0.	0.
0.	0.	0.	0.	1.0000	0.	0.	0.	0.	0.	0.	0.
0.	-1.0975	-0.8847	-0.0600	0.	0.	0.	0.	0.	0.	0.	0.
0.	-17.2670	-5.0777	2.3493	-3.1000	0.	0.	0.	0.	0.	0.	0.
0.	0.	0.	0.	0.	0.	0.	0.	0.	1.0000	0.	0.
0.	0.	0.	0.	0.	0.	0.	0.	0.	0.	1.0000	0.
0.	0.	0.	0.	0.	0.	0.	0.	0.	0.	0.	1.0000
0.	0.	0.	0.	0.	-0.5620	0.	1.0975	-0.0600	0.	0.	0.
0.	0.	0.	0.	0.	0.	0.	17.2670	2.3493	-3.1000	0.	0.
					0.4679	-0.3885	2.0233	0.	0.	-0.3361	0.
					-0.2220	0.1844	-9.5654	-0.6308	0.9116	0.1595	0.

$B_p =$

4.0985	0.	0.	0.
0.	0.	0.	0.
0.	0.	0.	0.
0.	0.4782	0.	0.
0.	-47.2400	0.	0.
0.	0.	0.	0.
0.	0.	0.	0.
0.	0.	0.	0.
0.	0.	0.	0.
0.	0.	0.	0.4782
0.	0.	5.7789	-47.2400
0.	0.	-2.7423	0.
			13.4136

$C_p =$

1.0000	0.	0.	0.	0.	0.	0.	0.	0.	0.	0.	0.
0.	1.0000	0.	0.	0.	0.	0.	0.	0.	0.	0.	0.
0.	0.	0.	0.	0.	0.2941	0.5000	1.0000	0.	0.	0.	0.
0.	0.	0.	0.	0.	0.	0.	0.	1.0000	0.	0.	0.

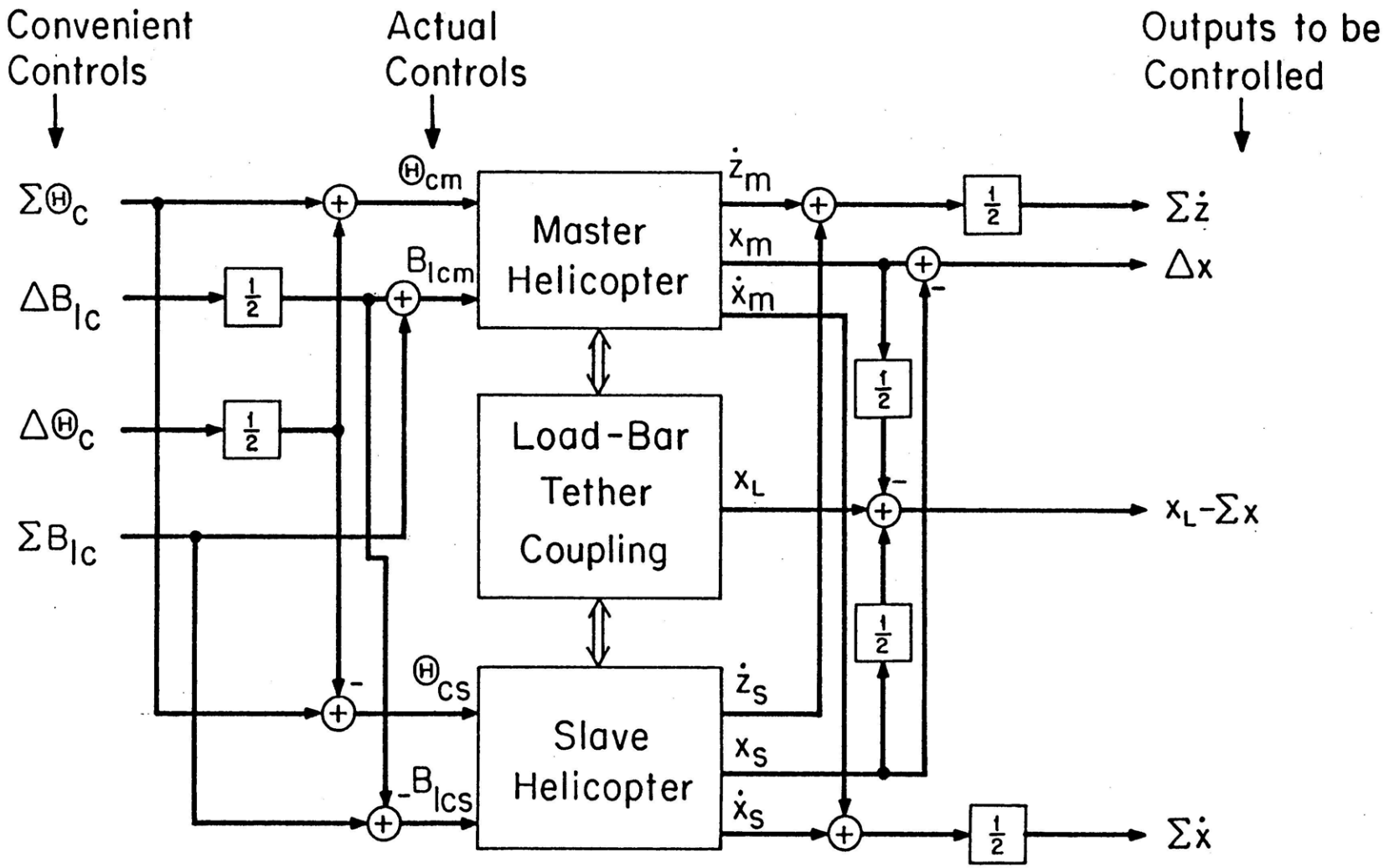

Fig. 3.4.4.1: Input/Output Visualization of TLHS

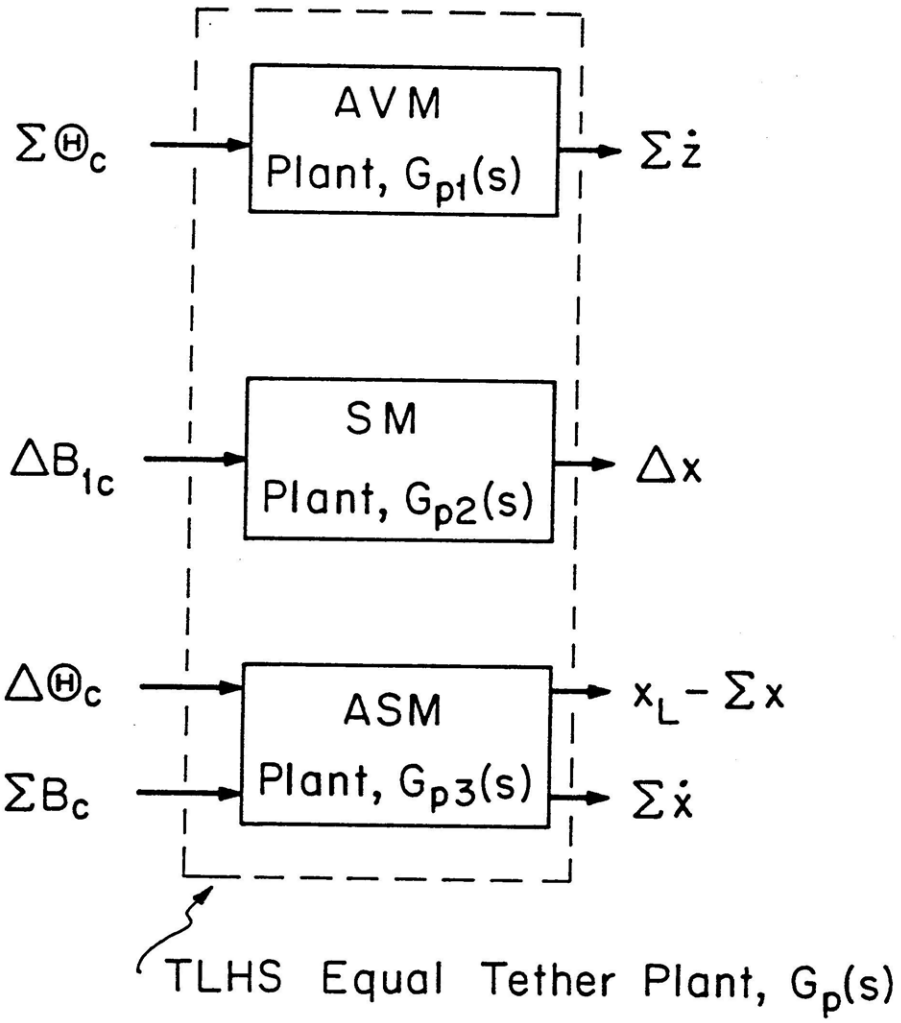

Fig. 3.4.4.2: Input/Output Visualization of TLHS Equal Tether Plant

3.5 Frequency Domain Analysis of Equal Tether Plant

Before presenting performance and stability robustness specifications, we examine the "functions to be shaped".* The notion of shaping is fundamental to classical SISO control theory and, as will be demonstrated in this thesis, fundamental to MIMO feedback control system design. The functions to be shaped are precisely the transfer functions of the AVM, SM, and ASM Plants since these make up the transfer function matrix (tfm) of our Equal Tether Plant. In this section we thus examine, in great detail, the Bode plots of the AVM and the SM Plants (both SISO systems). For the ASM Plant, the singular values are analyzed.

3.5.1 Frequency Domain Analysis of AVM Plant

The AVM Plant transfer function, $G_{pl}(s)$, was given by eqs. (3.36). This SISO, first order, system has control input $\Sigma\Theta_c$ (degs.) and output $\Sigma\dot{z}$ (fps). The Bode magnitude and phase plots for the AVM Plant are given in Fig. 3.5.1.1.

The magnitude plot shows a dc gain of:

$$\Sigma\dot{z} / \Sigma\Theta_c = G_{pl}(j0) = - Z_{\Theta c} / Z_w = 17.2 \text{ fps / degree} \quad (24.7 \text{ db}) \qquad (3.116)$$

which is in agreement with eq. (3.30). It thus follows that to have a steady state average vertical velocity of $\Sigma\dot{z} = 5$ fps, it is necessary to have a steady state average collective of $\Sigma\Theta_c = 0.2907$ degrees. The magnitude plot has a break at the pole frequency $\omega = Z_w / (1+\mu) = - 0.2384$ rad/sec. The gain crossover frequency* for the AVM Plant is seen to be $\omega_{g1} \approx 4.1$ rad/sec. For frequencies above the break, the magnitude rolls off at -20 db/dec and the phase rolls off at appproximately - 45 degrees/dec to - 90 degrees as expected for a first order system.

The above characteristics imply that the AVM shall be relatively easy to control. It must be emphasized, however, that although the AVM control strategy will not affect the ASM, it will affect

---

* Gain crossover frequency is the frequency at which the magnitude is unity.

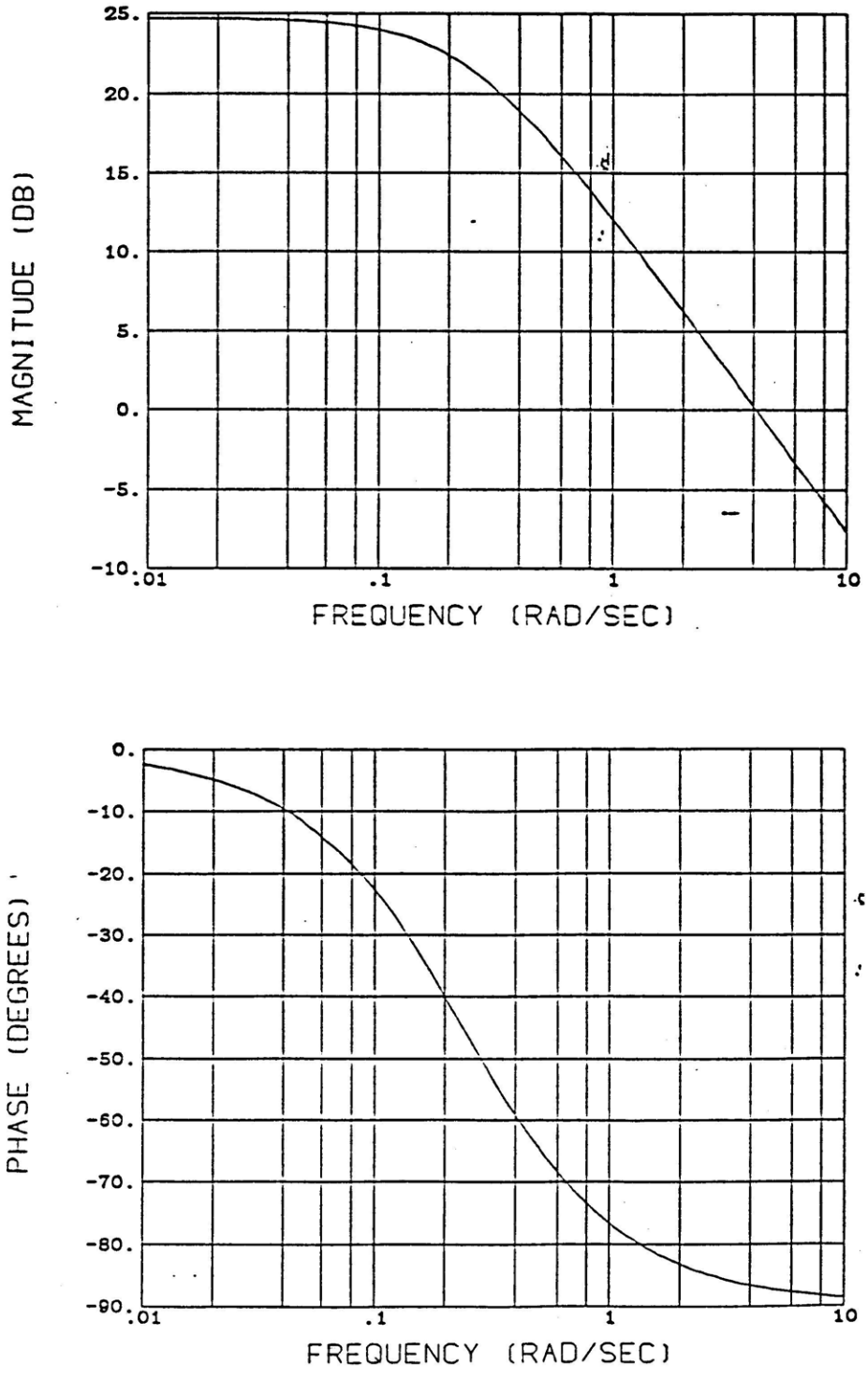

Fig. 3.5.1.1: Bode Magnitude and Phase Plots for AVM Plant
Input: $\Sigma\Theta_c$ (degrees) Output: $\Sigma\dot{z}$ (feet / second)

the Δz motion and hence the individual helicopter velocities (e.g. $z_m = \Sigma z + 0.5\,\Delta z$). It thus follows that the AVM should not be treated completely independently from the ASM.

3.5.2 Frequency Domain Analysis of SM Plant

The SM Plant transfer function, $G_{p2}(s)$, was given by eqs. (3.43) - (3.50). This fourth order, SISO system has control input ΔB_{lc} (degs.) and output Δx (ft.). We now analyze this transfer function for s = 0; i.e. at dc.

Assume that the SM has been stabilized and that a steady state differential cyclic of 1 degree is applied to the SM Plant; i.e.

$$\Delta B_{lc} = 1 \text{ degree.} \tag{3.117}$$

Computation of $(-A_{p2})^{-1}B_{p2}$ shows that the following steady state values will result (and are hence necessary for equilibrium):

$$\Delta x = -4.558 \text{ feet} \quad (13.18 \text{ db}) \tag{3.118}$$
$$\Delta\theta = 6.194 \text{ degrees} \tag{3.119}$$
$$\Delta\varepsilon = 18.03 \text{ degrees} \tag{3.120}$$

Fig. 3.5.2.1 gives one possible visualization ($\Sigma x = 0, \Sigma\theta = 0, \Sigma\varepsilon = 0$) of the above steady state conditions.

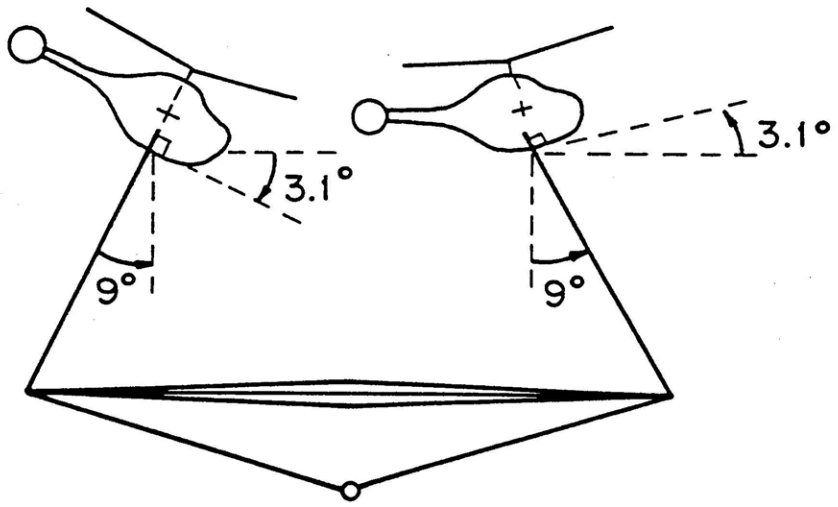

Fig. 3.5.2.1: Visualization of SM Steady State for $\Delta B_{lc} = 1$ degree.

From the analysis, it follows that in order to bring the helicopters closer together ($\Delta x < 0$), a positive differential cyclic must be applied. At first this might seem counter-intuitive; i.e. one might expect that a positive differential cyclic is needed to sustain a helicopter separation ($\Delta x > 0$). This line of thinking is in flaw because it fails to consider the effect of the equilibrium (large signal) components of thrust provided by the main rotor on each helicopter. These components of thrust have lines of action which are assumed to pass through the helicopter-tether attachment points as well as the helicopter c.g.'s. The differential cyclic should be thought of as providing that force which keeps the helicopters from toppling over. The analysis also shows that the needed positive differential cyclic produces a positive differential pitch attitude. This is explained by noticing that if the contrary were true; i.e. if a positive differential cyclic produced a negative differential pitch attitude, then the helicopters would have net horizontal forces acting on them and hence equilibrium would be impossible.

The Bode magnitude and phase plots for the SM Plant are given in Fig. 3.5.2.2. The dc magnitude and phase confirms eq. (3.118); i.e. the helicopter horizontal separation will decrease by 4.558 feet for every degree of steady state differential cyclic. The plots show that this dc gain holds almost up to 0.2 rad/sec. It should be noted that the minus sign in eq. (3.118) is attributable to the unstable Tethered Helicopter Mode. At $\omega \approx 0.75$ rad/sec the magnitude breaks downward at - 20 db/dec due to this mode. At $\omega \approx 2.4$ rad/sec another break occurs due to the Symmetric Damping Mode. Finally, at $\omega \approx 2.4$ we have a final break due to the Horizontal Spring Mode.

Above $\omega \approx 2.5$ rad/sec the magnitude plot exhibits a -80 db/dec (4 pole) roll-off. This considerably large roll-off continues paast the gain crossover frequency ($\omega \approx 3$ rad/sec) until about 10 rad/sec where the SM Plant's lightly damped zeros provide an upward break. The magnitude then rolls off at - 40 db/dec. This is due to the fact that $\Delta x \approx M_u (\Delta B_{lc}/s^2)$ for "large" s.

The phase plot shows the 180 degree phase lag due to the Tethered Helicopter Mode at dc, its initial lead effect at low frequencies, and the combined phase lag due to the Translational Spring and Symmetric Damping Modes near gain crossover. The phase lead due to the zero is observed

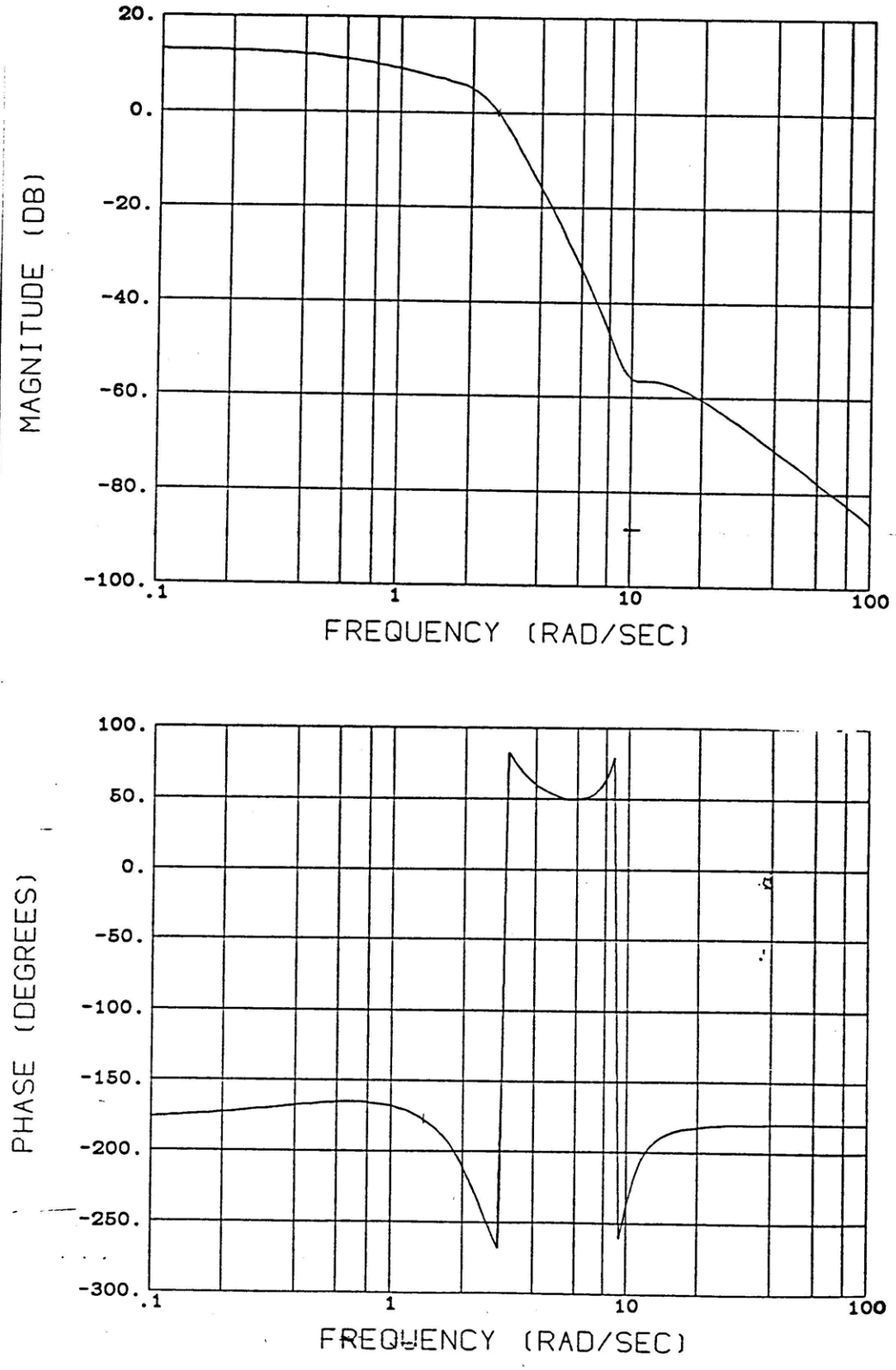

Fig. 3.5.2.2: Bode Magnitude and Phase Plots for SM Plant.
Input: ΔB_{lc} (degrees) Output: Δx (feet)

near 10 rad/sec. It should also be noted that the SM Plant has two phase crossover frequencies; i.e. frequencies at which the phase is ± 180 degrees. One is at dc and the other is near 1.5 rad/sec. This implies that the SM Plant can be stabilized with a single gain (~ 0.22); i.e. via separation feedback alone. Doing so, however, would certainly not result in a high performance design.

3.5.3 Frequency Domain Analysis of ASM Plant

The ASM Plant transfer function matrix, $G_{p3}(s)$, was given by eqs. (3.88) - (3.90). This seventh order, TITO (two-input two-output) system has inputs $\Delta\Theta_c$ (degs.) and ΣB_{lc}(degs.) and outputs x_L - Σx (ft.) and $\Sigma\dot{x}$ (ft./sec.). This section studies the singular values of $G_{p3}(j\omega)$. Before proceeding, however, it is convenient to recall the definition of the singular values of a matrix, the singular value decomposition of a matrix, and their ramifications in the frequency domain [7] [13].

Consider the square (m x m) non-singular complex matrix, G. G can be witten as follows:

$$G = U\Sigma V^H = \sum_{i=1}^{m} \sigma_i \underline{u}_i \underline{v}_i^H \tag{3.121}$$

where

$$\Sigma \equiv \text{diag}(\sigma_1, ..., \sigma_m) \qquad \sigma_i > 0 \tag{3.122}$$

$$U \equiv [\underline{u}_1 \cdots \underline{u}_m] \qquad U^{-1} = U^H \tag{3.123}$$

$$V \equiv [\underline{v}_1 \cdots \underline{v}_m] \qquad V^{-1} = V^H \tag{3.124}$$

and

$$G^H G \, \underline{v}_i = \sigma_i^2 \, \underline{v}_i \tag{3.125a}$$

$$G G^H \underline{u}_i = \sigma_i^2 \, \underline{u}_i. \tag{3.125b}$$

Equation (3.121) is referred to as the singular value decomposition (SVD) of G. The σ_i are called the singular values of G. The $\underline{u}_i$ are called left singular vectors of G and the $\underline{v}_i$ are called right singular vectors of G. Eqs. (3.123) - (3.124) show that U and V are, by definition, unitary matrices. It thus follows that the following relationships hold:

$$\underline{u}_i^H \underline{u}_i = \delta_{ij} \qquad i = 1, ..., m \tag{3.126a}$$

$$\underline{v}_i^H \underline{v}_i = \delta_{ij} \qquad i = 1, ..., m \tag{3.126b}$$

Equations (3.125) - (3.126) show that the $\sigma_i = (\lambda_i(G^HG))^{0.5} = (\lambda_i(GG^H))^{0.5}$, i = 1, ..., m. σ_1 is by convention the maximum singular value of G and σ_m the minimum singular value of G. The maximum and minimum singular values of G are particularly important. Their importance stems from the following fact [7]:

The matrix G is said to be large (small) if and only if its minimum (maximum) singular value is large (small).	(3.127)

This notion of large and small is motivated from the fact that σ_1 and σ_m may be defined in terms of the Euclidean two-norm $\|x\|_2 = (x^Hx)^{0.5}$ as follows:

$$\sigma_1 \equiv \max \{ \|G\underline{u}\|_2 / \|\underline{u}\|_2 \mid \underline{u} \neq 0 \} \tag{3.128a}$$

$$\sigma_m \equiv \min \{ \|G\underline{u}\|_2 / \|\underline{u}\|_2 \mid \underline{u} \neq 0 \} \tag{3.128b}$$

Now use eq. (3.121) to consider the multiplication of the matrix G by the m-vector $\underline{u}$; i.e. let

$$\underline{y} = G\underline{u} = \sum_{i=1}^{m} \sigma_i \underline{u}_i (\underline{v}_i^H \underline{u}). \tag{3.129}$$

Equations (3.128) and (3.129) show that

$$\text{If } \underline{u} = \underline{v}_i \quad \Rightarrow \quad \underline{y} = \sigma_i \underline{u}_i. \tag{3.130}$$

Now let $G = G_{p3}(j\omega)$. Suppose further, that the left and right singular vectors of $G_{p3}(j\omega)$, at ω, are given by:

$$\underline{u}_i \equiv [\ |u_{i1}|e^{-j\beta_{i1}} \quad |u_{i2}|e^{-j\beta_{i2}}\ ]^H \qquad i = 1, 2 \tag{3.131}$$

$$\underline{v}_k \equiv [\ |v_{k1}|e^{-j\alpha_{k1}} \quad |v_{k2}|e^{-j\alpha_{k2}}\ ]^H \qquad k = 1, 2 \tag{3.132}$$

and that the corresponding maximum and minimum singular values are σ_1 and σ_2, respectively. Now suppose that the ASM has been stabilized and that a steady state sinusoidal control vector

$\underline{u}_p(t)$ is applied to the ASM Plant. Equations (3.129) - (3.130) then imply that:

$$\text{If} \quad \underline{u}_p(t) = \text{Re}\left\{ \underline{v}_k e^{j\omega t} \right\}$$
$$= \left\{ \left[|v_{k1}| \cos(\omega t + \alpha_{k1}) \quad |v_{k2}| \cos(\omega t + \alpha_{k2}) \right] \right\}^T \quad k = 1, 2 \qquad (3.133a))$$

$$\Rightarrow \quad \underline{y}_p(t) = \text{Re}\left\{ \sigma_k \underline{u}_k e^{j\omega t} \right\}$$
$$= \left\{ \sigma_k \left[|u_{k1}| \cos(\omega t + \beta_{k1}) \quad |u_{k2}| \cos(\omega t + \beta_{k2}) \right] \right\}^T \quad k = 1, 2. \qquad (3.133b)$$

The ideas contained in eqs. (3.129) - (3.133) shall be used considerably throughout the thesis. These equations will provide us with a way of understanding the input/output properties of the Equal Tether AFCS to be designed in Chapter 4 and the Unequal Tether AFCS to be designed in Chapter 6. Before studying the singular values of $G_{p3}(j\omega)$, we study $G_{p3}(j\omega)$ for $\omega = 0$; i.e. at dc.

Assume that the ASM has been stabilized and that a steady state differential collective of 1 degree is applied to the ASM Plant; i.e.

$$\Delta\Theta_c = 1 \text{ degree}; \quad \Sigma B_{lc} = 0 \text{ degrees.} \qquad (3.134)$$

Computation of $(-A_{p3})^{-1}B_{p3}$ shows that the following steady state values will result (and are hence necessary for equilibrium):

$$\Sigma\dot{x} = \Sigma\theta = \Sigma\varepsilon = x_L' = 0 \qquad (3.135)$$

$$\Delta z = 14.872 \text{ feet} \qquad (\varepsilon_B = 12.4 \text{ degrees}) \qquad (3.136)$$

$$x_L - \Sigma x = 7.436 \text{ feet} \qquad (17.43 \text{ db}) \qquad (3.137)$$

Fig. 3.5.3.1 gives one possible visualization ($\Delta x = 0$, $\Delta\theta = 0$, $\Delta\varepsilon = 0$) of the above steady state conditions

The above discussion indicates, for example, that a steady state load deviation of - 1 foot requires a steady state differential collective of - 0.1345 degrees accompanied by a steady state vertical separation of - 2 feet. We note that in the steady state $x_L - \Sigma x = \hat{Z}\,\Delta z = 0.5\,\Delta z$.

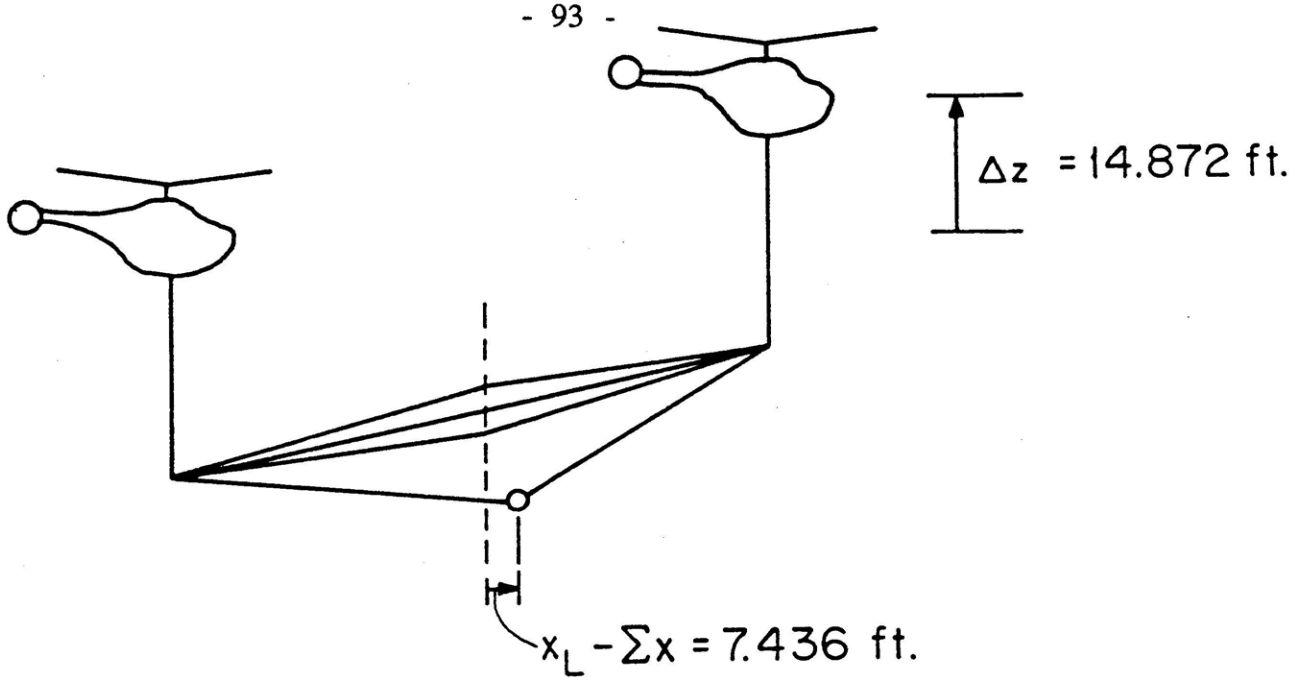

Fig. 3.5.3.1: Visualization of ASM Steady State for $\Delta\Theta_c = 1$ degree.

Assume now that the ASM has been stabilized and that a steady state average cyclic of 1 degree is applied to the ASM Plant; i.e.

$$\Delta\Theta_c = 0 \text{ degrees}; \quad \Sigma B_{lc} = 1 \text{ degree.} \tag{3.138}$$

From $(-A_{p3})^{-1}B_{p3}$ it follows that the following steady state values will result (and are hence necessary for equilibrium):

$$\Sigma\dot{x} = 18.76 \text{ feet / sec} \qquad (25.46 \text{ db}) \tag{3.139}$$

$$\Sigma\theta = -\ 0.7936 \text{ degrees} \tag{3.140}$$

$$\Sigma\varepsilon = \Delta z = 0 \tag{3.141}$$

$$x_L' = 0.1835 \text{ feet} \tag{3.142}$$

$$x_L - \Sigma x = -\ 0.0499 \text{ feet.} \tag{3.143}$$

Fig. 3.5.3.2 gives one possible visualization ($\Delta x = 0$, $\Delta\theta = 0$, $\Delta\varepsilon = 0$) of the above steady state conditions.

The above discussion indicates, for example, that a steady state average horizontal velocity of 5 feet / sec will require a steady state average cyclic of 0.2665 degrees accompanied by a steady state average pitch of - 0.2115 degrees and load deviation from center of - 0.0133 feet.

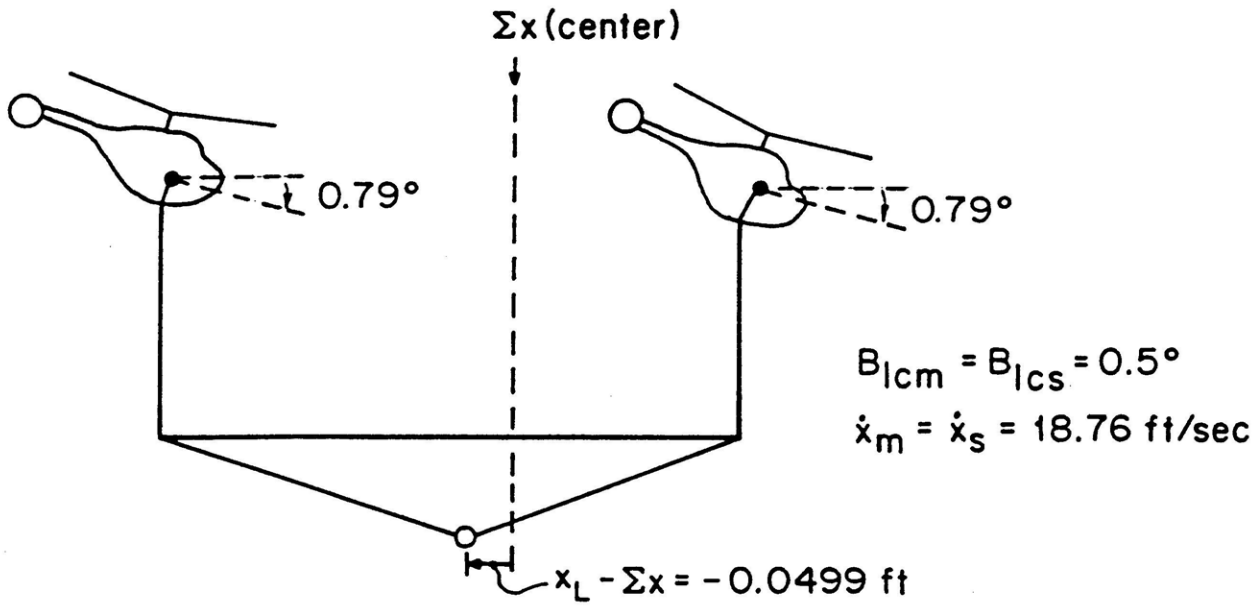

Fig. 3.5.3.2: Visualization of ASM Steady State for $\Sigma B_{lc} = 1$ degree.

Note that in both cases discussed above the steady state $\Sigma\varepsilon = 0$ degrees. This follows from the fact that

$$\ddot{x}_L = M_B \hat{Z} / [M_L + M_B] \Delta\ddot{z} - g \Sigma\varepsilon \tag{3.144}$$

(Chapter 2) and in the steady state $\ddot{x}_L = \Delta\ddot{z} = 0$. Intuitively, this also follows from the fact that the aerodynamic forces and moments acting on the spreader bar have been assumed negligible.

From the above dc analysis, it follows by linearity that the following relationships hold at dc:

$$x_L - \Sigma x = 7.436\, \Delta\Theta_c - 0.0499\, \Sigma B_{lc} \tag{3.145}$$

$$\Sigma\dot{x} = 18.76\, \Sigma B_{lc}. \tag{3.146}$$

The first term in eq. (3.145) is associated with the Δz degree of freedom and the second term with the $\Sigma\dot{x}$ and $\Sigma\theta$ degrees of freedom. Equation (3.146) is, of course, associated with the $\Sigma\theta$ degree of freedom since the helicopters must pitch in order to move fore and aft. These equations show that at low frequencies ΣB_{lc} has little affect on $x_L - \Sigma x$ and $\Delta\Theta_c$ has no affect on $\Sigma\dot{x}$; i.e. at low

frequencies the Δz degree of freedom and the $\Sigma\dot{x}$, $\Sigma\theta$ degrees of freedom are, for all intents and purposes, decoupled. This confirms our intuition which tells us that $x_L - \Sigma x$ should be controlled through Δz via $\Delta\Theta_c$ and $\Sigma\dot{x}$ should be controlled through $\Sigma\theta$ via ΣB_{lc}. The following singular value decomposition of $G_{p3}(s) = C_{p3}(sI - A_{p3})^{-1}B_{p3}$ at dc confirms our intuition:

$$G_{p3}(j\,0) = C_{p3}\,(sI - A_{p3})^{-1}\,B_{p3} \tag{3.147a}$$

$$= \begin{bmatrix} 7.436 & -0.0499 \\ 0 & 18.76 \end{bmatrix} \tag{3.147b}$$

$$= \begin{bmatrix} 0.003 & 1 \\ 1 & 0.003 \end{bmatrix} \begin{bmatrix} 18.76 & 0 \\ 0 & 7.437 \end{bmatrix} \begin{bmatrix} 0.0013 & 1 \\ 1 & 0.0013 \end{bmatrix} \tag{3.147c}$$

$$= \begin{bmatrix} | & | \\ \underline{u}_1 & \underline{u}_2 \\ | & | \end{bmatrix} \begin{bmatrix} \sigma_1 & \\ & \sigma_2 \end{bmatrix} \begin{bmatrix} -\underline{v}_1^T- \\ -\underline{v}_2^T- \end{bmatrix} \tag{3.147d}$$

These show that if $\underline{u}_{p3} = \underline{v}_1 \approx [\,0\;\;1\,]^T$ then $\underline{y}_{p3} = \sigma_1\underline{u}_1 \approx 18.76\,[\,0\;\;1\,]^T$. ΣB_{lc} thus has little affect on $x_L - \Sigma x$. Similarly, if $u_{p3} = \underline{v}_2 \approx [\,1\;\;0\,]^T$ then $\underline{y}_{p3} = \sigma_2\underline{u}_2 \approx 7.437\,[\,1\;\;0\,]^T$. $\Delta\Theta_c$ thus has little affect on $\Sigma\dot{x}$. It thus follows that $x_L - \Sigma x$ should be controlled by $\Delta\Theta_c$ and $\Sigma\dot{x}$ by ΣB_{lc}.

The ASM Plant singular values ($\sigma_i(G_{p3}(j\omega))$; i = 1, 2) have been plotted in Fig. 3.5.3.3. At low frequencies we see that $\sigma_1 \approx 25.46$ db (18.76) and $\sigma_2 \approx 17.43$ (7.436) which agrees with our dc analysis.

Near $\omega = 0.5$ rad/sec, the maximum ASM singular values exhibit a hump. This hump is due to the unstable Backflapping Mode ($\zeta = 0.084$).

The Vertical Spring Mode ($\zeta = 0.26$), near $\omega = 0.76$ rad/sec, is seen to predominantly affect the maximum singular value. This follows from the fact that the maximum singular value roll-off at -80 db/dec (Backflapping Mode and Vertical Spring Modes) just after breaking downward near $\omega \approx 0.8$ rad/sec and before intersecting the minimum singular values at approximately $\omega \approx 1.5$ rad/sec. This indicates coupling between the $\Sigma\dot{x}$ and Δz degrees of freedom.

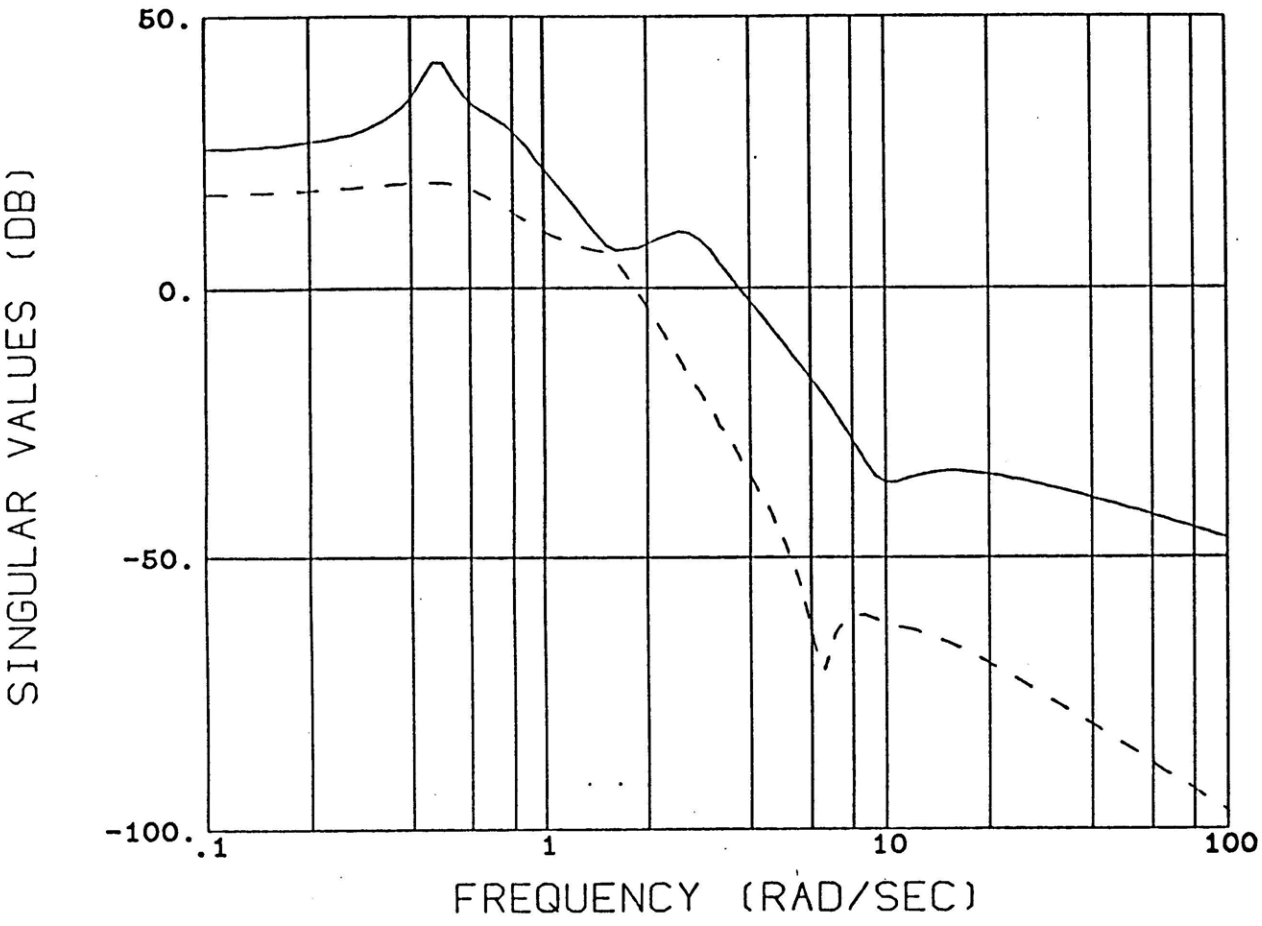

Fig. 3.5.3.3: Singular Values of ASM Plant.
Inputs: $\Delta\Theta_c$ (degrees) Outputs: $x_L - \Sigma x$ (feet)
ΣB_{lc} (degrees) $\Sigma\dot{x}$ (feet / second)

The Pendular Mode ($\zeta = 0.2$) is seen to cause a hump in the maximum singular value near $\omega = 2.7$ rad/sec.

The Anti-Symmetric Damping Mode ($\omega = 2.12$ rad/sec) is seen to predominantly affect the maximum singular value. This follows from the fact that the maximum singular value roll-off at -60 db/dec (Pendular and Anti-Symmetric Damping Modes) between $\omega \approx 4$ rad/sec and $\omega \approx 8$ rad/sec.

The maximum singular value crosses 0 db just below $\omega = 4$ rad/sec. The minimum singular value rolls-off at -80 db/dec (Backflapping and Vertical Spring Modes) between $\omega \approx 1.5$ rad/sec and $\omega \approx 2$ rad/sec. It crosses 0 db just below $\omega = 2$ rad/sec.

Near $\omega \approx 6.5$ rad/sec, the minimum singular value exhibit a downward blip and then an upward break. These are due to the ASM Plant's very lightly damped zeros ($\zeta = 0.028$) which are asssociated with the load motion. The minimum singular value then rolls-off at -40 db/dec. This "double integral" is associated with the load motion.

Near $\omega \approx 10$ rad/sec, the maximum singular values exhibit an upward break. This break is due to the ASM Plant's other lightly damped zeros ($\zeta = 0.138$) which are associated with the helicopters (Appendix 3). The maximum singular value then rolls-off at - 20 db/dec. This "integral" is associated with the average horizontal velocity.

The above analysis, loosely speaking, shows that singular value plots can be thought of as "MIMO Bode magnitude plots".

3.6 TLHS Equal Tether Control Problem Formulation

It has been shown that the Equal Tether Plant, $G_p(s)$, consists of three plants:

1. The AVM Plant, $G_{p1}(s) = C_{p1}\,(sI - A_{p1})^{-1}\,B_{p1}$,

2. The SM Plant, $G_{p2}(s) = C_{p2}\,(sI - A_{p2})^{-1}\,B_{p2}$,

3. The ASM Plant, $G_{p3}(s) = C_{p3}\,(sI - A_{p3})^{-1}\,B_{p3}$.

It thus follows that the final "Equal Tether AFCS", to be designed in the next chapter, will consist of three AFCS's; i.e. one for each of the above plants. In this section the structure of the final Equal Tether AFCS is presented and discussed. Performance and robustness specifications are presented for the Equal Tether AFCS; i.e. for the AVM, SM, and ASM AFCS's. To help meet the performance specifications, the Equal Tether Plants, $G_{p1}(s)$, $G_{p2}(s)$, and $G_{p3}(s)$ are dynamically augmented.

The purpose of this section is to formulate the Equal Tether Control Problem and to qualitatively discuss the feasibility of a high performance Equal Tether AFCS.

3.6.1 Structure of TLHS Equal Tether AFCS

Fig. 3.6.1.1 shows the structure of the Equal Tether AFCS to be developed in the next chapter. The AFCS is seen, simply, to possess a negative feedback MIMO structure. The AFCS consists of the 12^{th} oder Equal Tether Plant (ETP), $G_p(s)$, a 4^{th} order augmentation, a

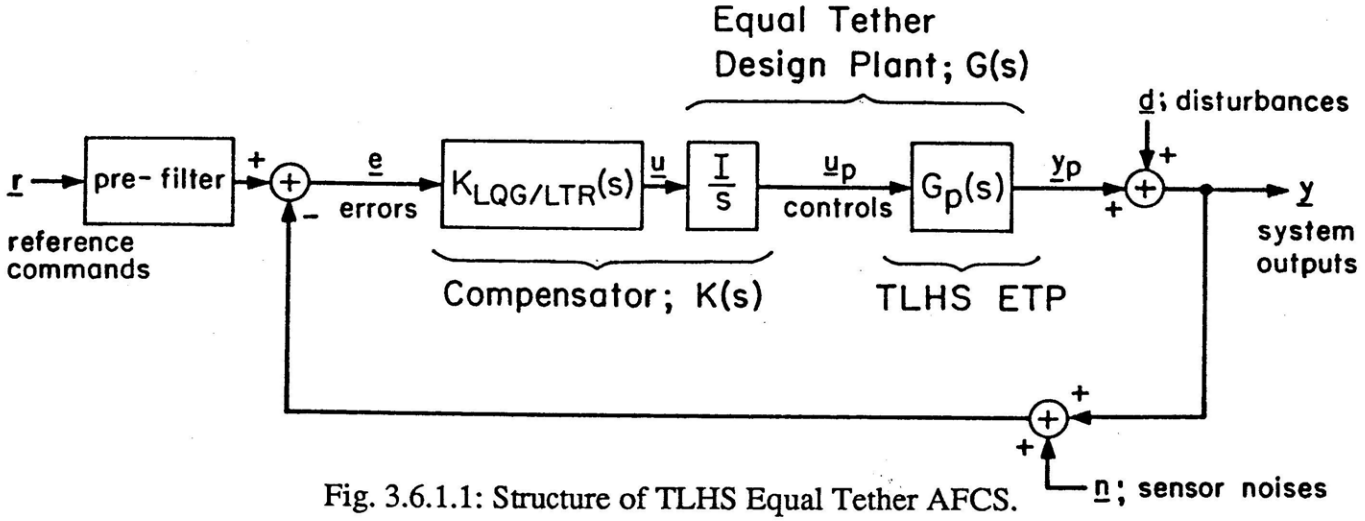

Fig. 3.6.1.1: Structure of TLHS Equal Tether AFCS.

dynamic LQG/LTR compensator, $K_{LQG/LTR}(s)$, and a pre-filter. When properly designed, the AFCS "minimizes" the effects of the disturbances, $\underline{d}$, and sensor noises, $\underline{n}$, so that the system outputs, $\underline{y}$, "approximate" the pilot reference commands, $\underline{r}$.

As noted earlier, the Equal Tether Plant, $G_p(s)$, consists of the AVM, SM, and ASM Plants; i.e. $G_p(s) = \text{diag}(G_{p1}(s), G_{p2}(s), G_{p3}(s))$ where $G_{pi}(s) = C_{pi}\,(sI - A_{pi})^{-1}\,B_{pi}$, $i = 1, 2, 3$.

The dynamic augmentation consists of four integrators (one per input channel). Reasons for their introduction shall be provided subsequently.

The Equal Tether Plant plus the four integrators shall be referred to as the Equal Tether Design Plant. The Equal Tether Design Plant consists of an AVM Design Plant, a SM Design Plant, and an ASM Design Plant. These design plants have state space representations given by:

$$\dot{\underline{x}}_i = A_i\,\underline{x}_i + B_i\,\underline{u}_i \tag{3.148}$$

$$\underline{y}_i = C_i\,\underline{x}_i + \underline{d}_i\ * \tag{3.149}$$

where

$$A_i = \begin{bmatrix} A_{pi} & B_{pi} \\ 0 & 0 \end{bmatrix} \tag{3.150}$$

$$B_i = [\,0 \quad I\,]^T \tag{3.151}$$

$$C_i = [\,C_{pi} \quad 0\,] \tag{3.152}$$

and

$$\underline{x}_i = [\,\underline{x}_{pi}^T \ \underline{u}_{pi}^T\,]^T \qquad i = 1, 2, 3 \tag{3.153}$$

where $i = 1, 2, 3$ denote the AVM, SM, and ASM Design Plants, respectively. Their inputs are:

$$u_1 \equiv \dot{u}_{p1} = \Sigma\dot{\Theta}_c \tag{3.154}$$

$$u_2 \equiv \dot{u}_{p2} = \Delta\dot{B}_{lc} \tag{3.155}$$

$$\underline{u}_3 \equiv \dot{\underline{u}}_{p3} = [\,\Delta\dot{\Theta}_c \quad \Sigma\dot{B}_{lc}\,]^T \tag{3.156}$$

These are the inputs to the four integrators.

---

*In previous section we had $d_i = 0$ and hence $y_{p1} = y_i$.

Their outputs are:

$$y_1 \equiv \Sigma \dot{z} \tag{3.157}$$

$$y_2 \equiv \Delta x \tag{3.158}$$

$$\underline{y}_3 \equiv [\, x_L - \Sigma x \quad \Sigma \dot{x}]^T \tag{3.159}$$

Their transfer functions (assuming $\underline{d}_i = \underline{0}$) are given by:

$$G_i(s) = G_{pi}(s) / s = C_i\,(sI - A_i\,)^{-1} B_i \tag{3.160}$$

The Equal Tether Design Plant has state space representation given by:

$$\dot{\underline{x}} = A\,\underline{x} + B\,\underline{u}; \qquad \underline{x} \in \mathbf{R}^{16},\ \underline{u} \in \mathbf{R}^4 \tag{3.161}$$

$$\underline{y} = C\underline{x} + \underline{d}; \qquad \underline{y} \in \mathbf{R}^4,\quad \underline{d} \in \mathbf{R}^4 \tag{3.162}$$

$$\underline{x} = [x_1 \quad \underline{x}_2{}^T \quad \underline{x}_3{}^T]^T \tag{3.163}$$

$$\underline{u} = [u_1 \quad u_2 \quad \underline{u}_3{}^T]^T \tag{3.164}$$

$$A = \mathrm{diag}(A_1, A_2, A_3) \tag{3.165}$$

$$B = \mathrm{diag}(B_1, B_2, B_3) \tag{3.166}$$

$$C = \mathrm{diag}(C_1, C_2, C_3) \tag{3.167}$$

Its transfer function matrix (tfm) is given by:

$$G(s) \equiv G_p(s) / s \tag{3.168a}$$

$$= \mathrm{diag}(G_1(s), G_2(s), G_3(s)) \tag{3.168b}$$

$$= C(sI - A)^{-1} B \tag{3.168c}$$

The Equal Tether LQG/LTR compensator consists of three compensators; one for each of the Equal Tether Design Plants. It shall be denoted as follows:

$$K_{LQG/LTR}(s) = \mathrm{diag}\ \{\, K^i_{LQG/LTR}(s)\} \quad i = 1, 2, 3 \tag{3.169}$$

where i = 1, 2, 3 denote the LQG/LTR compensators for the AVM, SM, and ASM Design Plants,

respectively. The order of the Equal Tether LQG/LTR compensator is 16. This is the order of the Equal Tether Design Plant, G(s). Reasons for this, as well as the exact structure of $K_{LQG/LTR}(s)$, shall be presented in the next chapter.

Since the total compensation consists of the dynamic augmentation plus the LQG/LTR compensator, it makes sense to define the compensator, K(s), as follows:

$$K(s) \equiv K_{LQG/LTR}(s) / s \tag{3.170a}$$

$$= \text{diag}\{ K_i(s) \} \qquad i = 1,\ 2,\ 3 \tag{3.170b}$$

where i = 1, 2, 3 denote the AVM, SM, and ASM compensators.

The pre-filter consists of three Butterworth filters; one for the SM reference and the other two for the ASM references. Reasons for their introduction shall be provided subsequently. A more detailed visualization of the Equal Tether AFCS is given in Fig. 3.6.1.2.

Before presenting design specifications for the AVM, SM, and ASM AFCS's, we must first define some very important functions.

One important function to consider is the final loop tfm, $G_L(s)$, given by:

$$G_L(s) \equiv G_p(s)K(s) \tag{3.171a}$$

$$= \text{diag}(G_{L1}(s),\ G_{L2}(s),\ G_{L3}(s)) \tag{3.171b}$$

$$G_{Li}(s) = G_{pi}(s)K_i(s) \qquad i = 1,\ 2,\ 3 \tag{3.171c}$$

and the $G_{Li}(s)$ denote the final AVM, SM, and ASM loop functions.

Another important function is the final sensitivity tfm, S(s), given by:

$$S(s) \equiv [I + G_L(s)]^{-1} \tag{3.172a}$$

$$= \text{diag}(S_1(s),\ S_2(s),\ S_3(s)) \tag{3.172b}$$

where $$S_i(s) = [I + G_{Li}(s)]^{-1} \qquad i = 1, 2, 3 \tag{3.172c}$$

and the $S_i(s)$ denote the final AVM, SM, and ASM sensitivity functions.

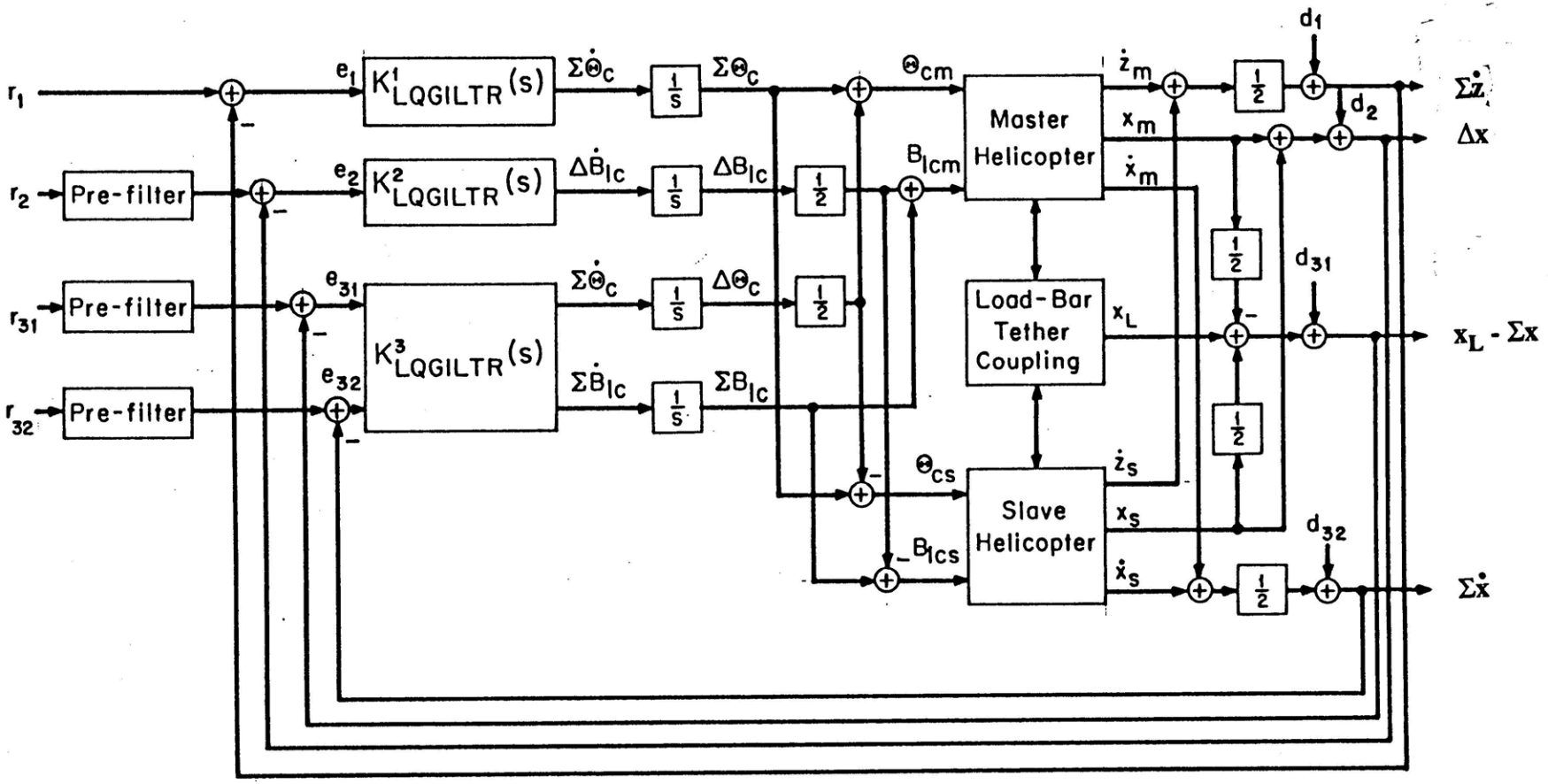

Fig. 3.6.1.2: Visualization of Equal Tether AFCS.

Finally, it is important to consider the final closed loop tfm, T(s), given by:

$$T(s) \equiv [I + G_L(s)]^{-1} G_L(s) \tag{3.173a}$$

$$= \text{diag}(T_1(s), T_2(s), T_3(s)) \tag{3.173b}$$

where $$T_i(s) \equiv [I + G_{Li}(s)]^{-1} G_{Li}(s) \qquad i = 1,\ 2,\ 3 \tag{3.173c}$$

and the $T_i(s)$ denote the final AVM, SM, and ASM closed loop functions.

The prime objectives of the Equal Tether AFCS, in addition to guaranteeing nominal stability, can be listed as follows:

1. Low frequency command following;
2. Low frequency disturbance rejection;
3. Insensitivity to low frequency modeling errors;
4. High frequency sensor noise attenuation;
5. Robustness to high frequency unmodeled dynamics.

To assure the first three requires that the sensitivity functions, $S_i(s)$, be "small" at "low" frequencies where reference commands, disturbances, and "unintentional" modeling errors have their greatest spectral content. To assure the last two requires that the closed loop functions, $T_i(s)$, be "small" at "high" frequencies where sensor noises and "intentionally" unmodeled dynamics have their greatest spectral content.

In addition to the above five desirable feedback properties, the Equal Tether AFCS must be designed so that the closed loop system exhibits "good internal" performance. This means that the pitch rates of the helicopters, as well as their vertical and horizontal acceleration characteristics, must be "passenger friendly". It also implies that the amplitude and/or spectral content of references, as well as the closed loop bandwidth must be restricted so that the control transients do not exceed the control limits. This saturation issue is particularly important to Twin Lift control engineers because

of the the inherent open loop instabilities associated with the Equal Tether Configuration. The presence of these unstable modes implies that the closed loop system will have a finite "downward gain margin". Consequently, if the controls are permitted to saturate an effective loop gain reduction will occur and the system may become highly oscillatory and possibly go unstable. Kapasouris, [18], provides a design methodology for plants with saturating actuators.

The sections which follow shall present performance and stability robustness specifications for the final Equal Tether AFCS. These design specifications shall be presented in terms of the final AVM, SM, and ASM loop, sensitivity, and closed loop functions. The specifications will primarily be based on TLHS capabilities, as reflected in the linear model. Before presenting the specifications it is important to put our goals into proper perspective.

In contrast to the gain stabilization methods employed in [1], the approach taken in this thesis will be to dynamically stabilize the TLHS and use the many degrees of freedom in the compensator to systematically develop a high performance (high bandwidth) Equal Tether AFCS. The emphasis of this chapter and the next, however, is not so much the design itself, but the description of the design procedure and the trade-offs involved when a high bandwidth is desired.

In the remaining sections of this chapter we present performance and robustness specifications for the AVM, SM, and ASM AFCS's.

3.6.2 Design Specifications for AVM AFCS

The structure of the final AVM AFCS is shown in Fig. 3.6.2.1.

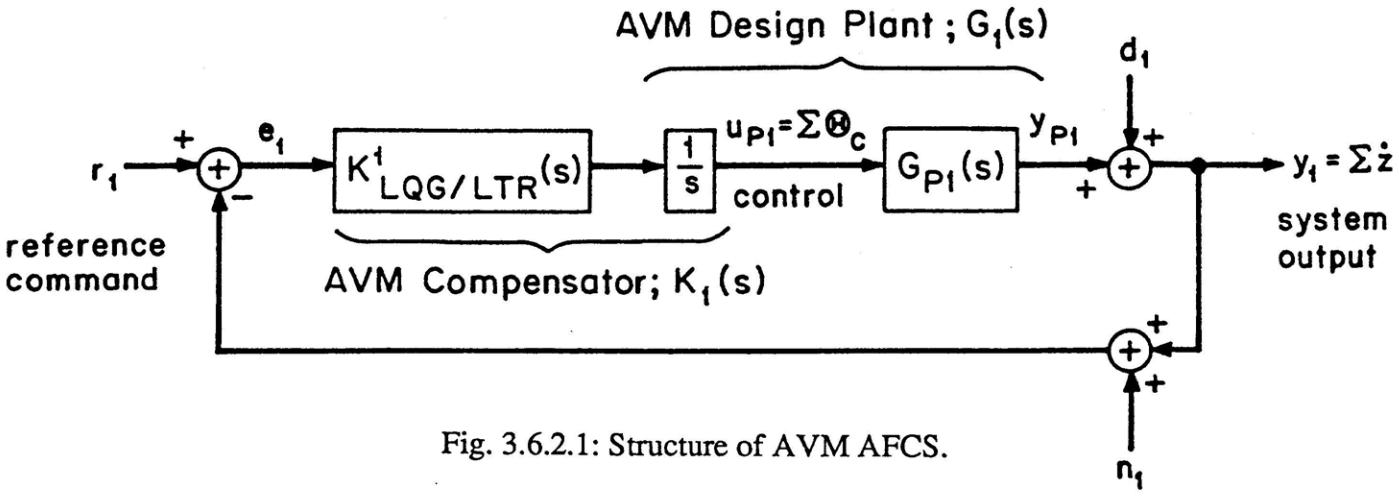

Fig. 3.6.2.1: Structure of AVM AFCS.

It was shown in section 3.5.1 that the AVM Plant, $G_{p1}(s)$, with input $\Sigma\Theta_c$ and output $y_{p1} \equiv \Sigma\dot{z}$, is nothing more than a simple first order lag. To assure zero steady state error to step reference commands, r_1, for $\Sigma\dot{z}$, the AVM Plant has been augmented with an integrator (at the plant input). The combined AVM Plant integrator, as stated earlier, shall be referred to as the AVM Design Plant, $G_1(s)$, where

$$G_1(s) \equiv G_{p1}(s) / s \tag{3.174a}$$

$$= C_1(sI - A_1)^{-1}B_1 \tag{3.174b}$$

The integrator will also guarantee complete steady state rejection of step disturbances, d_1 (Internal Model Principal) (Athans, [7]) .

In Chapter 4, the AVM LQG/LTR compensator, $K^1_{LQG/LTR}(s)$, shall be developed. Since a high performance design is desired, the specifications for the final AVM AFCS were selected as follows.

AVM AFCS Design Specifications

Performance

1. Zero steady state error to step commands and step output disturbances.
   To guarantee this the AVM Plant was augmented with an integrator.

2. Less than 10% steady state error to sinusoidal commands and output disturbances with spectral content at or below 0.08 rad/sec. This requires that the final AVM sensitivity tf satisfy:

$$| S_1(j\omega) | \leq -20 \text{ db for all } \omega \leq 0.08 \text{ rad/sec.}$$

3. Gain crossover frequency: $\omega_g \approx 0.5$ rad/sec.

4. Noise attenuation: $| T_1(j\omega) | \leq -20$ db for all $\omega \geq 20$ rad/sec.

Robustness

1. Robustness to low frequency uncertainty and high frequency unmodeled rotor dynamics ($\omega_r = 27$ rad/sec).

   To ensure this we require that the final AVM AFCS sensitivity tf satisfy:

$$| S_1(j\omega) | \leq \beta_1 = 1.31 \quad (2.3 \text{ db}) \quad \text{for all } \omega \geq 0.$$

   Since the AVM loop will not contain any unstable poles this specification can be translated [21] into the following SISO stability margins.

$$\text{Gain Margins: } \downarrow GM_1 = -\infty$$

$$\uparrow GM_1 \geq \beta_1 / (\beta_1 - 1) = 4.23 \quad (12.5 \text{ db})$$

$$\text{Phase Margin: } | PM_3 | \geq 2\sin^{-1}(1 / 2\beta_1) = \underline{45^\circ}$$

2. Closed loop gain crossover frequency (bandwidth): $\omega_{CL1} \leq 0.5$ rad/sec.

We note that the above method of presenting the AVM AFCS specifications is based on classical Bode SISO loop shaping ideas.

Because of the simplicity of the AVM Design Plant, $G_1(s)$, the above design specifications should be very easy to satisfy. Its Bode magnitude and phase plots, given in Fig. 3.6.2.2, indicate

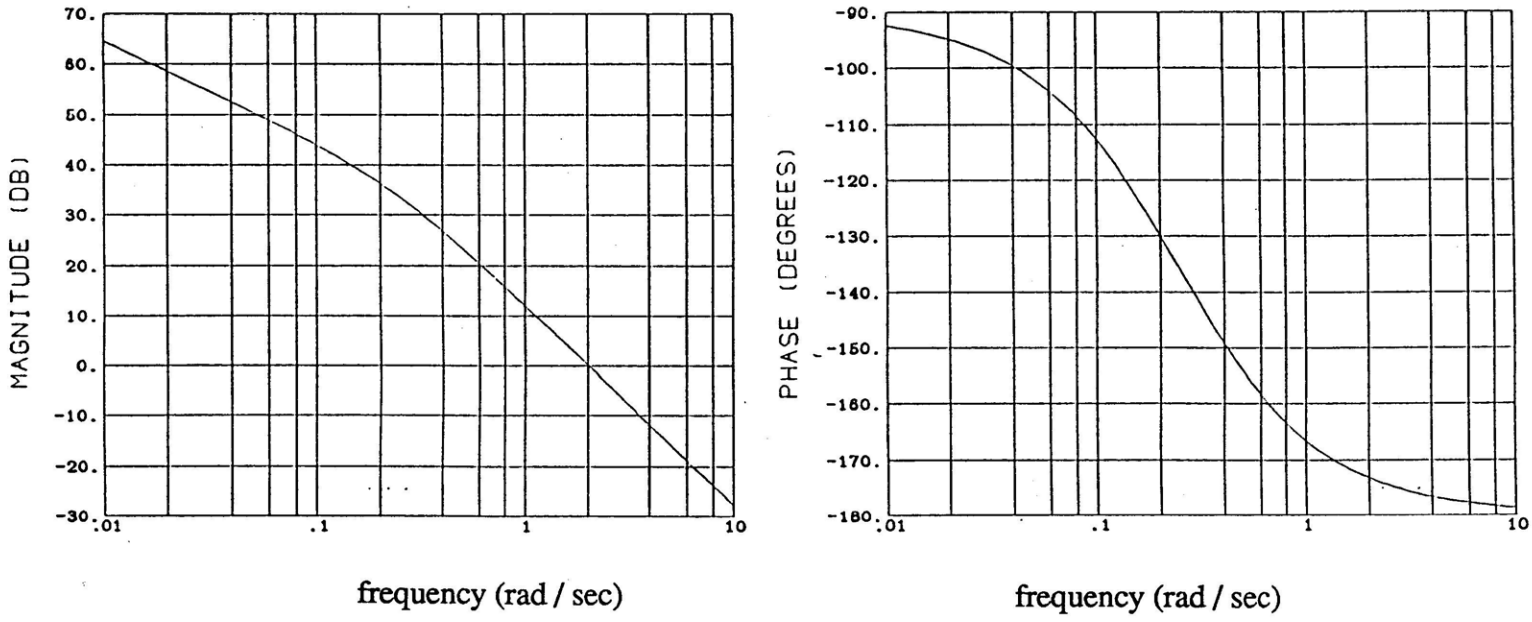

Fig. 3.6.2.2: Bode Magnitude and Phase Plots for AVM Design Plant.

that a simple lead-lag compensator, $K_1(s)$, may be all that is needed. More specifically, it is seen that a $K^1_{LQG/LTR}(s)$ with a zero at low frequencies (to draw the AVM Design Plant poles to "nice" locations) and poles at high frequencies (to provide sufficient roll-off in the loop) would suffice. The development of such a compensator, using the LQG/LTR design methodology, will be addressed in Chapter 4.

3.6.3 Design Specifications for SM AFCS

The structure of the final SM AFCS is shown in Fig. 3.6.3.1.

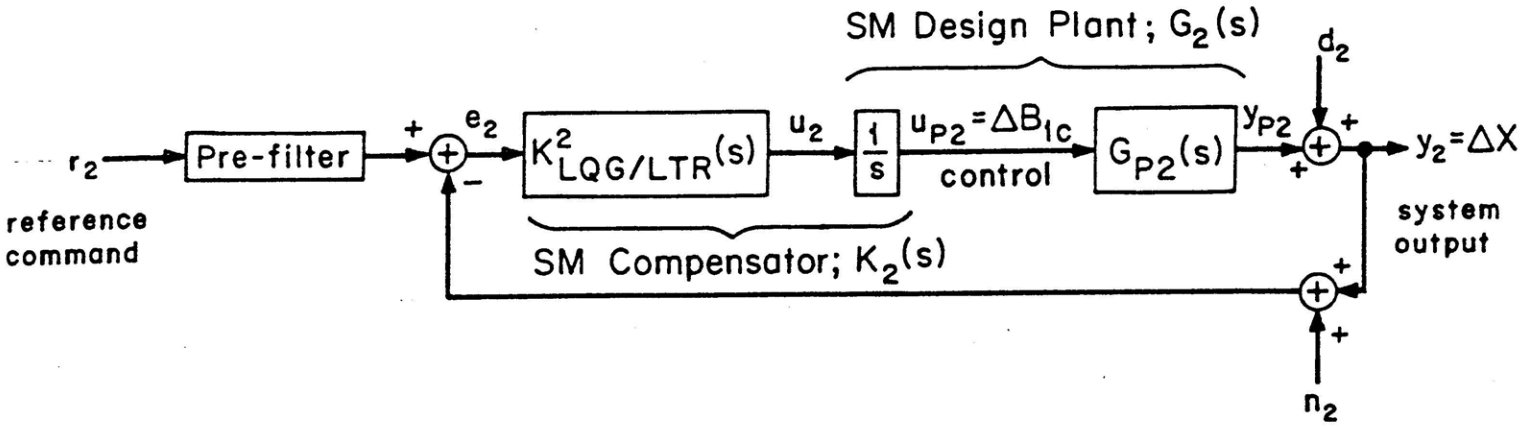

Fig. 3.6.3.1: Structure of SM AFCS.

It was shown in subsection 3.5.2 that the SM Plant, $G_{p2}(s)$, with input $u_{p2} \equiv \Delta B_{lc}$ and output $y_{p2} \equiv \Delta x$, is an unstable fourth order system with a pair of lightly damped zeros.

Since the SM Plant does not contain any natural integrators, it has been augmented with one (at the plant input) so that we are guaranteed zero steady state error to step reference commands, r_2, for Δx. Typically, however, Δx will be commanded to zero; i.e. $r_2 = 0$. The integrator will also guarantee complete steady state rejection of step disturbances, d_2. The combined SM Plant and integrator, as stated earlier, shall be referred to as the SM Design Plant, $G_2(s)$, where

$$G_2(s) \equiv G_{p2}(s) / s \tag{3.134}$$

$$= C_2 (sI - A_2)^{-1} B_2 . \tag{3.135}$$

In Chapter 4, the SM LQG/LTR compensator, $K^2_{LQG/LTR}(s)$, and the SM pre-filter shall be developed. Since a high performance design is desired, the specifications for the final SM AFCS were selected as follows.

SM AFCS Design Specifications

Performance

1. Zero steady state error to step commands and step output disturbances.
2. Less than 10% steady state error to sinusoidal commands and output disturbances with spectral content at or below 0.04 rad/sec. This requires that the final SM sensitivity tf satisfy:

$$| S_2(j\omega) | \leq - 20 \text{ db for all } \omega \leq 0.04 \text{ rad/sec.}$$

3. Gain crossover frequency: $\omega_{g2} \approx 1.5$ rad/sec.

4. Noise attenuation: $| T_2(j\omega) | \leq - 20$ db for all $\omega \geq 20$ rad/sec.

Robustness

1. Robustness to low frequency and high frequency unmodeled rotor dynamics.

   ($\omega_r \approx 27$ rad/sec).

   To ensure this we require that the final SM sensitivity tf satisfy:

$$| S_2(j\omega) | \leq \beta_2 = 1.93 \ \ (5.72 \text{ db}) \ \text{ for all } \omega \geq 0.$$

   It can be shown that this translates into the following SISO stability margins:

$$\text{Gain Margins: } \downarrow GM_2 \geq \beta_2 / (\beta_2 + 1) = 0.66 \ (-3.6 \text{ db})$$

$$\uparrow GM_2 \geq \beta_2 / (\beta_2 - 1) = 2.08 \ \ (6.3 \text{ db})$$

$$\text{Phase Margin: } 2\sin^{-1}(1 / 2\beta_2) = \underline{30^\circ}$$

2. Closed loop gain crossover frequency (bandwidth): $\omega_{CL2} \leq 3$ rad/sec

The SM pre-filter shall be selected so that references are appropriately bandlimited. A Butterworth filter shall be used since it is "maximally flat" in the passband. The order of the filter, as well as its cut-off frequency, will be selected from the final reference to control tf since this tf shows clearly what reference frequencies are amplified by the AFCS.

We note that, as with the AVM AFCS specifications, the above method of presenting the SM AFCS specifications is based on classical Bode SISO loop shaping ideas.

The Bode magnitude and phase plots for the SM Design Plant are given in Fig. 3.6.3.2. These plots indicate that the horizontal separation will be difficult to control, even under full automatic control. The sources of this difficulty are now described.

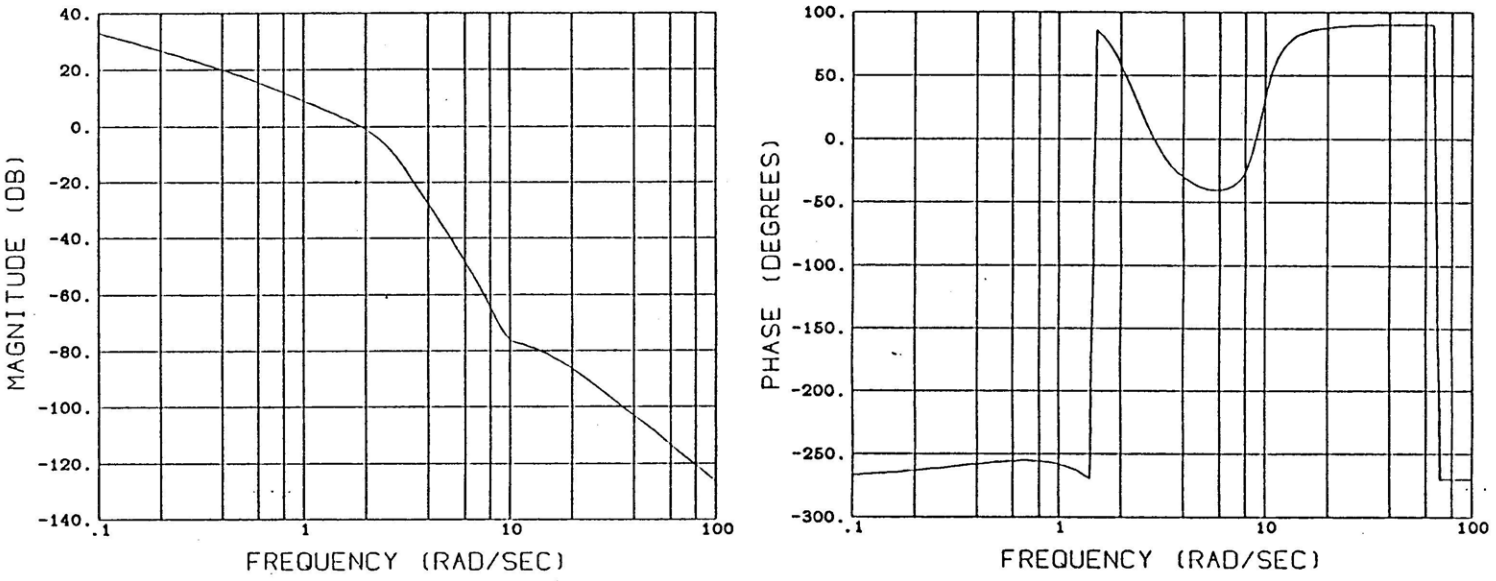

Fig. 3.6.3.2: Bode Magnitude and Phase for SM Design Plant.

The primary source of difficulty is due to the unstable Tethered Helicopter Mode (Section 3.3.2) which has a time to double of approximately 1 second.* Because of this unstable mode and the downward gain margin specification, the SM AFCS will require a minimum bandwidth just to stabilize the SM Design Plant.

* This mode is much too fast for open loop master-slave pilot control. Pilot workload would be too high.

Accompanying this minimum bandwidth there will be minimum differential pitch rates and differential cyclic rates (for fixed reference commands). These rates may be untolerable depending upon the size and frequency content of disturbances and noise. (Pilot reference commands for Δx are typically zero). In order to keep these rates to a minimum, it makes sense to keep the SM AFCS bandwidth small. Doing so, however, would necessarily mean giving up performance (speed). Since the central theme of this thesis is to address the feasibility of a high performance AFCS for TLHS's, we chose a relatively high SM AFCS bandwidth specification. More specifically, the SM AFCS gain crossover frequency specification was chosen to be on the order of the SM Design Plant's gain crossover frequency (2 rad/sec). The implications of selecting such a gain crossover frequency is well understood from classical SISO loop shaping theory [14].

There are 5 SM Design Plant poles which the SM LQG/LTR compensator, $K^2_{LQG/LTR}(s)$, will have to deal with. These consist of the unstable Tethered Helicopter Mode (ω = 0.7561 rad/sec), the Horizontal Spring Mode (ζ = 0.34, ω_n = 2.37 rad/sec.), the Symmetric Damping Mode (ω = 2.29 rad/sec.), and the integrator. Each of these poles contribute phase lag at the desired SM AFCS gain crossover frequency, $\omega_{g2} \approx 1.5$ rad/sec. The Tethered Helicopter Mode contributes 117° of lag, the Horizontal Spring Mode contributes 36°, the Symmetric Damping Mode contributes 33°, and the integrator contributes 90°. Collectively, the 5 poles contribute a total of 276° of phase lag at the desired gain crossover. Because of this huge amount of phase lag, the SM LQG/LTR compensator will require a great deal of lead (derivative action) in order for the resulting SM AFCS loop to have a nice phase margin. This follows from the fact that the phase margin (PM_2) is measured at the open loop gain crossover frequency. Moreover, the more lead introduced near crossover, the better our phase margin will be. More lead, however, translates into more control activity and larger pitch rates. Consequently, the poles force us to trade-off performance versus stability robustness.

So far we have only addressed the implication of the SM Design Plants' poles with respect to

obtaining a high performance SM AFCS design. What about the implication of the SM Design Plants' lightly damped zeros ($\zeta = 0.16$, $\omega_n = 9.62$ rad/sec) ? One might think that these zeros are helpful since they contribute lead at the desired gain crossover frequency ($\omega_{g2} \approx 1.5$ rad/sec). Although the zeros do contribute lead at ω_{g2}, the lead is very little (3°) contributes much lag near the desired gain crossover. In fact, the detrimental amplifying effect of the zeros, at high frequencies, far outweighs their "nice" lead effect at crossover. Above $\omega_n = 9.62$ rad/sec the zeros contribute 12 db (40 db) of amplification per octave (decade) increase in frequency. At $\omega \approx 30$ rad/sec, for example, they contribute about 20 db of amplification. This, of course, does not help us as far as high frequency noise is concerned. Since attenuation of noise is necessary for high performance it follows that the effect of these high frequency zeros must be reduced. To do this we must introduce phase lag into the loop. Introducing lag, however, reduces our stability margins. Consequently, the zeros also force us to trade-off performance versus stability robustness.

Because we seek a high bamdwidth design the trade-off between performance and robustness is exacerbated. The degree to which this happens shall be addressed in Chapter 4, where the SM AFCS is developed. From the above qualitative analysis, it is expected that a large robustness (lead) requirement would result in substantial control action. This, of course, implies substantial pitching in order to regulate the horizontal separation. The robustness specifications given for the SM AFCS were appropriately selected to illustrate this point.

In Chapter 4, the SM compensator, $K_2(s)$, shall be developed using the LQG/LTR design methodology. To address the lead issues described above a SM pre-filter shall also be developed.

3.6.4 Design Specifications for ASM AFCS

The structure of the final ASM AFCS is shown in Fig. 3.6.4.1.

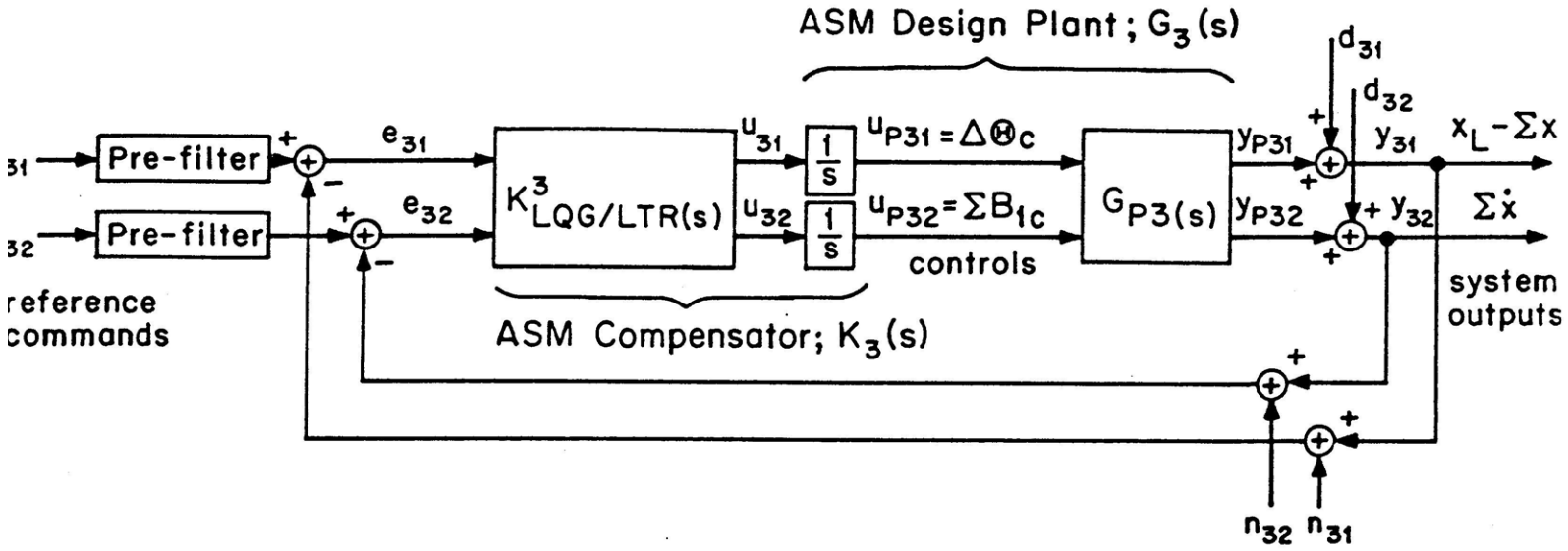

Fig. 3.6.4.1: Structure of ASM AFCS.

It was shown in section 3.5.3 that the ASM Plant, $G_{p3}(s)$, with inputs $\underline{u}_{p3} \equiv [\Delta\Theta_c \; \Sigma B_{1c}]^T$ and outputs $\underline{y}_{p3} \equiv [x_L - \Sigma x \; \Sigma\dot{x}]^T$, is an unstable seventh order system with two pairs of lightly damped zeros. Since the ASM Plant does not contain any natural integrators, it has been augmented with two (one per control channel) so that we are guaranteed zero steady state error to step reference commands, $\underline{r}_3 = [r_{31} \; r_{32}]^T$, for x_L-Σx and $\Sigma\dot{x}$. The integrators will also guarantee complete steady state rejection of step disturbances, $\underline{d}_3 = [d_{31} \; d_{32}]^T$. The combined ASM Plant and integrators, as stated earlier, shall be referred to as the ASM Design Plant, $G_3(s)$, where

$$G_3(s) \equiv G_{p3}(s) / s \qquad (3.175a)$$

$$= C_3 (sI - A_3)^{-1} B_3 \qquad (3.175b)$$

In Chapter 4, the ASM LQG/LTR compensator, $K^3_{LQG/LTR}(s)$, and the ASM pre-filters shall be developed. Since a high performance design is desired, the specifications for the final ASM AFCS were selected as follows.

ASM Design Specifications

Performance

1. Zero steady state error to step commands and step output disturbances in all directions. To guarantee this the ASM Plant was augmented with two integrators (one per control channel) at the plant input.

2. Less than 10% steady state error ($\|\underline{e}_3\|_2 \leq 0.1\ \|\underline{d}_3\|_2$)to sinusoidal commands and output disturbances with spectral content at or below 0.06 rad/sec. This requires that the final ASM sensitivity tfm satisfy:

$$\sigma_{max}[S_3(j\omega)] \leq -20 \text{ db for all } \omega \leq 0.06 \text{ rad/sec.}$$

3. Low frequency errors on the unit circle are of equal importance. This implies that the errors $\underline{e}_3 = [1\ \ 0]^T$, $[1\ \ 1]^T / \ 2$, $[0\ \ 1]^T$, and any error with two-norm $\|\underline{e}_3\|_2 = (\underline{e}_3^H \underline{e}_3)^{0.5} = 1$ are of equal importance and should thus receive equal steady state attenuation. This implies that the final ASM sensitivity tfm should satisfy:

$$\sigma_{max}[S_3(j\omega)] \approx \sigma_{min}[S_3(j\omega)] \ \text{(at each } \omega)$$

at low frequencies. If such is the case we say that the loop singular values are matched at low frequencies [7].

4. Gain crossover frequencies: $0.75 \leq \omega_{g3} \leq 2$ rad/sec. The gain crossover frequencies for a MIMO system are the frequencies at which the maximum and minimum loop singular values cross 0 db.

5. Noise attenuation: $\sigma_{max}[T_3(j\omega)] \leq -20$ db for all $\omega \geq 20$ rad/sec.

Robustness

1. Robustness to low frequency uncertainty and high frequency unmodeled rotor dynamics ($\omega_r = 27$ rad/sec).

To ensure this we require that the final ASM AFCS sensitivity tfm satisfy:

$$\sigma_{max}\,[S_3(j\omega)] \le \beta_3 = 1.93\ (5.72\ db)\ \text{for all}\ \omega \ge 0.$$

It can be shown [21] that this translates into the following mulivariable stability margins:

$$\text{Gain Margin:}\quad \downarrow GM \le \beta_3 / (\beta_3 + 1) = 0.66\ \ (-\ 3.6\ db)$$

$$\uparrow GM > \beta_3 / (\beta_3 - 1) = 2.08\quad (6.3\ db)$$

$$\text{Phase Margin:}\quad |PM_3| \ge 2\sin^{-1}(1 / 2\beta_3) = \underline{30^\circ}$$

2. Closed loop gaincrossover frequencies (bandwidth): $\omega_{CL3} \le 2$ rad/sec.

The ASM pre-filters shall be selected from the final reference to control singular values.

The above method of presenting design specifications shows that singular values help us extend the classical Bode SISO loop shaping ideas to the MIMO case. Consequently, even highly coupled MIMO TLHS control problems can be formulated in a manner which closely parallels classical SISO control problem formulations. This shows why in recent years, singular values have become particularly attractive to control system design engineers.

It should also be noted that the above design specifications have been expressed in terms of the loop, sensitivity, and closed loop tfm's associated with the plant output (or error signal). We thus say that the specifications have been presented at the plant output. We make this point because in general, a designer may also want to satisfy design specifications "at the plant input". Such specifications would be presented in terms of the singular values of the loop tfm obtained by breaking the loop at the plant input. This issue shall be revisited in Chapter 4.

The singular values of the ASM Design Plant are given Fig. 3.6.4.2. The large slope near 1 rad/sec, due to the unstable Backflapping Mode, the Vertical Spring Mode, and an integrator indicates the difficulty of the high performance (high bandwidth) ASM AFCS design problem. The

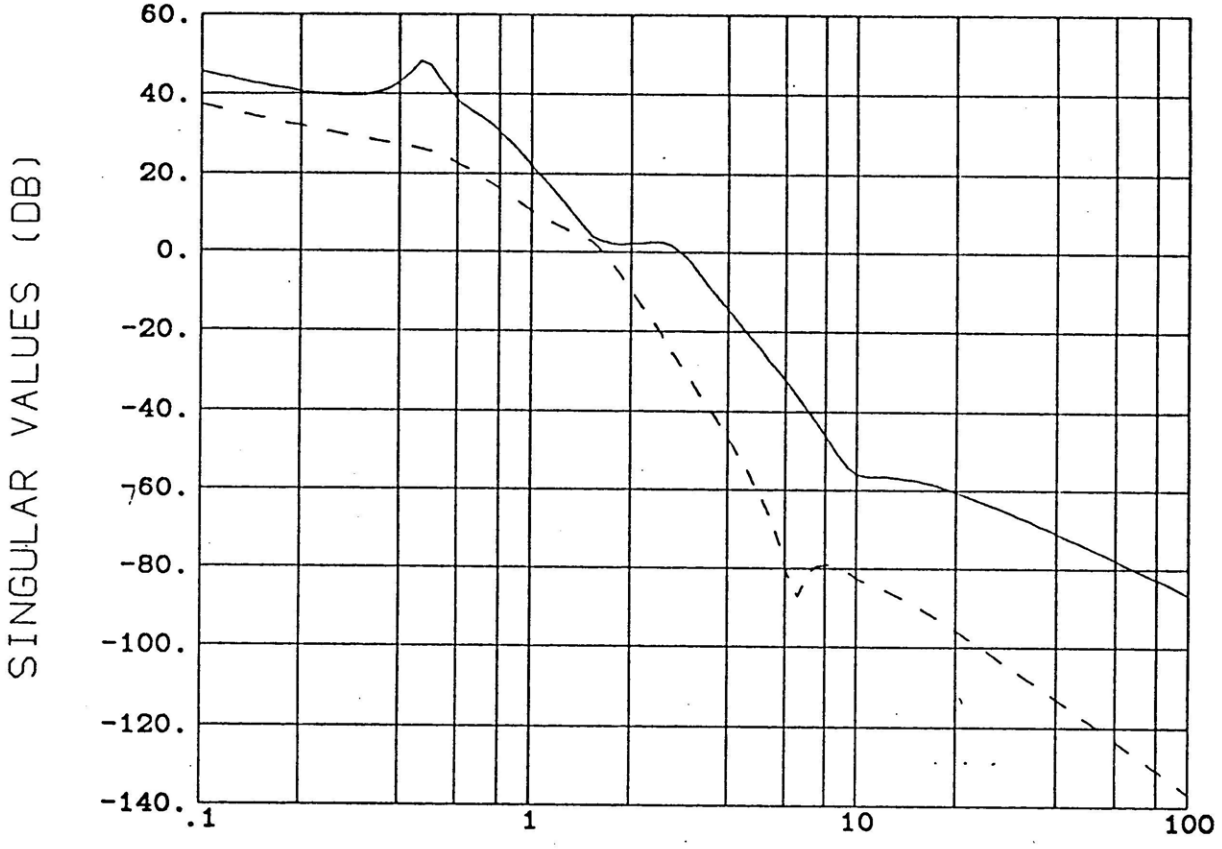

Fig. 3.6.4.2: Singular Values for ASM Design Plant

reasoning behind this is analogous to that used in the previous section for the SM Design Plant. In addition, the ASM Design Plant also possesses a Pendular Mode, an Anti-Symmetric Damping Mode, and another integrator. The bottom line is that many poles near the desired ASM AFCS gain crossovers, intuitively, even for a MIMO system, requires alot of lead to have nice stability margins. Furthermore, the ASM Design Plant has two pairs of lightly damped zeros. As with the SM AFCS design problem, the ASM AFCS design problem will require a trade-off between performance and stability robustness.

Because we seek a high bandwidth design the trade-off between performance and robustness is exacerbated. The degree to which this happens shall be addressed in Chapter 4, where the ASM

AFCS is developed. It is expected that having large stability margins would result in substantial pitching and oscilaations in the vertical plane in order to regulate the load motion when horizontal velocities are commanded. The robustness specifications given for the ASM AFCS were appropriately selected to illustrate this point.

In Chapter 4, the ASM compensator, $K_3(s)$, shall be developed using the LQG/LTR design methodology. To help address the ASM lead issues an ASM pre-filter shall also be developed.

It must be emphasized that although the design specifications have been presented in terms of the AVM, SM, and ASM AFCS's, it is important to make sure that overall Equal Tether AFCS performance is "adequate" for conducting typical Twin Lift maneuvers. "Large" pitch rates, accelerations, and controls for "simple" Twin Lift maneuvers, for example, would not be acceptable.

3.7 Summary

In this chapter the longitudinal dynamics of a TLHS near hovering trim were examined. For simplicity the tether lengths were assumed to be equal and fixed (Equal Tether Configuration). As a result of this assumption, the Twin Lift model developed in Chapter 2, was shown to decouple into three basic subsystems describing three basic motions: the Average Vertical Motion (AVM), the Symmetric Motion (SM), and the Anti-Symmetric Motion (ASM). The natural modes of each subsystem were identified and discussed. Outputs were then selected for each subsystem and three plants were defined, $G_{pi}(s) = C_{pi}(sI - A_{pi})^{-1}B_{pi}$; $i = 1,2,3$; the AVM Plant, the SM Plant, and the ASM Design Plant. The frequency response of each plant was then analyzed. The chapter concluded by formulating the high performance Equal Tether Control Problem. This involved describing the structure of the Equal Tether AFCS (to be developed in Chapter 4) as well as the structure of the individual AVM, SM, and ASM AFCS's which make it up. Also, part of the Equal Tether Control Problem formulation was the presentation of specifications for a high performance robust Equal Tether AFCS. Design specifications were presented in the frequency domain for the AVM and SM AFCS's using classical SISO Bode ideas. Singular value ideas were used to present the ASM AFCS specifications. This showed how classical SISO Bode loop

shaping concepts could easily be extended to the MIMO case. This also showed how one could formulate performance and robustness specifications in the frequency domain for even a highly coupled 16 degree of freedom Twin Lift model.

In order to meet the performance specifications, the three plants, $G_{pi}(s)$, were augmented with integrators (at the plant input) to obtain three design plants, $G_i(s) \equiv G_{pi}(s) / s = C_i (sI - A_i)^{-1} B_i$; $i = 1, 2, 3$; the AVM Design Plant, SM Design Plant, and ASM Design Plant. The ease/difficulty of meeting the high bandwidth design specifications was also discussed. In particular, the frequency response and pole-zero analyses were used to indicate trade-offs that must be made in designing high performance SM and ASM AFCS's. More specifically, the analysis suggested that in each case the trade-off would have to be made between performance and stability robustness. Since we seek a high bandwidth design this trade-off is exacerbated. The extent to which this happens shall be examined in the next chapter, where a high performance AFCS is developed for the Equal Tether Configuration. From the qualitative discussion presented in this section, however, we expect that a sufficiently large robustness (lead) requirement would require the helicopters to undergo substantial pitching and oscillations in the vertical plane in order to regulate the horizontal separation and load motion when horizontal or vertical velocites are commanded.

In the next chapter we shall use the LQG/LTR design methodology and simple filtering techniques to develop an AFCS for the Equal Tether Configuration.

CHAPTER 4: AFCS DESIGN FOR TLHS EQUAL TETHER CONFIGURATION

4.1 Introduction

In this chapter the LQG/LTR design methodology is described and applied to the Equal Tether Design Plant, discussed in Chapter 3*. The chapter shows how the methodology, coupled with singular value ideas, can be used to systematically develop an AFCS for the Equal Tether Configuration.** A design satisfying the specifications presented in Chapter 3 is obtained and evaluated.

In addition to demonstrating the power of LQG/LTR as a tool for developing multivariable control laws for TLHS's, the chapter identifies and discusses important trade-offs which Twin Lift control engineers must face. In particular, the chapter will show the extent to which Twin Lift control engineers must trade-off performance versus stability robustness when a high bandwidth design is the objective. Moreover, it is concluded that a high bandwidth AFCS design for the Equal Tether Configuration is feasible only when model uncertainty is sufficiently low. If model uncertainty is high, the design becomes unfeasible. This is because, in such a case, the large robustness requirement forces the helicopters to undergo substantial pitching and oscillations in the vertical plane in order to regulate the horizontal separation and load motion when horizontal and vertical velocity commands are issued. More specifically, if model uncertainty is high then only a low bandwidth design becomes feasible.

4.2 LQG/LTR Design Methodology

In this section the compensation scheme to be used by the Equal Tether AFCS is presented. After describing the "model based" compensator, the Linear Quadratic Gaussian with Loop Transfer Recovery (LQG/LTR) design methodology is described.

4.2.1 A Model Based Compensation Scheme

Consider the i^{th} Equal Tether Design Plant

$$G_i(s) \equiv G_{pi}(s) / s \qquad (4.1)$$

* The Equal Tether Design Plant consists of 3 design plants: the AVM Design Plant, the SM Design Plant, and the AVM Design Plant.

** The Unequal Tether Configuration is addressed in Chapters 5 and 6.

$$= C_i (sI - A_i)^{-1} B_i \qquad i = 1, 2, 3 \qquad (4.2)$$

where A_i is $n_i \times n_i$, B_i is $n_i \times m_i$, C_i is $m_i \times n_i$, and $i = 1, 2, 3$ denotes the AVM, SM, and ASM Design Plants, respectively ($m_1 = 1, n_1 = 1$; $m_2 = 1, n_2 = 5$; $m_3 = 2, n_2 = 9$). As discussed in Chapter 3, the i^{th} Design Plant consists of the i^{th} plant and an integral augmentation at the plant input. Although, in general, the designer can use any augmentation he or she deems appropriate, it must be introduced at the plant input. The reason for this is to preserve the quantities which we want to command. These quantities, of course, are at the plant output. (Note: An augmentation could also be introduced at the error; i.e. in front of $K^i_{LQG/LTR}(s)$. This, however, shall not be addressed in the thesis.)

Suppose now that a compensator, $K^i_{LQG/LTR}(s)$, is needed so that the closed loop system in Fig. 4.2.1.1 satisfies prescribed design specifications (at the plant output).

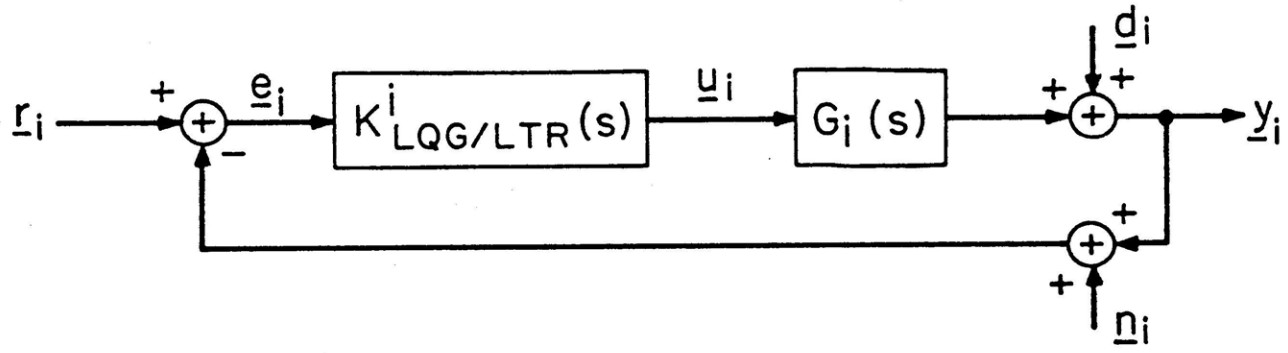

Fig. 4.2.1.1: Structure of i^{th} Equal Tether AFCS.

The structure for $K^i_{LQG/LTR}(s)$ to be used is given in Fig. 4.2.1.2. Since the matrices A_i, B_i, and C_i are contained within $K^i_{LQG/LTR}(s)$, we refer to it as a <u>model based compensator</u> (Athans, [7]).

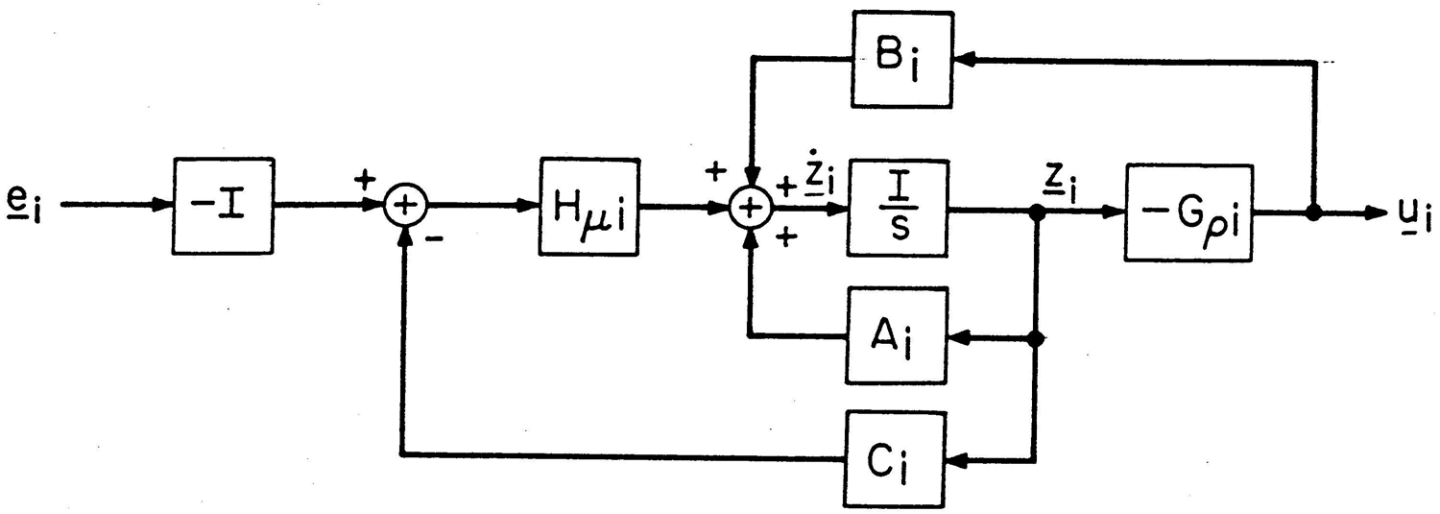

Fig. 4.2.1.2: Structure of i^{th} Model Based LQG/LTR Compensator.

The gain matrices $H_{\mu i}$ and $G_{\rho i}$ are chosen such that the closed loop system in Fig. 4.2.1.1 is nominally stable and meets prescribed design specifications. The tfm from $\underline{e}_i$ to $\underline{u}_i$ is given by:

$$K^i_{LQG/LTR}(s) = G_{\rho i}\,(sI - A_i + B_i\,G_{\rho i} + H_{\mu i}\,C_i)^{-1}\,H_{\mu i} \tag{4.3}$$

It can be shown that the closed loop system in Fig. 4.2.1.1 has state space representation given by:

$$\begin{bmatrix} \dot{\underline{x}}_i \\ \dot{\underline{z}}_i \end{bmatrix} = \begin{bmatrix} A_i & -B_i\,G_{\rho i} \\ H_{\mu i}\,C_i & A_i - B_i\,G_{\rho i} - H_{\mu i}\,C_i \end{bmatrix} \begin{bmatrix} \underline{x}_i \\ \underline{z}_i \end{bmatrix} + \begin{bmatrix} 0 & 0 & 0 \\ -H_{\mu i} & H_{\mu i} & H_{\mu i} \end{bmatrix} \begin{bmatrix} \underline{r}_i \\ \underline{n}_i \\ \underline{d}_i \end{bmatrix} \tag{4.4}$$

$$\underline{y}_i = [C_i \;\; 0] \begin{bmatrix} \underline{x}_i \\ \underline{z}_i \end{bmatrix} + [0 \;\; 0 \;\; I] \begin{bmatrix} \underline{r}_i \\ \underline{n}_i \\ \underline{d}_i \end{bmatrix} \tag{4.5}$$

where $\underline{x}_i \equiv [\underline{x}_{pi}{}^T \;\; \underline{u}_{pi}{}^T]^T$ is the state vector of the i^{th} design plant and $\underline{z}_i$ is that of the i^{th} LQG/LTR compensator.

The closed loop poles are the eigenvalues of the first matrix in eq. (4.4). Because of the complexity of this matrix the closed loop poles are not easily identified. To obtain a more "transparent" state space representation we perform the following change of basis (similarity transformation):

$$\begin{bmatrix} \underline{x}_i \\ \underline{x}_i - \underline{z}_i \end{bmatrix} = \begin{bmatrix} I & 0 \\ I & -I \end{bmatrix} \begin{bmatrix} \underline{x}_i \\ \underline{z}_i \end{bmatrix} \tag{4.6}$$

Substituting eq. (4.6) into eqs. (4.4) - (4.5) gives us the following "transparent" state space representation:

$$\begin{bmatrix} \dot{\underline{x}}_i \\ \dot{\underline{x}}_i - \dot{\underline{z}}_i \end{bmatrix} = \begin{bmatrix} A_i - B_i G_{\rho i} & -B_i G_{\rho i} \\ H_{\mu i} C_i & A_i - H_{\mu i} C_i \end{bmatrix} \begin{bmatrix} \underline{x}_i \\ \underline{x}_i - \underline{z}_i \end{bmatrix} + \begin{bmatrix} 0 & 0 & 0 \\ H_{\mu i} & -H_{\mu i} & -H_{\mu i} \end{bmatrix} \begin{bmatrix} \underline{r}_i \\ \underline{n}_i \\ \underline{d}_i \end{bmatrix} \tag{4.7}$$

$$\underline{y}_i = [C_i \quad 0] \begin{bmatrix} \underline{x}_i \\ \underline{x}_i - \underline{z}_i \end{bmatrix} + [0 \quad 0 \quad I] \begin{bmatrix} \underline{r}_i \\ \underline{n}_i \\ \underline{d}_i \end{bmatrix} \tag{4.8}$$

Eq. (4.8) shows that the poles of the closed loop system are given by the eigenvalues of $A_i - B_i G_{\rho i}$ and those of $A_i - H_{\mu i} C_i$ (Separation Principle).

Given the above compensation scheme, it is appropriate to ask how the gain matrices $H_{\mu i}$ and $G_{\rho i}$ are chosen so that the closed loop system is nominally stable and meets prescribed design specifications. To answer this question the LQG/LTR design procedure is described. The LQG/LTR procedure not only trivializes the stabilization problem but also possesses enough degrees of freedom which can be used to meet performance and stability robustness design specifications.

The LQG/LTR design procedure consists of essentially two steps. In the first step the designer develops a "target loop". In this step the "filter gain matrix," $H_{\mu i}^*$, is found by solving an appropriately formulated estimation problem (Athans, [7]). For our purposes, the fact that we are solving an optimal linear estimation problem is not important. In the second step the designer obtains a compensator $K^i_{LQG/LTR}(s)$, which "recovers" the target loop from the design plant, $G_i(s)$. In this step the "control gain matrix", $G_{\rho i}$, is found by solving an appropriately formulated optimal linear control problem. The two steps are now described in detail.

In our problem the design specifications heve been presented at the plant output. For this reason we compute the filter gain matrix first. If the specifications were at the plant input we would compute the control gain matrix first [7].

4.2.2 Developing a Target Loop

The first step of the design process is to develop a "target loop"; i.e. a loop transfer function matrix with desirable closed loop properties. We denote this target loop tfm by $G^i_{KF}(s)$, where

$$\boxed{G^i_{KF}(s) \equiv C_i\,(sI - A_i)^{-1}\,H_{\mu i}} \tag{4.9}$$

The subscript KF is used to emphasize that the target loop, and hence $H_{\mu i}$ are found by solving an appropriately formulated Kalman filtering problem. The main results for designing $G^i_{KF}(s)$ are now presented.

Let L_i be an n_i x m_i matrix design parameter and μ_i a positive scalar design parameter. The selection of L_i and μ_i shall be discussed subsequently. Assume that $(A_i,\ L_i)$ is at least stabilizable and that $(A_i,\ C_i)$ is at least detectable [11]. The filter gain matrix, $H_{\mu i}$, is then given by:

$$H_{\mu i} = \Sigma_{\mu i}\,C_i\,(1/\mu_i) \tag{4.10}$$

where the above stabilizability and detectability assumptions guarantee that $\Sigma_{\mu i}$ is the unique symmetric positive semi-definite solution of the following Filter Algebraic Riccati Equation (FARE):

$$0 = A_i\,\Sigma_{\mu i} + \Sigma_{\mu i}\,A_i^T + L_i\,L_i^T - \Sigma_{\mu i}\,C_i^T\,(1/\mu_i)\,C_i\,\Sigma_{\mu i}\,. \tag{4.11}$$

If $(A_i,\ C_i)$ is observable, as is the case for the AVM, SM, and ASM Design Plants, then $\Sigma_{\mu i}$ is the unique symmetric positive definite solution of the FARE.

It should be noted that the above stabilizability and detectability assumptions also guarantee that the eigenvalues of $A_i - H_{\mu i}\,C_i$ all lie in the open left half s-plane. This, of course, implies that the target loop or target Kalman Filter Loop, $G^i_{KF}(s)$, seen in Fig. 4.2.3.1 is guaranteed to be closed loop stable for all valid design parameters L_i, μ_i (i.e. $(A_i,\ L_i)$ at least stabilizable and $\mu_i > 0$) as long as $(A_i,\ C_i)$ is at least detectable; i.e.

$$\left.\begin{array}{l}(A_i,\ L_i)\ \text{stabilizable}\\ (A_i,\ C_i)\ \text{detectable}\\ \mu_i > 0\end{array}\right\} \Rightarrow \qquad \text{Re}\,\lambda_j\,(A_i - H_{\mu i}\,C_i) < 0 \quad \text{for all} \quad j = 1,\ldots,n_i. \tag{4.12}$$

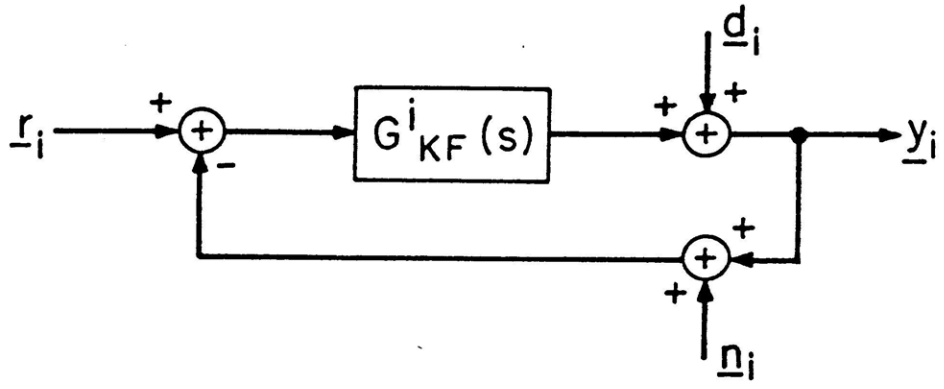

Fig. 4.2.2.1: Visualization of Target "Kalman Filter" Loop.

Although the above summarizes the target loop design process, it still remains to be shown how the design parameters L_i and μ_i are selected.

Suppose we define the "filter open loop" transfer function matrix, $G_{FOL}(s)$, as follows:

$$\boxed{G^i_{FOL}(s) \equiv C_i\,(sI - A_i)^{-1}\,L_i} \tag{4.13}$$

It can then be shown (from the FARE) that

$$[I + G^i_{KF}(s)]\,[I + G^i_{KF}(-s)]^T = I + (1/\mu_i)\,[G^i_{FOL}(s)]\,[G^i_{FOL}(-s)]^T \tag{4.14}$$

This relationship is known as the Kalman Filter Frequency Domain Equality (KFFDE). If $s = j\omega$ then we may write

$$\boxed{[I + G^i_{KF}(j\omega)]\,[I + G^i_{KF}(j\omega)]^H = I + (1/\mu_i)\,[G^i_{FOL}(j\omega)]\,[G^i_{FOL}(j\omega)]^H} \tag{4.15}$$

since $[N(j\omega)]^H = [N^*(j\omega)]^T = N(-j\omega)^T$ for any complex matrix $N(j\omega)$ (with real inverse Fourier Transform). From this equation, and the following two facts,

$$\sigma_j(N) = \lambda_j(N^H N) = \lambda_j(N\,N^H), \tag{4.16}$$

$$\lambda_j(I + N) = 1 + \lambda_j(N) \quad \text{for all matrices } N, \tag{4.17}$$

it can be shown that

$$\sigma_j[I + G^i_{KF}(j\omega)] = 1 + (1/\sqrt{\mu_i})\ \sigma_j[G^i_{FOL}(j\omega)] \quad \text{for all } j = 1,..., m_i. \tag{4.18}$$

This relationship provides us with incite on how we can intelligently choose the design parameters L_i and μ_i. From eq. (4.18) it follows that if $G^i_{KF}(j\omega)$ and $G^i_{FOL}(j\omega)$ are "large" at low frequencies (i.e. if their minimum singular values are "large"), then

$$\boxed{\sigma_j[G^i_{KF}(j\omega)] \cong (1/\sqrt{\mu_i})\ \sigma_j[G^i_{FOL}(j\omega)] \text{ at low frequencies.}} \tag{4.19}$$

From this equation it follows that L_i determines the low frequency shape of $\sigma_j[G_{KF}(j\omega)]$ and that μ_i just affects the low frequency "gain" at a particular frequency. The parameter μ_i can thus be used to control the open loop and hence the closed loop bandwidth. It should be emphasized that after the dynamic augmentation of the plant to form a design plant, the selection of L_i and μ_i is the most critical part of the LQG/LTR procedure. This is because L_i and μ_i completely determine what we want our final closed loop system to look like. Obviously, if we ask for foolish things we will get foolish things.

Suppose, for example, that one specification is that "low frequency steady state errors should be independent of the direction of the applied reference, r_i". This is the case for the ASM AFCS. In such a case it is necessary that the singular values of the target sensitivity function, $S^i_{KF}(j\omega) = [I + G^i_{KF}(j\omega)]^{-1}$, be "matched" at low frequencies, i.e. $\sigma_{min}[S^i_{KF}(j\omega)] \approx \sigma_{max}[S^i_{KF}(j\omega)]$ at low frequencies. This, however, can only be done if $\sigma_{min}[G^i_{KF}(j\omega)] \approx \sigma_{max}[G^i_{KF}(j\omega)]$ at low frequencies. To accomplish this we choose L_i as follows:

$$L_i = B_i\ [C_{pi}\,(-A_{pi})^{-1}\,B_{pi}]^{-1} \tag{4.20}$$

To show that this L_i matches the singular values of $G^i_{KF}(j\omega)$ at low frequencies, we substitute eq.

(4.20) into eq. (4.13) to get

$$G^i_{FOL}(s) = C_i\,(sI - A_i)^{-1}\,L_i \tag{4.21}$$

$$= [\,C_i\,(sI - A_i)^{-1}\,B_i\,]\;[\,C_{pi}\,(-A_{pi})^{-1}\,B_{pi}\,]^{-1} \tag{4.22}$$

Using the fact that $G_i(s) \equiv G_{pi}(s) / s = C_i\,(sI - A_i)^{-1}\,B_i$ in eq. (4.22) gives us

$$G_{FOL}(s) = [\,G_{pi}(s) / s\,]\;[\,C_{pi}\,(-A_{pi})^{-1}\,B_{pi}\,]^{-1}. \tag{4.23}$$

Recalling that $G_{pi}(s) = C_{pi}\,(sI - A_{pi})^{-1}\,B_{pi}$ and substituting this into eq. (4.23) gives us

$$G^i_{FOL}(s) = [\,C_i\,(sI - A_i)^{-1}\,B_i\,]\;[\,C_{pi}\,(-A_{pi})^{-1}\,B_{pi}\,]^{-1} / s. \tag{4.24}$$

This equation shows that, for low frequencies (small $s = j\omega$), we have

$$G^i_{FOL}(j\omega) \cong I / j\omega \tag{4.25}$$

and hence $\sigma_{min}[G^i_{FOL}(j\omega)] \cong \sigma_{max}[G^i_{FOL}(j\omega)]$ at low frequencies. This shows that selection of the matrix design parameter, L_i, in accordance with eq. (4.20) forces the singular values of $G^i_{FOL}(j\omega)$ to be "matched" at low frequencies. What about the singular values of our target loop, $G^i_{KF}(j\omega)$? Suppose further that μ_i is chosen sufficiently small so that $\sigma_j[G^i_{KF}(j\omega)] \cong (1 / \mu_i)\,\sigma_j[G^i_{FOL}(j\omega)]$ for all $j = 1,\ldots, m_i$ at low frequencies. This can always be done once realistic performance and robustness regions have been established. Fig. 4.2.2.2 shows what typical target loop singular values might look like.

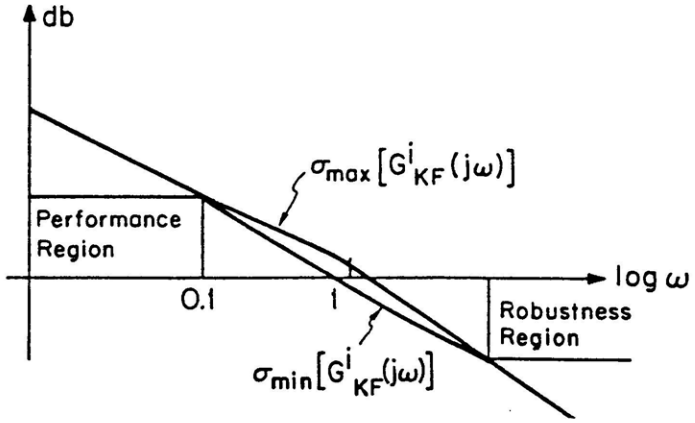

Fig. 4.2.2.2: Visualization of Typical Target Open Loop Singular Values.

It thus follows that if the singular values of $G^i_{FOL}(j\omega)$ are "matched" at low frequencies and if $G^i_{FOL}(j\omega)$ is "large" at low frequencies then the singular values of $G^i_{KF}(j\omega)$ will also be "matched" at low frequencies. It should be noted that the parameter μ_i can not be made too small for if this is done we run the risk of entering our robustness region (Fig. 4.2.2.2) and possibly exciting high frequency unmodeled (rotor) dynamics.

The first step of the LQG/LTR procedure has been completely described. It has been shown that to develop a target loop, $G^i_{KF}(s)$, a designer must pick a "nice" L_i and μ_i. The filter gain matrix, $H_{\mu i}$, is then found by solving the FARE. An appropriate question to ask is: "What are the benefits of chosing $H_{\mu i}$ in this manner ?" In addition to guaranteeing the stability of the target loop, i.e. Re $\lambda_j(A_i - H_{\mu i} C_i) < 0$ for all $j = 1,..., n_i$, there are two more properties which are guaranteed and extemely desirable. It is because of these two properties, and because our design specifications are at the plant output, that we compute the filter gain matrix, $H_{\mu i}$, first. (When the specifications are at the plant input we compute the control gain matrix, $G_{\rho i}$, first [7]). The two properties are now described. Both follow from the KFFDE and the singular value relationships (Lehtomaki, Sandell, Athans [8]). It can be shown, for example, that

$$\sigma_j[I + G^i_{KF}(j\omega)] \geq 1 \quad \text{for all} \quad j = 1,..., m_i \quad \text{for all} \quad \omega \geq 0. \tag{4.26}$$

From this it follows that

$$\sigma_{min}[I + G^i_{KF}(j\omega)] \geq 1 \quad \text{for all} \quad \omega \geq 0. \tag{4.27}$$

Using the fact that $\sigma_{max}(M) = 1 / \sigma_{min}(M^{-1})$ we get the desired inequality:

$$\boxed{\sigma_{max}[S^i_{KF}(j\omega)] \leq 1 \quad \text{for all} \quad \omega \geq 0.} \tag{4.28}$$

This inequality tells us that when the target loop is selected in accordance with the KF algorithm, described above, then the resulting target closed loop system will possess guaranteed (low frequency) performance properties at the plant output.

It can also be shown that

$$\sigma_j[I + G^i_{KF}(j\omega)] \geq 1/2 \qquad \text{for all } j = 1,..., m_i \text{ for all } \omega \geq 0. \tag{4.29}$$

From this it follows that

$$\sigma_{min}[I + G^i_{KF}(j\omega)] \geq 1/2 \qquad \text{for all } \omega \geq 0. \tag{4.30}$$

If we define $T^i_{KF}(s) \equiv G^i_{KF}(s)\,[I + G^i_{KF}(s)]^{-1}$ then using the fact that $\sigma_{max}(M) = 1/\sigma_{min}(M^{-1})$ for all nonsingular matrices M gives us the desired inequality:

$$\boxed{\sigma_{max}[T^i_{KF}(s)] \leq 2 \qquad \text{for all } \omega \geq 0.} \tag{4.31}$$

This inequality tells us that when the target loop is selected in accordance with the KF algorithm described above, then the resulting target closed loop system will possess guaranteed (high frequency) robustness properties at the plant output.

In addition to the above properties, eqs. (4.28) and (4.31) guarantee that the target loop $G^i_{KF}(s)$ can sustain modeling errors of the form $k\,e^{j\theta}$ on each channel (both independently and simultaneously) where $k \in (1/2, \infty)$ and $\theta \in (-60, 60)$ degrees (Safonov, Athans [21]).

We terminate this section by summarizing the target loop design procedure.

Summary of Target Loop Design Procedure

1. Given a plant $G_p(s) = C_p(sI - A_p)^{-1} B_p$ augment it at the input with any system, $G_a(s)$, that can help in meeting the design specifications. This gives us the Design Plant $G(s) = G_p(s)\,Ga(s) = C(sI - A)^{-1}B$. Typically $G_a(s) = I/s$.
2. Select a matrix L such that (A, L) is at least stabilizable and $\sigma_i[G_{FOL}(j\omega)] = \sigma_i[C(sI - A)^{-1}L]$ look "nice".
3. Select a positive scalar μ (bandwidth parameter).
4. Solve the following FARE for Σ_μ:

$$0 = A\,\Sigma_\mu + \Sigma_\mu\,A^T + LL^T - \Sigma_\mu\,C^T\,(1/\mu)\,C\,\Sigma_\mu$$

5. The target (desired) loop is then given by:

$$G_{KF}(s) = C(sI - A)^{-1}H_{\mu}$$

where $H_{\mu} = \Sigma_{\mu}C^{T}(1 / \mu)$.

Now that the procedure for designing a target loop with nice closed loop properties has been described, it is essential to identify a compensator which "recovers" the target loop from the design plant. (Note: The bandwidth parameter, μ, should not be confused with the Twin Lift parameter, $\mu \equiv [M_L + M_B] / 2 M_H$.).

4.2.3 Recovering the Target Loop

The second step of the LQG/LTR procedure is to develop a compensator, $K^{i}_{LQG/LTR}(s)$, which when placed in a unity feedback loop with the design plant $G_i(s)$, "recovers" the desired loop characteristics; i.e. the nice characteristics of $G^{i}_{KF}(s)$. As stated earlier this step involves the computation of the control gain matrix, $G_{\rho i}$. A method for computing $G_{\rho i}$ is now given.

Let M_i be an m_i x n_i matrix design parameter and ρ_i a positive scalar design parameter to be discussed subsequently. Assume that (A_i, B_i) is at least stabilizable and that (A_i, M_i) is at least detectable. The control gain matrix, $G_{\rho i}$, is then given by:

$$G_{\rho i} = (1 / \rho_i) B_i^{T} K_{\rho i} \qquad (4.32)$$

where the above stabilizability and detectability assumptions guarantee that $K_{\rho i}$ is the unique symmetric positive semi-definite solution of the following Control Algebraic Riccati Equation (CARE):

$$0 = - K_{\rho i} A_i - A_i^{T} K_{\rho i} - M_i^{T} M_i + K_{\rho i} B_i \ (1 / \rho_i) B_i^{T} K_{\rho i} . \qquad (4.33)$$

If (A_i, B_i) is controllable, as is the case for the AVM, SM, and ASM Design Plants, then $K_{\rho i}$ is the unique symmetric positive definite solution of the CARE.

It should be noted that the above stabilizability and detectability assumptions also guarantee that the eigenvalues of $A_i - B_i G_{\rho i}$ all lie in the open left half s-plane; i.e.

$$\left.\begin{array}{l}(A_i, B_i) \text{ stabilizable} \\ (A_i, M_i) \text{ detectable} \\ \rho_i > 0\end{array}\right\} \Rightarrow \quad \text{Re } \lambda_j(A_i - B_i G_{\rho i}) < 0 \quad \text{for all } j = 1,..., n_i . \tag{4.34}$$

What does this property tell us? In section 4.2.1 the model based compensator, $K^i_{LQG/LTR}(s)$, structure was described. It was also shown that the closed loop poles are exactly the eigenvalues of $A_i - H_{\mu i} C_i$ and those of $A_i - B_i G_{\rho i}$. We have presented a procedure for selecting $H_{\mu i}$ and $G_{\rho i}$ so that Re $\lambda_j(A_i - H_{\mu i} C_i) < 0$ and Re $\lambda_j(A_i - B_i G_{\rho i}) < 0$ for all $j = 1,..., n_i$; i.e. so that nominal closed loop stability is guaranteed. The stabilization problem has thus been trivialized. But what about the properties of the loop $G_i(s)K^i_{LQG/LTR}(s)$? In order to "recover" the nice properties of $G^i_{KF}(s)$ we proceed as follows.

Suppose that the transfer function matrix $G^i_{OL}(s) = M_i (sI - A_i)^{-1} B_i$ is minimum phase; i.e. all its zeros lie in the open left half s-plane. It can be shown (Athans, [7]) that the following is true:

$$\boxed{\lim_{\rho_i \to 0+} \sqrt{\rho_i}\, G_{\rho i} = \lim_{\rho_i \to 0+} [\, (1/\sqrt{\rho_i}\,)\, B_i^T K_{\rho i}\,] = W_i M_i} \tag{4.35}$$

where $W_i \in \mathbf{R}^{m_i \times m_i}$ is some orthogonal matrix ($W_i^{-1} = W_i^T$).

Suppose further that we select $M_i = C_i$. It then follows that $G_{FOL}(s) = G_i(s)$. Since the AVM, SM, and ASM Design Plants, $G_i(s)$, are minimum phase we know that eq. (4.35) holds for $M_i = C_i$. Using this "recovery" relationship it can be shown (Doyle, Stein [5]) that

$$\boxed{\lim_{\rho_i \to 0+} G_i(s)\, K^i_{LQG/LTR}(s) = G^i_{KF}(s)} \tag{4.36}$$

from which it follows that

$$\lim_{\rho_i \to 0+} K^i_{LQG/LTR}(s) = G_i^{-1}(s)\, G^i_{KF}(s). \tag{4.37}$$

It is because of eq. (4.36) that ρ_i is referred to as a "recovery parameter". It can be shown that the convergence in eqs. (4.36) - (4.37) is pointwise in s.

A summary of the recovery procedure is now given.

Summary of Procedure for Recovering Target Loop

1. Given the minimum phase design plant, $G(s) = C(sI - A)^{-1}B$, and the target loop tfm $G_{KF}(s) = C(sI - A)^{-1}H_\mu$ choose a "small" positive ρ.

2. Solve the following CARE for K_ρ:

$$0 = - K_\rho A - A^T K_\rho - C^T C + K_\rho B(1 / \rho)B^T K_\rho$$

3. The compensator which recovers $G_{KF}(s)$ from $G(s)$ is then given by:

$$K_{LQG/LTR}(s) = G_\rho(sI - A + BG_\rho + H_\mu C)^{-1}H_\mu$$

where $G_\rho = (1 / \rho)B^T K_\rho$.

4. A rule of thumb for deciding whether the recovery is good, is having

$$\sigma_i[G(j\omega)K_{LQG/LTR}(j\omega)] \approx \sigma_i[G_{KF}(j\omega)] \quad \text{for all} \quad \omega \leq 10\ \omega_i$$

where $\sigma_i\ [G(j\omega_i)K_{LQG/LTR}(j\omega_i)] = 0$ db.

Because the gains $H_{\mu i}$ and $G_{\rho i}$ are computed using results from classical LQG (Linear Quadratic Gaussian) theory and since the properties of the loop tfm are approaching those of $G^i_{KF}(s)$ we call the procedure the LQG/LTR (Linear Quadratic Gaussian with Loop Transfer Recovery) design methodology. Actually, since we are recovering the properties of $G^i_{KF}(s)$ at the plant output, the procedure is called LQG/LTR at the plant output. A more detailed discussion of the LQG/LTR design methodology can be found in references [5] - [8]. The procedure is now applied to the AVM, SM, and ASM Design Plants, $G_i(s) \equiv G_{pi}(s) / s = C_i\ (sI - A_i)^{-1}\ B_i$ i = 1, 2, 3.

4.3 Design and Evaluation of AVM AFCS

4.3.1 Introduction

In this section the LQG/LTR design methodology is applied to the AVM Design Plant, $G_1(s) \equiv G_{p1}(s) / s = C_1 (sI - A_1)^{-1} B_1$. A compensator satisfying the performance and robustness specifications presented in section 3.6 is obtained. The AVM Design Plant consists of the AVM Plant, $G_{p1}(s) = C_{p1}(sI - A_{p1})^{-1} B_{p1}$, preceded by an integral augmentation. We recall that the AVM Plant has input $\Sigma\Theta_c$ (average collective control) and output $\Sigma\dot{z}$ (average vertical velocity). $\Sigma\Theta_c$ is assumed to be measured in degrees (degs.) and $\Sigma\dot{z}$ in feet / second (ft./sec.).

In developing the target AVM loop, $G_{KF}(s) = C_1(sI - A_1)^{-1} H_{\mu i}$, the design parameters, L_1 and μ_1, were chosen to be

$$L_1 = B_1 \ [C_{p1} (-A_{p1})^{-1} B_{p1}]^{-1} \tag{4.38}$$

$$\mu_1 = 1 \qquad \text{(AVM AFCS bandwidth parameter).} \tag{4.39}$$

The AVM loop recovery parameter, ρ_1, was chosen to be

$$\rho_1 = 10^{-6} \quad \text{(AVM AFCS recovery parameter).} \tag{4.40}$$

Given the above parameters, the filter and control gain matrices, $H_{\mu 1}$ and $G_{\rho 1}$, can be computed using the LQG/LTR procedure described in section 4.2. These matrices completely specify the AVM compensator, $K_1(s)$, given by:

$$K_1(s) \equiv K^1_{LQG/LTR}(s) / s \tag{4.41a}$$

$$= G_{\rho 1}(sI - A_1 + B_1 G_{\rho 1} + H_{\mu 1} C_1)^{-1} H_{\mu 1} / s. \tag{4.41b}$$

Since $K_1(s)$ specifies the entire AVM AFCS, eq. (4.42) tells us that $H_{\mu 1}$ and $G_{\rho 1}$ completely specify the AVM AFCS. These matrices are given below:

$$H_{\mu 1} = [\ 0.4921 \quad 0.582\ ]^T \tag{4.42a}$$

$$G_{\rho 1} = [\ 994.75 \quad 90.3\ ] \tag{4.42b}$$

4.3.2 Frequency Domain Evaluation of AVM AFCS

Fig. 4.3.2.1 shows the Bode magnitude and phase plots for the target and recovered AVM open loop transfer functions, $G^1_{KF}(j\omega)$ and $G_{L1}(j\omega)$. The plots show that the recovered AVM loop magnitude approximates the target magnitude almost up to approximately $\omega \approx 40$ rad/sec which is almost two decades above the gain crossover frequency $\omega_{g1} = 0.6$ rad/sec. The recovered phase margin, measured at ω_{g1}, is seen to be greater than 70 degrees. This easily satisfies our phase margin spaceification ($|PM_1| \geq 45°$). The recovered downward gain margin is seen to be infinite. This, of course, is due to the fact that the AVM AFCS is open loop stable. The recovered upward gain margin, measured at the phase crossover frequency $\omega \approx 81$ rad/sec, is seen to be greater than

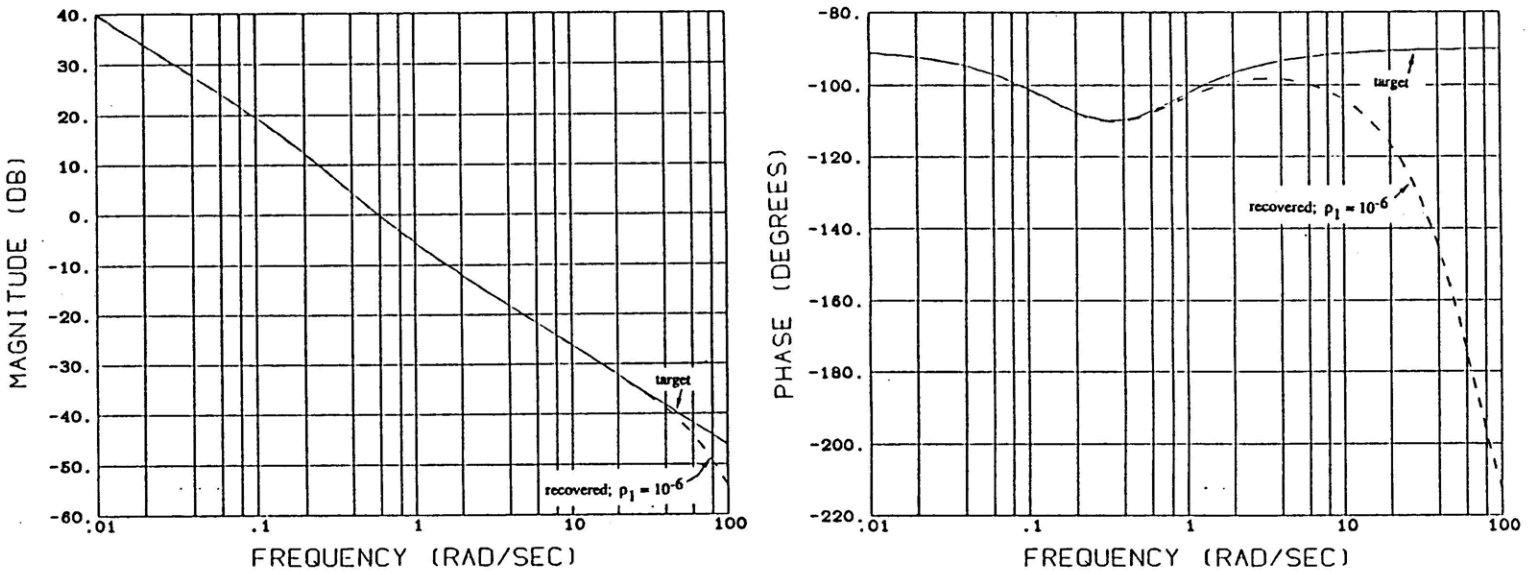

Fig. 4.3.2.1 Recovery of Target AVM Open Loop Transfer Function.

40 db. Our upward gain margin specification is thus easily satisfied ($\uparrow GM_1 \geq 12.5$ db). It should be noted that recovery can be improved by decreasing the recovery parameter, ρ_1. By doing so the phase crossover frequency moves toward infinity and so does the upward gain margin. Decreasing ρ_1 can thus considerably improve our upward gain margin. In doing so, however, the phase margin

remains relatively unchanged since, for all practical purposes, we have already recovered our target phase margin. It should also be noted that for frequencies below $\omega = 0.01$ rad/sec the recovered loop looks like an integrator.

To evaluate the performance properties of the recovered AVM AFCS, we need to quantify its ability to follow low frequency commands for $\Sigma\dot{z}$ and reject low frequency disturbances on $\Sigma\dot{z}$. This is best done by evaluating the Bode magnitude plot of the recovered AVM sensitivity function. The Bode magnitude plots of the target and recovered AVM sensitivity functions, $S^1_{KF}(j\omega)$ and $S_1(j\omega)$, are given in Fig. 4.3.2.2.

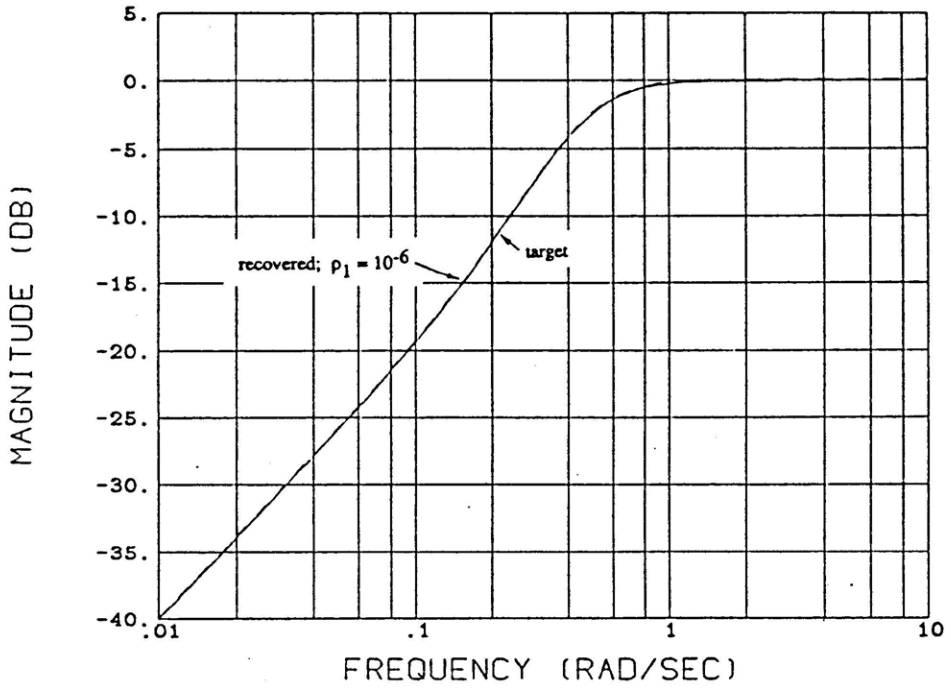

Fig. 4.3.2.2 Recovery of Target AVM Sensitivity Transfer Function.

The figure indicates that for all practical purposes the target sensitivity has been completely recovered. Since $|S_1(j\omega)| < -20$ db for all $\omega \leq 0.09$ rad/sec, we are guaranteed that steady state errors due to reference commands or output disturbances, with spectral content at or below $\omega = 0.09$ rad/sec, will be less than 10%. This satisfies our low frequency performance specification. In addition to this, the low frequency slope of + 20 db/dec will guarantee zero steady state error to step commands and step output disturbances in $\Sigma\dot{z}$.

To evaluate the stability robustness of the AVM AFCS to high frequency unmodeled rotor dynamics, as well as its ability to attenuate high frequency noise in our $\Sigma\dot{z}$ measurement, we examine the recovered AVM closed loop transfer function, $T_1(j\omega)$. Its Bode magnitude plot, as well as that of the target AVM closed loop transfer function, $T^1_{KF}(j\omega)$, are given in Fig. 4.3.2.3.

The figure shows that the recovered AVM closed loop magnitude approximates the target AVM closed loop magnitude up to $\omega = 40$ rad/sec. The recovered AVM closed loop bandwidth is seen to be approximately $\omega_{CL1} = 0.4$ rad/sec and the peak value of $|T_1(j\omega)|$ is seen to be well below 2 db for all frequencies. It is also seen that $|T_1(j\omega)| < -20$db for all $\omega \geq 5$ rad/sec. This satisfies

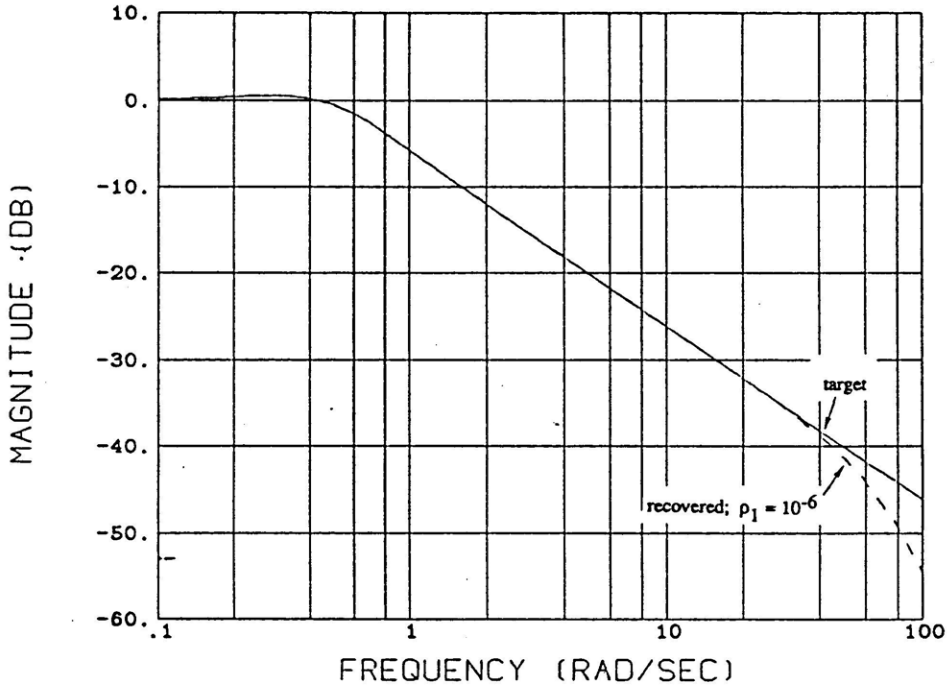

Fig. 4.3.2.3: Recovery of Target AVM Closed Loop Transfer Function

our high frequency noise attenuation specification. Also, for the selected value of ρ_1, the recovered AVM closed loop magnitude rolls off at -20 db/dec between $\omega = 1$ rad/sec and $\omega = 40$ rad/sec. Above $\omega = 40$ rad/sec, the recovered AVM closed loop magnitude rolls off at -60 db/dec (one pole roll-off due to $G_{p1}(s)$ and two pole roll-off due to $K_1(s)$). The high frequency break at $\omega = 40$ rad/sec is due to two "far away" poles of the recovered AVM LQG/LTR compensator. These

poles shall be discussed subsequently. It should be noted that in order to achieve a faster roll-off near the first harmonic (ω_r) of the main rotor, we need the "far away" compensator poles to break earlier, say 1 octave below $\omega_r = 27$ rad/sec. This can be done by selecting a larger value of ρ_1. In doing so, however, we must sacrifice our upward gain margin as well as our phase margin (unless, of course, the gain crossover frequency is reduced). This tradeoff is easily explained as follows. As ρ_1 is increased the "far away" poles of the AVM compensator move closer to the origin of the s-plane. As a result of this, the phase crossover frequency decrease and so does the resulting upward gain margin. Furthermore, because of the larger phase lag contribution at gain crossover due to the AVM compensator's "far away" poles, the resulting phase margin is also reduced. These trade-offs may or may not be tolerable depending on the extent of modeling errors near gain and phase crossover. This trade-off is fundamental to all control systems; i.e. we cannot have an arbitrary large roll-off near gain crossover and still maintain "nice" phase and gain margins.

To understand the AVM compensator "strategy", we evaluate the Bode magnitude and phase plots of the recovered AVM LQG/LTR compensator transfer function . The Bode magnitude and phase plots for the target and recovered AVM LQG/LTR compensators, $G_1^{-1}(j\omega)\, G^1_{KF}(j\omega)$ and $K^1_{LQG/LTR}(j\omega)$, are given in Fig. 4.3.2.4.

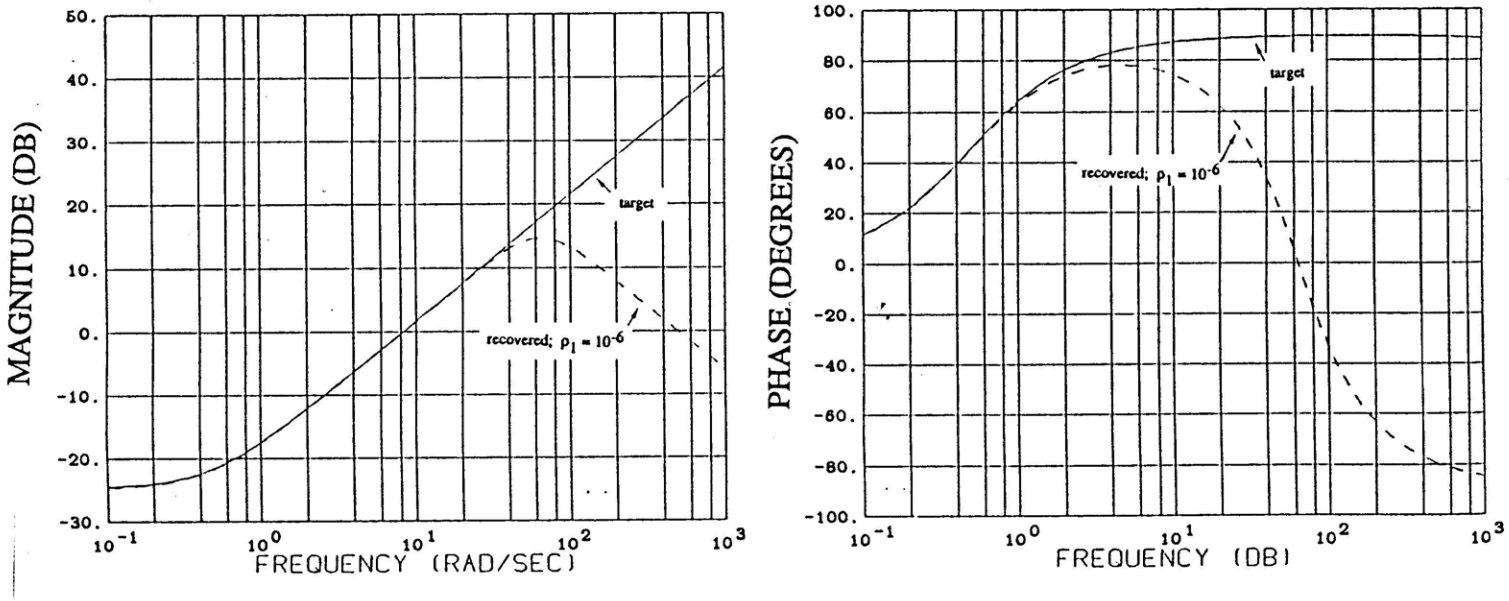

Fig. 4.3.2.4: Recovery of Target AVM LQG/LTR Compensator Transfer Function.

The plots show that the recovered AVM LQG/LTR compensator approximates the target AVM compensator up to $\omega \approx 40$rad/sec in magnitude and $\omega \approx 2$ rad/sec in phase. The recovered AVM LQG/LTR compensator is seen to exhibit a low frequency gain of - 25 db. The reason for this low frequency gain is simply because the recovered AVM LQG/LTR compensator is trying to invert the AVM Plant, $G_{p1}(s)$, which has a dc gain of 24.7 db, in order to make the recovered AVM loop look like an integrator at low frequencies. Near $\omega = 0.5$ rad/sec the recoverd AVM LQG/LTR compensator exhibits an upward break in magnitude corresponding to a phase lead. It is this phase lead, due to a compensator zero, that allows us to meet our nice phase and upward gain margin specification. The plots indicate that the target compensator has the form $\beta_1(1 + a / s)$ (at low frequencies) where $a = 0.5$ and $\beta_1 = (2 / 17.2)$. The target AVM AFCS thus implements a simple PI (proportional plus integral) type control strategy. This implies that velocity ($\Sigma\dot{z}$) and position (Σz) error information are being used to generate the average collective control signal, $\Sigma\Theta_c$.

Fig. 4.3.2.5 shows the Bode magnitude plot of the target and recovered tf's from the reference command, r_1, to the control, $\Sigma\Theta_c$. The figure shows that the most control activity will result when references, noise, or output disturbances with appreciable spectral content near our gain crossover frequency, $\omega_g \approx 0.6$ rad/sec, are present. It also shows that as $\rho \rightarrow 0$ the high

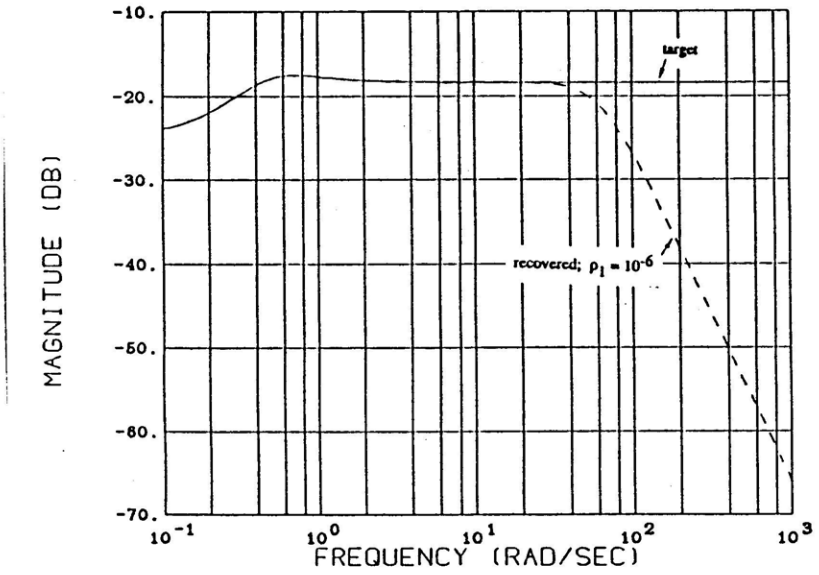

Fig. 4.3.2.5: Recovery of Target AVM Reference to Control Transfer Function.

frequency gain approaches a constant (~18 db). This implies that for ρ_1 sufficiently small, step commands for $\Sigma\dot{z}$ will result in step-like control action, $\Sigma\Theta_c$. This follows from the Initial Value Theorem from the theory of Laplace Transforms [14]. It will be demonstrated when simulations are presented. We note that since the reference to control tf is always "small", pre-filtering of $\Sigma\dot{z}$ commands is not necessary. It is always "small" because the lead requirement is small.

4.3.3 AVM AFCS Poles and Zeros

To further understand the strategy of the recoverd AVM LQG/LTR compensator and its asymptotic properties, it is instructive to compare the target AVM open loop poles and zeros with the recovered AVM open loop poles and zeros. The target AVM open loop poles and zeros are given in Table 4.3.3.1. These are the poles and zeros associated with the target AVM open loop transfer function, $G^1_{KF}(s) = C_1 (sI - A_1)^{-1} H_{\mu 1}$. The recovered AVM open loop poles and zeros are given in Table 4.3.3.2. These are the poles and zeros associated with the recoverd AVM loop transfer function, $G_{p1}(s)K_1(s)$.

Table 4.3.3.1: Target AVM Open Loop Poles and Zeros

Poles: $s = 0$
$s = - 0.2384$; $\tau = 4.2$ sec

Zero: $s = - 0.4845$

Table 4.3.3.2: Recovered AVM Open Loop Poles and Zeros

AVM Plant:
Poles: $s = -0.2384$; $\tau = 4.2$ sec

Zeros: None

AVM Compensator:

Poles: Integrator: $s = 0$
Far away poles: $s = - 45.515 \pm j\,45.515$; $\zeta = 0.707$; $\tau = 0.02$ sec; $\omega_n = 64$ rad/sec.

Zeros: $s = - 0.4818$; $\tau = 2.1$ sec.

Tables 4.3.3.1 and 4.3.3.2 show that the recovered AVM loop poles and zeros are nearly identical to those of the target AVM loop poles and zeros. One small difference is that the recovered AVM compensator zero is slightly to the right of the target AVM loop zero. It can be shown that the recovered zeros of the tf $G_{\rho 1}(sI - A_1)^{-1}H_{\mu 1}$. The major difference between the recovered and target AVM loop poles and zeros is the presence of "far away" poles in the recoverd AVM loop. As alluded to earlier, these poles can be made larger by recovering more of the target AVM loop; i.e. by choosing a smaller value of ρ_1.

Before driving the recovered AVM AFCS with a typical step commands for $\Sigma\dot{z}$, it is instructive to compare the target AVM closed loop poles and zeros with the recovered AVM closed loop poles and zeros. The target AVM closed loop poles and zeros are given in Table 4.3.3.3. These are the poles and zeros associated with the target AVM closed loop transfer function, $T^1_{KF}(s) = G^1_{KF}(s)[I + G^1_{KF}(s)]^{-1} = C_1(sI - A_1 + H_{\mu 1} C_1)^{-1} H_{\mu 1}$. The recovered AVM closed loop poles and zeros are given in Table 4.3.3.4. These are the poles and zeros associated with the recovered AVM closed loop transfer function, $T_1(s) = G_{p1}(s)K_1(s)\ [I + G_{p1}(s)K_1(s)]^{-1} = G_{p1}(s)\ [I + G_{\rho 1}\Phi_1(s)B_1]^{-1}\ G_{\rho 1}\Phi_1(s)H_{\mu 1}[I + C_1\Phi_1(s)\ H_{\mu 1}]^{-1}$ where $\Phi_1(s) \equiv (sI - A_1)^{-1}$ (Athans [7]).

Table 4.3.3.3: Target AVM Closed Loop Poles and Zeros

Poles: $s = \lambda_i(A_i - H_{\mu 1}C_1) = -0.3653 \pm j\,0.3240$; $\zeta = 0.75$; $\tau = 2.7$ sec; $\omega_n = 0.49$ rad/sec.

Zero: $s = -0.4845$.

Table 4.3.3.4 Recovered AVM Closed Loop Poles and Zeros

Poles: $s = \lambda_i(A_1 - H_{\mu 1}C_1) = -0.36525 \pm j\,0.32402$; $\zeta = 0.75$; $\tau = 2.7$ sec; $\omega_n = 0.49$ rad/sec.

$s = \lambda_i(A_1 - B_1G_{\rho 1}) = -45.269 \pm j\,45.268$; $\zeta = 0.707$; $\tau = 0.02$ sec; $\omega_n = 64$ rad/sec.

Zero: $s = -0.4818$

Tables 4.3.3.3 and 4.3.3.4 show that the recovered AVM closed loop poles and zeros are nearly identical to those of the target AVM closed loop poles and zeros. The major difference is due to the presence of "far away" closed loop poles in the recovered AVM closed loop system. It should be clear from Table 4.3.3.4 that the dominant closed loop poles are those due to $A_1 - H_{\mu 1} C_1$ ($\zeta = 0.75$, $\tau = 2.7$ sec, $\omega_n = 0.49$ rad/sec).. These closed loop poles are thus attributable to the AVM filter (target loop), $G^1_{KF}(s)$. The far away poles are due to $A_1 - B_1 G_{\rho 1}$. These closed loop poles are attributable to the so-called AVM LQ-Loop, $G_{LQ}(s) \equiv G_{\rho 1}(sI - A_1)^{-1} B_1$ [7].

4.3.4 Time Domain Evaluation of AVM AFCS

Finally, it is necessary to test the recovered AVM AFCS's command following properties for a typical $\Sigma\dot{z}$ reference command. Fig. 4.3.4.1(a) shows the $\Sigma\dot{z}$ response to an AVM step reference command, $r_1 = 5$ ft / sec (no pre-filter). Fig. 4.3.4.1(b) shows the corresponding $\Sigma\Theta_c$ response to the reference command.

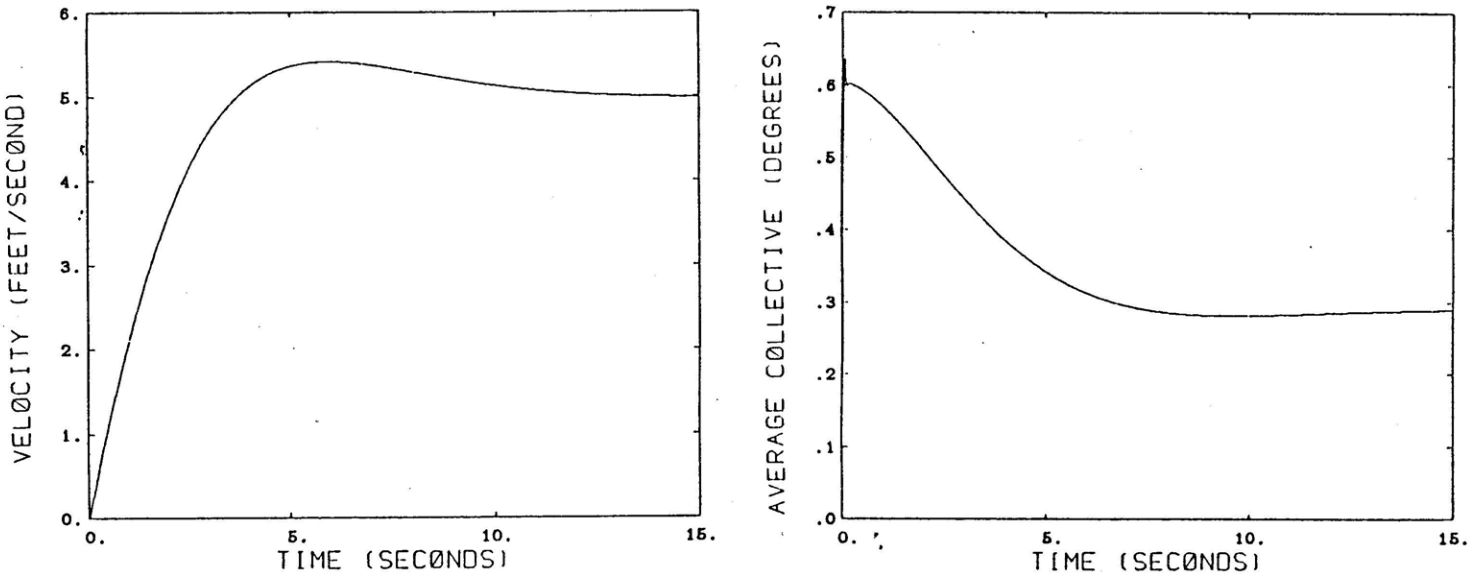

(a) Average Vertical Velocity (b) Average Collective Control

Fig. 4.3.4.1: AVM AFCS Response to a $\Sigma\dot{z} = 5$ ft / sec Step Command.

The $\Sigma\dot{z}$ response in Fig. 4.3.4.1(a) is quite acceptable. The settling time is approximately 11 seconds and the overshoot is less than 10% .

The $\Sigma\Theta_c$ response in Fig. 4.3.4.1(b) is extraordinarily fast at the beginning. This is due to the "high-pass" characteristic of the AVM reference to control magnitude plot in Fig. 4.3.2.5. This high-pass characteristic is attributable to two zeros which are present in the AVM reference to control transfer function. One zero is due to the AVM compensator zero. The other zero is due to the AVM Plant pole. Although the initial $\Sigma\Theta_c$ rate may be large, the peak value is well within the usually permitted control authority. Finally, it should be noted that the steady state collective is in agreement with the AVM plant dc gain which dictates an average vertical velocity of 17.2 ft/sec per degree of average collective control or equivalently, 0.2907 degrees of average collective control per 5 ft/sec of average vertical velocity.

4.3.5 Summary of AVM AFCS Design

In this section the LQG/LTR design methodology was applied to the AVM Design Plant; a simple SISO system consisting of an integrator and a stable real pole. It was shown, as expected, that controlling the AVM Plant presents relatively little difficulty; even when the specifications call for a high performance (high bandwidth) design. In conclusion, the LQG/LTR-based AVM AFCS obtained in this section satisfies all of the AVM design specifications presented in section 3.6.2. Furthermore, for a typical $\Sigma\dot{z}$ reference command, the AVM AFCS response is quite good. The AVM AFCS design is thus acceptable.

4.4 Design and Evaluation of SM AFCS

4.4.1 Introduction

In this section the LQG/LTR design methodology is applied to the SM Design Plant, $G_2(s) = G_{p2}(s) / s = C_2(sI - A_2)^{-1}B_2$. A high performance (high bandwidth) compensator satisfying the specifications presented in section 3.6 is obtained. The SM Design Plant consist of the SM Plant,

$G_{p2}(s) = C_{p2}(sI - A_{p2})^{-1}B_{p2}$, preceded by an integral augmentation. We recall that the SM Plant has input ΔB_{1c} (differential cyclic control) and output Δx (horizontal separation). ΔB_{1c} is assumed to be measured in degrees and Δx in feet. Scaling is not an issue since the SM is represented by a SISO system.

In developing the target SM loop, $G^2_{KF}(s) = C_2(sI - A_2)^{-1}H_{\mu 2}$, the design parameters, L_2 and μ_2, were chosen as follows:

$$L_2 = B_2 \, [C_{p2} \, (-A_{p2})^{-1} \, B_{p2}]^{-1} \tag{4.43}$$

$$\mu_2 = 1 \qquad \text{(SM AFCS bandwidth parameter).} \tag{4.44}$$

The SM loop recovery, ρ_2, was initially chosen to be $\rho_2 = 10^{-12}$. For reasons to be explained subsequently the recovery parameter was increased to

$$\rho_2 = 10^{-6} \quad \text{(SM AFCS recovery parameter).} \tag{4.45}$$

Given the above parameters, the filter and control gain matrices, $H_{\mu 2}$ and $G_{\rho 2}$, can be computed using the LQG/LTR procedure described in section 4.2. These matrices completely specify the SM compensator, $K_2(s)$, given by:

$$K_2(s) \equiv K^2_{LQG/LTR}(s) \, / \, s \tag{4.46a}$$

$$= G_{\rho 2}(sI - A_2 + B_2 \, G_{\rho 2} + H_{\mu 2} \, C_2)^{-1} \, H_{\mu 2} \, / \, s. \tag{4.46b}$$

Since $K_2(s)$ specifies the entire SM AFCS, eq. (4.46) tells us that $H_{\mu 2}$ and $G_{\rho 2}$ completely specify the SM AFCS. These matrices are given below:

$$H_{\mu 2} = [\ 2.2063 \quad -4.9246 \quad 2.4339 \quad -4.5238 \quad 0.21943\ ]^T \tag{4.47}$$

$$G_{\rho 2} = [\ 955.46 \quad -36.449 \quad 282.73 \quad -2.6377 \quad 22.795\ ] \tag{4.48}$$

4.4.2 Frequency Domain Evaluation of SM AFCS

Fig. 4.4.1 shows the Bode magnitude and phase plots for the target SM open loop transfer function, $G^2_{KF}(j\omega)$. The Bode magnitude and phase plots for the recovered SM open loop transfer function, $G_{L2}(j\omega)$, are also shown in the figure for $\rho_2 = 10^{-12}$ and $\rho_2 = 10^{-6}$.

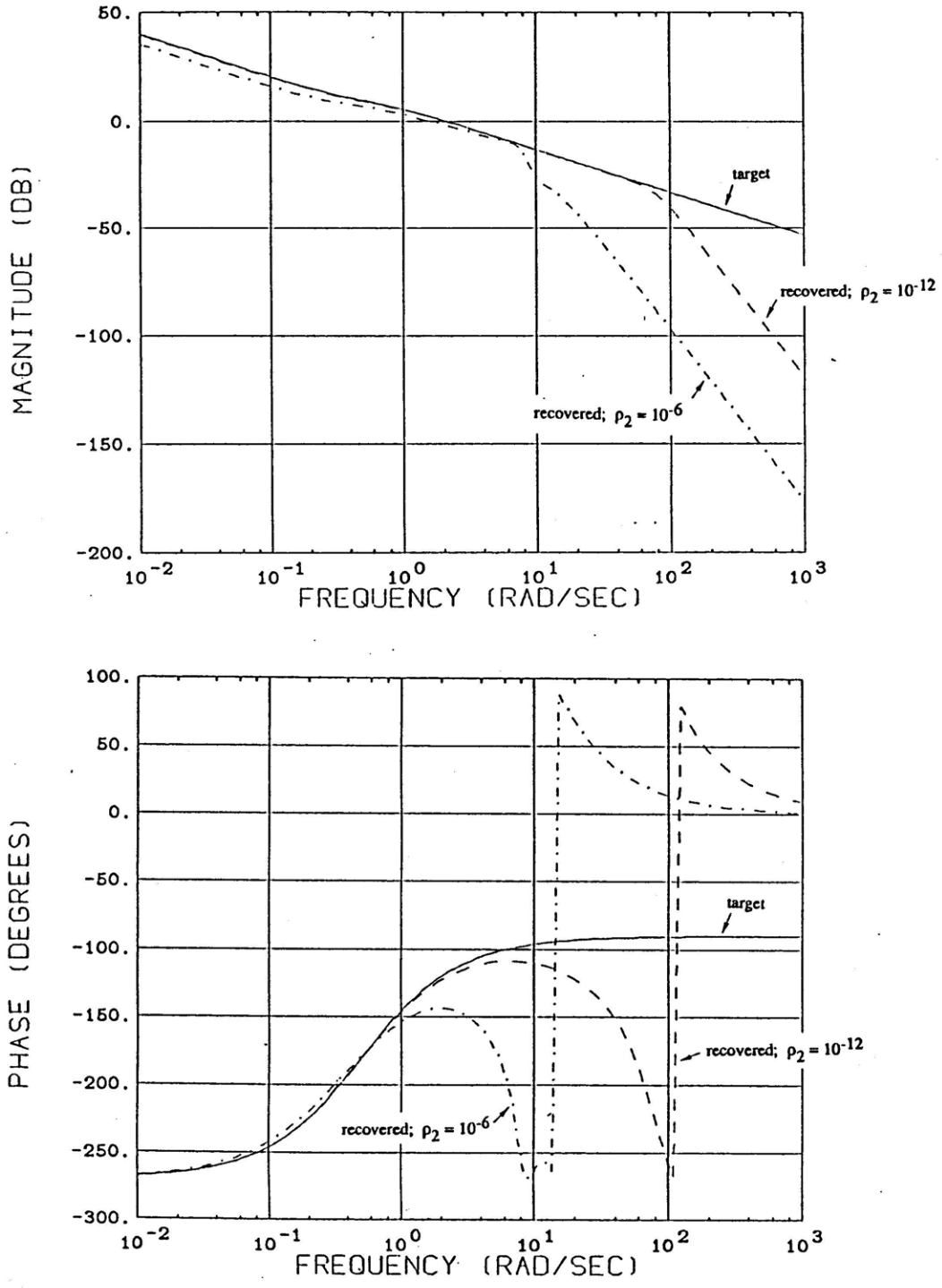

Fig. 4.4.2.1: Recovery of SM Target Open Loop Transfer Function.

rad/sec and the associated phase margin is $PM_2 \approx 55°$. Both of these exceed our gain crossover and phase margin specifications. The phase phase crossover frequencies are $\omega_{p21} \approx 0.55$ rad/sec and $\omega_{p22} \approx 60$ rad/sec. Corresponding to these phase crossovers we have a downward gain margin of $\downarrow GM_2 \approx -10$ db and an upward gain margin of $\uparrow GM_2 \approx 30$ db. Both meet our gain margin specifications. All of these properties are very good but for reasons to be explained later in the section we had to reduce the amount recovered. We thus increased our recovery parameter to $\rho_2 = 10^{-6}$.

For $\rho_2 = 10^{-6}$ the recovered SM loop magnitude is seen to approximate the target SM loop magnitude, within 6 db, up to $\omega \approx 8$ rad/sec. The corresponding SM loop phase is seen to approximate the target SM loop phase, within 5°, up to $\omega \approx 1$ rad/sec. The recovered gain crossover frequency and phase marin are now $\omega_{g2} \approx 1.4$ rad/sec and $PM_2 \approx 34°$, respectively. Both of these just satisfy our specifications. The phase crossover frequencies are $\omega_{p21} \approx 0.5$ rad/sec and $\omega_{p22} \approx 5$ rad/sec. Corresponding to these phase crossover frequencies we have a downward gain margin of $\downarrow GM \approx -7$ db and an upward gain margin of $\uparrow GM \approx 10$ db. Both of these also satisfy our gain margin specifications.

To evaluate the performance properties of the recovered SM AFCS, we need to quantify its ability to follow low frequency commands for Δx and reject low frequency disturbances on Δx. This is best done by evaluating the Bode magnitude plot of the recovered SM sensitivity function. The Bode magnitude plots of the target and recovered SM sensitivity transfer functions, $S^2_{KF}(j\omega)$ and $S_2(j\omega)$, are given in Fig. 4.4.2.2.

The figure shows that for $\rho_2 = 10^{-12}$ the target SM sensitivity is for all purposes completely recovered. For $\rho_2 = 10^{-6}$, however, the recovered SM sensitivity approximates the target SM sensitivity, within 5 db, for all frequencies. The plot shows that the AFCS will especially be

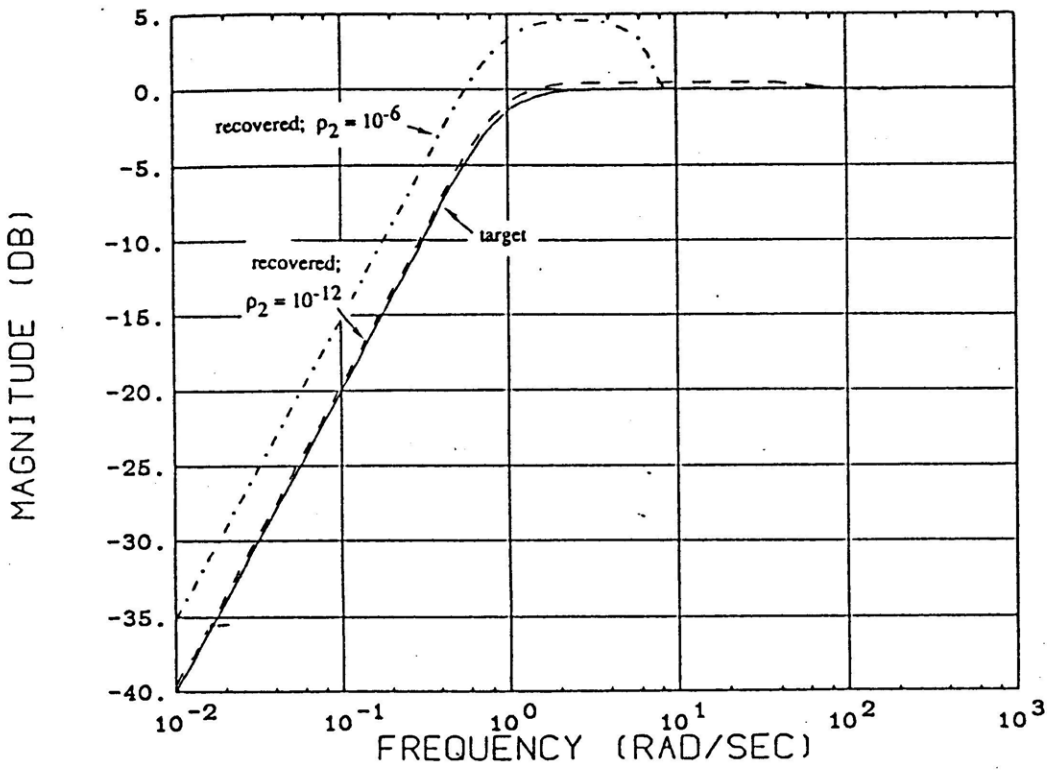

Fig. 4.4.2.2: Recovery of Target SM Sensitivity Transfer Function.

sensitive to references and output disturbances with spectral content between $\omega = 0.7$ rad/sec and $\omega = 7$ rad/sec. The low frequency slope of 20 db/dec, however, guarantees zero steady state error to step to step commands and output step disturbances in Δx. Furthermore, since $|S_2(j\omega)| \leq -20$ db for all $\omega \leq 0.04$ rad/sec we are guaranteed that steady state errors due to references or output disturbances, with spectral content at or below $\omega = 0.04$ rad/sec, will be less than 10%. Our performance specifications are thus met.

To evaluate the ability of the SM AFCS to attenuate high frequency noise in our Δx measurement, we examine the recovered SM closed loop tf $T_2(j\omega)$. Its Bode magnitude plot, as well as that of the target SM closed loop transfer function, $T^2_{KF}(j\omega)$, are given in Fig. 4.4.2.3.

The figure shows that for $\rho_2 = 10^{-12}$ the target SM closed loop magnitude is recovered up to $\omega \approx 60$ rad/sec. For $\rho_2 = 10^{-6}$, however, the recovered SM closed loop magnitude approximates the target SM closed loop magnitude, within 3 db, up to $\omega \approx 8$ rad/sec. The plot shows that the

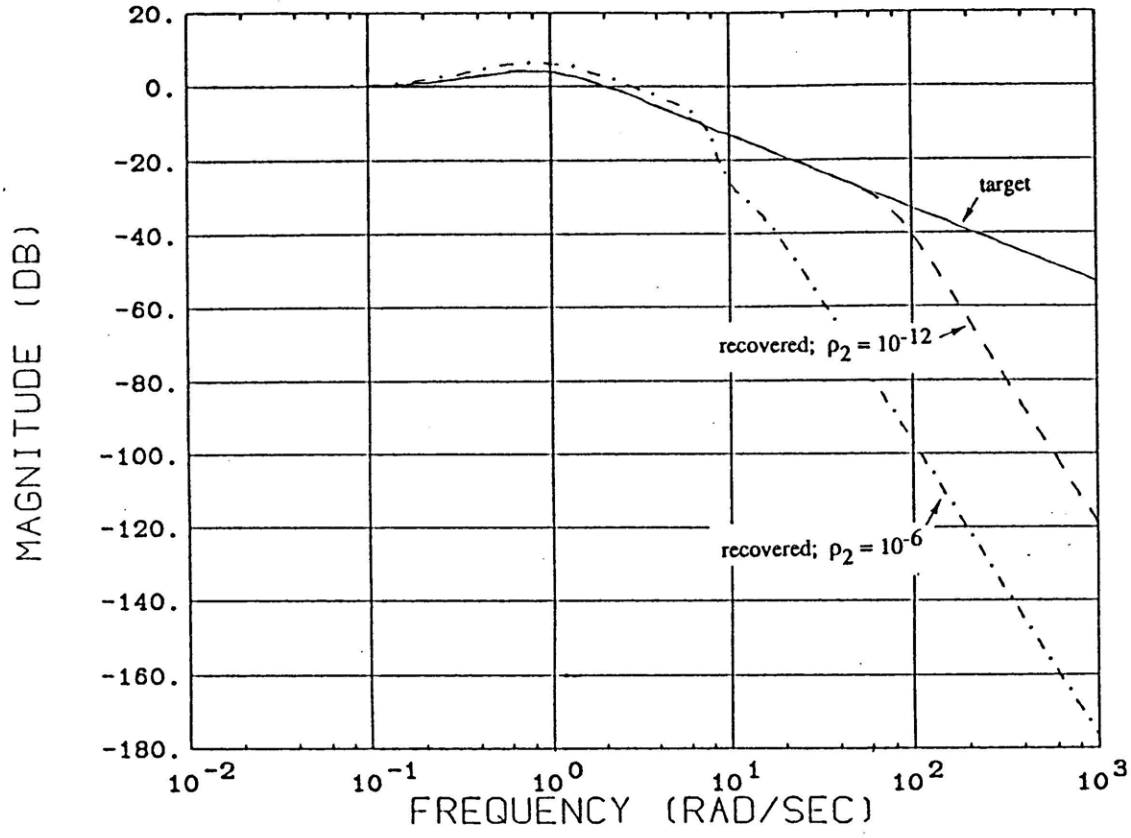

Fig. 4.4.2.3: Recovery of Target SM Closed Loop Transfer Function.

AFCS will especially be sensitive to modeling errors and sensor noise near $\omega \approx 1$ rad/sec since at this frequency we have a closed loop gain of about 6 db. The recovered SM closed loop crossover (bandwidth) is seen to be approximately $\omega_{CL2} \approx 2.5$ rad/sec. It is also seen that $|T_2(j\omega)| \leq -20$ db for all $\omega \geq 10$ rad/sec. This satisfies our high frequency noise attenuation specification. The figure also shows that for $\rho_2 = 10^{-6}$, the recovered SM closed loop magnitude rolls off at - 20 db/dec between $\omega \approx 2$ rad/sec $\omega \approx 8$ rad/sec. Above $\omega \approx 8$ rad/sec, the recovered SM closed loop magnitude rolls off at -80 db/dec (2 pole roll-off due to $G_{p2}(s)$ and 2 pole roll-off due to $K_2(s)$). The 3 pole break above $\omega \approx 10$ rad/sec is due to three "far away" poles of the recovered SM LQG/LTR compensator. These poles shall be discussed subsequently.

To understand the SM compensator "strategy", we evaluate the Bode magnitude plot for the recovered SM LQG/LTR compensator. The Bode magnitude plot of the recovered SM LQG/LTR compensator, $K^2_{LQG/LTR}(j\omega)$, is given in Fig. 4.4.2.4 for $\rho_2 = 10^{-6}$, 10^{-12}, and 10^{-15}.

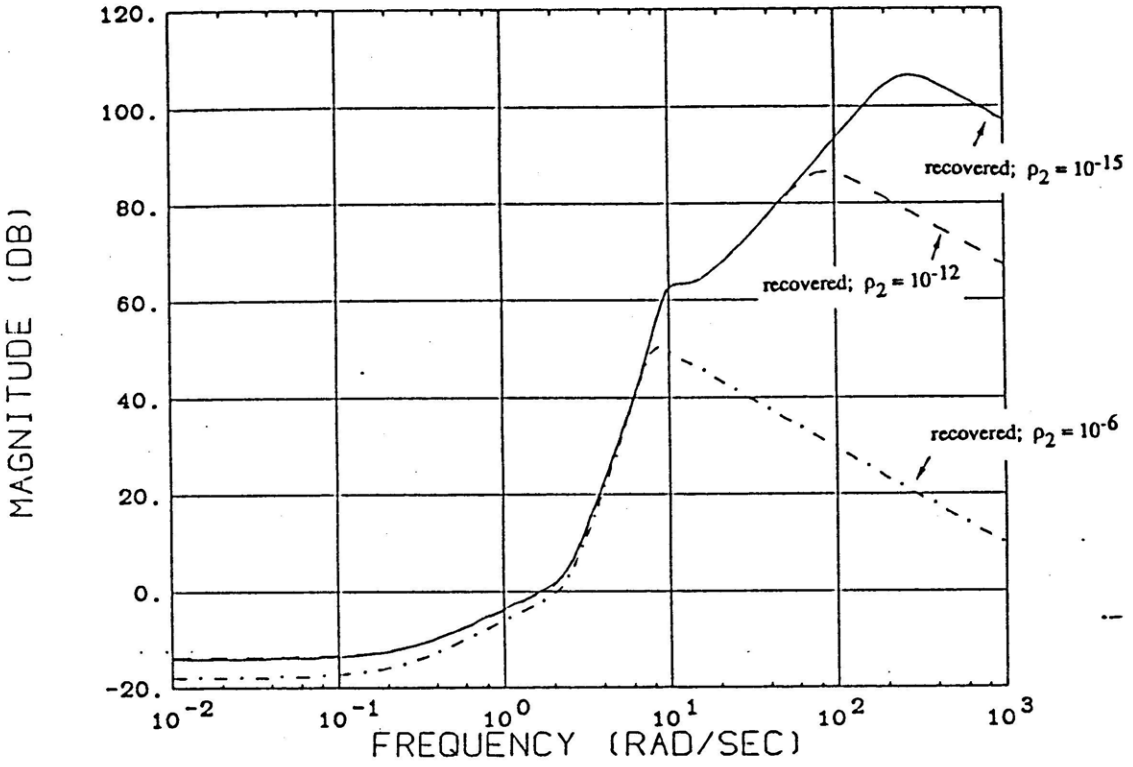

Fig. 4.4.2.4: Recovery of Target SM LQG/LTR Compensator Transfer Function.

The figure shows that for $\rho_2 = 10^{-6}$, the recovered SM LQG/LTR compensator magnitude approximates the target SM LQG/LTR compensator magnitude up to $\omega \approx 8$ rad/sec. The recovered SM LQG/LTR compensator is seen to exhibit a low frequency gain of about -16 db. The reason for this low frequency gain is simply because the recovered SM LQG/LTR compensator is trying to invert the SM Plant, $G_{p2}(s)$, (which has a dc gain of 13.18 db) in order to make the recovered SM loop look like an integrator at low frequencies. Near $\omega = 0.25$ rad/sec the recovered SM LQG/LTR compensator magnitude exhibits a +20 db/dec upward break. This slope is sustained until $\omega = 2.3$ rad/sec by a compensator zero. At $\omega = 2.3$ rad/sec a +60 db/dec upward break occurs thus giving us a +80 db/dec slope which is sustained by four compensator zeros. It is important to emphasize that all four zeros are absolutely necessary to have "nice" stability margins for the selected gain crossover frequency. One zero stabilizes the SM Design Plant, $G_2(s) \equiv G_{p2}(s) / s$, and the other three compensator zeros provide derivative action to decrease the phase lag associated with the Horizontal Spring and Symmetric Damping Modes at the SM loop gain crossover frequency ($\omega_{g2} \approx$

1.5 rad/sec). The plot shows that the 80 db/dec slope provided by these zeros is sustained until about $\omega \approx 10$ rad/sec. Above this frequency the recovered SM LQG/LTR compensator exhibits a five pole downward break which gives us a final slope of - 20 db/dec. Finally, the figure shows that as $\rho_2 \rightarrow 0$ the compensator becomes more and more improper with a limiting slope of 40 db/dec. In addition, the amount by which errors with spectral content above the closed loop bandwidth ($\omega_{CL2} \approx 2.5$ rad/sec) get amplified increases imensely as $\rho_2 \rightarrow 0$. It is because of this great amplification of high frequency errors (to generate controls) that one is forced to use $\rho_2 = 10^{-6}$ rather than $\rho_2 = 10^{-12}$. This very important trade-off between stability robustness and performance is addressed below.

Fig. 4.4.2.5 shows the Bode magnitude plots of the recovered transfer function from the reference command, r_2, to the control, ΔB_{lc}, for $\rho_2 = 10^{-6}, 10^{-12}$, and 10^{-15}. The figure shows

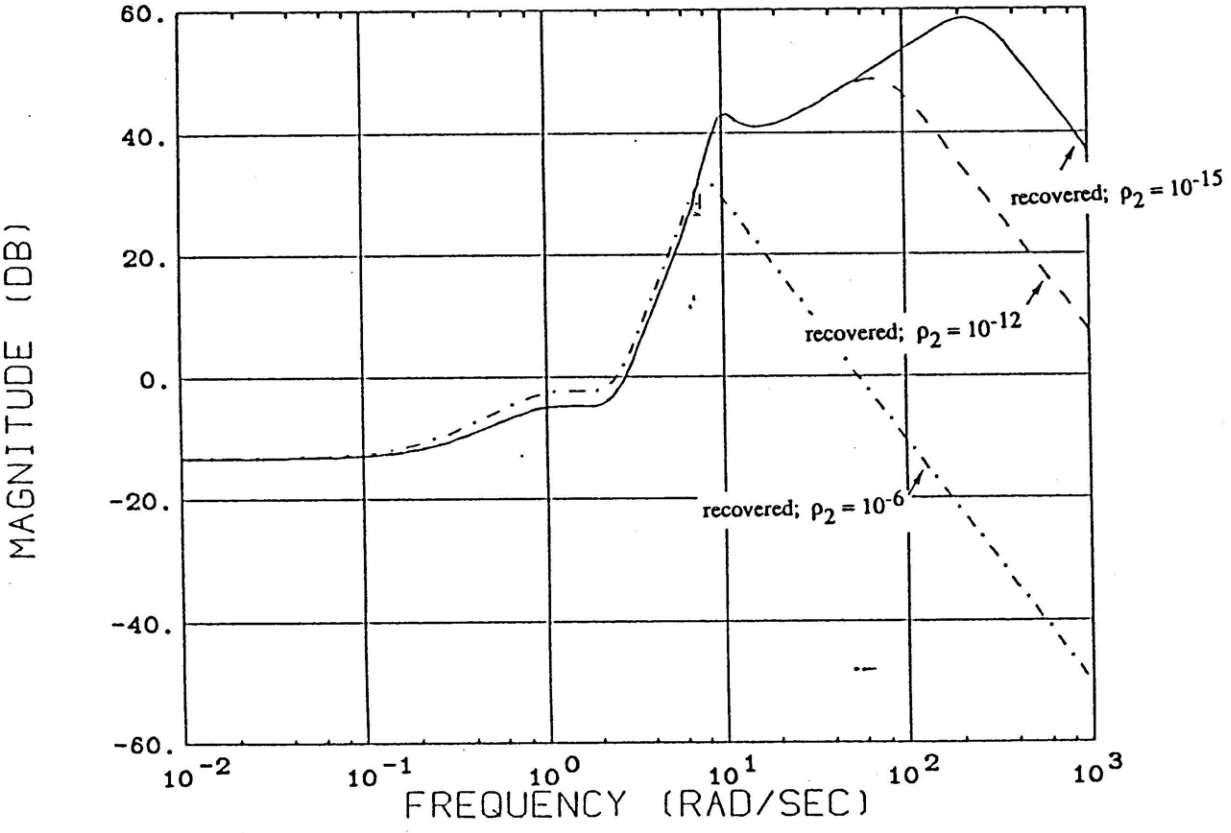

Fig. 4.4.2.5: Recovery of Target SM Reference to Control Transfer Function.

that reference commands, sensor noises, and output disturbances with spectral content above 3 rad/sec will be amlified to produce the necessary differential cyclic control action. The figure further indicates that as ρ_2 is decreased below 10^{-6}, and the recovery improves, the amount by which high-frequency exogenous signals get amplified, increases substantially. Although the horizontal separation, Δx, will usually be commanded to zero, so that SM references do not contribute much to the SM control activity, sensor noise and disturbances are always present. it thus follows that if high frequency sensor noise and disturbancesare present, as is always the case, then large differential cyclic controls may result. Large differential cyclic controls would necessarily result in large differential pitch rates. In order to avoid the large control activity and pitch rates one is forced to hold back on the recovery. Holding back on the recovery, however, means trading off stability robustness. Consequently, we conclude that a trade-off must be made between performance and stability robustness. It thus follows that because we have a high bandwidth design, this trade-off is expected to be particularly pronounced. Moreover, because of this, we expect a large robustness (lead) requirement to cause problems. More specifically, the more model uncertainty the larger the robustness (lead) requirement and the more control activity and pitching needed to regulate the horizontal separation. The extent to which this occurs shall be seen when time simulations are presented for the recovered SM AFCS ($\rho_2 = 10^{-6}$). Finally, it should be noted that as $\rho_2 \rightarrow 0$ the reference to control tf high frequency slope approaches 20 db/dec. This implies that if step-like commands are issues for Δx then the resulting control ΔB_{lc} will be impulse-like. Typically, however, Δx is commanded to zero and only disturbances affecting the horizontal separation matter.

4.4.3 SM AFCS Poles and Zeros

To further understand the strategy of the recovered SM LQG/LTR compensator ($\rho_2 = 10^{-6}$) and its asymptotic properties, it is instructive to compare the target SM loop poles and zeros with the recovered SM loop poles and zeros. The target SM loop poles and zeros are given in Table

4.4.3.1. These are the poles and zeros associated with the target SM loop tf, $G^2_{KF}(s) = C_2 (sI - A_2)^{-1} H_{\mu 2}$. The recovered SM loop poles and zeros (for $\rho_2 = 10^{-6}, 10^{-12}$) are given in Table 4.4.3.2. These are the poles and zeros associated with the recovered SM open loop transfer function, $G_{p2}(s)K_2(s)$.

Tables 4.4.3.1 and 4.4.3.2 show that for $\rho_2=10^{-6}$ the recovered SM open loop poles include the target SM open loop poles, a pair of lightly damped compensator poles, and three "far away" compensator poles. The recovered SM open loop zeros include the SM Plants' lightly damped zeros and four compensator zeros. The lightly damped compensator poles decrease the amplifying effect that the SM Plants' lightly damped zeros have on high frequency sensor noise. The four compensator zeros, as expected from the discussion in Chapter 3, provide our stability robustness properties. The three "far away" compensator poles provide roll-off in the SM loop so that the four-zero compensator lead does not result in substantial control activity (ΔB_{lc}) and pitching ($\Delta\theta$) in order to regulate the horizontal separation (Δx).

Table 4.4.3.1: Target SM Open Loop Poles and Zeros

Poles:	Zeros:
s = 0	s = - 0.34183
s = 0.7561	s = - 0.8175 ± j 2.2269
s = - 0.8122 ± j 2.2228	s = - 2.2286
s = - 2.2919	

Table 4.4.3.2: Recovered SM Open Loop Poles and Zeros

SM Plant Poles:	s = 0.7561	SM Plant Zeros:	s = - 1.55 ± j 9.4906
	s = - 0.8122 ± j 2.2228		
	s = - 2.2919		
SM Compensator Poles:	($\rho_2 = 10^{-6}$)		($\rho_2 = 10^{-12}$)
	s = 0		s = 0
	s = - 1.4266 ± j 7.6892		s = - 1.55 ± j 9.4906
"far away" poles	s = - 6.6325 ± j 7.7966		s = - 39.303 ± j 68.686
	s = - 12.043		s = - 80.738
SM Compensator Zeros:	s = - 0.2525		s = - 0.33239
	s = - 0.8160 ± j 2.2228		s = - 0.81742 ± j 2.2264
	s = - 2.2898		s = - 2.2869

Table 4.4.3.2 shows that as ρ_2 is decreased from 10^{-6} to 10^{-12}, two of the recovered lightly damped poles move on top of the SM Plants' lightly damped zeros. On the one hand, having this pole-zero cancellation is good in that it nullifies the high frequency lead effect of the zeros. On the other hand, however, having this pole-zero cancellation implies the pesence of lightly damped poles. Although these poles are unobservable and hence would not affect Δx, they would affect $\Delta\theta$ and ΔB_{lc}. This gives us one reason why we would not want to make ρ_2 any smaller than 10^{-6}, although doing so would improve our robustness. This, however, is not the main reason. The main reason for not decreasing ρ_2 below 10^{-6} (and improving our robustness) is because, as shown in the table, this moves the compensator's "far away" poles to very high frequencies. As discussed earlier, and as seen in Figs. (4.4.2.4) - (4.4.2.5), this results in an untolerable amount of error to control amplification which in turn means untolerable pitch rates. Because of this performance-robustness trade-off we fixed the value of ρ_2 at 10^{-6}.

Before studying the recovered SM AFCS's ($\rho_2 = 10^{-6}$) time response characteristics, it is instructive to compare the target SM closed loop poles and zeros with the recovered SM closed loop poles and zeros. The target SM closed loop poles and zeros are given in Table 4.4.3.3. These are the poles and zeros associated with the target SM closed loop transfer function, $T^2_{KF}(s) = G^2_{KF}(s)\,[I + G^2_{KF}(s)]^{-1} = C_2(sI - A_2 + H_{\mu 2}\,C_2)^{-1}\,H_{\mu 2}$. The recovered SM closed loop poles and zeros are given in Table 4.4.3.4 and are plotted in Fig. 4.4.3.4. These are the poles and zeros associated with the recovered SM closed loop transfer function, $T_2(s) = G_{p2}(s)K_2(s)\,[I + G_{p2}(s)K_2(s)]^{-1} = G_{p1}(s)\,[I + G_{\rho 2}\,\Phi_2(s)\,B_2]^{-1}\,G_{\rho 2}\,\Phi_2(s)\,H_{\mu 2}\,[I + C_2\,\Phi_2(s)\,H_{\mu 2}]^{-1}$ where $\Phi_2(s) \equiv (sI - A_2)^{-1}$.

In examining the closed loop poles and zeros presented in Tables 4.4.3.3 and 4.4.3.4, it is essential to identify which modes shall have the greatest impact on our output, Δx, and which modes shall have the greatest impact on "internal" quantities such as $\Delta\theta$ and ΔB_{lc}. First lets examine the target SM closed loop poles and zeros

Table 4.4.3.3: Target SM Closed Loop Poles and Zeros

Poles: $\lambda_i(A_2\text{-}H_{\mu 2}C_2)$: $s = -0.7245 \pm j\,0.47483$; $\zeta = 0.84$; $\omega_n = 0.75$ rad/sec; $\tau = 1.4$ sec
$s = -0.8084 \pm j\,2.2288$; $\zeta = 0.34$; $\omega_n = 2.37$ rad/sec; $\tau = 1.24$ sec
$s = -2.3006$; $\tau = 0.44$sec

Zeros: $s = -0.3412$
$s = -0.8175 \pm j\,2.2269$; $\zeta = 0.35$; $\omega_n = 2.37$ rad/sec; $\tau = 1.22$ sec
$s = -2.2864$

Table 4.4.3.4: Recovered SM Closed Loop Poles and Zeros

Poles:	$\lambda_i(A_2\text{-}H_{\mu 2}C_2)$:	$s = -0.72449 \pm j\,0.47483$; $\zeta = 0.84$; $\omega_n = 0.75$ rad/sec; $\tau = 1.4$ sec	
		$s = -0.80839 \pm j\,2.2288$; $\zeta = 0.34$; $\omega_n = 2.37$ rad/sec; $\tau = 1.24$ sec	
		$s = -2.3006$; $\tau = 0.44$sec	
	$\lambda_i(A_2\text{-}B_2G_{\rho 2})$:	($\rho_2 = 10^{-6}$)	($\rho_2 = 10^{-12}$)
		$s = -1.6909 \pm j\,7.3321$	$s = -1.55 \pm j\,9.4906$
	"far away" poles	$s = -6.4223 \pm j\,6.2478$	$s = -39.288 \pm j\,67.403$
		$s = -9.77284$	$s = -78.561$
Zeros:	Plant:	$s = -1.55 \pm j\,9.4906$	$s = -1.55 \pm j\,9.4906$
	Compensator:	$s = -0.25254$	$s = -0.33239$
		$s = -0.81602 \pm j\,2.2228$	$s = -0.81742 \pm j\,2.2264$
		$s = -2.2898$	$s = -2.2869$

Table 4.4.3.3, shows clearly that the dominant closed loop poles, i.e. those poles which will have the greates impact upon Δx are those with $\zeta = 0.84$, $\omega_n = 0.75$ rad/sec, and $\tau = 1.4$ sec. This follows obviously since the other target closed loop poles are approximately cancelled by compensator zeros. It should be emphasized, however, that although the other target closed loop poles have essentially no impact on Δx, they will have a large impact on $\Delta\theta$ and ΔB_{lc} (i.e. on internal variables). Similar comments hold for the recovered closed loop poles in Table 4.4.3.4.

This will be seen when transient responses are presented. The impact of the ($\zeta = 0.23$, $\omega_n = 7.53$, $\tau = 0.59$) pole, near the SM lightly damped zeros, will be of particular interest. Although Δx is usually commanded to zero, it must be noted that when such commands are issued the low frequency compensator zero at s = - 0.25 will have a tremendous impact on the output Δx [14].

4.4.4 Time Domain Evaluation of SM AFCS

(A) Δx Command Following

Typically the horizontal separation, Δx, will be commanded to be zero. When it is commanded, however, the command should be pre-filtered so that the high-pass effect of the compensator lead on control activity and pitching is reduced. To decide on the filter structure we referred to the reference to control Bode magnitude plot in Fig. 4.4.2.5. In order to reduce the 80 db/dec slope, between $\omega = 3$ rad/sec to $\omega = 8$ rad/sec, to 20 db/dec we chose a third order Butterworth filter:

$$H(s) = \frac{\omega_o^3}{s^3 + 2\omega_o s^2 + 2\omega_o s^2 + \omega_o^3} \qquad (4.47)$$

with $\omega_o = 4$ rad/sec. Fig. 4.4.4.1 shows the responses of the recovered SM AFCS ($\rho_2 = 10^{-6}$) to a step and filtered step command for Δx.

Fig. 4.4.4.1a shows the step response of the third order Butterworth filter ($\omega_o = 4$ rad/sec).

Fig. 4.4.4.1b shows the horizontal separation, Δx, responses to a step and to a pre-filtered step. The figure shows a tremendous overshoot in Δx. This overshoot is attributable to the interaction between the dominant closed loop poles ($\zeta = 0.84$, $\omega_n = 0.75$) and the low frequency compenator zero (s = - 0.25) (Ogata, [14]). We see that pre-filtering commands does not help this overshoot.

Fig. 4.4.4.1c shows the corresponding differential pitch attitude, $\Delta\theta$, responses. Without pre-filtering we have a peak $\Delta\theta$ of about 10 degs. When the pre-filter is used, the peak $\Delta\theta$ decreases to 5 degs. The figure also shows clearly that when references are pre-filtered the effect of the lightly damped pole ($\zeta = 0.23$, $\omega_n = 7.53$, $\tau = 0.59$) is substantially reduced. Pre-filtering

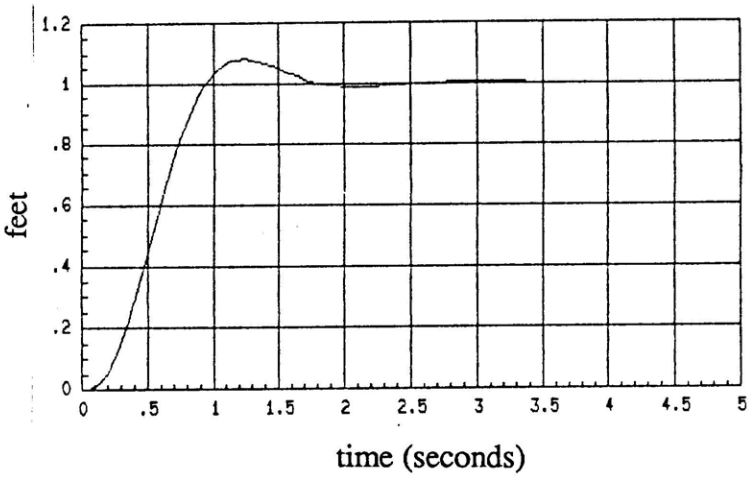

a) SM Pre-filter Step Response

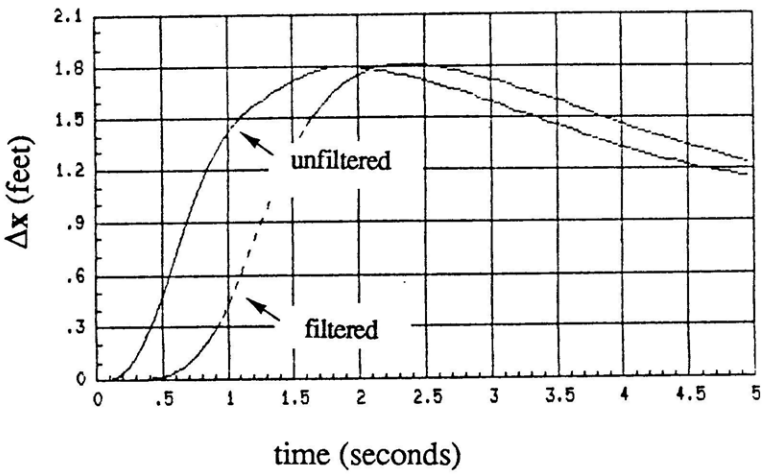

b) Horizontal Separation

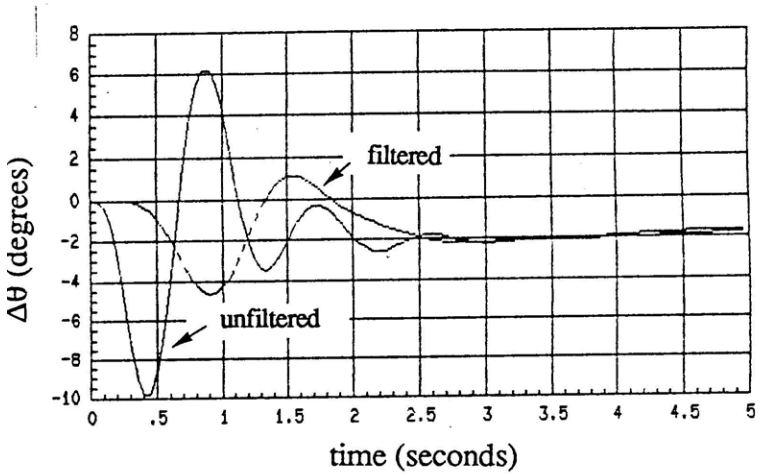

c) Differential Pitch

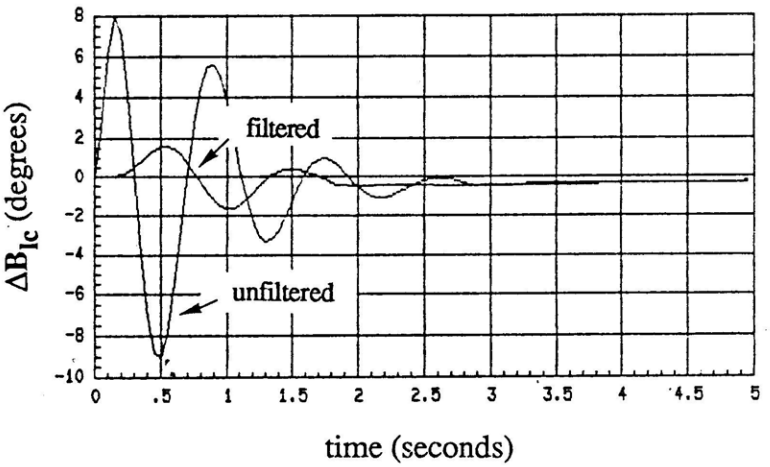

d) Differential Cyclic Control

Fig. 4.4.4.1: SM AFCS Response to a Step and Filtered Step Command for Δx.

references thus makes a big difference.

Similar comments hold for the differential cyclic control ΔB_{lc}, responses in Fig. 4.4.4.1d

(B) Δx Disturbance Rejection

Next we examine the ability of the SM AFCS to regulate the horizontal separation. Fig. 4.4.4.2 shows the response of the SM AFCS for an initial condition of $\Delta x = 1$ ft. One can think of this as a disturbance rejection evaluation. (We note that the SM pre-filter does not play a role in this simulation).

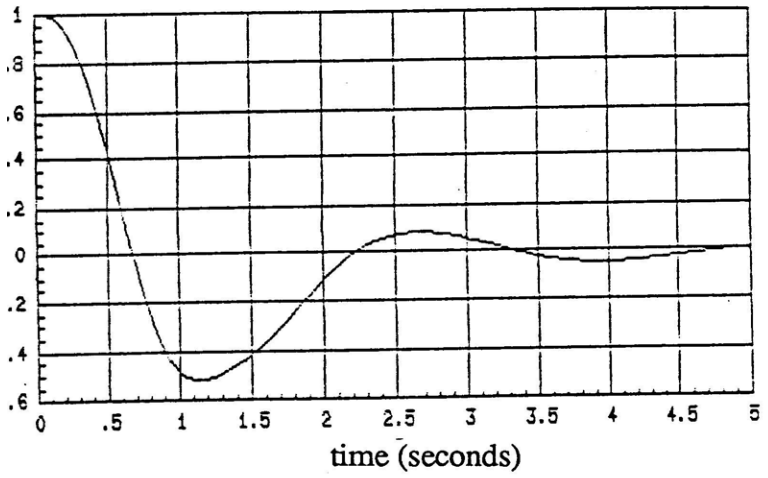

a) Horizontal Separation

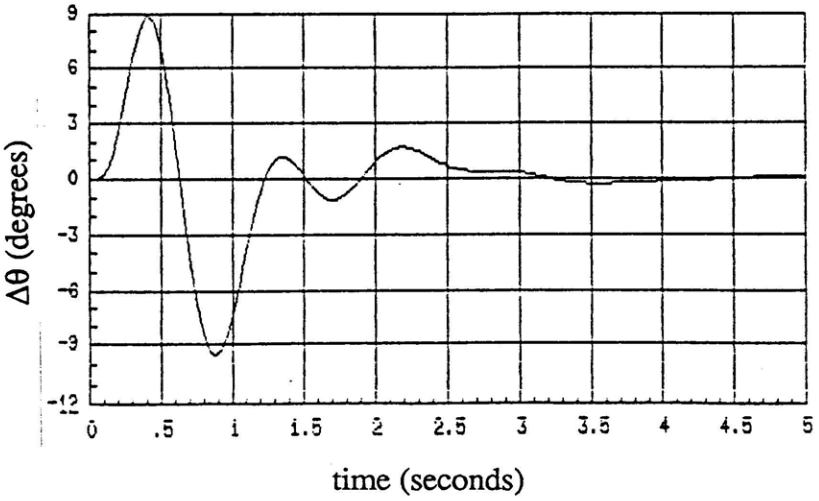

b) Differential Pitch Attitude

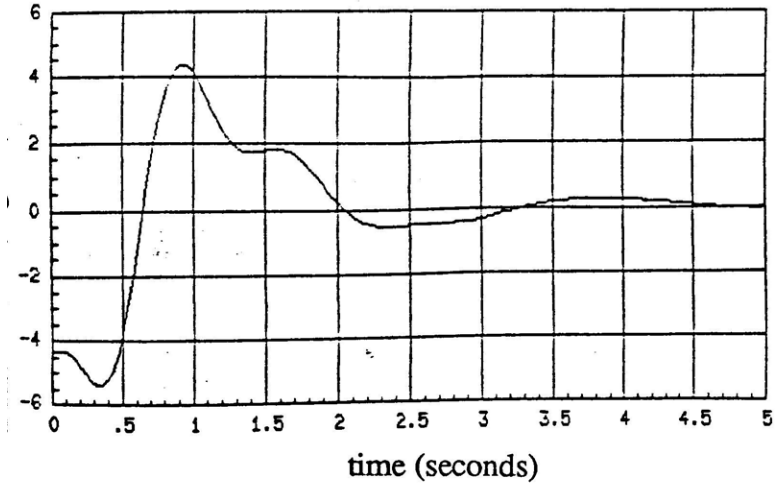

c) Differential Tether Angle

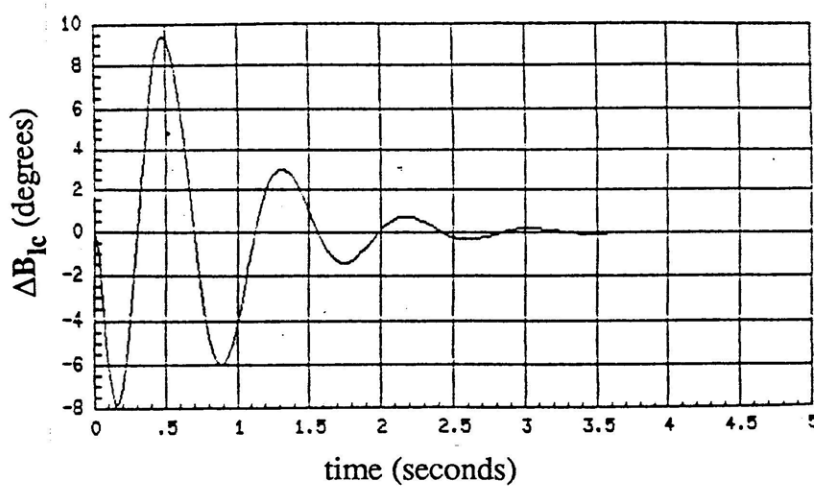

d) Differential Cyclic Control

Fig. 4.4.4.2: SM AFCS Response to a $\Delta x = 1$ft. Initial Condition.

Fig. 4.4.4.2a shows a very good Δx response; Δx settling down in about 3 seconnds. The corresponding differential pitch response (Fig. 4.4.4.2b), however, shows rather large pitch rates. The corresponding differential cyclic control (Fig. 4.4.4.2d) is also a bit excessive for the relatively small initial condition (Δx = 1 ft.). Obviously, this could be reduced by lowering the bandwidth. This, however, would mean less performance. If a high bandwidth design is indeed the objective then the only way to reduce the amount of control activity and pitching is by reducing the effect of the lead. This amounts to reducing the robustness requirement. This, however, can be done only if model uncertainty is low. Thinking in terms of the Nyquist plot for the SM AFCS loop tf, this amounts to having sufficiently small net uncertainty between the two phase crossover frequencies. Consequently, a high performance SM AFCS is feasible only if model uncertainty is sufficiently low. If model uncertainty is high then such a design becomes unfeasible. This is because, in such a case, the large robustness requirement forces the helicopters to undergo substantial pitching in order to regulate the horizontal separation. More specifically, the simulations show that if model uncertainty is high then only a low bandwidth design becomes feasible. Sucha design can be obtained by increasing the SM AFCS bandwidth parameter μ_2 and selecting ρ_2 small enough so that the robustness requirement is met. Finally, it should be pointed out that removing the integrator would significantly reduce the extent to which performance and robustness must be traded off.

4.4.5 Summary of SM AFCS Design

In this section the LQG/LTR design methodology was applied to the SM Design Plant; an unstable SISO system with considerable low frequency phase lag and two lightly damped high frequency zeros. It was shown , as expected from Chapter 3, that controlling the SM Plant is ver difficult; particularly when the specifications call for a high performance (high bandwidth) design. More specifically, it was shown that a trade-off must be made between performance and stability robustness. In addition, it was shown that when the specifications call for a high bandwidth design then this trade-off becomes particularly pronounced.

In summary, we conclude that a high performance SM AFCS is feasible only if model uncertainty is sufficiently low. If model uncertainty is high then such a design becomes unfeasible. In such a case, only a low bandwidth design becomes feasible.

4.5 Design and Evaluation of ASM AFCS

4.5.1 Introduction

In this section the LQG/LTR design methodology is applied to the ASM Design Plant, $G_3(s) = G_{p3}(s) / s = C_3(sI - A_3)^{-1} B_3$. A high performance (high bandwidth) compensator satisfying the specifications presented in section 3.6 is obtained. The ASM Design Plant consists of the ASM Plant, $G_{p3}(s) = C_{p3}(sI - A_{p3})^{-1}B_{p3}$, preceded by an integral augmentation (one integrator per command channel). We recall that the ASM Plant has inputs $\Delta\Theta_c$ (differential collective control) and ΣB_{lc} (average cyclic control) and outputs x_L-Σx (load deviation from center) and $\Sigma \dot{x}$ (average horizontal velocity).

It is assumed that the controls are assumed to be in degrees (degs) and the outputs in feet (ft) and feet/second (ft / sec), respectively.

In developing the target ASM open loop transfer function matrix (tfm), $G^3_{KF}(s) = C_3(sI - A_3)^{-1} H_{\mu 3}$, the design parameters, L_3 and μ_3, were chosen as follows:

$$L_3 = B_3 \ [C_{p3}(-A_{p3})^{-1}B_{p3}]^{-1} \tag{4.48}$$

$$\mu_3 = 1 \text{ (ASM AFCS bandwidth parameter)} \tag{4.49}$$

Choosing L_3 as in Eq. (4.48) assures that the target ASM singular values are matched at low frequencies. This was shown in section 4.2.2. We want the loop singular values matched because the design specifications presented in Chapter 3 stated that "low frequency errors are equally important in all directions". The recovery parameter, ρ_3, was chosen to be

$$\rho_3 = 10^{-5} \quad \text{(ASM AFCS recovery parameter).} \tag{4.50}$$

For reasons similar to those given for the SM AFCS, ρ_3 was not decreased any further. Given the

above parameters, the filter and control gain matrices, $H_{\mu 3}$ and $G_{\rho 3}$, can be computed by using the LQG/LTR procedure described in section 4.2. These matrices completely specify the ASM compensator, $K_3(s)$, given by

$$K_3(s) \equiv K^3_{LQG/LTR}(s) / s \tag{4.51a}$$

$$= G_{\rho 3}(sI - A_3 + B_3 G_{\rho 3} + H_{\mu 3} C_3)^{-1} H_{\mu 3} / s \,. \tag{4.51b}$$

Since $K_3(s)$ specifies the entire ASM AFCS, eq. (4.51) tells us that $H_{\mu 3}$ and $G_{\rho 3}$ completely specify the ASM AFCS. These matrices are given below:

$$H_{\mu 3} = \begin{bmatrix} 0.3605 & 1.6237 & 0.0017 & -0.1552 & 0.2494 & 0.6729 & 0.025 & 0.1201 & -0.0239 \\ -1.0979 & 0.3121 & 0.0117 & 1.0734 & 0.0244 & -0.2014 & -0.0129 & 0.0605 & 0.0477 \end{bmatrix}^T \tag{4.52}$$

$$G_{\rho 3} = \begin{bmatrix} 49.7344 & 138.3322 & 156.5858 & 149.8413 & 45.5383 & 87.648 & 153.479 & 13.0342 & -1.1653 \\ -63.2715 & -74.8953 & -79.9454 & 275.6631 & -17.1355 & -27.2046 & -49.3773 & -1.1653 & 23.592 \end{bmatrix} \tag{4.53}$$

4.5.2 Frequency Domain Evaluation of ASM AFCS

Fig. 4.5.2.1. shows the singular values of the target ASM open loop tfm, $G^3_{KF}(j\omega)$. The singular values of the recovered ASM loop tfm, $G^3_L(j\omega)$, are also shown in the figure.

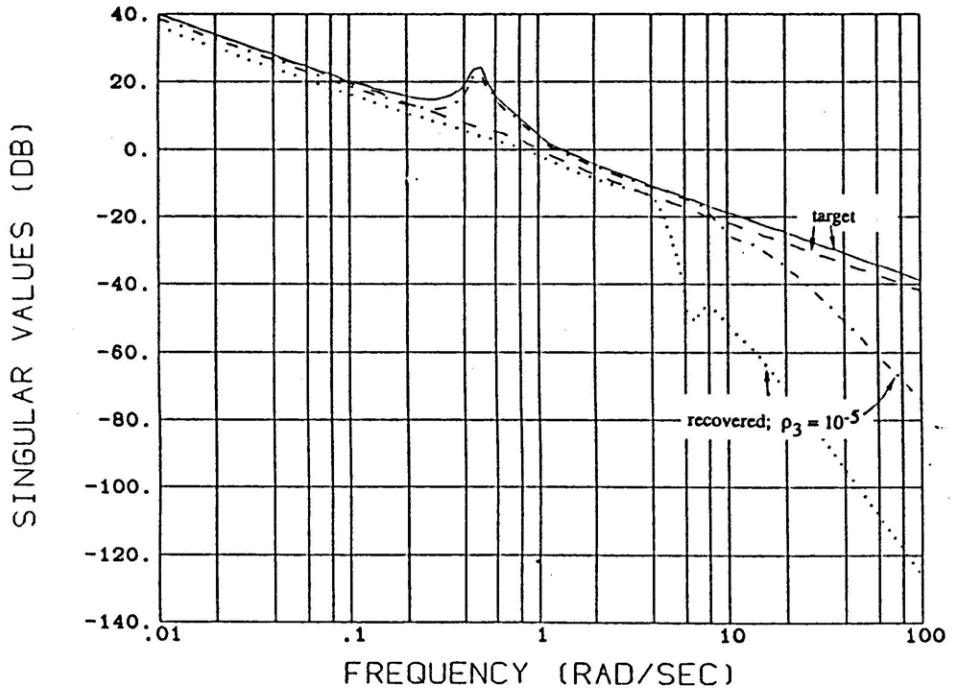

Fig. 4.5.2.1: Recovery of Target ASM Open Loop Singular Values.

The figure shows that the recoverd maximum and minimum ASM loop singular values approximate the target singular values within 3 db up to about 8 rad/sec. The recovered maximum and minimum singular values cross 0 db at about 1.5 rad/sec and 0.8 rad/sec, respectively. Both satisfy the gain crossover specifications presented in section 3.6.

To evaluate the performance properties of the recovered ASM AFCS, we need to determine its ability to follow typical reference commands and reject typical disturbances in x_L-Σx and $\Sigma\dot{x}$. This is best done by studying the input/output frequency domain properties of the recovered ASM sensitivity transfer function matrix, $S_3(j\omega)$. This matrix should be thought of as relating the ASM references, $\underline{r}_3(j\omega)$, and disturbances, $\underline{d}_3(j\omega)$, to the ASM tracking error $\underline{e}_{t3}(j\omega)$. The ASM tracking error is given by

$$\underline{e}_{t3}(j\omega) \equiv \underline{r}_3(j\omega) - \underline{y}_3(j\omega) \tag{4.54}$$

$$= S_3(j\omega)\,[\underline{r}_3(j\omega) - \underline{d}_3(j\omega)] + T_3(j\omega)\,\underline{n}_3(j\omega) \tag{4.55}$$

where $T_3(j\omega)$ is the recovered ASM closed loop transfer function matrix and $\underline{n}_3(j\omega)$ is the ASM noise vector due to feedback measurement error in x_L-Σx and $\Sigma\dot{x}$. $T_3(j\omega)$ and $\underline{n}_3(j\omega)$ shall be discussed subsequently. For now, however, we focus on the first half of eq. (4.55).

Equation (4.57) shows that to keep the ASM tracking error "small" we will need $S_3(j\omega)$ to be "small" at low frequencies where the ASM references, $\underline{r}_3(j\omega)$, and output disturbances, $\underline{d}_3(j\omega)$, typically have their greatest spectral content. From section 3.5.3 we recall that a matrix, say $S_3(j\omega)$, is "small" (in the sense of the two-norm) if and only if its maximum singular value is "small". Fig. 4.5.2.2 shows the singular values of the target and recovered ASM sensitivity transfer function matrices, $S^3{}_{KF}(j\omega)$ and $S_3(j\omega)$.

The figure shows that for $\rho_3 = 10^{-5}$ the recovered ASM sensitivity approximates the target ASM sensitivity, within 3 db, for all frequencies. The worst case sensitivity is 3 db ($\beta_3 = 1.4125$) and it is seen to occur near $\omega \approx 1.5$ rad/sec. This worse case sensitivity translates into the following guaranteed stability margins:

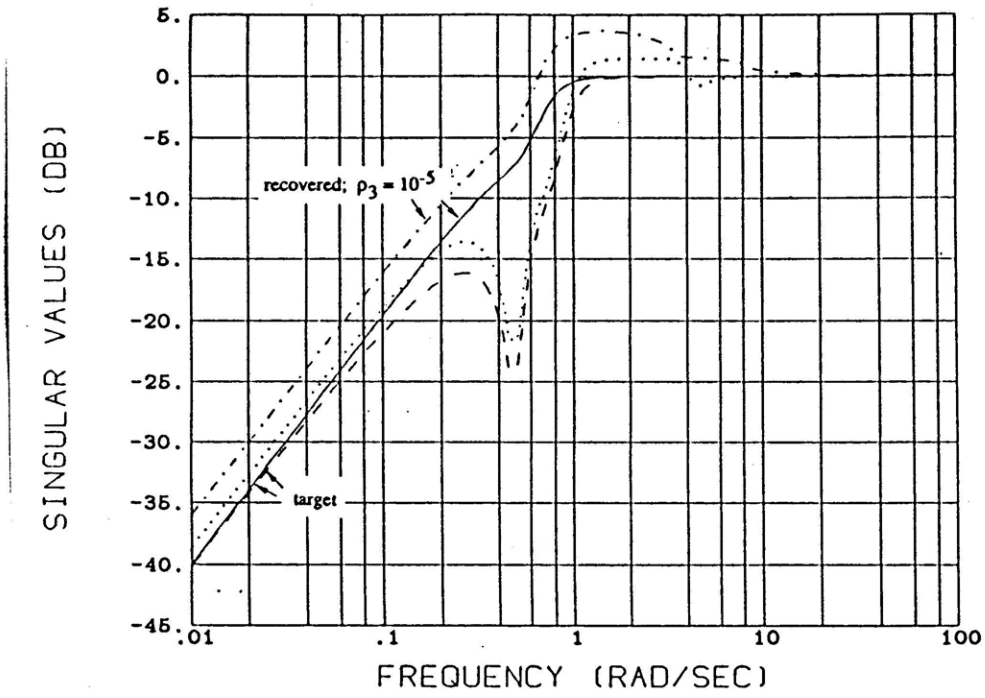

Fig. 4.5.2.2: Recovery of Target ASM Sensitivity Singular Values.

$$\downarrow GM_3 = \beta_3 / (\beta_3 + 1) = 0.59 \text{ (- 4.6 db)} \tag{4.56}$$

$$\uparrow GM_3 = \beta_3 / (\beta_3 - 1) = 3.42 \text{ (10.7 db)} \tag{4.57}$$

$$| PM_3 | = \pm 2 \sin^{-1}(1 / 2\beta_3) = \pm 41.5^\circ \tag{4.58}$$

all of which satisfy our margin specifications ($\beta_3 \leq 1.718$ (4.7 db)). The figure also shows that for all frequencies below $\omega = 0.06$ rad/sec, the maximum singular value of $S_3(j\omega)$ is below - 20 db. This satisfies our low frequency performance specification.

If $S_3(j\omega)$ consisted of two decoupled SISO sensitivity transfer functions then the interpretation of these facts would be clear since each singular value would simply be an independent Bode magnitude plot. Because $S_3(j\omega)$ is a coupled TITO transfer function matrix, it is necessary to carefully explain the significance of the above facts. This is best done by providing a graphical interpretation for the singular value decomposition (SVD) of a matrix.

Consider the matrix $S(j\omega)$ relating $\underline{e}(j\omega)$ and $\underline{d}(j\omega)$ as follows:

$$\underline{e}(j\omega) = S(j\omega)\, \underline{d}(j\omega) \tag{4.59}$$

where

$$\underline{d}(t) = \begin{bmatrix} d_1 \sin(\omega t + \theta_1) \\ d_2 \sin(\omega t + \theta_2) \end{bmatrix} = \mathrm{Im}\{\underline{d}\, e^{j\omega t}\} \qquad d_1, d_2 \in \mathbf{R} \tag{4.60}$$

$$\underline{e}(t) = \begin{bmatrix} e_1 \sin(\omega t + \phi_1) \\ e_2 \sin(\omega t + \phi_2) \end{bmatrix} = \mathrm{Im}\{\underline{e}\, e^{j\omega t}\} \tag{4.61}$$

$$\underline{d} = [d_1 e^{-j\theta_1} \quad d_2 e^{-j\theta_2}]^H \tag{4.62}$$

$$\underline{e} = [e_1 e^{-j\phi_1} \quad e_2 e^{-j\phi_2}]^H \tag{4.63}$$

In the discussion which follows, we refer to the time signal $\underline{d}(t)$ and the complex vector $\underline{d}$ interchangeably. We do the same for $\underline{e}(t)$ and $\underline{e}$. Suppose that S has SVD given by:

$$S = U \Sigma V^H \tag{4.64}$$

$$= \begin{bmatrix} | & | \\ \underline{u}_1 & \underline{u}_2 \\ | & | \end{bmatrix} \begin{bmatrix} \sigma_1 & 0 \\ 0 & \sigma_2 \end{bmatrix} \begin{bmatrix} -\underline{v}_1^H- \\ -\underline{v}_2^H- \end{bmatrix} \tag{4.65}$$

$$= \sigma_1 \underline{u}_1 \underline{v}_1^H + \sigma_2 \underline{u}_2 \underline{v}_2^H \tag{4.66}$$

where

$$S^H S\, \underline{v}_i = \sigma_i^2\, \underline{v}_i \qquad i = 1, 2 \tag{4.67}$$

$$S S^H \underline{u}_i = \sigma_i^2\, \underline{u}_i \qquad i = 1, 2 \tag{4.68}$$

$$\underline{v}_i^H \underline{v}_j = \delta_{ij} \tag{4.69}$$

$$\underline{u}_i^H \underline{u}_j = \delta_{ij} \qquad i, j = 1, 2 \tag{4.70}$$

$$\delta_{ij} = \begin{cases} 1 & \text{if } i = j \\ 0 & \text{if } i \neq j \end{cases} \tag{4.71}$$

$$\underline{v}_i = [v_{i1} e^{-j\alpha_{i1}} \quad v_{i2} e^{-j\alpha_{i2}}]^H \qquad i = 1, 2 \tag{4.72}$$

$$\underline{u}_i = [u_{i1} e^{-j\beta_{i1}} \quad u_{i2} e^{-j\beta_{i2}}]^H \qquad i = 1, 2 \quad \alpha, \beta \in (-\pi, \pi) \tag{4.73}$$

$$\sigma_1 = \max \{\|S\underline{d}\|_2 / \|\underline{d}\|_2 \mid \underline{d} \neq \underline{0} \quad \underline{d} \in C^2\} \tag{4.74}$$

$$\sigma_2 = \min \{\|S\underline{d}\|_2 / \|\underline{d}\|_2 \mid \underline{d} \neq \underline{0} \quad \underline{d} \in C^2\} \tag{4.75}$$

where $\|x\|_2 \equiv (\underline{x}^H \underline{x})^{1/2}$ is the standard Euclidean norm (two-norm).From these facts it follows that

$$\sigma_2 \leq \frac{\|S\underline{d}\|_2}{\|\underline{d}\|_2} \leq \sigma_1 \tag{4.76}$$

where the left equality holds if and only if $\underline{d} = \underline{v}_2$ and the right inequality holds if and only if $\underline{d} = \underline{v}_1$. These inequalities tell us that σ_1 and σ_2 represent the maximum and minimum amplifications of S in the sense of the Euclidean norm, $\|\ \|_2$. It follows from eq. (4.76) that if $\|\underline{d}\|_2 \equiv \sqrt{d_1^2 + d_2^2} = r$, where $r > 0$, then $\sigma_2 r \leq \|\underline{e}\|_2 = \|S\underline{d}\|_2 = \sqrt{e_1^2 + e_2^2} \leq \sigma_2 r$ for all $\underline{d} \in C^2$. This tells us that all disturbances $\underline{d} \in C^2$, such that $\|\underline{d}\|_2 = r$, get mapped to a point on an annulus in e_1e_2-space. Furthermore, it follows from eq. (4.66) that if

$$\underline{d} = k_1 \underline{v}_1 + k_2 \underline{v}_2 \qquad k_1, k_2 \in \mathbf{R}^2 \tag{4.77}$$

then

$$\underline{e} = S\,\underline{d} \tag{4.78}$$

$$= (\underline{v}_1^H \underline{d})\, \sigma_1\, \underline{u}_1 + (\underline{v}_2^H \underline{d})\, \sigma_1\, \underline{u}_2 \tag{4.79}$$

$$= k_1\, \sigma_1\, \underline{u}_1 + k_2\, \sigma_2\, \underline{u}_2. \tag{4.80}$$

From eqs. (4.68) and (4.76) we see that

$$\|\underline{d}\|_2^2 = \underline{d}^H \underline{d} \tag{4.81}$$

$$= [k_1 \underline{v}_1^H + k_2 \underline{v}_2^H]\, [k_1 \underline{v}_1 + k_2 \underline{v}_2] \tag{4.82}$$

$$= k_1^2 + k_2^2 \tag{4.83}$$

This implies that $\|\underline{d}\|_2^2 = r^2$ if and only if $k_1^2 + k_2^2 = r^2$, or equivalently $d_1^2 + d_2^2 = r^2$. It thus follows from eq. (4.80) that the circle $\|\underline{d}\|_2 = r$ (i.e. $k_1^2 + k_2^2 = r^2$) in the d_1d_2-plane gets mapped, via S, to an ellipse in the e_1e_2 -plane. This is visualized in Fig. 4.5.2.3. The equation of the ellipse in the e_1e_2-plane is given by:

$$(\hat{e}_1 / \sigma_1)^2 + (\hat{e}_2 / \sigma_2)^2 = 1 \tag{4.84}$$

where

$$\begin{bmatrix} \hat{e}_1 \\ \hat{e}_2 \end{bmatrix} = \begin{bmatrix} \sigma_1 u_{11} & \sigma_2 u_{21} \\ \sigma_1 u_{12} & \sigma_2 u_{22} \end{bmatrix} \begin{bmatrix} e_1 \\ e_2 \end{bmatrix} \tag{4.85}$$

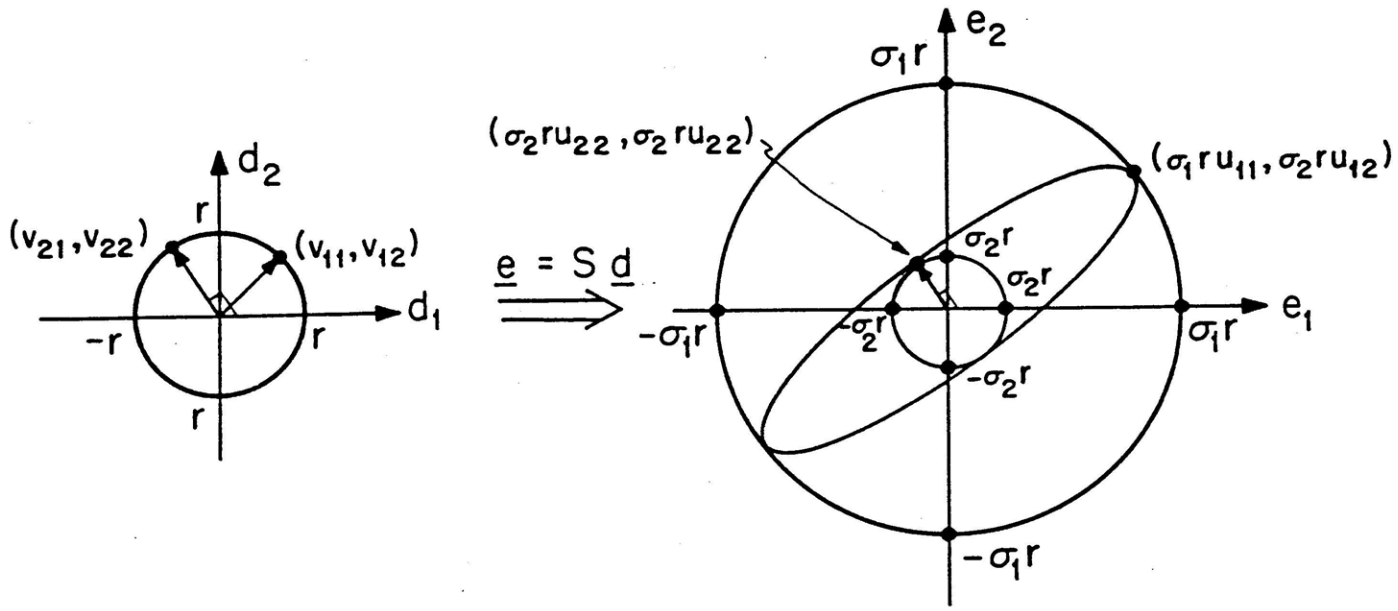

Fig. 4.5.2.3: Graphical Interpretation of Singular Values.

It is also useful to note that eq. (4.76) implies that

$$\sigma_2 \|\underline{d}\|_2 \leq \|\underline{e}\|_2 \leq \sqrt{m}\, \|\underline{e}\|_\infty \quad \text{for all } \underline{d}, \underline{e} \in \mathbf{C}^m \quad (m = 2 \text{ here}) \qquad (4.86)$$

and

$$\|\underline{e}\|_\infty \leq \|\underline{e}\|_2 \leq \sigma_1 \|\underline{d}\|_2 \qquad (4.87)$$

since $\|\underline{e}\|_\infty \equiv \max\{|e_1|, |e_2|\} \leq \sqrt{e_1^2 + e_2^2} \equiv \|\underline{e}\|_2$. The above inequalities in turn imply that

$$\boxed{(1/\sqrt{m})\, \sigma_2\, \|\underline{d}\|_2 \leq \|\underline{e}\|_\infty \leq \|\underline{e}\|_2 \leq \sigma_1 \|\underline{d}\|_2} \quad (m = 2 \text{ here}) \qquad (4.88)$$

The inequalities in eqs. (4.86) - (4.88) combined with the geometric interpretation provided by fig. 4.5.2.3 is all we need to interpret the singular values of $S_3(j\omega)$ in Fig. 4.5.2.2.

Assume for notational simplicity that $\underline{e} = \underline{e}_{t3}$, $\underline{d} = -\underline{d}_3$, and that $S = S_3$ so that $e = S\, d$. Since $\sigma_{max}\{S(j\omega)\} \leq 0.1$ (-20 db) for all $\omega \leq 0.06$ rad/sec. it follows from eq. (4.88) that

$$\|\underline{e}\|_\infty \leq \|\underline{e}\|_2 \leq 0.1\, \|\underline{d}\|_2 \leq 0.1\sqrt{2}\, \|\underline{d}\|_\infty \qquad (4.89)$$

for all $\omega \leq 0.06$ rad/sec for all $\underline{d} \in \mathbf{C}^2$. This inequality tells us that for all $\omega \leq 0.06$ rad/sec the ASM AFCS provides at least -17 db ($0.1\sqrt{2} = 0.14$) disturbance attenuation or equivalently

about 86% disturbance rejection in the sense of the infinity norm, $\|\cdot\|_\infty$. Replacing $\underline{d}$ with $\underline{r}_3$ in eq. (4.89) tells us that over this frequency range we also have 86% command following (in the sense of $\|\cdot\|_\infty$). It is emphasized that these statements are statements about the nominal ASM AFCS, i.e. they are statements of guaranteed nominal performance. After guaranteeing nominal performance a designer must address the issue of performance robustness. To do so an unstructured characterization of modeling errors is needed and the concept of structured singular values (Doyle, [10]) must be used. Performance robustness is an area of ongoing research and is beyond the scope of this thesis.

Fig. 4.5.2.2 shows that the worst case amplification of disturbances (in the sense of the two-norm) occurs at $\omega_o = 1.485$ rad/sec. At this frequency we have

$$\max_{\omega \geq 0} \sigma_{max}[S(j\omega_0)] = \sigma_1[S(j\omega_0)] = 1.5252 \quad (3.67 \text{ db}) \tag{4.90}$$

A SVD of $S(j\omega)$ at this frequency provides us with two important facts. One of the facts can be stated mathematically as follows:

$$\underline{d} = \begin{bmatrix} \underline{0.97988} \sin \omega_0 t & \text{ft} \\ 0.1996 \sin(\omega_0 t + 40.95^o) & \text{ft/sec} \end{bmatrix} \quad \underline{e} = S\underline{d} \Rightarrow \underline{e} = 1.5252 \begin{bmatrix} \underline{0.98996} \sin(\omega_0 t + 27.76^o) & \text{ft} \\ 0.14132 \sin(\omega_0 t + 40.48^o) & \text{ft/sec} \end{bmatrix} \tag{4.91}$$

This fact summarizes the information contained in the singular vectors associated with the maximum singular value at ω_0. It tells us, loosely speaking, that payload disturbances, due to wind gusts, at this frequency will be particularly troublesome. It is interesting to note that the frequency $\omega_o = 1.485$ is very close to the "effective pendular frequency" given by $g / H \cong 1.56$ rad/sec. The other fact can be stated mathematically as follows:

$$\underline{d} = \begin{bmatrix} -0.1996 \sin \omega_0 t & \text{ft} \\ \underline{0.9798} \sin(\omega_0 t + 40.95^o) & \text{ft/sec} \end{bmatrix} \quad \underline{e} = S\underline{d} \Rightarrow \underline{e} = 1.161 \begin{bmatrix} 0.14132 \sin(\omega_0 t - 104.4^o) & \text{ft} \\ \underline{0.98996} \sin(\omega_0 t + 88.4^o) & \text{ft/sec} \end{bmatrix} \tag{4.92}$$

This fact summarizes the information contained in the singular vectors associated with the minimum singular value at ω_o. It tells us that horizontal wind gusts at this frequency will make it

difficult to control $\Sigma\dot{x}$.

Since $\sigma_{max}[S(j\omega)]$ provides us with the "maximum amplifications" of disturbances (and references) it is useful to get a feel for the type of disturbances that result in this maximum amplification. To do so we plot $|v_{11}|$ and $|v_{12}|$ versus frequency. This plot shall be referred to as a Maximum Output-Input Direction (MOID) plot. Corresponding to this MOID plot we can plot $\sigma_1|u_{11}|$ and $\sigma_1|u_{12}|$ versus frequency. Such a plot will be referred to as a Maximum Output-Output Direction (MOOD) plot. It should be noted that similar plots can be constructed for the minimum singular value. Also we can similarly plot the phase information contained in the singular vectors. Since only magnitude information is typically known about disturbances and since we're interested in "maximum amplifications", the MOID and MOOD plots are by far the most useful. The information which such plots provide, as will be demonstrated in this chapter, is extremely valuable for understanding the directionality properties of any MIMO feedback system.

Fig. 4.5.2.4. contains a MOID plot for the ASM sensitivity tfm, $S(j\omega) = S_3(j\omega)$. In this plot the solid curve corresponds to $|v_{11}|$ and the dashed curve corresponds to $|v_{12}|$. This convention shall be used throughout the remainder of the thesis. Since the output vector is given by $\underline{y} = [x_L\text{-}\Sigma x \;\; \Sigma\dot{x}]^T$, and since $S(j\omega)$ relates disturbances to tracking errors, it follows that $|v_{11}|$ corresponds to $x_L\text{-}\Sigma x$ disturbances and $|v_{12}|$ corresponds to $\Sigma\dot{x}$ disturbances. The plot should be interpreted as specifying the magnitudes of sinusoidal disturbances which when properly coordinated in time will result in maximum amplification; i.e. given $|v_{11}|$ and $|v_{12}|$, where $|v_{11}|^2 + |v_{12}|^2 = 1$, there exist phase angles $\theta_{11}, \theta_{12} \in (-\pi,\pi]$ such that if

$$\underline{d} = \|\underline{d}\|_2 \begin{bmatrix} |v_{11}| \sin(\omega t + \theta_{11}) & \text{ft} \\ |v_{12}| \sin(\omega t + \theta_{12}) & \text{ft/sec} \end{bmatrix} \tag{4.93}$$

for some $\|\underline{d}\|_2 < \infty$, then

$$\|e\|_2 = \max_{d \neq 0} \{ \|e\|_2 \} \tag{4.94}$$

$$= \sigma_1 \|\underline{d}\|_2 \leq \sigma_1 \sqrt{m} \; \|\underline{d}\|_\infty \qquad (m = 2 \text{ in our problem}) \tag{4.95}$$

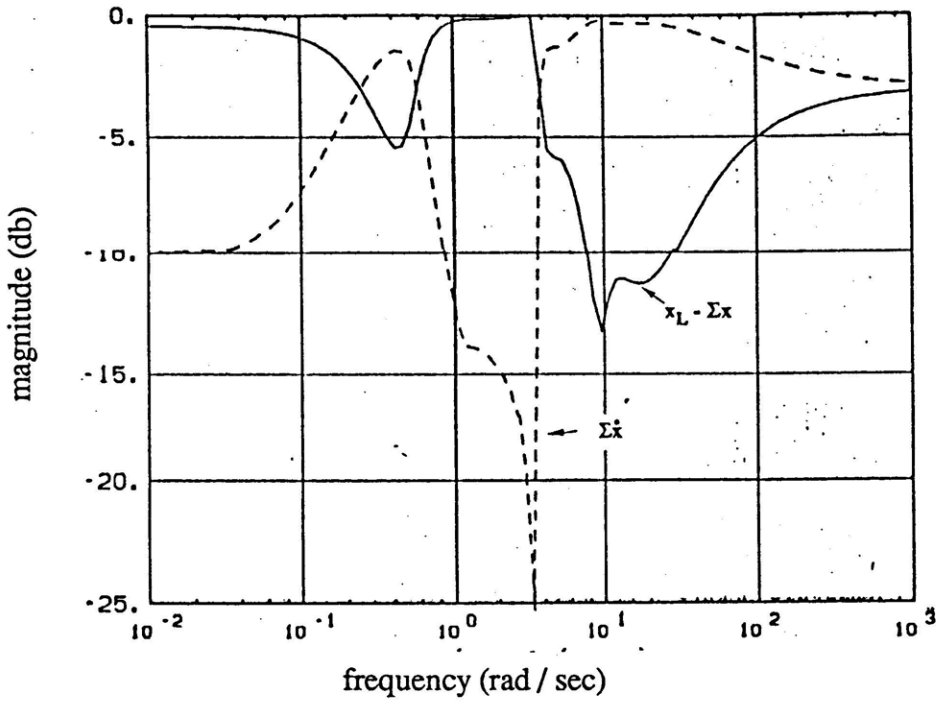

Fig. 4.5.2.4: Maximum Output Input Direction (MOID) Plot for ASM Sensitivity.

With this interpretation of the MOID plot in Fig. 4.5.2.4 we see that the ASM AFCS will be most sensitive to x_L-Σx disturbances at low frequencies. As the frequency is increased above 0.2 rad/sec, however, the sensitivity to such disturbances decreases while the sensitivity to $\Sigma \dot{x}$ disturbances increases. This continues until approximately 0.4 rad/sec. Above this frequency the sensitivity to x_L-Σx disturbances increases and the sensitivity to $\Sigma \dot{x}$ disturbances decrease rapidly. Between 1 and 3.5 rad/sec we are particularly sensitivity to x_L-Σx disturbances. Just above this frequency range the $\Sigma \dot{x}$ disturbances will be particularly troublesome and at high frequencies x_L- Σx and $\Sigma \dot{x}$ disturbances will be equally troublesome.

Fig. 4.5.2.5 contains the MOOD plot which corresponds to Fig. 4.5.2.4. In this plot the solid curve corresponds to $\sigma_1 |u_{11}|$ and the dashed curve corresponds to $\sigma_1 |u_{12}|$. This convention shall also be used throughout the chapter. The $\sigma_1 |u_{11}|$ corresponds to errors in x_L-Σx and the $\sigma_1 |u_{12}|$ corresponds to errors in $\Sigma \dot{x}$. Given a disturbance $\underline{d}$ as in eq. (4.93), the corresponding tracking error, $\underline{e} = S\,\underline{d}$, will be given by

$$\underline{e} = \sigma_1 \|\underline{d}\|_2 \begin{bmatrix} |u_{11}| \sin(\omega t + \phi_{11}) \text{ ft} \\ |u_{12}| \sin(\omega t + \phi_{12}) \text{ ft/sec} \end{bmatrix} \tag{4.96}$$

for some phase angles $\phi_{11}, \phi_{12} \in (-\pi,\pi]$.

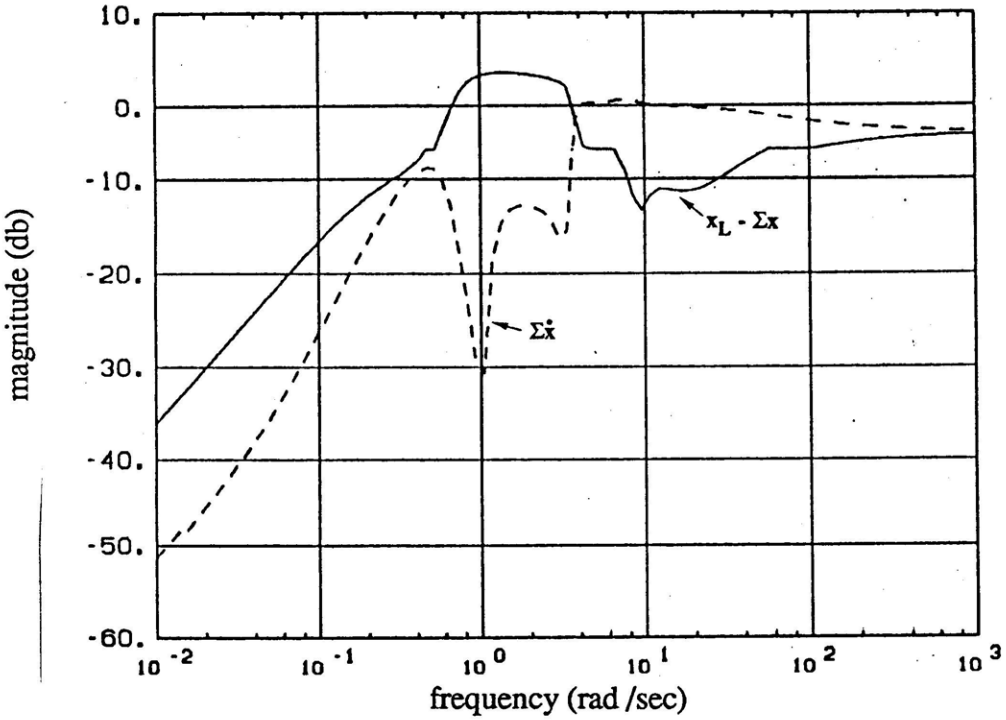

Fig. 4.5.2.5: Maximum Output Output Direction (MOOD) plot for ASM Sensitivity.

The figure shows that for all frequencies below about 4 rad/sec. we will have our largest tracking errors in x_L-Σx when the disturbances are collinear with the right singular vectors of $S_3(j\omega)$; i.e.

$$\text{If} \quad \underline{d} = \text{Im} \quad \{ |k| e^{j\theta_k} \underline{v}_1 e^{j\omega t} \} \tag{4.97}$$

$$= |k| \begin{bmatrix} |v_{11}| \sin(\omega t + \theta_{11} + \theta_k) \text{ ft} \\ |v_{12}| \sin(\omega t + \theta_{12} + \theta_k) \text{ ft/sec} \end{bmatrix} \tag{4.98}$$

where $k = |k| e^{j\theta} \in \mathbf{C}$, then

$$\underline{e} = \text{Im} \{ \sigma_1 |k| \underline{u}_1 e^{j\omega t} \} \tag{4.99}$$

$$= \sigma_1 |k| \begin{bmatrix} |u_{11}| \sin(\omega t + \phi_{11}) \text{ ft} \\ |u_{12}| \sin(\omega t + \phi_{12}) \text{ ft/sec} \end{bmatrix} \tag{4.100}$$

Above 4 rad/sec if $\underline{d}$ is collinear with $\underline{v}_1$ then $\Sigma\dot{x}$ errors will be larger than x_L-Σx errors but not by

more than 12 db.

To evaluate the ability of the ASM AFCS to attenuate high frequency noise in our x_L-Σx and $\Sigma \dot{x}$ measurements, we examine the recovered ASM closed loop tfm, $T_3(j\omega)$. Its singular values, as well as those of the target ASM closed loop tfm, $T^3_{KF}(j\omega)$, are given in Fig. 4.5.2.6. The corresponding MOID and MOOD plots for $\sigma_1[T_3(j\omega)]$ are given in Figs. 4.5.2.7 and 4.5.2.8, respectively.

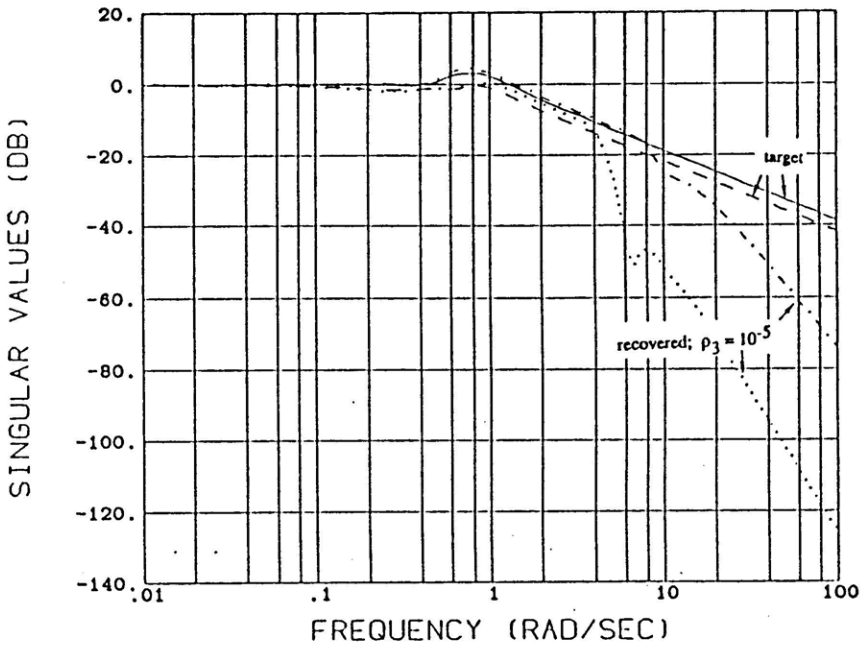

Fig. 4.5.2.6: Recovery of Target ASM Closed Loop Singular Values.

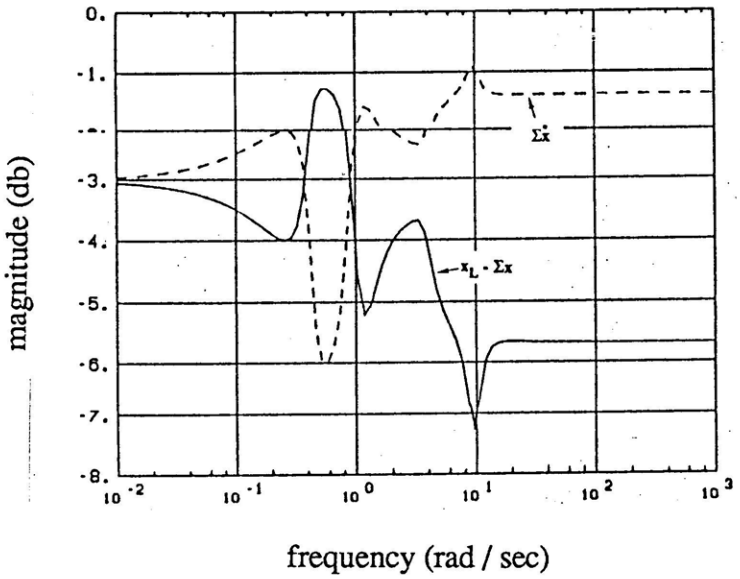

Fig. 4.5.2.7: Closed Loop TFM MOID Plot

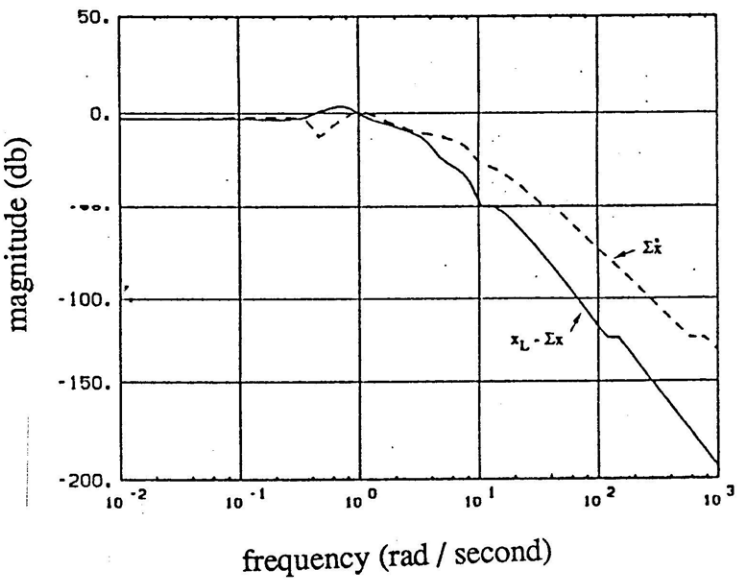

Fig. 4.5.2.8: Closed Loop TFM MOOD Plot

Fig. 4.5.2.6 shows that the worst case frequency (in the sense of the two-norm) is at ω_o = 0.73907 rad/sec. A SVD of $T_3(j\omega)$ at ω_o gives us the following two very useful pieces of information. For notational simplicity let $\underline{e} = \underline{e}_{t3}$, $T = T_3$, and $\underline{n} = \underline{n}_3$. It can be shown that

$$\underline{n} = \begin{bmatrix} \underline{0.833} \sin \omega_o t & \text{ft} \\ \underline{0.553} \sin(\omega_o t + 121.1^o) & \text{ft/sec} \end{bmatrix} \quad \underline{e} = T\,\underline{n} \;\Rightarrow\; \underline{e} = 1.654 \begin{bmatrix} \underline{0.903} \sin(\omega_o t - 42.29) & \text{ft} \\ 0.43 \sin(\omega_o t + 122.1^o) & \text{ft/sec} \end{bmatrix} \tag{4.101}$$

and that

$$\underline{n} = \begin{bmatrix} -0.553 \sin\omega_o t & \text{ft} \\ \underline{0.833} \sin(\omega_o t + 121.1^o) & \text{ft/sec} \end{bmatrix} \quad \underline{e} = T\,\underline{n} \;\Rightarrow\; \underline{e} = 0.93 \begin{bmatrix} 0.43 \sin(\omega_o t + 11.9^o) & \text{ft} \\ \underline{0.903} \sin(\omega_o t + 96.2^o) & \text{ft/sec} \end{bmatrix} \tag{4.102}$$

Eq. (4.101), loosely speaking, implies that the ASM AFCS will be particualarly sensitive to noisy measurements in x_L-Σx. These equations tell us about noise attenuation.

At this point it is useful to point out two very useful and inciteful stability robustness tests due to Lehtomaki and Athans [9]. Suppose that the "true linear" loop tfm can be written as:

$$G_{L3}(j\omega) = [I + \Delta_m(j\omega)]\, G_{L3}(j\omega) \tag{4.103}$$

where

$$\sigma_{max}[\Delta_m(j\omega)] < l_m^{-1}(j\omega) \quad \text{for all } \omega \geq 0 \tag{4.104}$$

It can then be shown that the "true linear" closed loop system (with Dm at the plant output) will be stable if

$$\sigma_{max}[T_3(j\omega)] < l_m^{-1}(j\omega) \quad \text{for all } \omega \geq 0 \tag{4.105}$$

This condition is a sufficient condition for the stability of the "true linear" closed loop system. The condition, however, becomes necessary if no directional information is known about $\Delta_m(j\omega)$. $\Delta_m(j\omega)$ is referred to as a <u>pre-multiplicative modeling error</u>. If no directional information is known about $\Delta_m(j\omega)$ then it is said to be an <u>unstructured modeling error</u>.

For simplicity suppose that

$$I + \Delta_m(s) = \omega_r^2 / (s^2 + 2\zeta\, \omega_r\, s + \omega_r^2)\, I \tag{4.106}$$

where ω_r = 27 rad/sec is the first harmonic of the main rotor. We then have

$$\Delta_m(s) = -\, s[s + 2\zeta\omega_r]\; I / (s^2 + 2\zeta\omega_r s + \omega_r^2) \tag{4.107}$$

Suppose all we know is that

$$\sigma_{max}[\Delta_m(j\omega)] \leq l_m(j\omega) = | s[s + 2\zeta\omega_r] / [s^2 + 2\zeta\omega_r s + \omega_r^2] |_{s=j\omega} \qquad (4.108)$$

We then have

$$l_m^{-1}(j\omega) = | [s^2 + 2\zeta\omega_r s + \omega_r^2] / s[s + 2\zeta\omega_r] |_{s=j\omega} \qquad (4.109)$$

We then ask the following important question: How small a ζ can we tolerate before losing our guaranteed stability ? To answer this all we need do is consider $\text{smax}[T_3(j\omega)]$ from Fig. 4.5.2.6 and $l_m^{-1}(j\omega)$. The stability test can be visualized as in Fig. 4.5.2.9. The answer to this question falls out easily by making Bode magnitude approximations for $l_m^{-1}(j\omega)$ at $\omega = \omega_r = 27$ rad/sec. Doing so gives us

$$\sigma_{max}[T_3(j\omega)] = 0.0316 \leq l_m^{-1}(j\omega) = 2\zeta\sqrt{1 - \zeta^2} \approx 2\zeta \qquad (4.110)$$

which yields

$$\zeta \geq 0.0158 \qquad (4.111)$$

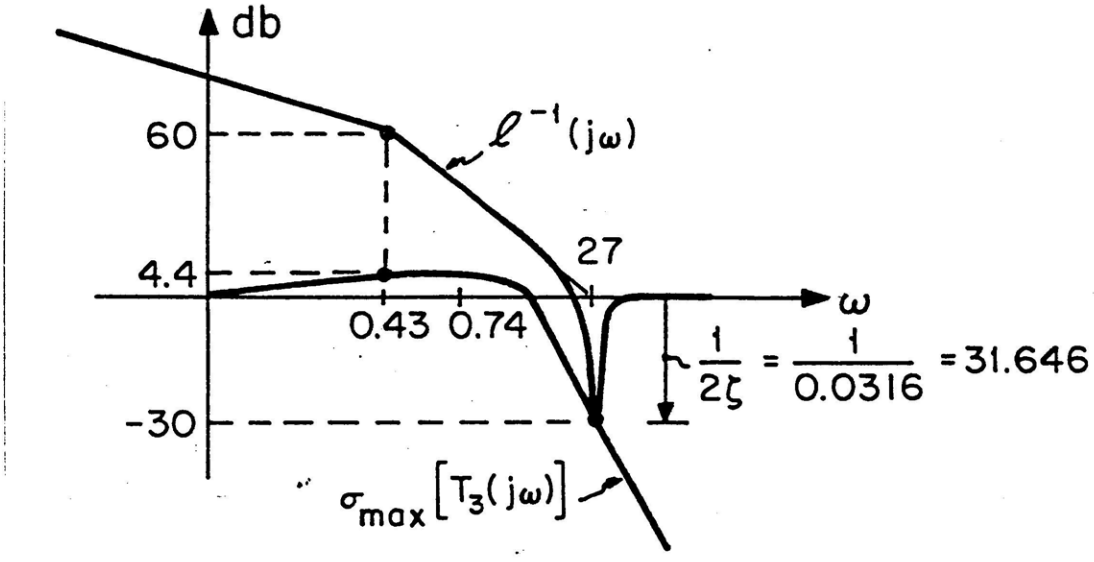

Fig. 4.5.2.9: Visualization of Pre-Multiplicative Stability Robustness Test.

Fig.4.5.2.9 shows that if $\zeta \leq 0.0158$ and if we know nothing about the directionality (phase) properties of $\Delta_m(j\omega)$ then the closed loop may go unstable.

Now suppose that the "true linear" loop tfm can be written as:

$$G_{L3}(j\omega) = [I + \Delta_d(j\omega)]^{-1} G_{L3}(j\omega) \tag{4.112}$$

where

$$\sigma_{max}[\Delta_d(j\omega)] \leq l_d(j\omega) \quad \text{for all } \omega \geq 0 \tag{4.113}$$

It can then be shown that the "true linear" closed loop system (with Δ_d at the plant output) will be stable if

$$\sigma_{max}[S_3(j\omega)] < l_d^{-1}(j\omega) \quad \text{for all } \omega \geq 0 \tag{4.114}$$

This condition is also a sufficient condition for the stability of the "true linear" closed loop system. The condition becomes necessary if no directional information is known about $\Delta_d(j\omega)$. $\Delta_d(j\omega)$ is referred to as a pre-division modeling error. If no directional information is known about $\Delta_d(j\omega)$ then it is said to be an an unstructured modeling error.

The stability robustness conditions in eqs. (4.102) and (4.111) are very useful since they show us how to determine stability given only magnitude information about the error in our linear model. These results should be particularly attractive to classically-oriented design engineers since they are direct multivariable extensions of classical SISO Nyquist ideas. It should also be noted that the conditions in eqs. (2.102) and (4.111) show why the target loop properties:

$$\sigma_{max}[T^3_{KF}(j\omega)] \leq 2 \text{ db} \quad \text{for all } \omega \geq 0 \tag{4.115}$$

$$\sigma_{max}[S^3_{KF}(j\omega)] \leq 0 \text{ db} \quad \text{for all } \omega \geq 0 \tag{4.116}$$

are very desirable to have. Other stability robustness tests are given in [9].

Fig. 4.5.2.10 shows the singular values of the recovered ASM LQG/LTR compensator, $K^3_{LQG/LTR}(j\omega)$. Fig. 4.5.2.11 shows the singular values of the ASM compensator, $K_3(s) = K^3_{LQG/LTR}(s) / s$. $K_3(s)$ takes the error signals, $\underline{e}_3$, and generates the control signals, $\underline{u}_{p3}$, to the ASM plant, $G_{p3}(s)$.

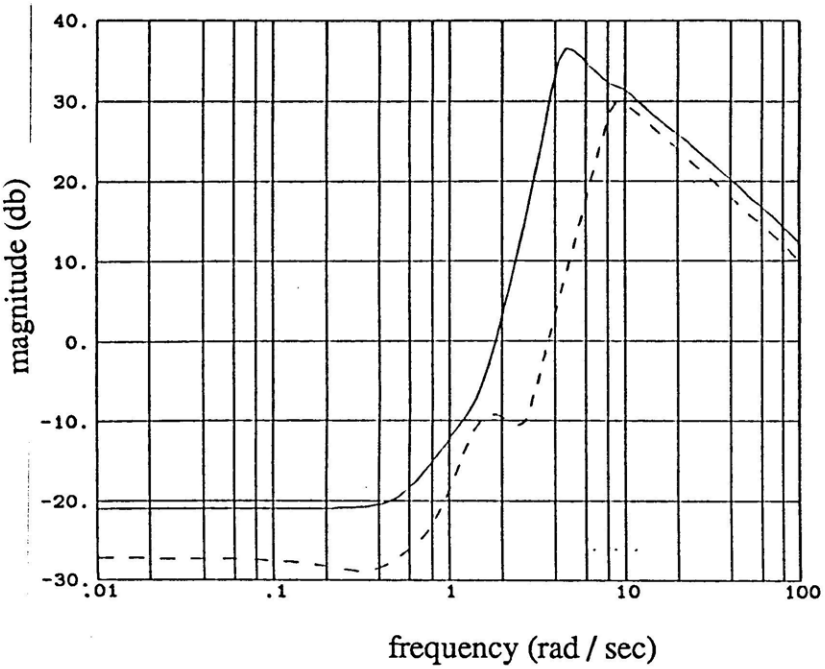

Fig. 4.5.2.10: Recovered ASM LQG/LTR Compensator Singular Values

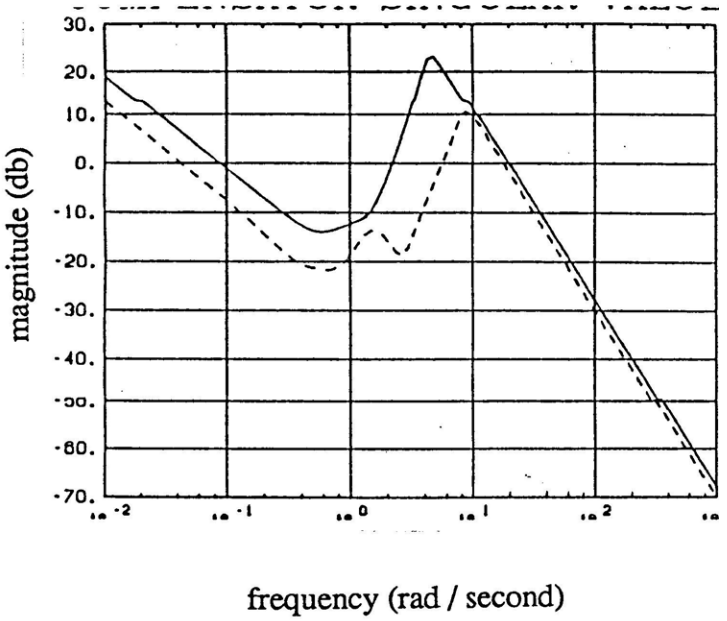

Fig. 4.5.2.11: Recovered ASM Compensator Singular Values

In these figures we see the high-pass structure of the recovered ASM compensator. This high-pass structure is due to the fact that the ASM Design Plant, $G_3(s) = G_{p3}(s) / s$ has singular values which roll-off at -40 db/dec and -60 db/dec whereas the target ASM (Kalman filter-based) loop, $G^3_{KF}(s)$, has singular values which both roll off at -20 db/dec.

In fig. 4.5.2.11 we see that errors in the frequency range 2 to 20 rad/sec will be amplified to generate the controls ($\Delta\Theta_c$ and ΣB_{lc}) to the ASM plant, $G_{p3}(s)$. A SVD at the worst case frequency (ω_o = 4.75 rad/sec) shows that errors which are collinear with

$$\underline{e}(t) = \begin{bmatrix} \underline{0.8703} \sin \omega_o t & \text{ft} \\ 0.493 \sin(\omega_o t + 37.8^o) & \text{ft/sec} \end{bmatrix} \tag{4.117}$$

will produce controls which are collinear with

$$\underline{u}_p(t) = 1.4374 \begin{bmatrix} \underline{0.988} \sin(\omega_o t + 30.3^o) & \text{deg of } \Delta\Theta_c \\ 0.157 \sin(\omega_o t - 6.1^o) & \text{deg of } \Sigma B_{lc} \end{bmatrix} \tag{4.118}$$

This implies that large errors in x_L-Σx (load deviation from center) will require a large $\Delta\Theta_c$ (differential collective).

In order to better understand the directionality properties of the ASM compensator, we have provided MOID and MOOD plots for $K_3(s)$ in figs. 4.5.2.12 and 4.5.2.13, respectively.

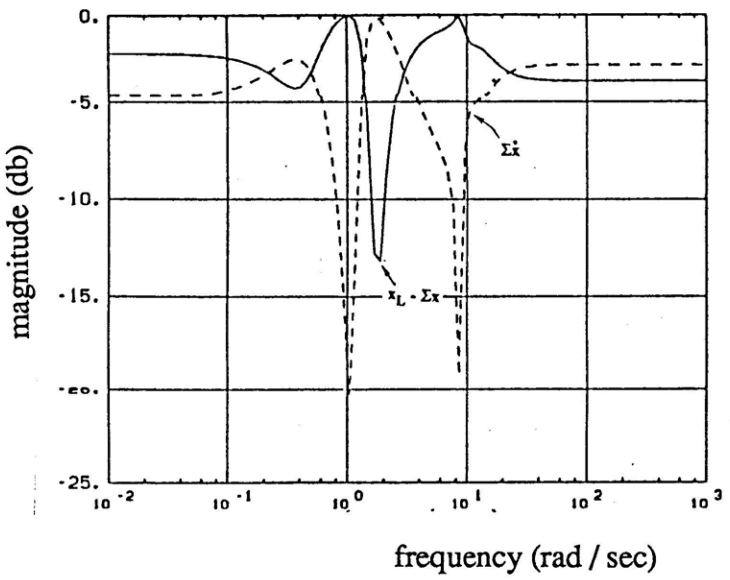

Fig. 4.5.2.12: ASM Compensator MOID Plot

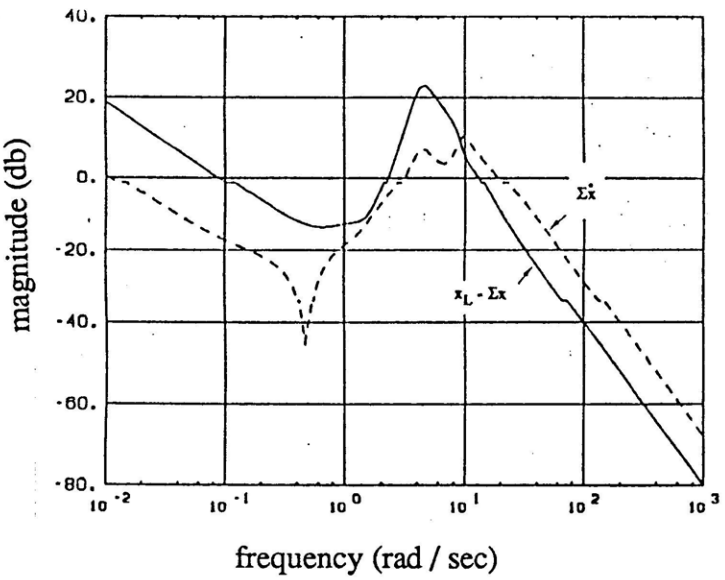

Fig. 4.5.2.13: ASM Compensator MOOD Plot

The MOID plot in Fig. 4.5.2.12 shows that the error directions which receive maximum amplification vary considerably with frequency. The MOOD plot in Fig. 4.5.2.13 shows much less variation in the corresponding outputs.

Finally, it is important to understand the effect of reference commands and sensor noise on the controls. This is best done by examining the reference to control tfm. Fig. 4.5.2.14 shows the singular values for the recovered ASM reference to control tfm. Figs. 4.5.2.15 and 4.5.2.16 show the corresponding MOID and MOOD plots, respectively.

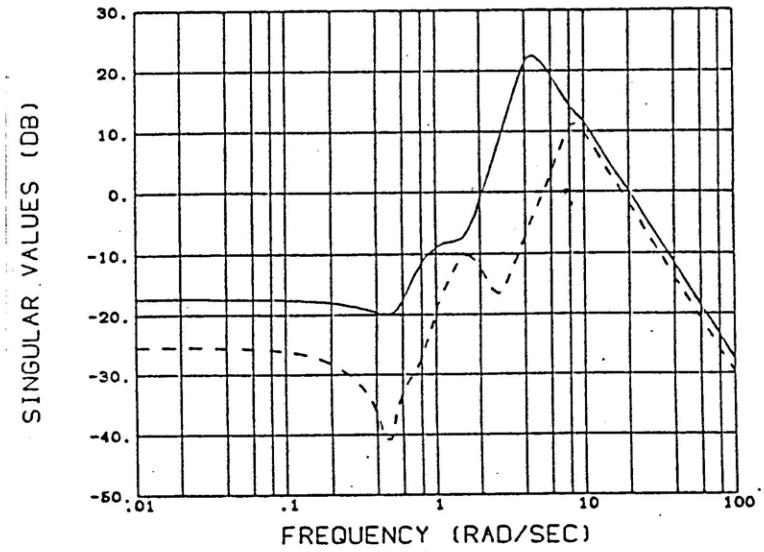

Fig. 4.5.2.14: Recovered ASM Reference to Control Singular Values.

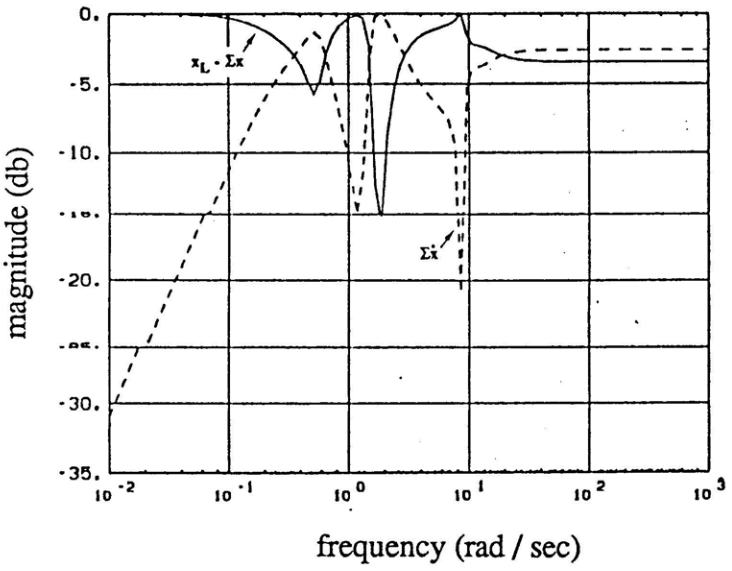

Fig. 4.5.2.15: Reference to Control MOID Plot

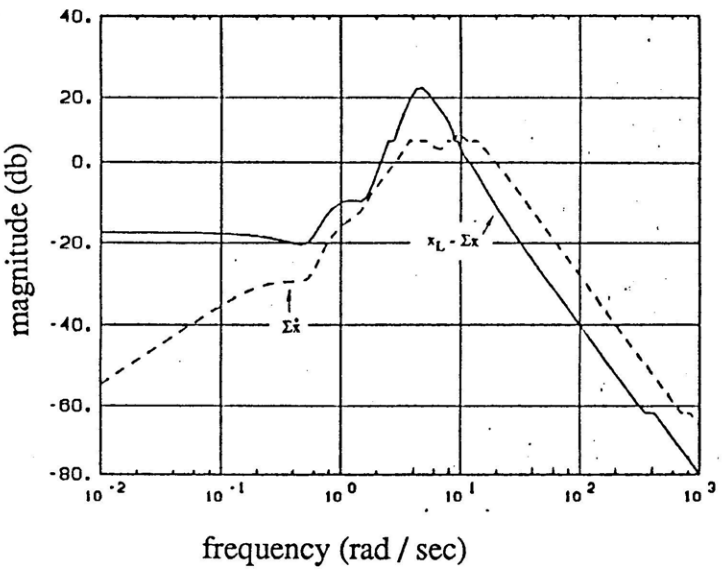

Fig. 4.5.16: Reference to Control MOOD Plot

Fig. 4.5.2.14 indicates that some references commands for x_L-Σx and $\Sigma \dot{x}$ in the frequency range 2 - 20 rad/sec and 6-20 rad/sec will be amplified to generate the appropriate controls $\Delta\Theta_c$ and ΣB_{lc}. A SVD at the worst case freqeuncy (ω_o = 4.75 rad/sec) shows us that references which are colinear with

$$\underline{r}(t) = \begin{bmatrix} \underline{0.863} \sin \omega_o t & \text{ft} \\ 0.506 \sin(\omega_o t + 24^o) & \text{ft/sec} \end{bmatrix} \tag{4.119}$$

produce controls which are colinear with

$$\underline{u}_p(t) = 1.33 \begin{bmatrix} \underline{0.987} \sin(\omega_o t + 23.3^o) & \text{deg} \\ 0.16 \sin(\omega_o t - 11.9^o) & \text{deg} \end{bmatrix}. \tag{4.120}$$

Typically we want to regulate the load motion ($x_L - \Sigma x = 0$) and command $\Sigma \dot{x}$. To assure reasonable controls for given reference commands, Fig. 4.5.2.14 indicates that pre-filtering is desirable. For this reason we recommend that $x_L - \Sigma x$ and $\Sigma \dot{x}$ reference commands be passed through a 3rd order Butterworth filter:

$$H(s) = \omega_0^3 / (s^2 + 2\omega_0 s^2 + 2\omega_0^2 s + \omega_0^3) \tag{4.121}$$

with ω_0 = 4 rad/sec. This reduces the + 80 db/dec slope between ω = 2 to 4 rad/sec to 20 db/dec.

Finally it is important to emphasize the affect of decreasing ρ_3. Decreasing ρ_3 causes the "far away" compensator poles (to be discussed subsequently) to move further from the origin. This improves our stability robustness. Doing so, however, increases the amount that errors and references are amplified to generate controls. This means more control action, pitching, and oscillations in the vertical plane. In order to keep the control action, pitching, and oscillations "somewhat reasonable" we did not lower ρ_3 below 10^{-5}; i.e. we traded-off stability robustness for performance. The extent to which this trade-off is pronounced shall be shown when time simulat - ions are presented. It should be noted that as $\rho_3 \rightarrow 0$, however, the reference to control tfm becomes improper. This implies that for small enough ρ_3, step-like commands result in impulse-like controls.

4.5.3 ASM AFCS Poles and Zeros

To further understand the strategy of the recovered ASM LQG/LTR compensator, it is instructive to compare the target ASM loop poles and zeros with the recovered ASM loop poles and zeros. The target ASM loop poles and zeros are given in Table 4.5.3.1 and are plotted in Fig. 4.5.3.1. These are the poles and zeros associated with the Target ASM open loop tfm, $G^3_{KF}(s) = C_3(sI - A_3)^{-1} H_{\mu 3}$. The recovered ASM open loop poles and zeros ($\rho_3 = 10^{-5}$) are given in Table 4.5.3.2. These are the poles and zeros associated with the recovered ASM open loop tfm, $G_{p3}(s)K_3(s)$.

Tables 4.5.3.1 and 4.5.3.2 show that for $\rho_2=10^{-5}$ the recovered ASM loop poles include the 7 poles of the ASM plant, $G_{p3}(s)$, 2 poles associated with the integrators, and 9 poles associated with the ASM LQG/LTR compensator, $K^3_{LQG/LTR}(s)$. The poles of $K^3_{LQG/LTR}(s)$ are simply the eigenvalues of the 9 x 9 matrix A_3-$B_3G_{\rho 3}$-$H_{\mu 3}C_3$. The tables also show that the recovered ASM loop zeros include the 4 zeros of the ASM plant, $G_{p3}(s)$, and 7 zeros associated with the ASM LQG/LTR compensator, $K^3_{LQG/LTR}(s)$. The zeros of $K^3_{LQG/LTR}(s) = G_{\rho 3}(sI - A_3 + B_3G_{\rho 3} + H_{\mu 3}C_3)^{-1}H_{\mu 3}$ can be shown to be the zeros of the transfer function matrix, $G_{\rho 3}(sI - A_3)^{-1}H_{\mu 3}$. This

follows from the fact that

$$\begin{bmatrix} sI-A_3+B_3G_{\rho 3}+H_{\mu 3}C_3 & -H_{\mu 3} \\ G_{\rho 3} & 0 \end{bmatrix} = \begin{bmatrix} I & -B_3 \\ 0 & I \end{bmatrix} \begin{bmatrix} sI-A_3 & -H_{\mu 3} \\ G_{\rho 3} & 0 \end{bmatrix} \begin{bmatrix} I & 0 \\ -C_3 & I \end{bmatrix} \qquad (4.122)$$

The tables show that the 9 ASM LQG/LTR compensator poles consist of 5 poles which would move off toward infinity if ρ_3 were decreased. These poles are referred to as "far away poles" in Table 4.5.3.2. The other 4 ASM LQG/LTR compensator poles are lightly damped poles which would move toward the ASM plants' lightly damped zeros if ρ_3 were decreased. This follows from the fact that the ASM plants' lightly damped zeros do not appear in Fig. 4.5.3.1 which shows the target ASM loop poles and zeros. That is, they are not zeros of the target ASM open loop tfm,

Table 4.5.3.1: Target ASM Open Loop Poles and Zeros

Poles:	Zeros:
s = 0, 0 (Integrator per channel)	
s = 0.04022 ± j 0.4785; ζ = 0.084; ω_n = 0.4802	s = - 0.3754 ± j 0.71707; ζ = 0.4671; ω_n = 0.8038
s = - 0.1976 ± j 0.7364; ζ = 0.2592; ω_n = 0.7624	s = - 0.2724 ± j 0.735; ζ = 0.5877; ω_n = 0.4635
s = - 2.119	s = - 2.127
s = - 0.5313 ± j 2.624; ζ = 0.1984; ω_n = 2.678	s = - 0.5349 ± j 2.622; ζ = 0.199; ω_n = 2.676

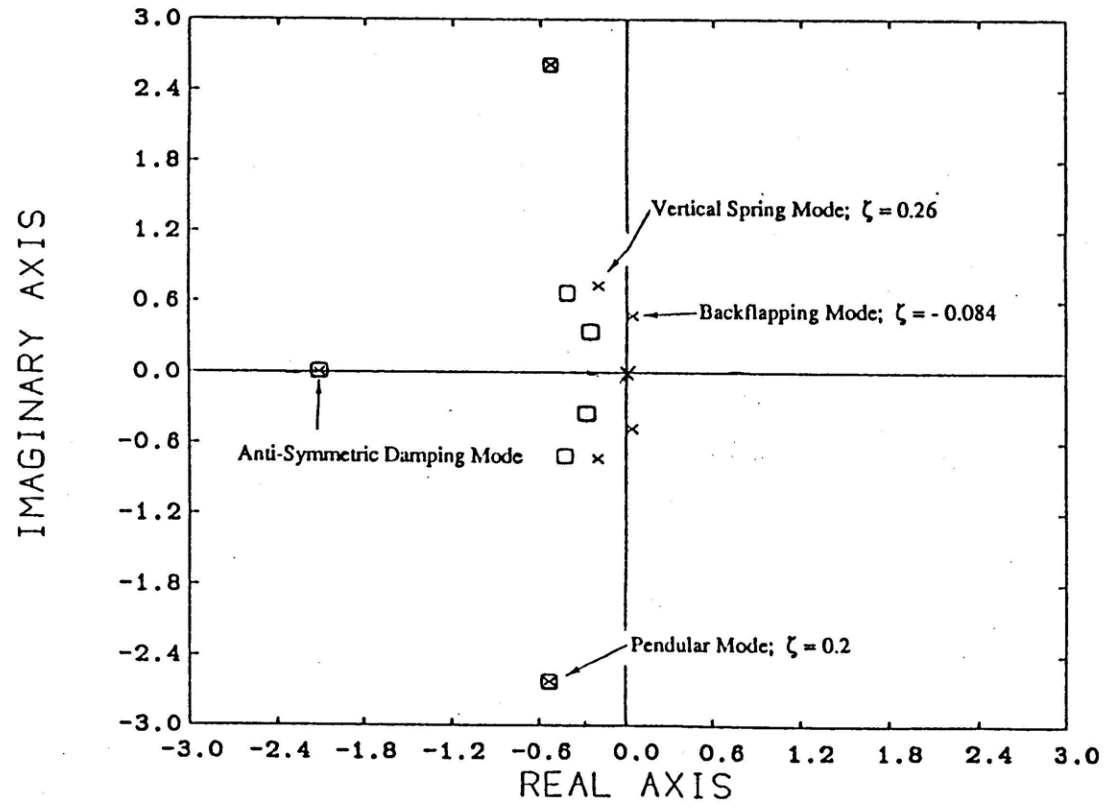

Fig. 4.5.3.1: Visualization of Target ASM Open Loop Poles and Zeros.

Table 4.5.3.2: Recovered ASM Open Loop Poles and Zeros

ASM Plant Poles:	$s = 0.04022 \pm j\ 0.4785$, $\omega_n = 0.4802$, $\zeta = -0.084$
	$s = -0.1976 \pm j\ 0.7364$, $\omega_n = 0.7624$, $\zeta = 0.2592$
	$s = -2.119$
	$s = -0.5313 \pm j\ 2.624$, $\omega_n = 2..678$, $\zeta = 0.1984$
ASM Plant Zeros:	$s = -0.1786 \pm j\ 6.413$, $\omega_n = 6.415$, $\zeta = 0.02784$
	$s = -1.3371 \pm j\ 9.807$, $\omega_n = 9.902$, $\zeta = 0.1385$
ASM Compensator Poles:	$s = 0,\ 0$ (Integrator per channel)
	$s = -1.887 \pm j\ 8.578$, $\omega_n = 8.783$, $\zeta = 0.2149$
	$s = -0.8031 \pm j\ 4.311$, $\omega_n = 4.386$, $\zeta = 0,1831$
	$s = -3.635 \pm j\ 3.942$, $\omega_n = 5.362$, $\zeta = 0.6779$
	$s = -5.974$
	$s = -11.75 \pm j\ 8.402$, $\omega_n = 14.44$, $\zeta = 0.8133$
ASM Compensator Zeros:	$s = -0.2272 \pm j\ 0.344$, $\omega_n = 0.4122$, $\zeta = 0.5511$
	$s = -0.3391 \pm j\ 0.6977$, $\omega_n = 0.7785$, $\zeta = 0.4372$
	$s = -2.124$
	$s = -0.5319 \pm j\ 2.621$, $\omega_n = 2.675$, $\zeta = 0.1989$.

$G^3_{KF(s)} = C_3(sI - A_3)^{-1}H_{\mu 3}$. These lightly damped poles shall be discussed in more details subsequently.

The tables also show that the 7 zeros of the ASM LQG/LTR compensator consist of 3 zeros which make the Anti-symmetric Damping and Pendular Modes uncontrollable, and 4 more zeros which provide damping for the Vertical Spring and Backflapping Modes. The fact that the Anti-symmetric Damping and Pendular Modes have been made uncontrollable is not very alarming since these modes are near our gain crossover frequencies and would otherwise deteriorate our stability margins.

Finally, the trade-off between performance and stability robustness should be made apparent.

Decreasing ρ_3 improves our stability margins. This, however, results in a loop with more lead and lightly damped poles. This, of course, results in larger controls, pitching, and oscillations in the vertical plane. Increasing ρ_3, worsens our stability margins but improves our performance. The trade-off is thus apparent.

Before studying the recovered ASM AFCS time response characteristics, it is instructive to compare the target ASM closed loop poles and zeros with the recoverd ASM closed loop poles and zeros. The target ASM closed loop poles and zeros are given in Table 4.5.3.3. These are the poles and zeros associated with the target ASM closed loop transfer function matrix, $T^3_{KF}(s) = G^3_{KF}(s)$ $[I+G^3_{KF}(s)]^{-1} = C_3(sI-A_3+H_{\mu 3}C_2)^{-1}H_{\mu 3}$. The recovered ASM closed loop poles and zeros are given in Table 4.5.3.4. These are the poles and zeros associated with the recovered ASM closed loop tfm, $T_3(s) = G_3(s)K_3(s)\ [I+G_3(s)K_3(s)]^{-1} = G_3(s)\ [I+G_{\rho 3}\Phi_3(s)B_3]^{-1}G_{\rho 3}\Phi_3(s)H_{\mu 3}$ $[I+C_3\Phi_3(s)H_{\mu 3}]^{-1}$ where $\Phi_3(s) \equiv (sI - A_3)^{-1}$. For convenience the target and recovered closed loop poles and zeros have been plotted in Figs. (4.5.3.2) - (4.5.3.3).

In examining the closed loop poles and zeros in Table 4.5.3.3 and 4.5.3.4, it is essential to identify which modes will have the greatest impact on our outputs, $x_L - \Sigma x$ ansd Σx, and which modes will have the greatest impact on internal quantities such as $\Delta\Theta_c$, Δz, ΣB_{lc}, and $\Sigma\theta$. First we examine the target ASM closed loop poles and zeros.

Figs. 4.5.3.1 - 4.5.3.2 convey the basic strategy of the ASM AFCS. The figures show that the Anti-Symmetric Damping and Pendular Modes will be made uncontrollable and that the Vertical Spring and Backflapping Modes will be drawn toward compensator zeros. From these figures we expect the ($\zeta = 0.42$, $\omega_n = 0.69$, $\tau = 3.5$) poles, associated with the Backflapping Mode, to have a predominant effect on Σx, $\Sigma\theta$, and ΣB_{lc}. Because of coupling, however, this mode may also affect $x_L - \Sigma x$. Similarly the ($\zeta = 0.32$, $\omega_n = 0.95$, $\tau = 3.2$) poles, associated with the Vertical Spring Mode, is expected to have a predominant effect on $x_L - \Sigma x$, Δz, and $\Delta\Theta_c$. As far as the recovered closed loop poles are concerned the poles of greatest impact are those which approach the

Table 4.5.3.3: Target ASM Closed Loop Poles and Zeros

Poles $\lambda_i(A_3 - H_{\mu 3}C_3)$:	$s = -0.5423$
	$s = -0.5748$
	$s = -0.2907 \pm j\,0.6241$, $\omega_n = 0.6885$, $\zeta = 0.4222$
	$s = -0.3062 \pm j\,0.9024$, $\omega_n = 0.9529$, $\zeta = 0.3214$
	$s = -2.113$
	$s = -0.5323 \pm j\,2.626$, $\omega_n = 2.679$, $\zeta = 0.1987$
Zeros:	$s = -0.2724 \pm j\,0.375$, $\omega_n = 0.4635$, $\zeta = 0.5877$
	$s = -0.3754 \pm j\,0.7107$, $\omega_n = 0.8038$, $\zeta = 0.4671$
	$s = -2.127$
	$s = -0.5349 \pm j\,2.622$, $\omega_n = 2.676$, $\zeta = 0.1999$

Table 4.5.3.4: Recovered ASM Closed Loop Poles and Zeros

Poles:	$\lambda_i(A_3-H_{\mu 3}C_3)$:	$s = -0.5423$
		$s = -0.5748$
		$s = -0.2907 \pm j\,0.6241$, $\omega_n = 0.6885$, $\zeta = 0.4222$
		$s = -0.3062 \pm j\,0.9024$, $\omega_n = 0.9529$, $\zeta = 0.3214$
		$s = -2.113$
		$s = -0.5323 \pm j\,2.626$, $\omega_n = 2.679$, $\zeta = 0.1987$
	$\lambda_i(A_3-B_3G_{\rho 3})$:	$s = -1.005 \pm j\,4.177$, $\omega_n = 4.296$, $\zeta = 0.2339$
		$s = -3.463 \pm j\,3.199$, $\omega_n = 4.715$, $\zeta = 0.7346$
		$s = -4.907$
		$s = -1.891 \pm j\,8.47$, $\omega_n = 8.679$, $\zeta = 0.2180$
		$s = -11.25 \pm j\,7.797$, $\omega_n = 13.69$, $\zeta = 0.8218$
Zeros: ASM Plant :		$s = -0.1786 \pm j\,6.413$, $\omega_n = 6.415$, $\zeta = 0.027841$
		$s = -1.371 \pm j\,9.807$, $\omega_n = 9.902$, $\zeta = 0.1385$
ASM LQG/LTR Compensator:		$s = -0.2272 \pm j\,0.344$, $\omega_n = 0.4122$, $\zeta = 0.511$
		$s = -0.3391 \pm j\,0.6977$, $\omega_n = 0.7758$, $\zeta = 0.4372$
		$s = -2.124$
		$s = -0.5319 \pm j\,2.621$, $\omega_n = 2.675$, $\zeta = 0.1989$

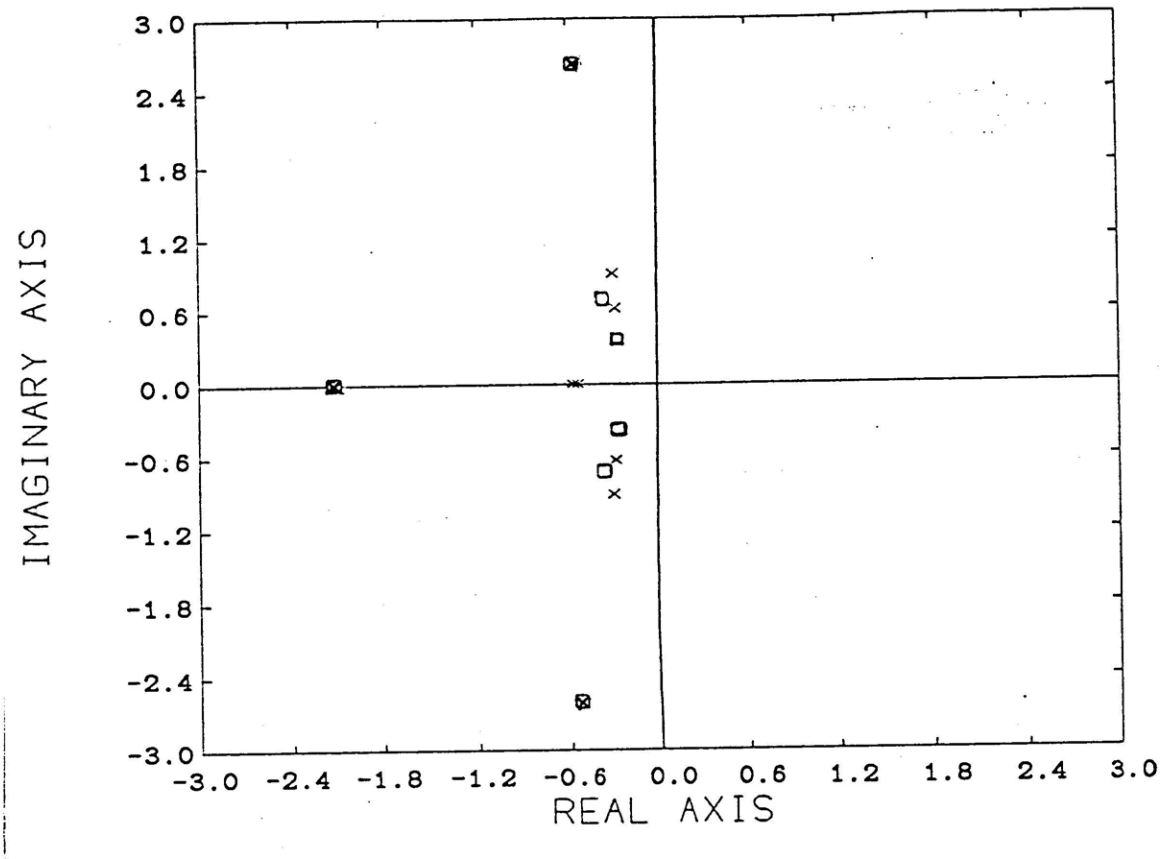

Fig. 4.5.3.2: Visualization of Target ASM Closed Loop Poles and Zeros.

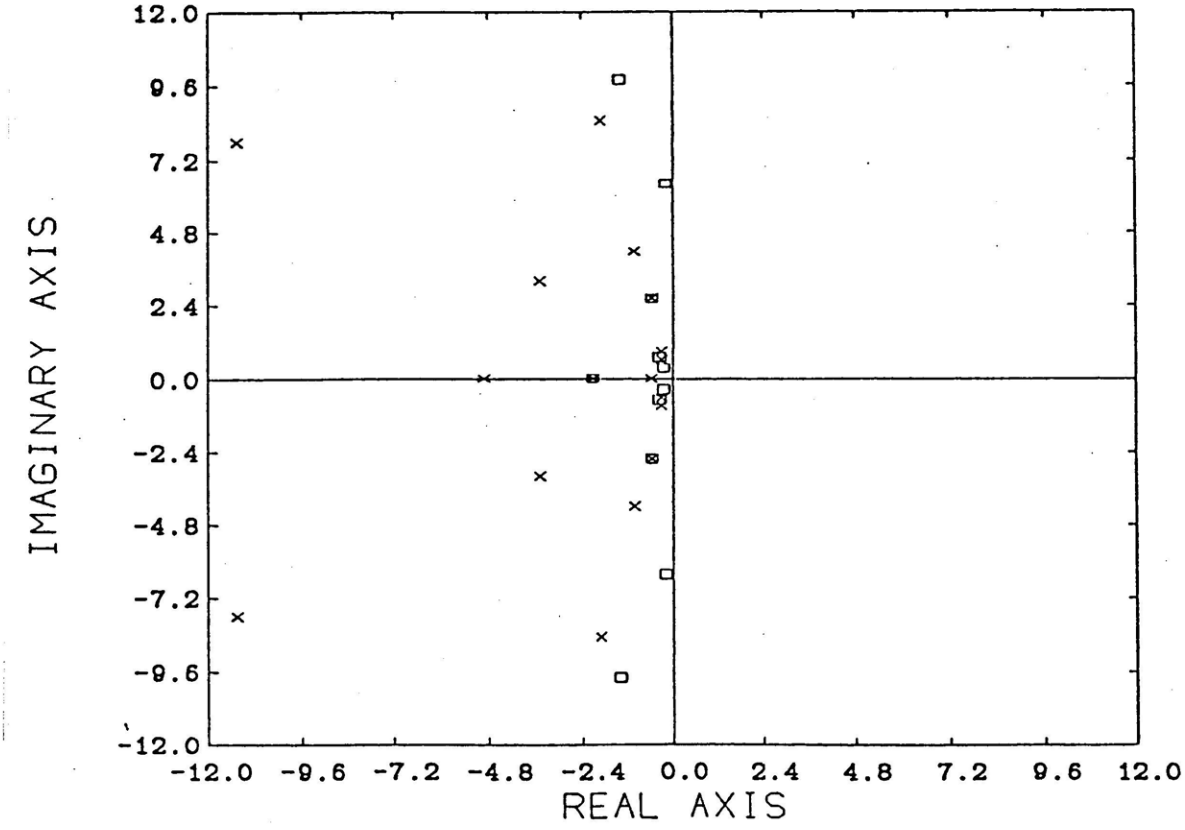

Fig. 4.5.3.3: Visualization of Recovered ASM Closed Loop Poles and Zeros.

lightly damped zeros ($\zeta = 0.23,\ \omega_n = 4.3,\ \tau = 1$) and ($\zeta = 0.22,\ \omega_n = 8.7,\ \tau = 0.22$). Because the $\tau = 0.22$ pole, approaching the "helicopter zero", decays so rapidly we expect it to have little affect on the outputs. Its greatest impact is expected to be on ΣB_{lc}. The impact of the $\tau = 1$ pole, approaching the "load motion zero", is expected to affect the output $x_L - \Sigma x$ somewhat. Its greatest impact, however, is expected to be on Δz.

4.5.4 Time Domain Evaluation of ASM AFCS

In this section the ability of the ASM AFCS to regulate the load deviation from center ($x_L - \Sigma x$) and follow average horizontal velocity ($\Sigma \dot{x}$) commands is examined. Although $x_L - \Sigma x$ is usually commanded to zero we'll also look at a nonzero command for the variable.

(A) $\Sigma \dot{x}$ Command Following

To examine the ASM AFCS's ability to follow $\Sigma \dot{x}$ commands we will drive it with a pre-filtered step. The pre-filtered step will be the output of a 3rd order Butterworth filter with cut-off frequency at $\omega_0 = 4$ rad/sec which is above the closed loop bandwidth ($\omega_{CL3} \approx 1.5$ rad/sec). The resulting time responses are given in Figs. 4.5.4.1 - 4.5.4.2.

Fig. 4.5.4.1a shows the resulting average horizontal velocity, $\Sigma \dot{x}$, response with an overshoot of 5% and an undershoot of 15%. The risetime (time to reach 1 ft/sec) is seen to be on the order of 1.5 secs and the response takes about 12 secs to settle down. Because of the integral augmentation we see that the $\Sigma \dot{x}$ response exhibits zero steady state error. This response is primarily governed by the closed loop poles ($\zeta = 0.32,\ \omega_n = 0.96,\ \tau = 3.2$) which are associated with the ASM Backflapping Mode.

Fig. 4.5.4.1b shows the resulting load deviation from center, $x_L - \Sigma x$, response which is dominated by the ($\zeta = 0.32,\ \omega_n = 0.96,\ \tau = 3.2$) pole associated with the Vertical Spring Mode. The lightly damped pole ($\zeta = 0.23,\ \omega_n = 4.3,\ \tau = 1$) which would approach the "load motion zero" if ρ_3 werte decreased, also has a noticeable impact on the response. The response shows

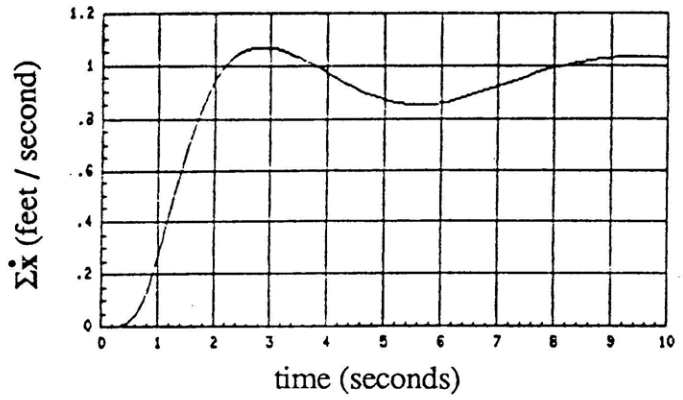

a) Average Horizontal Velocity

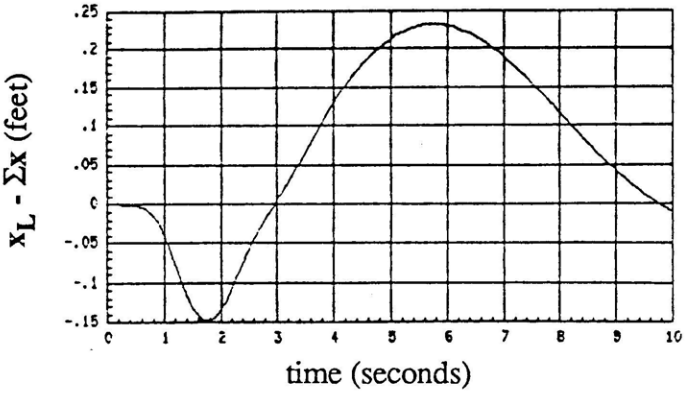

b) Load Deviation from Center

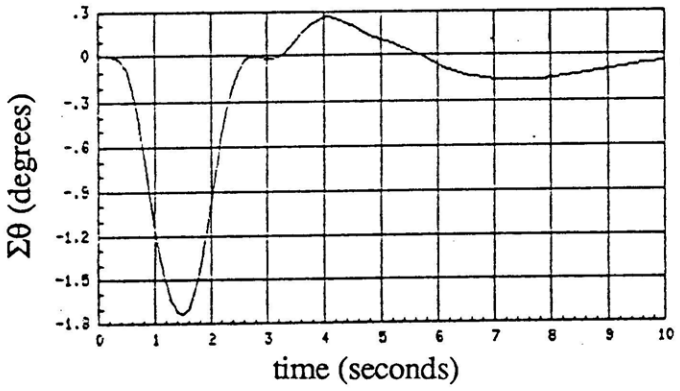

c) Average Pitch Attitude

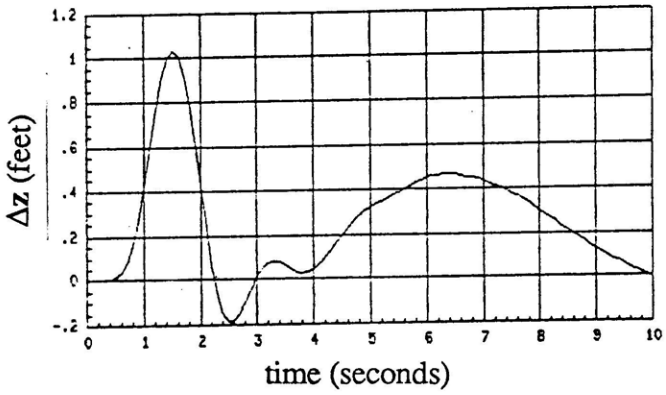

d) Vertical Separation

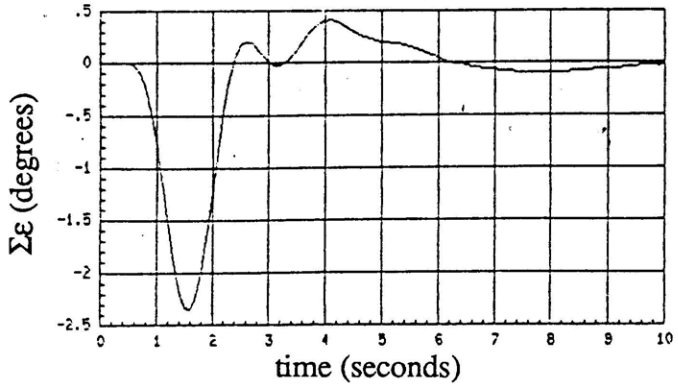

e) Average Tether Angle

Fig. 4.5.4.1: ASM AFCS Response to a $\Sigma\dot{x}$ = 1 ft / sec Filtered Step Command.

that a filtered Σx = 1 ft / sec command results in a peak x_L - Σx of about 0.225 ft.

Fig. 4.5.4.1.c and 4.5.4.1d show the corresponding average pitch attitude, $\Sigma\theta$, and vertical separation, Δz, responses. Although the $\Sigma\theta$ response is quite reasonable, the Δz response exhibits far too large rates. The reasons for the large rates are two-fold. One reason, obviously, has to do with the lightly damped poles near the lightly damped load motion zeros. If we were to make ρ_3 larger (recover less of our target loop) then these rates would decrease substantially but they would do so at the expense of our stability margins; i.e. a trade-off between performance and stability robustness. Because we have a high bandwidth design this trade-off is exacerbated. It thus follows that the main reason for the large rates is because of the high bandwidth specification coupled with the "relatively large" stability robustness specification. Consequently, a high performance (high bandwidth) design is feasible only if modeling errors are sufficiently small.

The $\Sigma\varepsilon$ response shown in Fig. 4.5.4.1e also exhibits more oscillation than desired.

Finally, the ΣB_{lc} and $\Delta\Theta_c$ responses in Fig. 4.5.4.2 exhibit similar characteristics to the $\Sigma\theta$ and Δz responses.

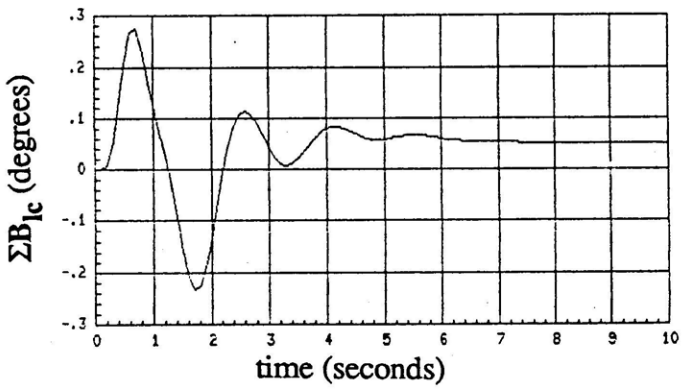

a) Average Cyclic Control

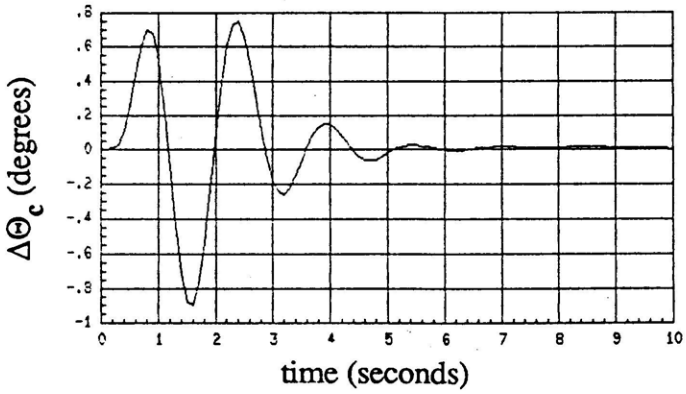

b) Differential Collective Control

Fig. 4.5.4.2: ASM AFCS Controls for a $\Sigma\dot{x}$ = 1 ft / sec Filtered Step Command.

In summary, thes responses confirm the rather intuitive fact that a high performance (high bandwidth) design is feasible only if model uncertainty is sufficiently low. If model uncertainty is high then a high bandwidth Equal Tether AFCS becomes unfeasible. This is because, in such a case, the large robustness requirement forces the helicopters to undergo substantial oscillations in the vertical plane in order to regulate the load motion when horizontal velocities are commanded. Moreover, if model uncertainty is high then only a low bandwidth design becomes feasible.

(B) $x_L - \Sigma x$ Command Following

Although typically the load deviation, $x_L - \Sigma x$, will be commanded to zero, it is instructive to see the effect of an $x_L - \Sigma x$ step command. In this section we drive the ASM AFCS with a pre-filtered $x_L - \Sigma x = -1$ ft step. Physically, this amounts to commanding a vertical separation, Δz, of - 2 ft (slave above master). This is because in the steady state $x_L - \Sigma x = \hat{Z}\,\Delta z = 0.5\,\Delta z$. As before, the pre-filter shall be a 3rd order Butterworth with cut-off frequency at $\omega_0 = 4$ rad/sec. The resulting time responses are given in Figs. 4.5.4.3 - 4.5.4.4.

Fig. 4.5.4.3a shows the resulting $\Sigma\dot{x}$ response. We see that a filtered $x_L - \Sigma x = -1$ step command results in a peak $\Sigma\dot{x}$ of about 0.19 ft / sec.

Fig. 4.5.4.3b shows the load deviation, $x_L - \Sigma x$, response. The figure shows that the response exhibits a 17% undershoot and about a 19% overshoot. These rather large excursions are due to the lightly damped poles ($\zeta = 0.23$, $\omega_n = 4.3$, $\tau = 1$) and the load motion zero's near them ($\zeta = 0.03$, $\omega_n = 6.42$, $\tau = 5.6$). The response's settling time is dominated by the ($\zeta = 0.32$, $\omega_n = 0.96$, $\tau = 3.2$) poles associated with the Vertical Spring Mode and the zeros ($\zeta = 0.44$, $\omega_n = 0.78$, $\tau = 2.95$) near them.

Figs. 4.5.4.3c and 4.5.4.3d show the corresponding $\Sigma\theta$ and Δz responses. As expected, they are more oscillatory than desired. If ρ_3 were increased these oscillations would decrease substantially. Increasing ρ_3, however, would result in smaller stability margins. For $\rho_3 = 10^{-5}$

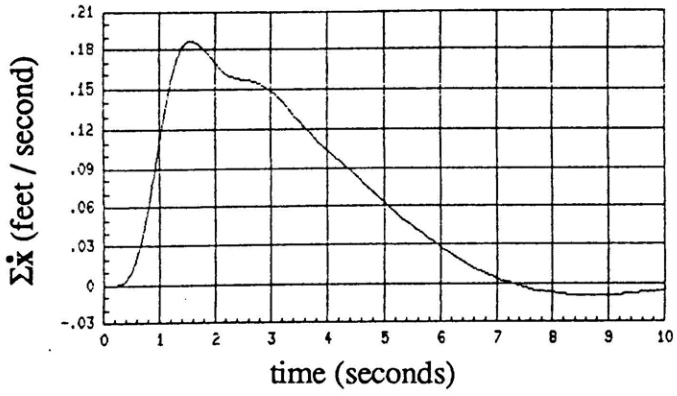

a) Average Horizontal Velocity

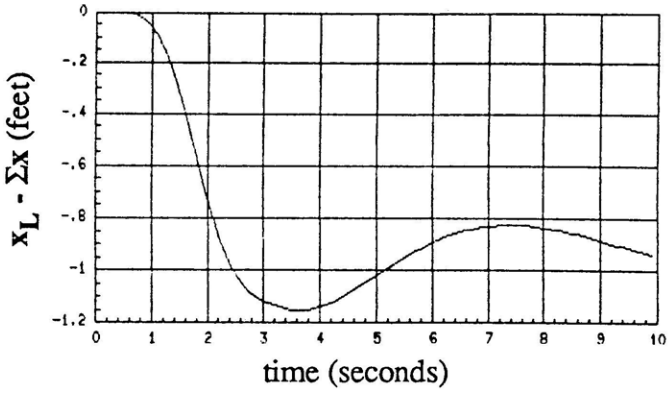

b) Load Deviation from Center

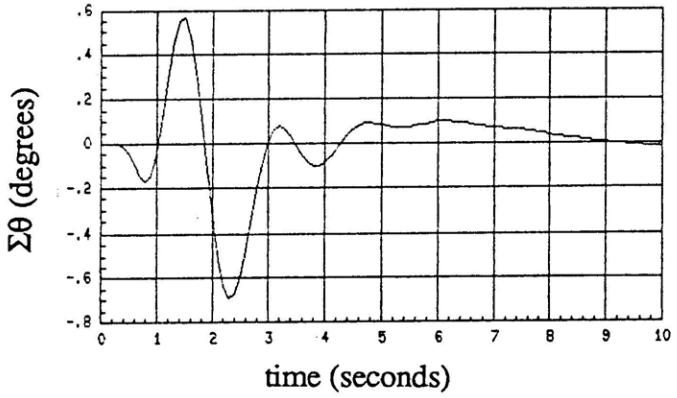

c) Average Pitch Attitude

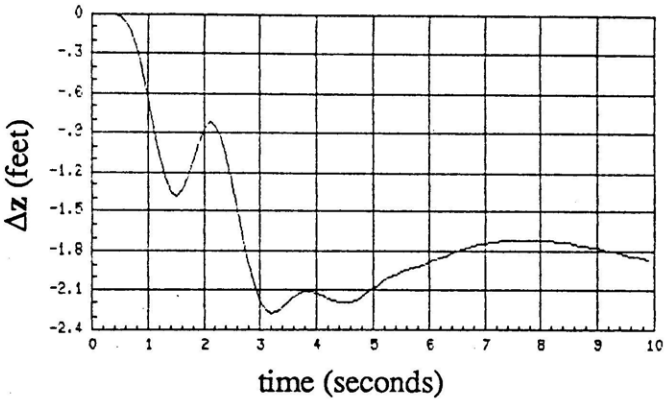

d) Vertical Separation

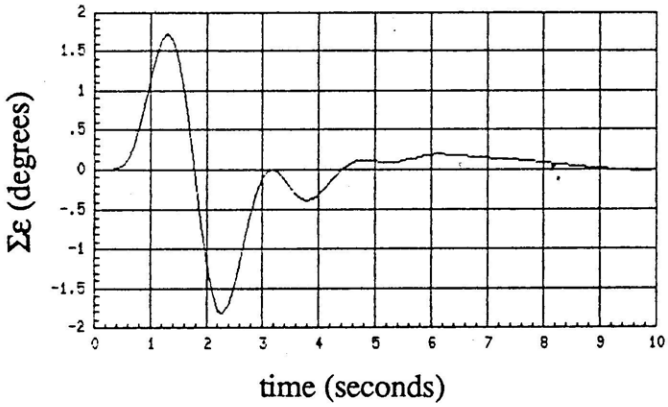

e) Average Tether Angle

Fig. 4.5.4.3: ASM AFCS Response to an x_L-Σx = -1 ft Filtered Step Command.

the ASM AFCS has a guaranteed multivariable phase margin of 41.5°. If the bandwidth of the design were reduced we could have such a margin without the substantial pitching and oscillations. The bottom line is that, in general, a trade-off must be made between performance and stability robustness and that the high performance specification only serves to make this trade-off worse.

Fig. 4.5.4.3e shows the average tether angle, $\Sigma\varepsilon$, response resulting from the filtered load deviation command. The response is seen to be dominated by the Pendular Mode ($\zeta = 0.2$, $\omega_n = 2.7$, $\tau = 1.9$).

Finally, Figs. 4.5.4.4a and 4.5.4.4b show the corresponding average cyclic, ΣB_{lc}, and differential collective, $\Delta\Theta_c$, responses. We see that these responses have characteristics similar to those exhibited by the $\Sigma\theta$ and Δz responses.

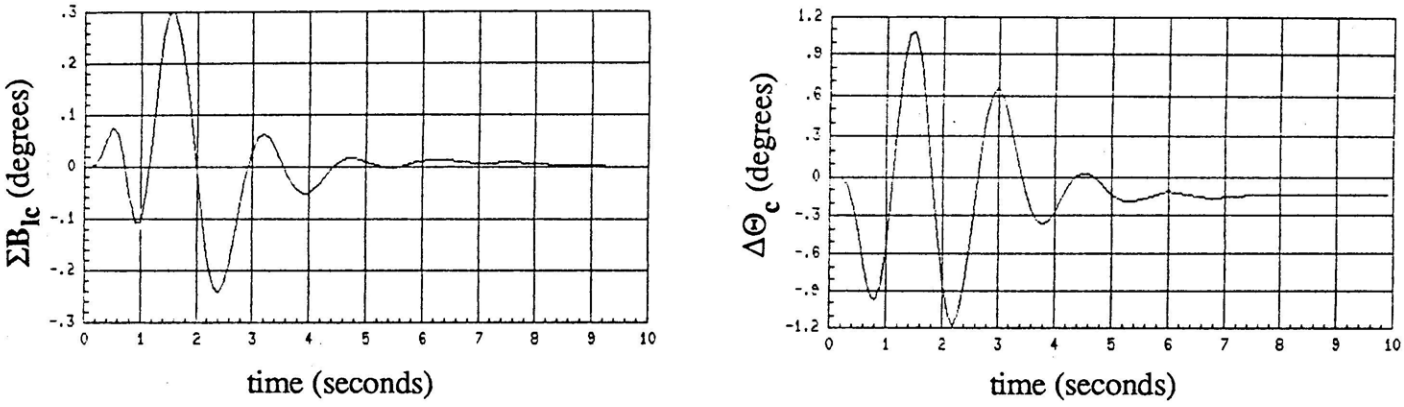

a) Average Cyclic Control

b) Differential Collective Control

Fig. 4.5.4.4: ASM AFCS Controls for an $x_L - \Sigma x = -1$ ft Filtered Step Command.

In summary, the above time responses further confirm the fact that a high performance (high bandwidth) ASM AFCS is feasible only if modeling uncertainty is sufficiently low.

(C) x_L - Σx Disturbance Rejection

Finally, to examine the ability of the ASM AFCS to regulate the load motion (x_L - Σx) in the presence of disturbances, we shall consider an initial condition response in which initially the load is displaced 1 ft to the left of the center (x_L - Σx = - 1 ft) due to an initial average tether angle, $\Sigma\varepsilon$ = - 4.3 degs (initially we have $\Sigma\theta = \Delta z = 0$ and $x_L - \Sigma x = x_L' = H\,\Sigma\varepsilon$). The resulting time responses are given in Fig. 4.5.4.5 - 4.5.4.6.

Fig. 4.5.4.5a shows the resulting Σx response. The response shows that a peak value of about 0.8 ft/sec occurs. The response takes about 10 seconds to settle down to zero.

Fig. 4.5.4.5b shows the corresponding x_L - Σx response. The response exhibits a very large overshoot and is dominated by the ($\zeta = 0.32$, $\omega_n = 0.96$, $\tau = 3.2$) pole, associated with the Vertical Spring Mode, and the zeros ($\zeta = 0.44$, $\omega_n = 0.78$, $\tau = 2.95$) near them.

Figs. 4.5.4.5c and 4.5.4.5d show the corresponding $\Sigma\theta$ and Δz responses. As with the command following responses, these responses are too fast. To remedy this we can either increase ρ_3 and give up stability robustness or increase μ_3 and give up performance (speed).

Fig. 4.5.4.5e shows the $\Sigma\varepsilon$ response and Figs. 4.5.4.6a and 4.5.4.6b contains the corresponding controls, ΣB_{lc} and $\Delta\Theta_c$, respectively.

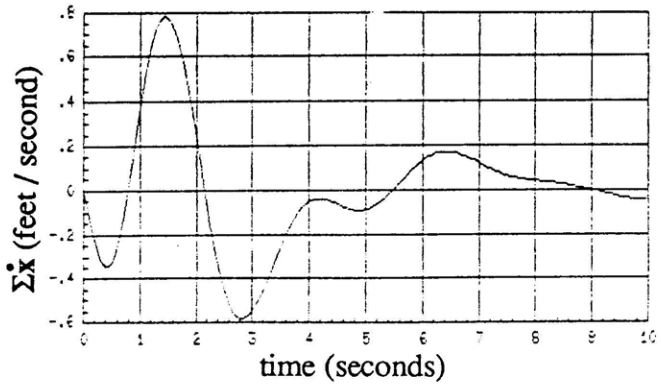

a) Average Horizontal Velocity

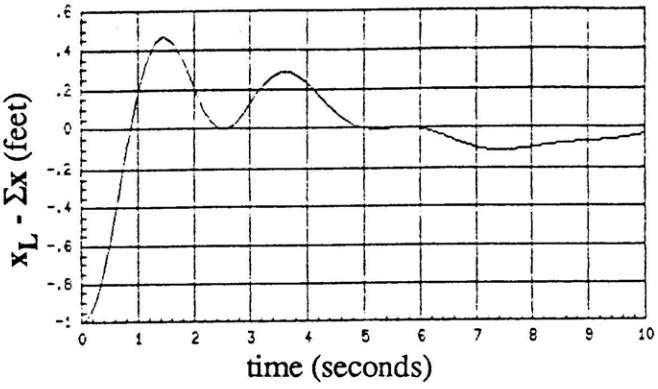

b) Load Deviation from Center

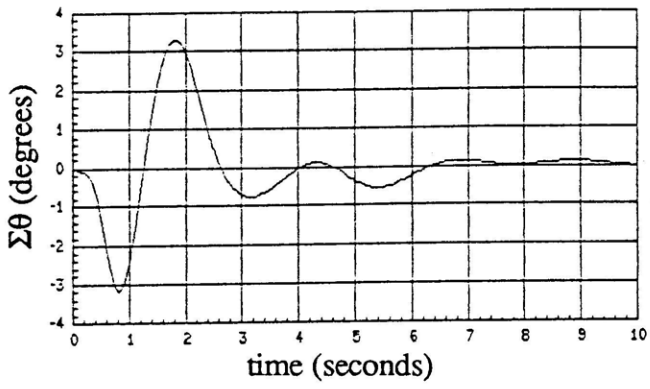

c) Average Pitch Attitude

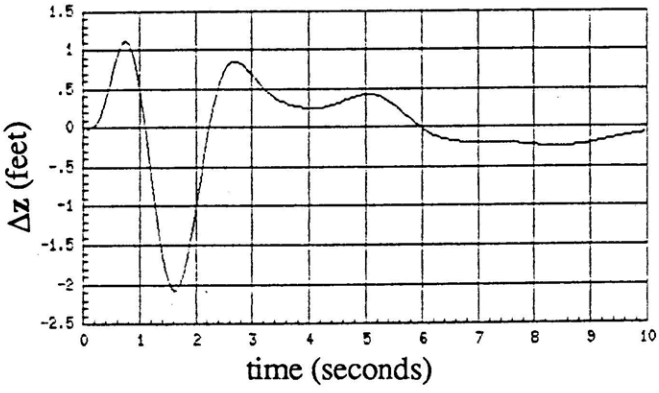

d) Vertical Separation

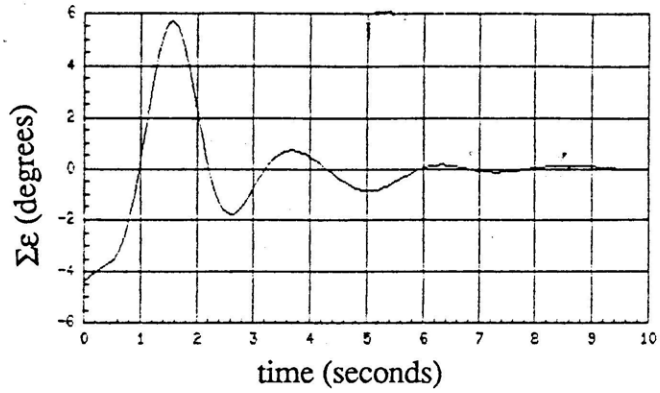

e) Average Tether Angle

Fig. 4.5.4.5: ASM AFCS Response to an x_L - Σx = - 1 ft Initial Condition.

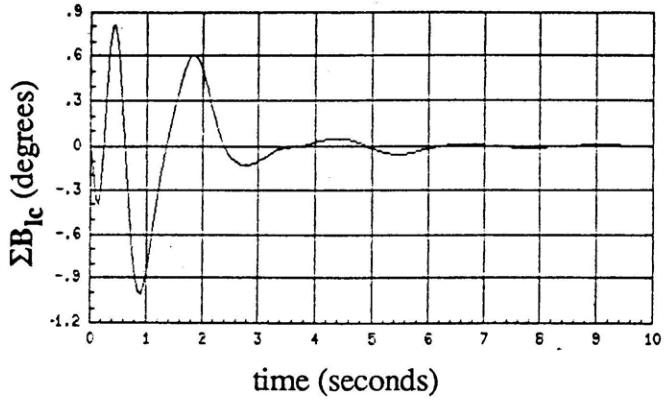

a) Average Cyclic Control

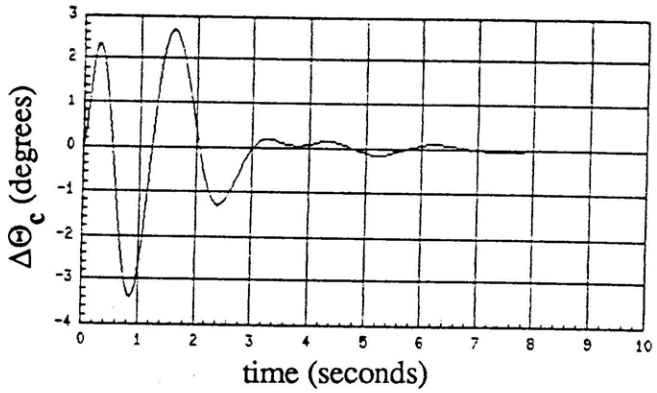

b) Differential Collective Control

Fig. 4.5.4.6: ASM AFCS Controls for an x_L - Σx = - 1 ft Initial Condition

In summary, the responses show that a high performance (high) bandwidth) design is feasible only if model uncertainty is sufficiently low. In such a case we can increase ρ_3 to reduce the substantial pitching and oscillations that the helicopters must undergo in regulating the load motion. If model uncertainty is high, however, then the above high bandwidth ASM AFCS becomes unfeasible. Chapters 5 and 6 attempt to remedy this by examining the virtues of a TLHS in which the master and slave tether lengths are unequal. Comparisons are made with the Equal Tethered AFCS developed in this chapter.

4.5.5 Summary of ASM AFCS Design

In this section, the LQG/LTR design methodology was applied to the ASM Design Plant; an unstable TITO system with considerable low frequency phase lag and four lightly damped high frequency zeros. It was shown, as expected from Chapter 3, that controlling the ASM PLant is very difficult; particularly when the specifications call for a high performance (high bandwidth) robust design. More specifically, it was shown that for such specifications the trade-off between stability robustness and performance is particularly pronounced. Raising the bandwidth would

exacerbate the situation since this would result in more control action and larger oscillations in the vertical plane. Lowering the bandwidth would, of course, help but would be sacrificing our "high performance".

In summary, we conclude that the LQG/LTR design procedure can be used to develop a real world ASM AFCS. A high performance (high bandwidth) ASM AFCS, however, is only feasible if model uncertainty is sufficiently low. If model uncertainty is high then a high performance design becomes unfeasible. This is because, in such a case, the large robustness requirement forces the helicopters to undergo substantial pitching and oscillations in the vertical plane in order to regulate the load motion when horizontal velocity commands are issued. Moreover, if model uncertainty is high then only a low bandwidth design becomes feasible. Chapters 5 and 6 shall examine whether having unequal tether lengths lessons the above trade-off between performance and stability robustness.

4.6 Final Time Domain Evaluation of Equal Tether AFCS

For completeness, we examine the time characteristics of the combined AVM, SM, and ASM AFCS's. More specifically, in this section the following command scenario is studied:

$\Sigma\dot{z}$ = 5 ft / sec unfiltered step command;

Δx = 1 ft initial condition;

$x_L - \Sigma x = -1$ ft ($\Sigma\varepsilon = -4.3$ degs) initial condition;

$\Sigma\dot{x}$ = 5 ft / sec filtered step command.

As before, a 3rd order Butterworth filter with $\omega_0 = 4$ rad/sec is used to generate the $\Sigma\dot{x}$ step command. The resulting time responses for the individual helicopters and tethers are given in Fig. 4.6.1. As expected they exhibit the helicopters undergo substantial pitching and oscillations in the vertical plane in order to regulate the horizontal separation and load motion while following the horizontal and vertical velocity commands.

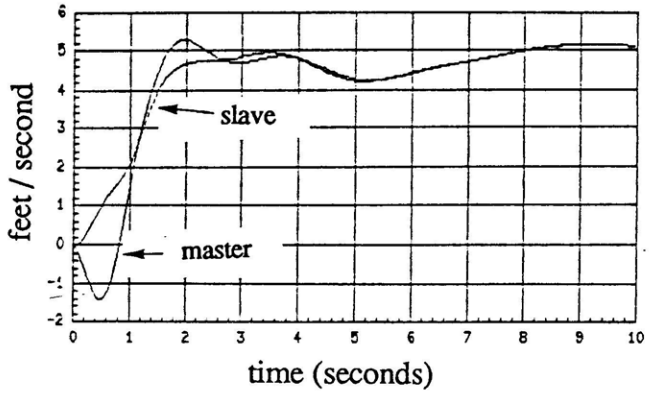

a) Horizontal Velocities

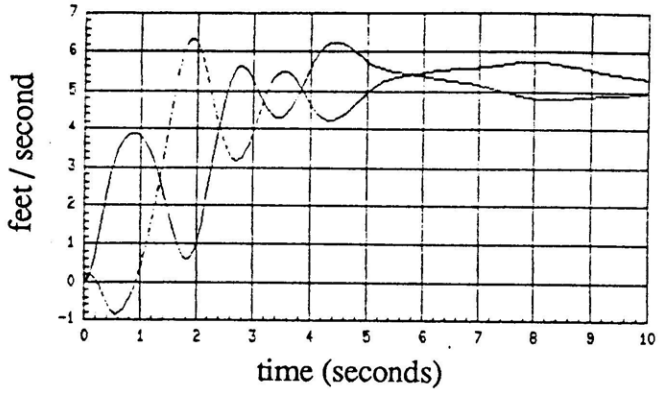

b) Vertical Velocities

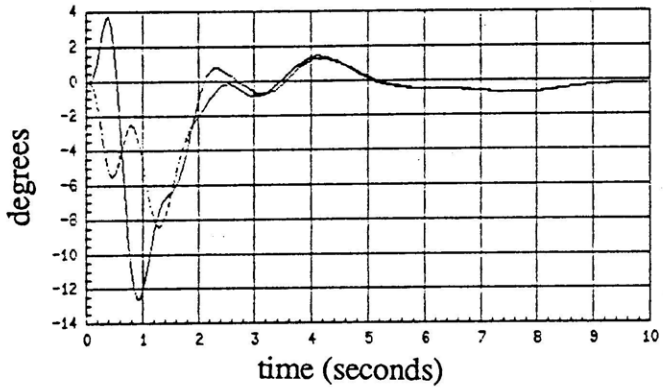

c) Pitch Attitudes

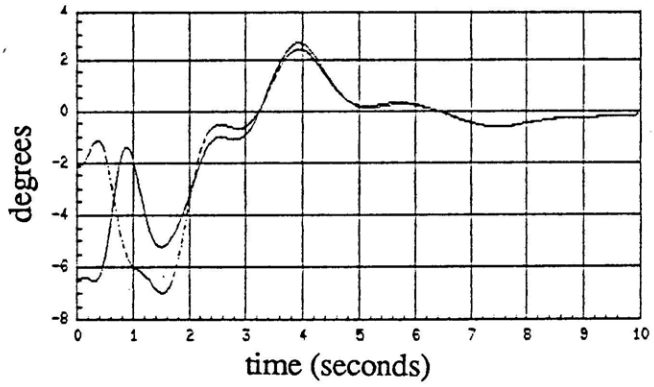

d) Tether Angles

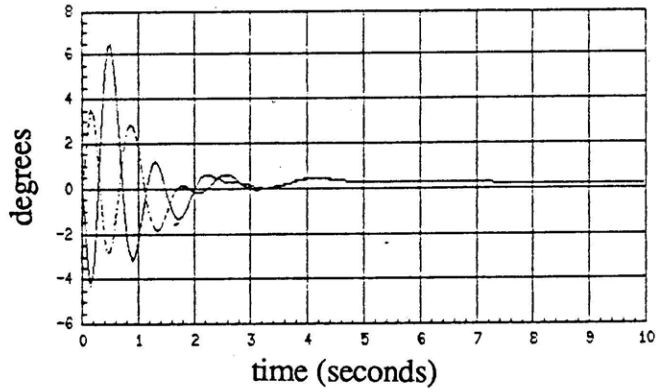

e) Cyclic Pitch Controls

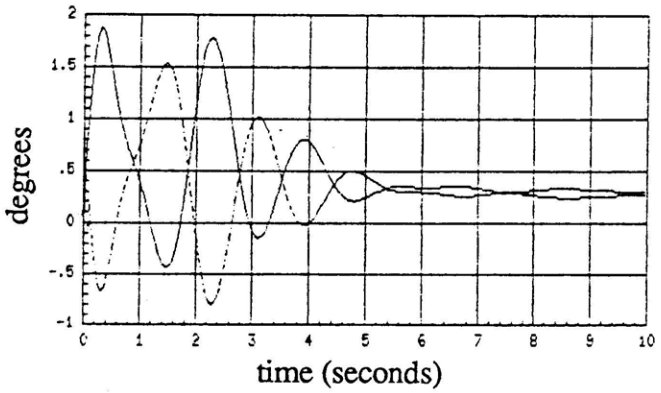

f) Collective Pitch Controls

Fig. 4.6.1: Individual Helicopter and Tether Response for Equal Tether AFCS.

4.7 Summary of Equal Tether AFCS Design

In this chapter the LQG/LTR design methodology was applied to the Equal Tether Design Plant discussed in Chapter 3. The method was used to systematically develop an Equal Tether AFCS satisfying the performance and robustness specifications presented in Chapter 3. The Equal Tether AFCS, consisting of an AVM AFCS, a SM AFCS, and an ASM AFCS, was evaluated in the frequency domain and in the time domain. The concept of MOID and MOOD plots were introduced to help visualize the directionality properties of the TITO ASM AFCS.

Finally, it was shown that a high performance (high bandwidth) Equal Tether AFCS is only feasible if model uncertainty is sufficiently low. If model uncertainty is high then such a design becomes unfeasible. This is because, in such a case, the large robustness requirement forces the helicopters to undergo substantial pitching and oscillations in the vertical plane in order to regulate the horizontal separation and load motion when horizontal and vertical velocities are commanded. Moreover, when model uncertainty is high then only a low bandwidth design becomes feasible. Such a design can be obtained by increasing μ_1, μ_2, and μ_3 in order to get target loops with lower bandwidths. Removing the integrators is another option to consider since it would lessen the trade-off between performance and stability robustness. Making $h = 0$; i.e. attaching the tethers directly to the helicopter c.g.'s may help considerably since in such a case the unstable Tethered Helicopter Mode moves to the origin giving us a natural integrator in the SM AFCS loop. None of these options shall be addressed in this thesis. Chapters 5 and 6, however, examine the feasibility of a high performance (high bandwidth) AFCS design for a TLHS with unequal tether lengths. It is hoped that having unequal tether lengths would lesson the trade-off between performance and stability robustness.

CHAPTER 5: ANALYSIS OF TLHS UNEQUAL TETHER MODEL

5.1 Introduction

In this chapter the linear model developed in Chapter 2 is analyzed using the nominal parameter values given in Appendix 1. In particular, the chapter will focus on the "Unequal Tether Problem," i.e. the case in which the master and slave tether lengths are unequal ($H_s = 2H_m$; $H_m = H$). The chapter discusses the coupling that results between two of the three basic motions (AVM, SM, and ASM) when the tether lengths are unequal. The natural modes of the Unequal Tether Configuration are identified and discussed. Comparisons are made between the Unequal Tether and Equal Tether Configuration properties. The purpose of this chapter is to provide an understanding of the "Unequal Tether Model" and how it differs from the Equal Tether Model so that we may formulate design specifications for the Unequal Tether AFCS to be developed in Chapter 6. The primary reason for studying the Unequal Tether Configuration here is to examine whether or not having unequal tether lengths lessens the trade-off between performance and stability robustness when a high performance (high bandwidth) design is desired.

5.2 Coupling Between the Symmetric and Anti-Symmetric Motions

5.2.1 Introduction

It was established in section 3.2 that, regardless of the tether lengths, the AVM is always decoupled from the Symmetric and Anti-Symmetric Motions. This is due to the fact that the vertical and horizontal linear dynamics for a hovering helicopter are decoupled (Bramwell, [1]). It was also shown that when the tether lengths are equal, H_s=H_m, the Symmetric and Anti-Symmetric Motions decouple from one another. This is due to the perfect symmetry of the TLHS when the helicopters are identical and the tether lengths are equal. When the tether lengths are not equal (Fig. 5.2.1.1)

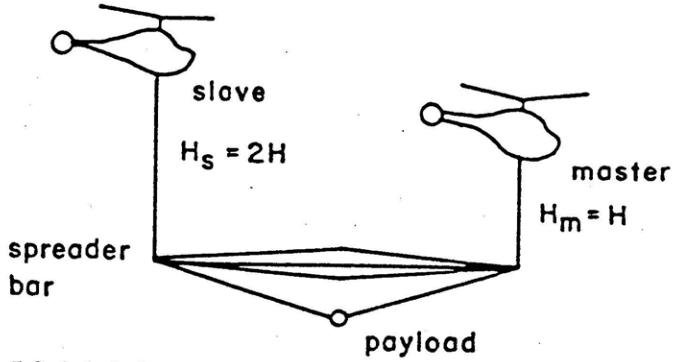

Fig. 5.2.1.1: Visualization of Unequal Tether Configuration.

($H_s \neq H_m$), however, this decoupling does not take place and one must analyze the Symmetric and Anti-Symmetric Motions simultaneously.

The Symmetric Motion (SM) involves the Δx and $\Delta\theta$ degrees of freedom and the control input ΔB_{lc}. The Anti-Symmetric Motion (ASM) involves the $\Sigma\dot{x}$, $\Sigma\theta$, Δz, and x_L' degrees of freedom and the control inputs $\Delta\Theta_c$ and ΣB_{lc}. The combined Symmetric and Anti-Symmetric Motions shall be referred to as the Symmetric-Anti Symmetric Motions (SASM).

To get a feel for the coupling that results when $H_s \neq H_m$, it is necessary to examine the linear model in Table 2.4.1 - 2.4.2. Inspection of Table 2.4.1 shows the presence of a tether length "coupling parameter", $S \equiv (H_m - H_s) / (H_m + H_s)$. It thus follows that if $H_s = 2H_m$, then $S < 0$. In such a case Table 2.4.1 shows that the ASM "drives" the SM with $\Sigma\theta$ and x_L', while the SM "drives" the ASM with Δx and $\Delta\theta$. This can be visualized as in Fig. 5.2.1.2.

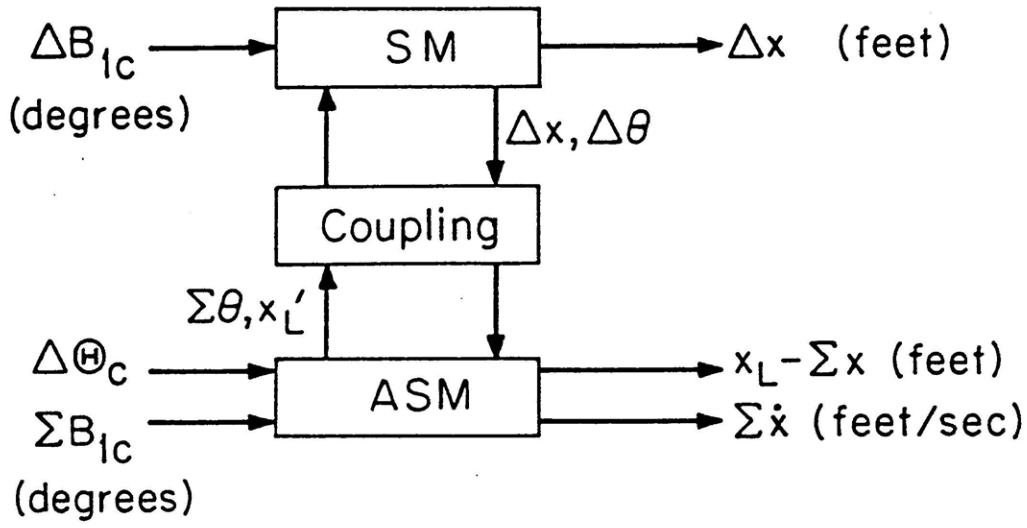

Fig. 5.2.1.2: Visualization of Symmetric - Anti Symmetric Motion (SASM).

The degree to which this coupling occurs (when $H_s = 2H_m$; $H_m = H$) shall be examined later in the section. Before proceeding with the analysis of the Unequal Tether Model, we recall some basic geometric relationships.

For the Equal Tether Problem the relationships for the horizontal separation, Δx, the generalized load coordinate, x_L', and the load deviation from center, $x_L - \Sigma x$, were simply as follows:

$$\Delta x = - [h\,\Delta\theta + H\,\Delta\varepsilon] \tag{5.1a}$$

$$x_L' = H\,[\Sigma\varepsilon - \Sigma\theta] \tag{5.1b}$$

$$x_L - \Sigma x = h\,\Sigma\theta + \hat{Z}\,\Delta z + H\,\Sigma\varepsilon \tag{5.1c}$$

These relationships, obviously, are not valid for the Unequal Tether Problem. When $H_s \neq H_m$ the relationships are as follows:

$$\Delta x = - [\, h\,\Delta\theta + H_m\,\varepsilon_m - H_s\,\varepsilon_s\,] \tag{5.2}$$

$$x_L' = 0.5\,[\, H_s(\varepsilon_s - \theta_s) + H_m(\varepsilon_m - \theta_m)\,] + 0.5\,[\, H_m - H_s\,]\,\theta_m \tag{5.3a}$$

$$= 0.5\,[\, H_s\,\varepsilon_s + H_m\,\varepsilon_m\,] - H_s\,\Sigma\theta \tag{5.3b}$$

$$x_L - \Sigma x = (h + H_s)\Sigma\theta + \hat{Z}\,\Delta z + x_L' \tag{5.4}$$

From eqs. (5.2) - (5.3) we get the following two useful expressions:

$$\varepsilon_m = \{\, 2\,[\, x_L' + H_s\,\Sigma\theta\,] - [\,\Delta x + h\,\Delta\theta\,]\,\} / 2\,H_m \tag{5.5}$$

$$\varepsilon_s = \{\, 2\,[\, x_L' + H_s\,\Sigma\theta\,] + [\,\Delta x + h\,\Delta\theta\,]\,\} / 2\,H_s \tag{5.6}$$

Eqs. (5.2) - (5.6) were given in Table 2.4.3.

5.2.2 Notation for Unequal Tether Model: The SASM and Unequal Tether Plants

This chapter shall focus on the case where $H_s = 2H_m$ and $H_m = H$. Since the SM was described by the state space triple (A_{p2}, B_{p2}, C_{p2}) and the ASM by (A_{p3}, B_{p3}, C_{p3}), the SASM shall be represented by the state space triple $(A_{p23}, B_{p23}, C_{p23})$. The SASM shall henceforth be denoted as follows:

$$\dot{\underline{x}}_{p23} = A_{p23}\,\underline{x}_{p23} + B_{p23}\,\underline{u}_{p23} \qquad \underline{x}_{p23} \in \mathbf{R^{11}};\ \underline{u}_{p23} \in \mathbf{R^3} \tag{5.7}$$

$$\underline{y}_{p23} = C_{p23}\,\underline{x}_{p23} \qquad \underline{y}_{p23} \in \mathbf{R^3} \tag{5.8}$$

$$G_{p23}(s) \equiv C_{p23}(sI - A_{p23})^{-1} B_{p23} \tag{5.9}$$

$$\underline{u}_{p23} = [\Delta B_{lc} \,||\, \Delta\Theta_c \;\; \Sigma B_{lc}]^T \tag{5.10}$$

$$\underline{x}_{p23} = [\Delta x \;\; \Delta\theta \;\; \Delta\dot{x} \;\; \Delta\dot{\theta} \,||\, \Sigma\theta \;\; \Delta z \;\; x_L' \;\; \Sigma\dot{x} \;\; \Sigma\dot{\theta} \;\; \Delta\dot{z} \;\; \dot{x}_L']^T \tag{5.11}$$

$$\underline{y}_{p23} = [\Delta x \,||\, x_L - \Sigma x \;\; \Sigma\dot{x}]^T \tag{5.12}$$

where Δx, x_L', and $x_L - \Sigma x$ are given by eqs. (5.2) and (5.4), respectively. The state space triple $(A_{p23}, B_{p23}, C_{p23})$ and the tfm $G_{p23}(s)$ shall be referred to as the SASM Plant. we note that the SASM Plant is a three-input three-output system.

Given that the SASM is described by eqs. (5.7) - (5.12), the entire Unequal Tether Model ($H_s = 2H_m$; $H_m = H$) is given as follows:

$$\dot{\underline{x}}_p = A_p \underline{x}_p + B_p \underline{u}_p \qquad \underline{x}_p \in \mathbf{R^{12}};\ \underline{u}_p \in \mathbf{R^4} \tag{5.13}$$

$$\underline{y}_p = \underline{C}_p \underline{x}_p \qquad \underline{y}_p \in \mathbf{R^4} \tag{5.14}$$

$$G_p(s) = C_p(sI - A_p)^{-1}B_p \tag{5.15}$$

where

$$\underline{u}_p = [u_{p1}\ \underline{u}_{p23}{}^T]^T \tag{5.16}$$

$$\underline{x}_p = [x_{p1}\ \underline{x}_{p23}{}^T]^T \tag{5.17}$$

$$\underline{y}_p = [y_{p1}\ \underline{y}_{p23}{}^T]^T \tag{5.18}$$

and

$$A_p = \mathrm{diag}(A_{p1}, A_{p23}) \tag{5.19}$$

$$B_p = \mathrm{diag}(B_{p1}, B_{p23}) \tag{5.20}$$

$$C_p = \mathrm{diag}(C_{p1}, C_{p23}) \tag{5.21}$$

The scalars A_{p1}, B_{p1}, C_{p1}, u_{p1}, x_{p1}, and y_{p1} were defined in Chapter 3. The matrices A_{p23}, B_{p23}, and C_{p23} are given in Table 5.2.2.1. The SASM Plant parameter values are given in Table 5.2.2.2.

Table 5.2.2.1.1a: State Space Representation For SASM Plant.

$$A_{p23} =$$

		1								
			1							
$-\mu w_A^2$	$-[g(1+\mu)+\mu w_A^2 h]$	X_u		$-2\mu w_A^2 S\Pi_s$		$-2\mu w_A^2 S$				
$-\epsilon\mu w_A^2$	$-\epsilon\mu w_A^2(h+H_A)$	H_u	H_q	$-2\mu\epsilon w_A^2 S\Pi_s$		$-2\mu\epsilon w_A^2 S$				
								1		
									1	
										1
$\frac{\mu}{2} w_A^2 S$	$\frac{\mu}{2} w_A^2 Sh$			$-g\left[1+\mu S\frac{\Pi_s}{\Pi_A}\right]$		μw_A^2	X_u			
$\frac{\mu}{2}\epsilon w_A^2 S$	$\frac{\mu}{2}\epsilon w_A^2 Sh$			$-\epsilon\mu w_A^2 S\Pi_s$		$\epsilon\mu w_A^2$	H_u	N_q		
$2TS$	$2TSh$			$4T\Pi_s$	$-4T\hat{\Pi}_A$	$4T$			$Z_w TJ$	
$-\left[\frac{\mu}{2} w_A^2 S\right]V$	$-\left[\frac{\mu}{2} w_A^2 S\right]Vh$			$g\left[1+\mu S\frac{\Pi_s}{\Pi_A}\right]+F$	$4T\delta_L\hat{Z}\hat{\Pi}_A$	D	E	$-N_q(h+H_s)$	$-Z_w TJ\delta_L\hat{Z}$	

Definitions:

$\Psi \equiv 1 + e_b + 4\mu\hat{Z}^2\delta_L(1-\delta_L)$

$D \equiv -\omega_A^2[1+\mu+(h+H_s)\mu\epsilon+(4T\delta_L\hat{Z}/\omega_A^2)]$

$E \equiv -[X_u + M_u(h+H_s)]$

$F \equiv (h+H_s)\epsilon\mu\omega_A^2 S H_s - \omega_A^2 H_s - 4T\delta_L\hat{Z}H_s$

$J \equiv [\mu\delta_L\hat{Z}\omega_A^2]^{-1}$

$T \equiv [J\Psi]^{-1}$

$V \equiv 1 + (h+H_s)\epsilon + (1/\mu) + (4\delta_L^2\hat{Z}^2/\Psi)$

$$=\begin{bmatrix}
0. & 0. & 1.0000 & 0. & 0. & 0. & 0. & 0. & 0. & 0. & 0. \\
0. & 0. & 0. & 1.0000 & 0. & 0. & 0. & 0. & 0. & 0. & 0. \\
-0.8231 & -0.8674 & -0.0600 & 0. & 0.2538 & 0. & 0.5187 & 0. & 0. & 0. & 0. \\
-12.9500 & -4.8065 & 2.3493 & -3.1000 & 3.9928 & 0. & 8.6336 & 0. & 0. & 0. & 0. \\
0. & 0. & 0. & 0. & 0. & 0. & 0. & 0. & 1.0000 & 0. & 0. \\
0. & 0. & 0. & 0. & 0. & 0. & 0. & 0. & 0. & 1.0000 & 0. \\
0. & 0. & 0. & 0. & 0. & 0. & 0. & 0. & 0. & 0. & 1.0000 \\
-0.1372 & -0.0006 & 0. & 0. & -0.4351 & 0. & 0.8231 & -0.0600 & 0. & 0. & 0. \\
-2.1584 & -0.1356 & 0. & 0. & 1.9964 & 0. & 12.9500 & 2.3493 & -3.1000 & 0. & 0. \\
-0.2529 & -0.0159 & 0. & 0. & 0.7018 & -0.3885 & 1.5175 & 0. & 0. & -0.3361 & 0. \\
1.6948 & 0.1065 & 0. & 0. & -1.7896 & 0.1844 & -10.1690 & -1.1741 & 1.6284 & 0.1595 & 0.
\end{bmatrix}$$

Notes: 1. Although the symbolic representations for A_{p23}, B_{p23}, C_{p23} assume that all pitch angles and controls are measured in radians, the numerical representations assumes them to be measured in degrees.

2. Displacements and velocities are assumed to be measured in feet and feet/second, respectively.

3. Forces (weights) are assumed to be measured in pounds.

Table 5.2.2.1b: State Space Representation For SASM Plant.

$$B_{p23} = \begin{array}{|c|c|c|}\hline & & \\ & & \\ X_{Blc} & & \\ M_{Blc} & & \\ & & \\ & & \\ & & \\ & & X_{Blc} \\ & & M_{Blc} \\ & Z_{\theta_c TJ} & \\ & -Z_{\theta_c TJ}\delta_L\hat{z} & -[X_{Blc}+M_{Blc}(h+H_s)] \\ \hline \end{array} = \begin{bmatrix} 0. & 0. & 0. \\ 0. & 0. & 0. \\ 0.4782 & 0. & 0. \\ -47.2400 & 0. & 0. \\ 0. & 0. & 0. \\ 0. & 0. & 0. \\ 0. & 0. & 0. \\ 0. & 0. & 0.4782 \\ 0. & 0. & -47.2400 \\ 0. & 5.7789 & 0. \\ 0. & -2.7423 & 24.3370 \end{bmatrix}$$

$$C_{p23} = \begin{bmatrix} 1 & 0 & 0 & 0 & 0 & 0 & 0 & 0 & 0 & 0 & 0 \\ 0 & 0 & 0 & 0 & (h+H_s) & Z & 1 & 0 & 0 & 0 & 0 \\ 0 & 0 & 0 & 0 & 0 & 0 & 0 & 1 & 0 & 0 & 0 \end{bmatrix}$$

$$= \begin{bmatrix} 1.0000 & 0. & 0. & 0. & 0. & 0. & 0. & 0. & 0. & 0. & 0. \\ 0. & 0. & 0. & 0. & 0.5253 & 0.5000 & 1.0000 & 0. & 0. & 0. & 0. \\ 0. & 0. & 0. & 0. & 0. & 0. & 0. & 1.0000 & 0. & 0. & 0. \end{bmatrix}$$

TLHS Parameters:

$\mu \equiv [M_L + M_B] / 2 M_H$

$\delta_L \equiv M_L / [M_L + M_B]$

$\omega_A^2 \equiv (g / H_A)$

$H_A \equiv 2 H_s H_m / [H_s + H_m]$

$\hat{H}_A \equiv H_A / L$

$S \equiv [H_m - H_s] / [H_s + H_m]$

$\varepsilon \equiv M_H h / I_y$

$\hat{Z} \equiv Z / L$

$e_b \equiv 2 I_B / M_H L^2$

$I_B \equiv (1 / 12) M_B L^2$

Table 5.2.2.2: SASM Plant Parameter Values.

$W_H = 14000$ lbs. $M_H = 434.78$ slugs $W_B = 644$ lbs. $M_B = 20$ slugs

$I_y = 5700$ slug ft^2 $L = 69$ ft. $h = 3.6$ ft. $Z = 13.25$ ft.

$g = 32.2$ ft sec^{-2} $H = 13\ .\ 25$ ft.

$\mu \equiv [M_L + M_B] / 2M_H = 0.4515$ $\delta_L \equiv M_L / [M_L + M_B] = 0.9491$

$I_B \equiv (1 / 12)\ M_B\ L^2 = 7935$ slug ft^2 $e_b \equiv 2\ I_B / M_H\ L^2 = 0.0077$

$\varepsilon \equiv M_H\ h / I_y = 0.2746$ $\hat{Z} \equiv Z / L = 0.5$

$H_m = H = 13.25$ ft. $H_s = 2H = 26.5$ ft.

$H_A \equiv 2\ H_s\ H_m / [\ H_m + H_s] = 17.6667$ $\hat{H}_A \equiv (H_A / L) = 0.2561$

$S \equiv [H_m - H_s] / [H_m + H_s] = - 0.3333$

$\omega_A^2 \equiv (g / H_A) = 1.8226$

$\Psi \equiv 1 + e_b + 4\ \mu\ \hat{Z}^2\ \delta_L\ (1 - \delta_L) = 1.0295$

$D \equiv - \omega_A^2\ [1 + \mu + (h + H_s)\ \mu\ \varepsilon + (4\ T\ \delta_L\ \hat{Z} / \omega_A^2)] = - 10.169$

$E \equiv - [X_u + M_u\ (h + H_s)] = - 1.1741$

$F \equiv (h + H_s)\ \varepsilon\ \mu\ \omega_A^2\ S\ H_s - \omega_A^2\ H_s - 4\ T\ \delta_L\ \hat{Z}\ H_s = -2.2247$ ft deg^{-1}

$J \equiv (1 / \mu\ \delta_L\ \hat{Z}\ \omega_A^2) = 2.561$

$T \equiv \mu\ \delta_L\ \hat{Z}\ \omega_A^2 / \Psi = 0.3793$

$V \equiv 1 + (h + H_s)\ \varepsilon + (1 / \mu) + (4\ \delta_L^2\ \hat{Z}^2 / \Psi) = 12.356$

$X_u = - 0.06$ ft sec^{-2} / ft sec^{-1} $X_{Blc} = 27.4$ ft sec^{-2} / rad

$M_u = 0.041$ rad sec^{-2} / ft sec^{-1} $M_{Blc} = - 47.24$ rad sec^{-2} / rad

$M_q = - 3.1$ rad sec^{-2} / rad sec^{-1} $Z_{\Theta c} = 340.9$ ft sec^{-2} / rad

$Z_w = - 0.346$ ft sec^{-2} / ft sec^{-1}

It can be shown that the state space triple (A_p, B_p, C_p) is controllable and observable. It thus follows that the state space and tfm representations are equivalent minimal realizations. From now on the state space representation, given by eqs. (5.13) - (5.14) and the equivalent input/output representation, given by eq. (5.15), shall be referred to as the "Unequal Tether Plant". Figs. 5.2.2.1 - 5.2.2.2 provide input/output visualizations for the TLHS and the Equal and Unequal Tether Plants.

In this chapter we analyze the internal as well as the input/output properties of the Unequal Tether Plant. Comparisons are made with the Equal Tether Plant. It should be emphasized that both the Equal and Unequal Tether Plants contain the AVM Plant. This follows from eqs. (5.19) - (5.21). The AVM Plant was carefully examined in Chapter 3. Consequently, we shall not pay much attention to it in this chapter. Instead we shall focus on the SM, ASM, and the SASM Plants.

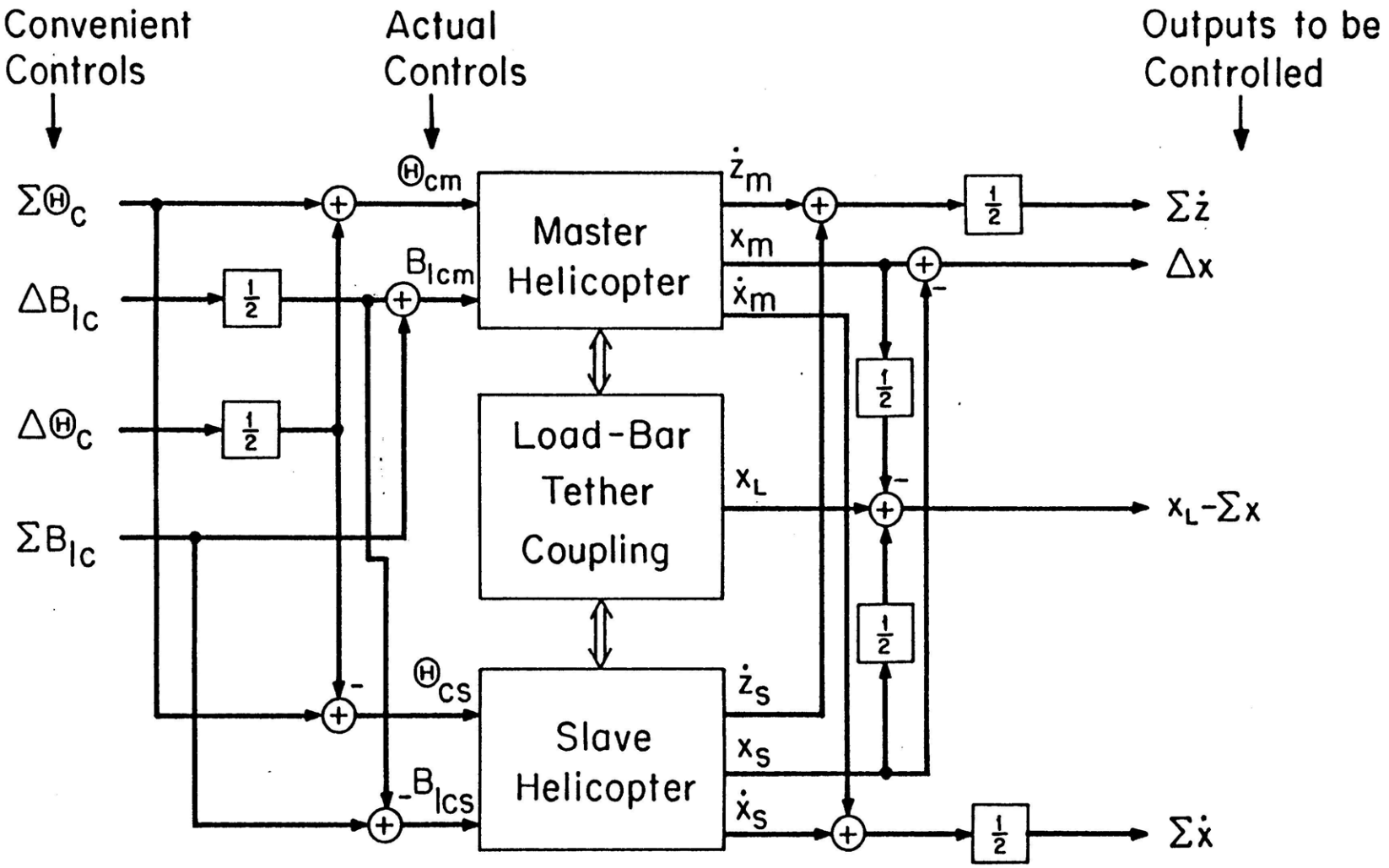

Fig. 5.2.2.1: Input/Output Visualization of TLHS.

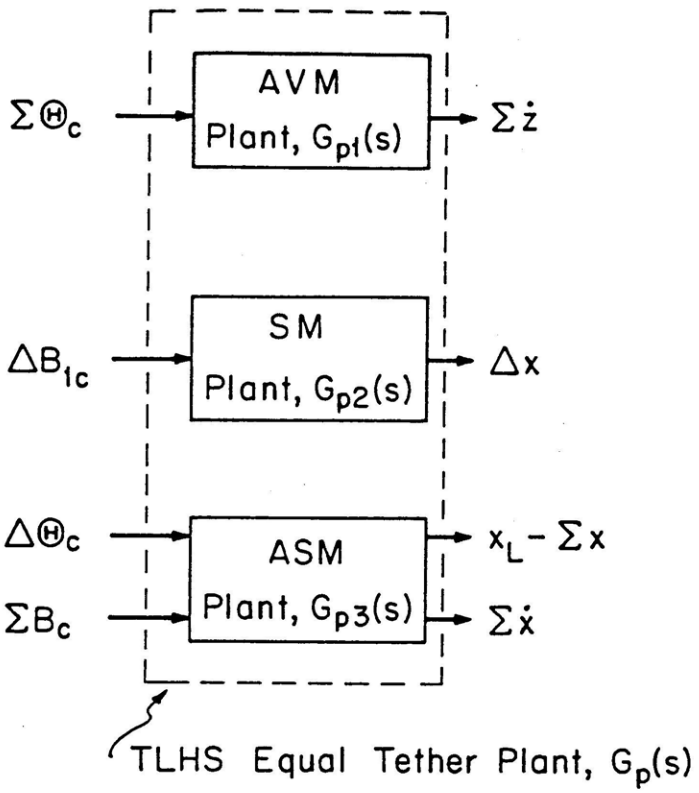

a) Equal Tether Plant

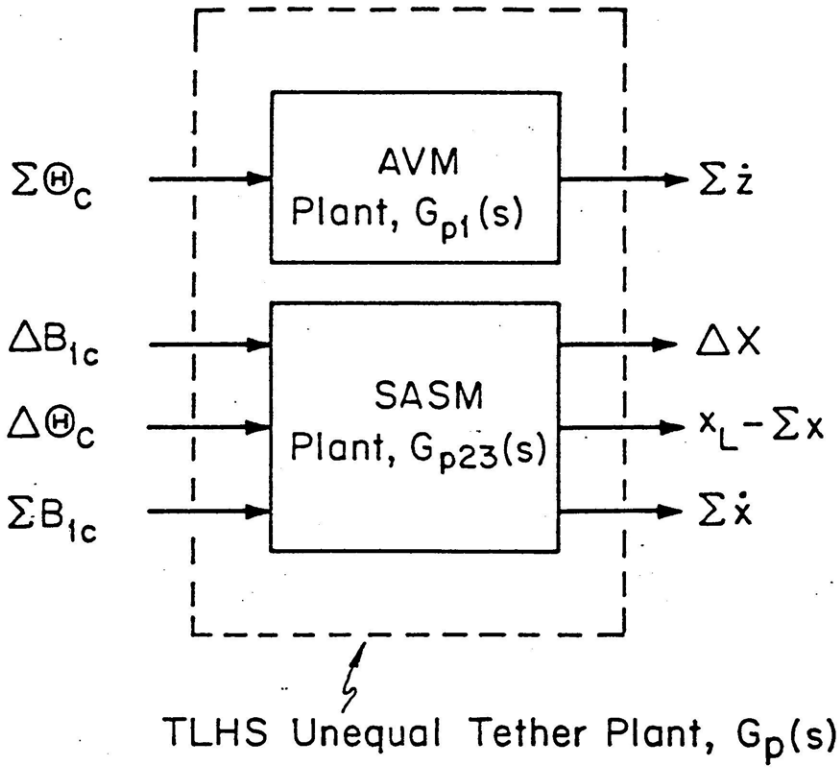

b) Unequal Tether Plant

Fig. 5.2.2.2: Input/Output Visualization of Equal and Unequal Tether Plants

5.3 Modal Analysis of TLHS Unequal Tether Configuration

5.3.1 Introduction

In this section the natural modes of the Unequal Tether Configuration ($H_s = 2H_m$; $H_m = H$) are identified and discussed. Comparisons are made between the modes of the Unequal Configuration and those of the Equal Tether Configuration. To facilitate the comparisons, the modes of the Unequal Tether Configuration shall be described using the same names used to describe the modes of the Equal Tether Configuration in section 3.3.

The natural modes of the Unequal Tether Configuration are found by solving the 12^{th} order ordinary eigenvalue problem associated with the homogenous system ($\underline{u}_p=\underline{0}$):

$$\dot{\underline{x}}_p = A_p \underline{x}_p \tag{5.20}$$

where $A_p = \text{diag}(A_{p1}, A_{p23})$ and $\underline{x}_p = [x_{p1}\ \underline{x}_{p23}{}^T]^T$. Before discussing the modes of the Unequal Tether Configuration, we compare the "Equal Tether and Unequal Tethjer A_p matrices" which are both given in Table 5.3.1.1.

It was shown in Chapter 2 that $\Delta\ddot{x}$ and $\Delta\ddot{\theta}$ are determined by the following two second order ordinary differential equations:

$$M_H \Delta\ddot{x} = 0.5\,[W_L + W_B]\,\Delta\varepsilon - [W_H + 0.5\,(W_L + W_B)]\,\Delta\theta + M_H[X_u\Delta\dot{x} + X_{Blc}\Delta B_{lc}] \tag{5.23}$$

$$I_y \Delta\ddot{\theta} = 0.5[W_L + W_B]\,h\,\Delta\varepsilon - 0.5\,[W_L + W_B]\,h\,\Delta\theta + I_y[M_u\Delta\dot{x} + M_q\Delta\dot{\theta} + M_{Blc}\Delta B_{lc}] \tag{5.24}$$

where

$$\Delta\varepsilon = -\,[\,(\Delta x + h\,\Delta\theta) + 2S\,(x_L{}' + H_s\,\Sigma\theta)\,]\,/\,H_A \tag{5.25}$$

From eq. (5.25) we have

$$\Delta\varepsilon = -\,[4.3245\,\Delta x + 0.2717\,\Delta\theta] \tag{5.26}$$

for the Equal Tether Configuration and

$$\Delta\varepsilon = -[3.2434\,\Delta x + 0.2038\,\Delta\theta] + [2.1623\,x_L{}' + 0.9999\,\Sigma\theta] \tag{5.27}$$

for the Unequal Tether Configuration. It follows from eqs. (5.23) - (5.25) that the only contribution

Table 5.3.1.1: Equal and Unequal Tether A_p Matrices

Equal Tether A_p Matrix: ($H_s = H_m = H$)

-0.2384	0.	0.	0.	0.	0.	0.	0.	0.	0.	0.	0.
0.	0.	0.	1.0000	0.	0.	0.	0.	0.	0.	0.	0.
0.	0.	0.	0.	1.0000	0.	0.	0.	0.	0.	0.	0.
0.	-1.0975	-0.8847	-0.0600	0.	0.	0.	0.	0.	0.	0.	0.
0.	-17.2670	-5.0777	2.3493	-3.1000	0.	0.	0.	0.	0.	0.	0.
0.	0.	0.	0.	0.	0.	0.	0.	0.	1.0000	0.	0.
0.	0.	0.	0.	0.	0.	0.	0.	0.	0.	1.0000	0.
0.	0.	0.	0.	0.	0.	0.	0.	0.	0.	0.	1.0000
0.	0.	0.	0.	0.	-0.5620	0.	1.0975	-0.0600	0.	0.	0.
0.	0.	0.	0.	0.	0.	0.	17.2670	2.3493	-3.1000	0.	0.
0.	0.	0.	0.	0.	0.4679	-0.3885	2.0233	0.	0.	-0.3361	0.
0.	0.	0.	0.	0.	-0.2220	0.1844	-9.5654	-0.6308	0.9116	0.1595	0.

Unequal Tether A_p Matrix ($H_s = 2\,H_m$; $H_m = H$)

-0.2384	0.	0.	0.	0.	0.	0.	0.	0.	0.	0.	0.
0.	0.	0.	1.0000	0.	0.	0.	0.	0.	0.	0.	0.
0.	0.	0.	0.	1.0000	0.	0.	0.	0.	0.	0.	0.
0.	-0.8231	-0.8674	-0.0600	0.	0.2538	0.	0.5487	0.	0.	0.	0.
0.	-12.9500	-4.8065	2.3493	-3.1000	3.9928	0.	8.6336	0.	0.	0.	0.
0.	0.	0.	0.	0.	0.	0.	0.	0.	1.0000	0.	0.
0.	0.	0.	0.	0.	0.	0.	0.	0.	0.	1.0000	0.
0.	0.	0.	0.	0.	0.	0.	0.	0.	0.	0.	1.0000
0.	-0.1372	-0.0086	0.	0.	-0.4351	0.	0.8231	-0.0600	0.	0.	0.
0.	-2.1584	-0.1356	0.	0.	1.9964	0.	12.9500	2.3493	-3.1000	0.	0.
0.	-0.2529	-0.0159	0.	0.	0.7018	-0.3885	1.5175	0.	0.	-0.3361	0.
0.	1.6948	0.1065	0.	0.	-1.7896	0.1844	-10.1690	-1.1741	1.6284	0.1595	0.

of Δx, x_L', and $\Sigma\theta$ to $\Delta\ddot{x}$ and $\Delta\ddot{\theta}$ is through $\Delta\varepsilon$. Equations (5.26) - (5.27) show that doubling the slave tether length reduces the contribution that Δx and $\Delta\theta$ have on $\Delta\ddot{x}$ and $\Delta\ddot{\theta}$. It also results in x_L' and $\Sigma\theta$ both driving $\Delta\ddot{x}$ and $\Delta\ddot{\theta}$. These observations are confirmed in Table 5.3.1.1.

It was also shown in Chapter 2 that $\Sigma\dot{x}$ and $\Sigma\theta$ are determined by the following two second order ordinary differential equations:

$$M_H\Sigma\ddot{x} = 0.5\,[W_L + W_B]\,\Sigma\varepsilon - [W_H + 0.5\,(W_L + W_B)]\,\Sigma\theta + M_H[X_u\Sigma\dot{x} + X_{Blc}\Sigma B_{lc}] \qquad (5.28)$$

$$I_y\,\Sigma\ddot{\theta} = 0.5[W_L + W_B]\,h\,\Sigma\varepsilon - 0.5\,[W_L + W_B]\,h\,\Sigma\theta + I_y[M_u\Sigma\dot{x} + M_q\Sigma\dot{\theta} + M_{Blc}\Sigma B_{lc}] \qquad (5.29)$$

where

$$\Sigma\varepsilon = \{S[\Delta x + h\,\Delta\theta] + 2[x_L' + H_s\,\Sigma\theta]\ \}\ /\ 2\,H_A \qquad (5.30)$$

From eq. (5.28) we have

$$\Sigma\varepsilon = 4.3245\,x_L' + \Sigma\theta \qquad (5.31)$$

for the Equal Tether Configuration and

$$\Sigma\varepsilon = -\,[0.5406\,\Delta x + 0.034\,\Delta\theta] + [3.2434x_L' + 1.4999\Sigma\theta] \qquad (5.32)$$

for the Unequal Tether Configuration. It follows from eqs. (5.28) - (5.30) that the <u>only contribution of Δx, $\Delta\theta$, and x_L' to $\Sigma\ddot{x}$ and $\Sigma\ddot{\theta}$ is through $\Sigma\varepsilon$</u>. Furthermore, it follows from eqs. (5.31) - (5.32) that <u>doubling the slave tether length reduces the contribution of x_L' to $\Sigma\ddot{x}$ and $\Sigma\ddot{\theta}$ while increasing the contribution of $\Sigma\theta$ to $\Sigma\ddot{x}$ and $\Sigma\ddot{\theta}$</u>. It also results in <u>Δx and $\Delta\theta$ both driving $\Sigma\ddot{x}$ and $\Sigma\ddot{\theta}$</u>. These observations are also confirmed in Table 5.3.1.1.

To understand the effect of doubling the slave tether length on the Δz and x_L' equations we recall the following differential equations from Chapter 2:

$$\Psi\,\Delta\ddot{z} = 4\,\mu\,\delta_L\,\hat{Z}\,g[\Sigma\varepsilon - \Delta z / L] + Z_w\,\Delta\dot{z} + Z_{\Theta c}\,\Delta\Theta_c \qquad (5.33)$$

$$\ddot{x}_L' = - g [1 + \mu + (h + H_s) \varepsilon \mu + 4 \delta_L^2 \hat{Z}^2 (1 / \Psi g)] \Sigma\varepsilon + g [1 + \mu + (h + H_s) \varepsilon \mu] \Sigma\theta$$

$$+ [4 \mu \delta_L^2 \hat{Z}^2 g] (1 / \Psi L) \Delta z - [X_u + (h + H_s) M_u] \Sigma\dot{x} - (h + H_s) M_q \Sigma\dot{\theta}$$

$$- (\hat{Z} \delta_L / \Psi) [Z_w \Delta\dot{z} + Z_{\Theta c} \Delta\Theta_c] - [X_{Blc} + (h + H_s) M_{Blc}] \Sigma B_{lc} \qquad (5.34)$$

Equation (5.33) shows that the only dependence of $\Delta\ddot{z}$ on Δx, $\Delta\theta$, x_L', and $\Sigma\theta$ is through $\Sigma\varepsilon$. Moreover, the only dependence that $\Delta\ddot{z}$ has on the tether lengths is through $\Sigma\varepsilon$.

Equation (5.34) shows that the only dependence of $\ddot{x}_L'$ on Δx, $\Delta\theta$, and x_L' is through $\Sigma\varepsilon$. The equation also shows that $\ddot{x}_L'$ depends explicitly on the slave tether length, H_s. This is because of the explicit dependence that x_L' has on H_s:

$$x_L' = 0.5 [H_m \varepsilon_m + H_s \varepsilon_s] - H_s \Sigma\theta \qquad (5.35)$$

From eqs. (5.31) - (5.34) it follows that doubling the slave tether length reduces the contribution of x_L' to $\Delta\ddot{z}$ and increases the contribution of $\Sigma\theta$ to $\Delta\ddot{z}$ and $\ddot{x}_L'$. The contribution of x_L' to $\ddot{x}_L'$, however, increases because of the increase in the $\Sigma\varepsilon$ coefficient. For a similar reason the contribution of $\Sigma\theta$ to $\ddot{x}_L'$ also increases.

Finally, eqs. (5.31) - (5.32) also show that doubling the slave tether length results in Δx and $\Delta\theta$ driving both $\Delta\ddot{z}$ and $\ddot{x}_L'$. These observations are confirmed in Table 5.3.1.1.

Having discussed the differences between the "Equal and Unequal Tether A_p matrices" we are now ready to discuss the differences between the natural modes of the Equal and Unequal Tether Configurations. The eigenvalues, λ_i, and right eigenvectors, $\underline{v}_i$, associated with the Equal and Unequal Tether A_p matrices are given in Tables 3.3.1.1 and 5.3.1.2, respectively. For convenience Table 5.3.1.3 contains the magnitudes and phases associated with the complex entries of the Unequal Tether complex eigenvectors. To facilitate the comparison between the Equal and Unequal Tether modes we have tabulated the Equal and Unequal Tether eigenvalues in Table 5.3.1.4. It is emphasized that the discussion which follows assumes that displacements are measured in feet and angle in degrees.

Table 5.3.1.2: Eigenvalues and Right Eigenvectors For Unequal Tether Model

AVM: Average Vertical Damping

Units: ft, degs, ft / sec, deg / sec

$\lambda_1 = -0.2384$

$$\underline{v}_1 = \begin{vmatrix} -1.0000 \\ 0. \\ 0. \\ 0. \\ 0. \\ 0. \\ 0. \\ 0. \\ 0. \\ 0. \\ 0. \\ 0. \end{vmatrix}$$

SASM: Tethered Helicopter

$\lambda_2 = 0.6604$

$$\underline{v}_2 = \begin{vmatrix} 0. \\ 0.4780 \\ -0.6795 \\ 0.3157 \\ -0.4488 \\ -0.0261 \\ -0.0221 \\ 0.0694 \\ 0.0121 \\ -0.0172 \\ -0.0146 \\ 0.0458 \end{vmatrix}$$

Horizontal Spring

$\lambda_{3,4} = -0.7883 \pm j\ 1.8885$

$$\underline{v}_3 = \begin{vmatrix} 0. + 0.\ i \\ 0.0685 - 0.0630i \\ 0.4029 + 0.0604i \\ 0.0649 + 0.1789i \\ -0.4317 + 0.7132i \\ -0.0851 - 0.0641i \\ -0.0062 + 0.0068i \\ 0.0771 + 0.0167i \\ 0.0074 - 0.0492i \\ 0.1882 - 0.1102i \\ -0.0080 - 0.0171i \\ -0.0924 + 0.1324i \end{vmatrix}$$

Symmetric Damping

$\lambda_5 = -2.227$

$$\underline{v}_5 = \begin{vmatrix} 0. \\ 0.0595 \\ -0.3897 \\ -0.1324 \\ 0.8679 \\ -0.1017 \\ -0.0032 \\ 0.0430 \\ -0.0345 \\ 0.2264 \\ 0.0072 \\ -0.0958 \end{vmatrix}$$

Backflapping

$\lambda_{6,7} = 0.0478 \pm j\ 0.4698$

$$\underline{v}_6 = \begin{vmatrix} 0. + 0.\ i \\ 0.0649 + 0.0559i \\ 0.0363 + 0.0103i \\ -0.0232 + 0.0332i \\ -0.0031 + 0.0175i \\ 0.2537 + 0.2581i \\ 0.7266 - 0.1603i \\ 0.0044 - 0.0325i \\ -0.3508 + 0.1664i \\ -0.1091 + 0.1315i \\ 0.1100 + 0.3336i \\ 0.0155 + 0.0005i \end{vmatrix}$$

Vertical Spring

$\lambda_{8,9} = -0.1897 \pm j\ 0.7291$

$$\underline{v}_8 = \begin{vmatrix} 0. + 0.\ i \\ 0.0452 - 0.0006i \\ 0.0354 + 0.0154i \\ -0.0081 + 0.0330i \\ -0.0179 + 0.0229i \\ 0.3727 + 0.0326i \\ -0.6410 + 0.0763i \\ -0.0907 - 0.0103i \\ 0.0274 + 0.3288i \\ -0.0945 + 0.2655i \\ 0.0660 - 0.4818i \\ 0.0247 - 0.0642i \end{vmatrix}$$

Pendular

$\lambda_{10,11} = -0.6119 \pm j\ 2.4381$

$$\underline{v}_9 = \begin{vmatrix} 0. + 0.\ i \\ 0.0425 - 0.0119i \\ 0.2336 + 0.1017i \\ 0.0029 + 0.1110i \\ -0.3910 + 0.5074i \\ 0.2032 + 0.0394i \\ 0.0131 - 0.0181i \\ -0.1569 + 0.0262i \\ 0.0219 + 0.0875i \\ -0.2205 + 0.4714i \\ 0.0360 + 0.0431i \\ 0.0321 - 0.3985i \end{vmatrix}$$

Anti-Symmetric Damping

$\lambda_{12} = -2.0053$

$$\underline{v}_{12} = \begin{vmatrix} 0. \\ -0.0558 \\ 0.2865 \\ 0.1119 \\ -0.5744 \\ -0.3120 \\ -0.0086 \\ 0.1168 \\ -0.1218 \\ 0.6256 \\ 0.0173 \\ -0.2342 \end{vmatrix}$$

Table 5.3.1.3: Polar Form of Unequal Tether Complex Eigenvectors

Horizontal Spring		Backflapping		Vertical Spring		Pendular	
MAG	PHAS	MAG	PHAS	MAG	PHAS	MAG	PHAS
0.0931	- 42.61°	0.0857	40.74°	0.0452	- 1°	0.0441	- 15.64°
0.4074	8.53°	0.0377	15.84°	0.0386	23.5°	0.2548	23.5°
0.1903	70.07°	0.0405	124.94°	0.0339	103.8°	0.111	88.5°
0.8337	121.2°	0.0178	100.1°	0.0291	128°	0.6406	127.6°
0.1065	- 143°	0.3619	45.5°	0.3741	5°	0.2069	10.97°
0.0092	132.4°	0.7441	- 12.4°	0.6455	173°	0.0223	- 54.11°
0.0184	65.25°	0.0328	- 82.3°	0.0913	- 173.5°	0.1591	170.5°
0.0498	- 81.5°	0.3883	154.6°	0.3299	85.2°	0.0902	76°
0.2181	- 30.4°	0.1709	129.7°	0.2818	109.6°	0.5204	115.1°
0.0189	- 115.1°	0.3513	71.8°	0.4863	- 82.2°	0.0562	50.1°
0.1615	124.92°	0.0155	1.85°	0.0688	-69°	0.3998	- 85.4°

MAG ≡ magnitude PHAS ≡ phase

Units: ft, deg, ft / sec, deg / sec

Table 5.3.1.4: Natural Modes of Equal and Unequal Tether Configurations

a) Equal Tether Configuration

AVM: Vertical Damping Mode: $\lambda_1 = -0.2384$; $\tau = 4.2$

SM: Tethered Helicopter Mode: $\lambda_2 = 0.7561$
Horizontal Spring Mode: $\lambda_{3,4} = -0.8122 \pm j\,2.2228$; $\zeta = 0.34$; $\omega_n = 2.37$; $\tau = 1.23$
Symmetric Damping Mode: $\lambda_5 = 2.2919$; $\tau = 0.44$

ASM: Backflapping Mode: $\lambda_{6,7} = 0.0402 \pm j\,0.4785$; $\zeta = 0.084$; $\omega_n = 0.48$
Vertical Spring Mode: $\lambda_{8,9} = -0.1976 \pm j\,0.7364$; $\zeta = 0.26$; $\omega_n = 0.76$; $\tau = 5.06$
Pendular Mode: $\lambda_{10,11} = -0.5314 \pm j\,2.6245$; $\zeta = 0.2$; $\omega_n = 2.7$; $\tau = 1.88$
Anti-Symmetric Damping Mode: $\lambda_{12} = -2.1187$; $\tau = 0.47$

b) Unequal Tether Configuration

AVM: Vertical Damping Mode: $\lambda_1 = -0.2384$; $\tau = 4.2$

SASM: Tethered Helicopter Mode: $\lambda_2 = 0.6604$
Horizontal Spring Mode: $\lambda_{3,4} = -0.7883 \pm j\,1.8885$; $\zeta = 0.39$; $\omega_n = 2.05$; $\tau = 1.27$
Symmetric Damping Mode: $\lambda_5 = -2.227$; $\tau = 0.45$

Backflapping Mode: $\lambda_{6,7} = 0.0478 \pm j\,0.4698$; $\zeta = -0.1$; $\omega_n = 0.47$
Vertical Spring Mode: $\lambda_{8,9} = -0.1897 \pm j\,0.7291$; $\zeta = 0.25$; $\omega_n = 0.75$; $\tau = 5.27$
Pendular Mode: $\lambda_{10,11} = -0.6119 \pm j\,2.4381$; $\zeta = 0.24$; $\omega_n = 2.51$; $\tau = 1.63$
Anti-Symmetric Damping Mode: $\lambda_{12} = -2.0053$; $\tau = 0.5$

5.3.2 Discussion of AVM Modes

We have already shown that the Unequal Tether Plant contains the AVM Plant studied in Chapter 3. It thus follows that the Unequal Tether Configuration, like the Equal tether Configuration, possesses an Average Vertical Damping Mode. As explained in subsection 3.3.1, this mode characterizes the effect of vertical aerodynamic drag forces on the TLHS during average vertical climbs ($\Sigma\dot{z}$). This mode is similar to that experienced by a single hovering helicopter (Appendix 3) but has a larger time constant due to the extra mass in the TLHS. For a single helicopter the time constant is $\tau = 1 / | Z_w | = 2.89$ secs whereas the Average Vertical Damping Mode has a time constant of $\tau = (1+\mu) / | Z_w | = 4.2$ secs ($Z_w = -0.346$, $\mu = [M_L+M_B] / 2M_H = 0.4516$).

The Unequal Tether Plant consists of the AVM Plant and the SASM Plant. Next we study the modes associated with the SASM Plant.

5.3.3 Discussion of SASM Modes

The eigenvalues and right eigenvectors for the SM (A_{p2}) and the ASM (A_{p3}) can be obtained from Table 3.3.3. The eigenvalues and right eigenvectors for the SASM (A_{p23}) can be obtained from Table 5.3.2. Upon comparison of these tables it becomes evident that increasing the slave tether length from $H_s = H$ to $H_s = 2H$ has not resulted in any large changes in the nature of the TLHS's modes.

All statements which follow in this section are based on the right eigenvectors in Tables 3.3.3 and 5.3.2, magnitude information in Tables 3.3.4 and 5.3.3, and the eigenvalues in Table 5.3.4. The magnitude information contained in the eigenvectors is particularly important since it conveys the extent to which Twin Lift variables are affected by the modes. This magnitude information is summarized in Table 5.3.2.1 for both the Equal and Unequal Tether Configurations.

For the SM, the unstable Tethered Helicopter Mode had a time to double of 0.92 seconds. For the SASM, however, the mode has a time to double of 1.1 seconds. The increase (19.5%) is primarily due to the decrease in the contributions of Δx and $\Delta\theta$ to $\Delta\ddot{x}$ and $\Delta\ddot{\theta}$, rather than the new coupling terms due to $\Sigma\theta$ and x_L'. This can be seen by noting that the SM has an eigenvalue of

Table 5.3.2.1: Comparison Between Equal and Unequal Tether Modes

Note: The variables listed below are listed (from left to right) in order of decreasing magnitude as determined from the eigenvectors in Tables 3.3.1.3 and 5.3.1.2 which assume units of ft, degs, etc.

Average Vertical Damping Mode

AVM: $\Sigma\dot{z}$	$\tau = 4.2$

Tethered Helicopter Mode

SM: $\Delta\theta$, $\Delta\dot{\theta}$, Δx, $\Delta\dot{x}$	$t_{double} = 0.92$
SASM: $\Delta\theta$, Δx, $\Delta\dot{\theta}$, $\Delta\dot{x}$, x_L', $\dot{x}_L'$, $\Sigma\theta$, Δz, $\Delta\dot{z}$, $\Sigma\dot{\theta}$, $\Sigma\dot{x}$	$t_{double} = 1.05$

Horizontal Spring Mode

SM: $\Delta\dot{\theta}$, $\Delta\theta$, $\Delta\dot{x}$, Δx	$\zeta = 0.34$, $\omega_n = 2.37$, $\tau = 1.23$
SASM: $\Delta\dot{\theta}$, $\Delta\theta$, $\Sigma\dot{\theta}$, $\Delta\dot{x}$, $\dot{x}_L'$, $\Sigma\theta$, Δx, $\Sigma\dot{x}$, $\Delta\dot{z}$, x_L', Δz	$\zeta = 0.39$, $\omega_n = 2.05$, $\tau = 1.27$

Symmetric Damping Mode

SM: $\Delta\dot{\theta}$, $\Delta\theta$, $\Delta\dot{x}$, Δx	$\tau = 0.44$
SASM: $\Delta\dot{\theta}$, $\Delta\theta$, $\Delta\dot{x}$, $\Sigma\dot{\theta}$, $\Sigma\theta$, $\dot{x}_L'$, Δx, x_L', $\Sigma\dot{x}$, $\Delta\dot{z}$, Δz	$\tau = 0.45$

Backflapping Mode

ASM: Δz, $\Sigma\dot{x}$, $\Delta\dot{z}$, $\Sigma\theta$, $\Sigma\dot{\theta}$, x_L', $\dot{x}_L'$	$t_{double} = 17.2$, $\zeta = -0.084$, $\omega_n = 0.48$
SASM: Δz, $\Sigma\dot{x}$, $\Sigma\theta$, $\Delta\dot{z}$, $\Sigma\dot{\theta}$, Δx, $\Delta\dot{x}$, $\Delta\theta$, x_L', $\Delta\dot{\theta}$, $\dot{x}_L'$	$t_{double} = 14.5$, $\zeta = -0.1$, $\omega_n = 0.4$

Vertical Spring Mode

ASM: Δz, $\Delta\dot{z}$, $\Sigma\theta$, $\Sigma\dot{x}$, $\Sigma\dot{\theta}$, x_L', $\dot{x}_L'$	$\zeta = 0.26$, $\omega_n = 0.76$, $\tau = 5.09$
SASM: Δz, $\Delta\dot{z}$, $\Sigma\theta$, $\Sigma\dot{x}$, $\Sigma\dot{\theta}$, x_L', $\dot{x}_L'$, Δx, $\Delta\theta$, $\Delta\dot{x}$, $\Delta\dot{\theta}$	$\zeta = 0.25$, $\omega_n = 0.75$, $\tau = 5.27$

Pendular Mode

ASM: $\Sigma\dot{\theta}$, $\dot{x}_L'$, $\Sigma\theta$, x_L', $\Sigma\dot{x}$, $\Delta\dot{z}$, Δz	$\zeta = 0.2$, $\omega_n = 2.7$, $\tau = 1.88$
SASM: $\Delta\dot{\theta}$, $\Sigma\dot{\theta}$, $\dot{x}_L'$, $\Delta\theta$, $\Sigma\theta$, x_L', $\Delta\dot{x}$, $\Sigma\dot{x}$, $\Delta\dot{z}$, Δx, Δz	$\zeta = 0.24$, $\omega_n = 2.51$, $\tau = 1.63$

Anti-Symmetric Damping Mode

ASM: $\Sigma\dot{x}$, $\dot{x}_L'$, $\Delta\dot{z}$, $\Sigma\dot{\theta}$	$\tau = 0.47$
SASM: $\Sigma\dot{\theta}$, $\Delta\dot{\theta}$, $\Sigma\theta$, $\Delta\theta$, $\dot{x}_L'$, $\Sigma\dot{x}$, x_L', $\Delta\dot{x}$, Δx, $\Delta\dot{z}$, Δz	$\tau = 0.5$

0.7561, the SASM an eigenvalue of 0.6604, and the 4 x 4 submatrix of A_{p23} associated with the SM an eigenvalue of 0.6835. This shows that the change in the Δx and $\Delta\theta$ terms accounts for about a 75.9% change in the eigenvalue, thus confirming our claim. We also note that for the SM this mode is primarily associated with $\Delta\theta$ and $\Delta\dot{\theta}$ whereas for the SASM, the mode is primarily associated with $\Delta\theta$ and Δx. This change in eigenstructure, due to doubling the slave tether length, is also primarily attributable to the decrease in the contributions of Δx and $\Delta\theta$ to $\Delta\ddot{x}$ and $\Delta\ddot{\theta}$. This follows by noting that the angle between the SM eigenvector and that associated with the submatrix of A_{p23} corresponding to the SM is 6.44°, whereas the angle between the SM and the SASM eigenvectors is 10.2°. The change of 6.44°, due to the Δx and $\Delta\theta$ contributions, represents a 63% change thus confirming our claim. Finally, it must be emphasized that because the above times to double are so small, manual Twin Lift operation would place an untolerable burden on the master and slave pilots. Automatic control (partial or full) is thus necessary.

In the above discussion we used the fact that the angle, ϕ, between two real-valued vectors $\underline{u}$ and $\underline{v}$ is defined according to the relation

$$\cos\phi \equiv \underline{u}^T\underline{v} \tag{5.36}$$

Here the concepts of orthogonality and collinearity are well defined and intuitive.

When the vectors $\underline{u}$ and $\underline{v}$ are complex-valued, however, we define ϕ as follows:

$$\cos\phi \equiv \underline{u}^T\underline{v} \tag{5.37}$$

where

$$\underline{u} \equiv [\mathrm{Re}\,\underline{u}^T \quad \mathrm{Im}\,\underline{u}^T]^T \tag{5.38}$$

$$\underline{v} \equiv [\mathrm{Re}\,\underline{u}^T \quad \mathrm{Im}\,\underline{v}^T]^T \tag{5.39}$$

With this definition the concepts of orthogonality and collinearity remain well defined and intuitive. More specifically, we say that the complex-valued vectors u and v are orthogonal if and only if the real-valued vectors $\underline{u}$ and $\underline{v}$ are orthogonal. Collinearity is similarly defined. Of course, if $\underline{u}$ and $\underline{v}$ are real-valued then the definition in eq. (5.37) reduces to that in eq. (5.36).

Given the definition in eq. (5.37), it can be shown that

$$\underline{u}^H\underline{v} = \mathrm{Re}\,(\underline{u}^H\underline{v}) \tag{5.40}$$

hence

$$\cos \phi \equiv \mathrm{Re}\,(\underline{u}^H \underline{v}) \tag{5.41}$$

It thus follows that if $\underline{u}^H\underline{v} = 0$ then $\cos\phi = 0$ and $\underline{u}$ and $\underline{v}$ are orthogonal. With this definition of orthogonality, however, the converse is not necessarily true. The complex "vectors" $\underline{u} = j1$ and $\underline{v} = 1$, for example, are orthogonal by our definition but have $\underline{u}^H\underline{v} = -j1 \neq 0$. From this example it should be apparent that orthogonality, with our definition, is not preserved under muliplication by a complex scalar; e.g. multiplyin $\underline{u} = j1$ by $-j1$ makes it collinear with $\underline{v} = 1$. This is intuitive since the complex number j1 represents a pure rotation by 90°. Our definition does, of course, preserve orthogonality under multiplication by a real scalar.

In the discussions which follow the definition in eq. (5.37) shall be used to compare the complex eigenstructures of the Equal and Unequal Tether Configurations and to understand the impact of coupling created by having unequal tether lengths. Tables 5.3.3.2 - 5.3.3.3 summarize the effects of coupling on the Equal Tether modes and eigenstructures. These tables are based on the Equal and Unequal Tether modes and eigenvectors as well as the modes and eigenvectors of the Unequal Tether Configuration with coupling purposely neglected. The tables form the basis for our discussion.

For the SM, the Horizontal Spring Mode ($\zeta = 0.34$, $\omega_n = 2.37$) had a time constant of $\tau = 1.23$ secs and a period of $T = 2.65$ secs. For the SASM, however, the Horizontal Spring Mode ($\zeta = 0.39$, $\omega_n = 2.05$) has a time constant of $\tau = 1.27$ secs and a period of $T = 3.06$ secs. The decrease in time constant (3.3%) is primarily due to the new coupling terms $\Sigma\theta$ and x_L'. The increase in the period of oscillation (15.5%), however, is primarily due to the decrease in the contributions of Δx and $\Delta\theta$ to $\Delta\ddot{x}$ and $\Delta\ddot{\theta}$. To understand why this is so we refer to Table 5.3.2.2. The table shows that for the SM $\lambda_{3,4} = -0.8122 \pm j\,2.2228$, for the SM part of the SASM $\lambda_{3,4} = -0.8194 \pm j\,2.0391$, and for the SASM $\lambda_{3,4} = -0.7883 \pm j\,1.8885$. From this we see that the changes in the Δx and $\Delta\theta$ terms are responsible for only a 30.3% change in the real part and a 54.9% change in the imaginary part. This implies, therefore, that the $\Sigma\theta$, x_L' coupling terms have their primary impact on the real part, and hence on the time constant, while the changes in

Table 5.3.3.2: Effect of Coupling on Equal Tether Modes

	SM and ASM Modes	SASM Modes (Coupling Neglected)			SASM Modes		
	$\lambda_i(A_{p3}), \lambda_i(A_{p3})$	$\lambda_i(A_{p23})$ coupling=0	%ΔReal	$\%\Delta I_{mag}$	$\lambda_i(A_{p23})$	ΔReal	ΔI_{mag}
Tethered Helicopter	0.7561	0.6835	75.9	0	0.6604	-0.0956	0
Horizontal Spring	-0.8121±j2.2226	-0.8194±j2.0391	30.3	54.9	-0.7883±j1.8885	0.0238	-0.334
Symmetric Damping	-2.2919	-2.2047	134.2	0	-2.227	0.0649	0
Backflapping	0.0402±j0.4785	0.0455±j0.4723	68.4	71.3	0.0478±j0.4698	0.0076	-0.008
Vertical Spring	-0.1976±j0.7364	-0.1918±j0.7314	73.4	69.4	-0.1897±j0.7291	0.0079	-0.0072
Pendular	-0.5313±j2.6243	-0.5712±j2.33	49.5	158.1	-0.6119±j2.4381	-0.0806	-0.1862
Anti-Symmetric Damping	-2.1187	-2.0609	50.9	0	-2.0053	0.1134	0

Δ≡change in

%Δ≡percent change in

Table 5.3.3.3: Effect of Coupling on Equal Tether Eigenstructure

		Angle Between Equal and Unequal Tether Eigenvectors	
		SASM (coupling neglected)	SASM
AVM:	Average Vertical Damping	0° (100 %)	0°
SM:	Tethered Helicopter	6.44° (63 %)	10.2°
	Horizontal Spring	7.25° (37.8 %)	19.2°
	Symmetric Damping	1.15° (7.3 %)	15.8°
ASM:	Backflapping	10° (66.2 %)	15.1°
	Vertical Spring	32.3° (102.9 %)	31.4°
	Pendular	31.5° (59.9 %)	52.6°
	Anti-Symmetric Damping	11.5° (27.4 %)	42°

the Δx, $\Delta\theta$ terms have their primary impact on the imaginary part, and hence on the period of oscillation. Table 5.3.3.1 shows that for both the SM and SASM this mode is primarily associated with $\Delta\theta$ and $\Delta\dot{\theta}$. The table also shows that although $\Sigma\dot{\theta}$ and $\dot{x}_L'$ play no role for the SM, they play an even more significant role than Δx for the SASM. This follows from the magnitude information in Table 5.3.1.3. Table 5.3.3.3 shows that when the slave tether length is doubled the directionality of the SM eigenvector is mainly affected by the new coupling terms which account for about 62.2% of the total change in direction.

For the SM, The Symmetric Damping Mode had a time constant of $\tau = 0.44$ secs. For the SASM, however, the mode has a time constant of $\tau = 0.45$ secs. Table 5.3.3.2 shows that this change is largely attributable to the change in the SM part of the SASM; i.e. to the decrease in the contributions of Δx and $\Delta\theta$ to both $\Delta\ddot{x}$ and $\Delta\ddot{\theta}$. For the Equal Tether Configuration this mode was primarily associated with $\Delta\theta$ and $\Delta\dot{\theta}$. Table 5.3.3.1 shows that doubling the slave tether length does not change this. The change in eigenstructure which occurs, however, makes $\Sigma\theta$, $\Sigma\dot{\theta}$, and $\dot{x}_L'$ even more significant than Δx. Table 5.3.3.3 shows that this change in eigenstructure is primarily due to the new $\Sigma\theta$ and x_L' coupling since it accounts for about 92.7% of the change in direction.

For the ASM, the unstable Backflapping Mode ($\zeta = -0.084$, $\omega_n = 0.48$) had a time to double of $t_d = 17.2$ secs. For the SASM this mode ($\zeta = -0.1$, $\omega_n = 0.47$) has a time to double of $t_d = 14.5$ secs. Upon inspection of Table 5.3.3.2 we see that the change in the real and imaginary parts are mainly due to the changes in the ASM part of the SASM. Table 5.3.3.1 shows that doubling the slave tether length has resulted in some reordering of the ASM variables in terms of relative magnitude. More specifically, Table 5.3.3.3 shows that the change in eigenstructure which occurs (15.1%) is predominantly due to the changes which occur in the ASM part of the SASM. This is because these changes account for about 66.2% of the total change in eigenstructure.

For the ASM, the Vertical Spring Mode ($\zeta = 0.26$, $\omega_n = 0.76$) had a time constant of $\tau = 5.06$ secs and a period of oscillation of $T = 8.27$ secs. For the SASM, however, the mode ($\zeta = 0.25$, $\omega_n = 0.75$) has a time constant of $\tau = 5.27$ secs and a period of $T = 8.37$ secs. Table 5.3.3.2

shows that the changes in the time constant and perod of oscillation are both primarily due to the changes which occur in the ASM part of the SASM. Table 5.3.3.1 shows that doubling the slave tether length has not resulted in any reordering of the ASM variables in terms of relative magnitude. More specifically, Table 5.3.3.3 shows that the change in eigenstructure which occurs (31.4°) is primarily due to the changes which occur in the ASM part of the SASM rather than the new coupling terms due to Δx and $\Delta\theta$.

For the ASM, the Pendular Mode ($\zeta = 0.2$, $\omega_n = 2.7$) had a time constant of t = 1.88 secs and a period of T = 2.33 secs. For the SASM, however, the mode ($\zeta = 0.24$, $\omega_n = 2.51$) has time constant t = 1.63 secs and a period of T = 2.5 secs. Upon inspection of Table 5.3.3.2 we see that the changes in time constant and period are roughly equally attributable to the changes in the ASM part of the SASM as well as thre new coupling due to Δx and $\Delta\theta$. Table 5.3.3.1 shows that doubling the slave tether length has resulted in $\Delta\dot{\theta}$ playing an even more significant role than $\Sigma\dot{\theta}$. In addition, Table 5.3.3.3 shows that the changes in eigenstructure is predominantly due to the changes which occur in the ASM part of the SASM.

Finally, for the ASM, the Anti-Symmetric Damping Mode had a time constant of $\tau = 0.47$ secs. For the SASM, however, this mode has a time constant of $\tau = 0.5$ secs. Table 5.3.3.2 shows that this change in time constant is equally attributable to the changes in the ASM part of the SASM as well as to the new coupling terms due to Δx and $\Delta\theta$. Table 5.3.3.1 shows that the relative impact of this mode on $\Sigma\dot{x}$ has been reduced significantly. Table 5.3.3.3 shows that the change in eigenstructure is predominantly associated with the new coupling terms to Δx and $\Delta\theta$.

In summary, the above discussion indicates that doubling the slave tether length has not resulted in any drastic changes of the SM and ASM modes. More specifically, while time constants and periods have renmaines essentially unchanged, directions have changed somewhat. In most cases the directional changes were attributable to changes in the SM and ASM parts of the SASM rather than the new coupling terms due to Δx, $\Delta\theta$, $\Sigma\theta$, and x_L'.

Having studied the differences between the natural modes (poles) of the Equal and Unequal Tether Plants, we now examine their zeros.

5.4 Input/Output Properties of the Unequal Tether Plant

5.4.1 Introduction

The previous section discussed internal properties of the Unequeal Tether Plant. This section shall discuss some of the input/output properties of the Unequal Tether Plant. Such properties include transmission zeros (and their directions) as well as singular valves. Since the I/O properties of the AVM do not change when $H_s = 2H_m = 2H$, the section shall focus on the input/output properties of the SASM Plant, $G_{p23} \equiv C_{p23}(sI-A_{p23})^{-1}B_{p23}$. Emphasis shall be placed on the coupling that occurs between the Symmetric and Anti-Symmetric Motions.

5.4.2 Transmission Zeros of Unequal Tether (SASM) Plant

The Unequal Tether Plant, $G_p(s)$, consists of the AVM Plant, $G_{p1}(s)$, and the SASM Plant, $G_{p23}(s)$. It was shown in section 3.4.1 that the AVM Plant has no zeros. It thus follows that the zeros of the Unequal Tether Plant are merely the zeros of the SASM Plant. To obtain them one solves the following right generalized eigenvalue problem:

$$\begin{bmatrix} A_{p23} & B_{p23} \\ C_{p23} & 0 \end{bmatrix} \begin{bmatrix} \underline{x}_o \\ \underline{u}_o \end{bmatrix} = z \begin{bmatrix} I & 0 \\ 0 & 0 \end{bmatrix} \begin{bmatrix} \underline{x}_o \\ \underline{u}_o \end{bmatrix} \tag{5.42}$$

for all transmission zeros, z, with right zero direction, $\underline{x}_o$, and zero input direction, $\underline{u}_o$. The zeros for the Equal and Unequal Tether Plants have been tabulated in Table 5.4.2.1.

Table 5.4.2.1: Zeros of Equal and Unequal Tether Plants

Equal Tether Plant: ($H_s = H_m = H$)

SM: $z_{1,2} = -1.55 \pm j\,9.491$, $\zeta = 0.16$, $\omega_n = 9.62$

ASM: $z_{3,4} = -0.1786 \pm j\,6.413$, $\zeta = 0.028$, $\omega_n = 6.42$

$z_{5,6} = -1.371 \pm j\,9.807$, $\zeta = 0.139$, $\omega_n = 9.9$

Unequal Tether Plant: ($H_s = 2H_m$; $H_m = H$)

SASM: $z_{1,2} = -1.54 \pm j\,9.334$, $\zeta = 0.17$, $\omega_n = 9.47$

$z_{3,4} = -0.01138 \pm j\,5.874$, $\zeta = 0.002$, $\omega_n = 5.874$

$z_{5,6} = -1.512 \pm j\,10.93$, $\zeta = 0.137$, $\omega_n = 11.03$

To facilitate the comparison between the Equal and Unequal Tether Plant zeros we shall refer to the Unequal Tether Plant zeros using the same names used for the Equal Tether Plant zeros; i.e. $z_{1,2}$ shall be referred to as SM Helicopter Pitching Zeros, $z_{3,4}$ as ASM Load Motion Zeros, and $z_{5,6}$ as ASM Helicopter Pitching Zeros.

Table 5.4.2.2 shows the effect of coupling on the zeros of the Equal Tether Plant. The table clearly shows that the effects of coupling, when the tether lengths are unequal, has a relatively small impact on the zeros of the Equal Tether Plant. More specifically, the table shows that it is the changes in the SM and ASM parts of the SASM, and not the new coupling due to the unequal tether lengths, which is responsible foor most of the small differences between the Equal and Unequal Tether Plants' zeros.

Table 5.4.2.3 gives the zero directions for both the Equal and Unequal Tether Plants. Table 5.4.2.4 summarizes the effects of coupling on the Equal Tether zero directions. The table shows that the SM Pitching and ASM Load Motion Zero directions are predominantly affected by the coupling which results from having unequal tether lengths. The ASM Pitching Zero directions, however, are also largely affected by the changes which occur in the ASM part of the SASM.

Table 5.4.2.2: Effects of Coupling on Equal Tether Zeros

	SM and ASM Plants $G_{p2}(s)$ and $G_{p3}(s)$	SM and ASM Part of SASM Plant (SASM with coupling neglected)			SASM Plant, $G_{p23}(s)$		
	z	z	%ΔReal	%ΔReal	z	ΔReal	ΔReal
SM Pitching Zero	$z = -1.55 \pm j9.491$	$z = -1.55 \pm j9.3861$	0	55.9	$z = -1.5437 \pm j9.3034$	0.0063	-0.1876
ASM Load Motion Zero	$z = -0.1786 \pm j6.413$	$z = -0.0861 \pm j5.6942$	105.8	96.4	$z = -0.0912 \pm j5.6677$	0.0874	-0.7453
ASM Pitching Zero	$z = -1.371 \pm j9.807$	$z = -1.4638 \pm j9.55$	98.8	159	$z = -1.4649 \pm j9.6454$	-0.0939	-0.1616

Table 5.4.2.3: Directions for Equal and Unequal Tether Plant Zeros

	SM Pitching Zero	ASM Load Motion Zero	ASM Pitching Zero
Equal Tether Plant:	$z \cong -1.55 + j\,9.4907$	$z \cong -0.1777 + j\,6.4172$	$z \cong -1.3722 + j\,9.8004$
	$\underline{x} =$	$\underline{x} =$	$\underline{x} =$
	0. + 0. i	0. + 0. i	0. + 0. i
	-0.0000 + 0.0000i	-0.0000 + 0.0000i	0.0000 - 0.0000i
	0.1013 + 0.0076i	-0.0000 + 0.0000i	-0.0000 - 0.0000i
	0.0000 - 0.0000i	-0.0000 + 0.0000i	0.0000 + 0.0000i
	-0.2290 + 0.9497i	-0.0000 - 0.0000i	0.0000 - 0.0000i
	-0.0000 + 0.0000i	-0.0026 - 0.0952i	0.0132 + 0.0908i
	0.0000 - 0.0000i	-0.0246 + 0.0776i	0.0063 + 0.0078i
	0.0000 - 0.0000i	0.0130 - 0.0108i	-0.0070 - 0.0306i
	0.0000 + 0.0000i	0.0000 - 0.0000i	-0.0000 + 0.0000i
	-0.0000 - 0.0000i	0.6112 + 0.0002i	-0.9079 + 0.0052i
	0.0000 + 0.0000i	-0.4938 - 0.1715i	-0.0855 + 0.0503i
	0.0000 + 0.0000i	0.0671 + 0.0857i	0.3098 - 0.0270i
	$\underline{u} =$	$\underline{u} =$	$\underline{u} =$
	0. + 0. i	0. + 0. i	0. + 0. i
	0.1874 + 0.0140i	-0.0000 + 0.0000i	-0.0000 - 0.0000i
	-0.0000 + 0.0000i	0.1709 - 0.5363i	-0.0691 - 0.1502i
	-0.0000 + 0.0000i	-0.0330 - 0.0870i	0.0317 + 0.1770i
Unequal Tether Plant:	$z = -1.5437 + j\,9.3034$	$z = -0.0912 + j\,5.6677$	$z = -1.4649 + j\,9.6454$
	$\underline{x} =$	$\underline{x} =$	$\underline{x} =$
	0. + 0. i	0. + 0. i	0. + 0. i
	-0.0000 + 0.0000i	0.0000 - 0.0000i	-0.0000 + 0.0000i
	0.0366 + 0.0908i	0.0082 + 0.0489i	-0.0002 - 0.0737i
	-0.0000 + 0.0000i	0.0000 - 0.0000i	-0.0000 + 0.0000i
	-0.9011 + 0.2002i	-0.2778 + 0.0423i	0.7110 + 0.1064i
	-0.0067 - 0.0292i	0.0156 + 0.0797i	-0.0081 - 0.0581i
	-0.0005 - 0.0009i	0.0085 - 0.1047i	-0.0029 - 0.0043i
	0.0038 + 0.0158i	-0.0126 + 0.0105i	0.0057 + 0.0326i
	0.0000 - 0.0000i	0.0000 + 0.0000i	0.0000 + 0.0000i
	0.2821 - 0.0173i	-0.4530 + 0.0813i	0.5721 + 0.0074i
	0.0096 - 0.0043i	0.5928 + 0.0578i	0.0452 - 0.0214i
	-0.1630 + 0.0112i	-0.0584 - 0.0716i	-0.3231 + 0.0068i
	$\underline{u} =$	$\underline{u} =$	$\underline{u} =$
	0. + 0. i	0. + 0. i	0. + 0. i
	0.0655 + 0.1621i	0.0210 + 0.0343i	-0.0025 - 0.1403i
	0.0048 + 0.0159i	-0.0296 + 0.5645i	0.0262 + 0.0776i
	-0.0120 - 0.0521i	0.0358 + 0.0553i	-0.0171 - 0.1104i

Table 5.4.2.4: Effects of Coupling on Equal and Unequal Tether Plant Zero Directions

	Angle Between Equal and Unequal Tether Plant Zero Directions			
	Coupling Neglected		With Coupling	
	Zero Vector	Input Vector	Zero Vector	Input Vector
SM Pitching Zero	10.6°	11.2°	48.4°	45.9°
ASM Load Motion	0.3°	1°	65.5°	65°
ASM Pitching Zero	48.5°	44.7°	26.1°	15.4°

5.4.3 Frequency Domain Analysis of Unequal Tether Plant

The Equal and Unequal Tether Plants have four control inputs $\Sigma\Theta_c$, ΔB_{lc}, $\Delta\Theta_c$, ΣB_{lc} and outputs $\Sigma\dot{z}$, Δx, x_L-Σx, and $\Sigma\dot{x}$. Typically, the four outputs will be commanded by the master pilot (or computer) to be constant (with $\Delta x = x_L - \Sigma x = 0$). Because of this we first compare the dc characteristics of each configuration.

To study the dc characteristics of each configuration we assume that each has been stabilized and that constant control inputs are applied. From the Twin Lift equations obtained in Chapter 2, we have the following steady state relationships:

$$Z_w \Sigma\dot{z} + Z_{\Theta c}\, \Sigma\Theta_c = 0 \tag{5.43}$$

$$\begin{bmatrix} W_H + 0.5\,(W_L + W_B) & -0.5\,(W_L + W_B) \\ 0.5\,(W_L + W_B)\,h & -0.5\,(W_L + W_B)\,h \end{bmatrix} \begin{bmatrix} \Delta\theta \\ \Delta x \end{bmatrix} = \begin{bmatrix} M_H\, X_{Blc} \\ I_y\, M_{Blc} \end{bmatrix} \Delta B_{lc} \tag{5.44}$$

$$\Sigma\varepsilon = 0 \tag{5.45}$$

$$-4\mu\delta_L\, \hat{Z}\, (g / L)\, \Delta\dot{z} + Z_{\Theta c}\, \Delta\Theta_c = 0 \tag{5.46}$$

$$\begin{bmatrix} W_H + 0.5\,(W_L + W_B) & -M_H\, X_u \\ 0.5\,(W_L + W_B)\,h & -Iy\, M_u \end{bmatrix} \begin{bmatrix} \Sigma\theta \\ \Sigma\dot{x} \end{bmatrix} = \begin{bmatrix} M_H\, X_{Blc} \\ I_y\, M_{Blc} \end{bmatrix} \Delta B_{lc} \tag{5.47}$$

Assuming angles to be measured in degs and displacements in ft, eqs. (5.43) - (5.47) can be used to obtain dc gains which are common to both the Equal and Unequal Tether Plants. These gains are tabulated in Table 5.4.3.1.

To understand the differences between the dc characteristics of each configuration we recall the following relationships:

$$\Delta x = -\,[\, h\,\Delta\theta + H_m\varepsilon_m - H_s\,\varepsilon_s\,] \tag{5.48}$$

$$x_L' = 0.5\,[\, H_m\,\varepsilon_m + H_s\,\varepsilon_s\,] - H_s\,\Sigma\theta \tag{5.49}$$

$$x_L - \Sigma x = (h + H_s)\,\Sigma\theta + \hat{Z}\,\Delta z + x_L' \tag{5.50}$$

Table 5.4.3.1: DC Gains Common to Both the Equal and Unequal Tether Plants

$$\Sigma\dot{z} / \Sigma\Theta_c = - Z_{\Theta c} / Z_w = 17.195 \text{ ft sec}^{-1} / \text{deg}$$

$$\Delta\theta / \Delta B_{lc} = [X_{Blc} / g] - [M_{Blc} I_y / g M_H h] = 6.194 \text{ deg / deg}$$

$$\frac{\Delta\varepsilon}{\Delta B_{lc}} = [X_{Blc} / g] - \frac{[(M_H + 0.5 (M_L + M_B)) I_y M_{Blc}]}{0.5 W_H (M_L + M_B) h} = 18.03 \text{ deg / deg}$$

$$\Sigma\varepsilon = 0 \text{ deg}$$

$$\Delta z / \Delta\Theta_c = 0.5 M_H L^2 Z_{\Theta c} / W_L Z = 14.873 \text{ ft / deg}$$

$$\frac{\Sigma\theta}{\Sigma B_{lc}} = \frac{[1 / g] [I_y (X_u M_{Blc} - M_u X_{Blc})]}{[0.5 (M_L + M_B) h X_u - (M_H + 0.5 (M_L + M_B)) I_y M_u]} = - 0.7936 \text{ deg /deg}$$

$$\frac{\Sigma\dot{x}}{\Sigma B_{lc}} = \frac{(M_H + 0.5 (M_L + M_B)) I_y M_{Blc} - 0.5 (M_L + M_B) h M_H X_{Blc}}{0.5 (M_L + M_B) h M_H X_u - (M_H + 0.5 (M_L + M_B)) I_y M_u} = 18.76 \text{ ft sec}^{-1} / \text{deg}$$

Using eqs. (5.48) - (5.50) we obtain the following relationships:

$$\Delta x = - [0.0628 \Delta\theta + 0.2312 \Delta\varepsilon] \tag{5.51}$$

$$x_L' = 0.2312 [\Sigma\varepsilon - \Sigma\theta] \tag{5.52}$$

$$x_L - \Sigma x = 0.2941 \Sigma\theta + 0.5 \Delta z + x_L' \tag{5.53}$$

for the Equal tether Configuration and

$$\Delta x = - [0.0628 \Delta\theta + 0.2312 \varepsilon_m - 0.4625 \varepsilon_s] \tag{5.54}$$

$$x_L' = 0.1156 \varepsilon_m + 0.2312 \varepsilon_s - 0.4625 \Sigma\theta \tag{5.55}$$

$$x_L - \Sigma x = 0.52531 \Sigma\theta + 0.5 \Delta z + x_L' \tag{5.56}$$

for the Unequal Tether Configuration. Using eqs. (5.51) - (5.56) we obtain the dc gains in Table 5.4.3.2.

The relationships in Table 5.4.3.2 show that whether the tether lengths are equal or not, the steady state Δx depends only on ΔB_{lc}. Moreover, when the slave tether length is doubled the dc gain associated with Δx increases by approximately 46%. This implies that a smaller differential cyclic, ΔB_{lc}, is needed to sustain a fixed horizontal separation, Δx, when the tether lengths are unequal. The table also shows that the steady state $x_L - \Sigma x$ for the Unequal Tether Configuration

Table 5.4.3.2: Differences Between Equal and Unequal Tether Plant DC Characteristics

Equal Tether Plant:

$$\Delta x / \Delta B_{lc} = -4.558 \text{ ft / deg}$$

$$x_L' / \Sigma B_{lc} = 0.1835 \text{ ft / deg}$$

$$x_L - \Sigma x = 7.4365\, \Delta\Theta_c - 0.0499\, \Sigma B_{lc}$$

Unequal Tether Plant:

$$\Delta x / \Delta B_{lc} = -6.643 \text{ ft / deg}$$

$$x_L' = -1.042\, \Delta B_{lc} + 0.0367 \Sigma B_{lc}$$

$$x_L - \Sigma x = -1.042\, \Delta B_{lc} + 7.4365\, \Delta\Theta_c - 0.0499\, \Sigma B_{lc}$$

depends on ΔB_{lc} as well as on $\Delta\Theta_c$ and ΣB_{lc}. Finally, it is worth noting that Tables 5.4.3.1 and 5.4.3.2 indicate that whether the tether lengths are equal or unequal, $\Sigma\dot{z}$ will be controlled with $\Sigma\Theta_c$, Δx with ΔB_{lc}, $x_L - \Sigma x$ with $\Delta\Theta_c$, and $\Sigma\dot{x}$ with ΣB_{lc}.

Having compared the dc characteristics of each configuration we now compare their characteristics at other frequencies. Since each configuration is a MIMO system this is best done by examining the singular values of the Equal and Unequal Tether Plants. These singular values have been plotted in Fig. 5.4.3.1.

Fig. 5.4.3.1a shows the singular values for the combined SM and ASM Plants. These consist simply of the Bode magnitude plot for the SISO SM Plant and the singular values for the TITO

ASM Plant. Fig. 5.4.3.1b shows the singular values for the three-input three-output SASM Plant. Upon comparing the figures one sees that there is little difference between the basic shapes of the Equal and Unequal Tether Plant singular values. For both configurations the maximum singular value is associated primarily with $\Sigma\dot{x}$ and ΣB_{lc}. At low frequencies (below 1.5 rad/sec) the minimum singular value is associated primarily with Δx and ΔB_{lc}. At high frequencies (above 1.5 rad/sec) the minimum singular value is associated primarily with x_L - Σx and $\Delta\Theta_c$.

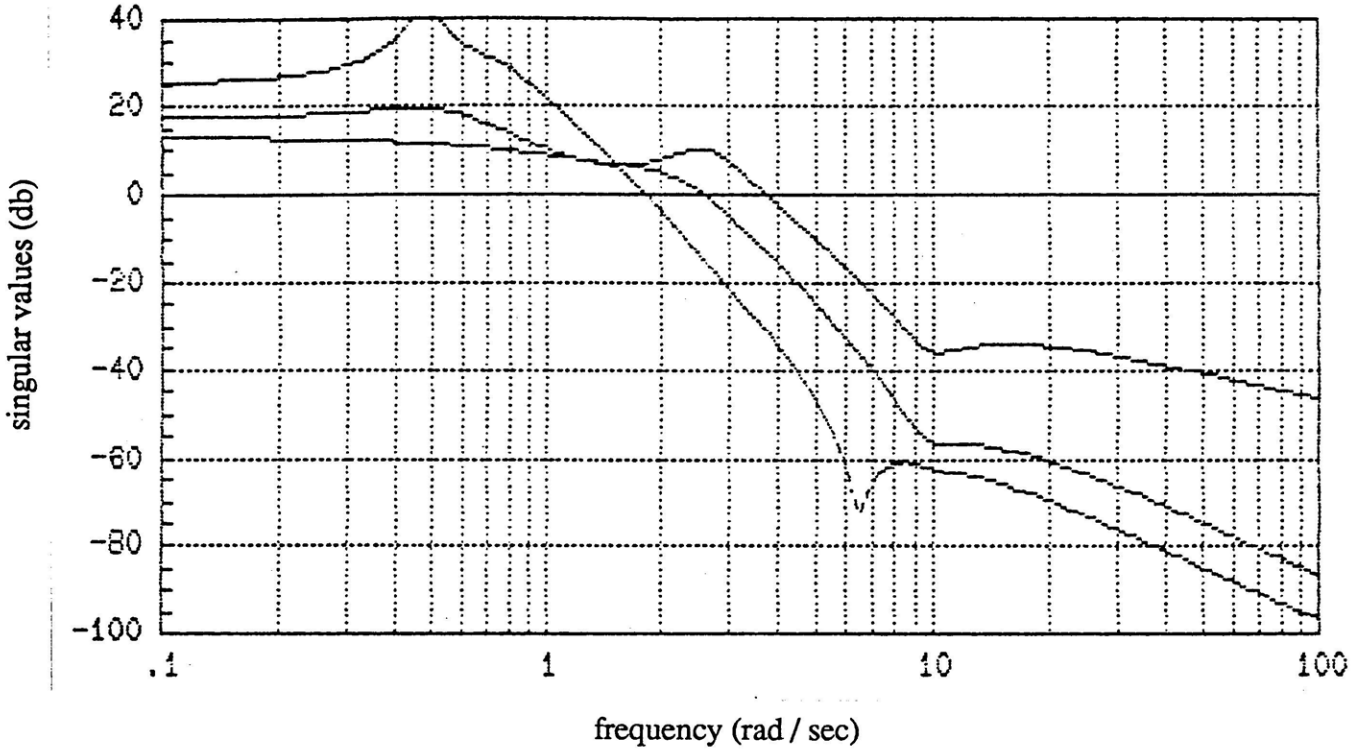

a) Equal Tether (SM and ASM) Plant

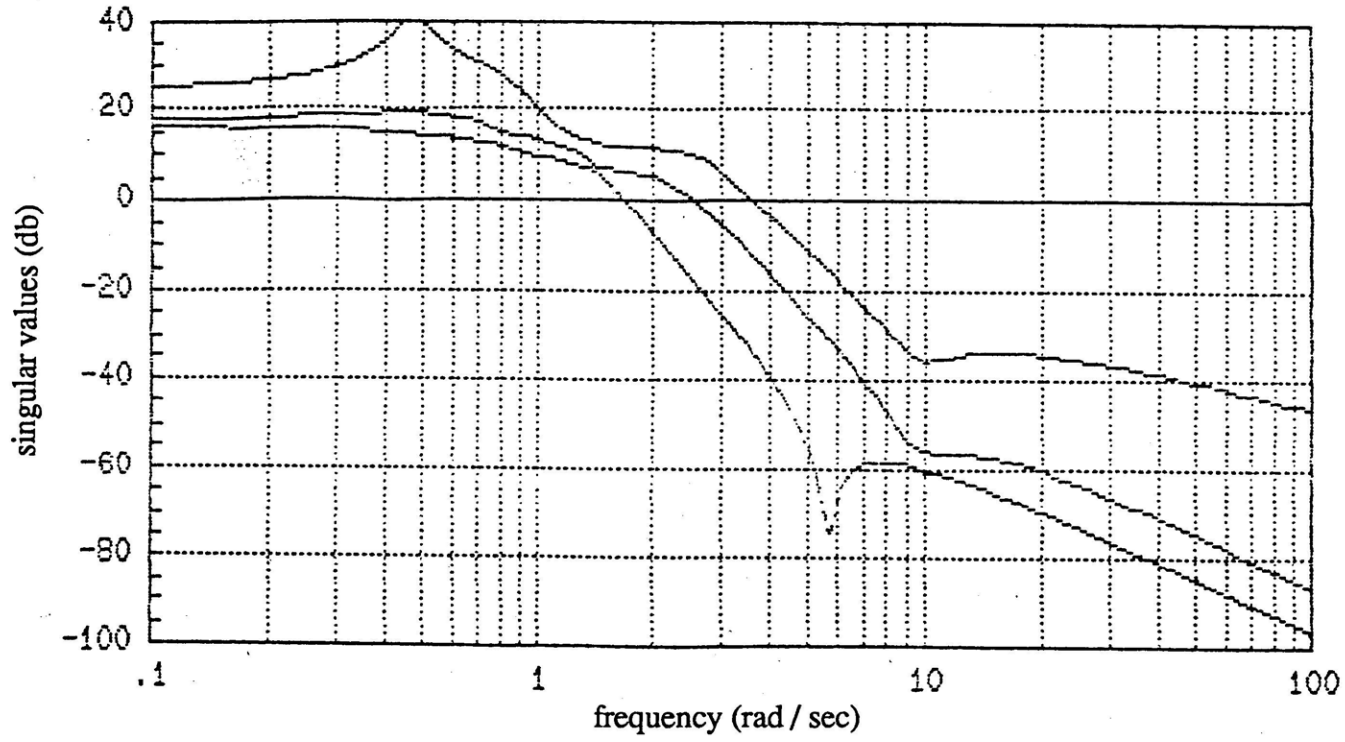

b) Unequal Tether (SASM) Plant

Fig. 5.4.3.1: Singular Values for Equal and Unequal Tether Plants.

5.5 TLHS Unequal Tether Control Problem Formulation

It has been shown tht the Unequal Tether Plant, $G_p(s)$, consists of two plants:

1. The AVM Plant, $G_{p1}(s) = C_{p1}(sI - A_{p1})^{-1}B_{p1}$,
2. The SASM Plant, $G_{p23}(s) = C_{p23}(sI - A_{p23})^{-1}B_{p23}$.

It thus follows that the final "Unequal Tether AFCS", to be designed in the next chapter, will consist of two AFCS's; i.e. one for each of the above plants.

In this section the structure of the final Unequal Tether AFCS. To help meet the performance specifications, the Unequal Tether Plant shall be augmented.

The purpose of this section is to formulate the Unequal Tether Control Problem and to qualitatively discuss the feasibility of a high performance Unequal Tether AFCS vis-a-vis a high performance Equal Tether AFCS..

5.5.1 Structure of Unequal Tether AFCS

Fig. 5.5.1.1 shows the structure of the final Unequal Tether AFCS to be developed in the next chapter. The AFCS is seen, simply, to possess a negative feedback MIMO structure. The AFCS consists of the 12th order Unequal Tether Plant (UTP), $G_p(s)$, a 4th order dynamic augmentation, a dynamic LQG/LTR compensator, $K_{LQG/LTR}(s)$, and a pre-filter. When properly designed, the AFCS "minimizes" the effects of the disturbances, $\underline{d}$, and sensor noises, $\underline{n}$, so that the system outputs, $\underline{y}$, "approximate" the pilot reference commands, $\underline{r}$.

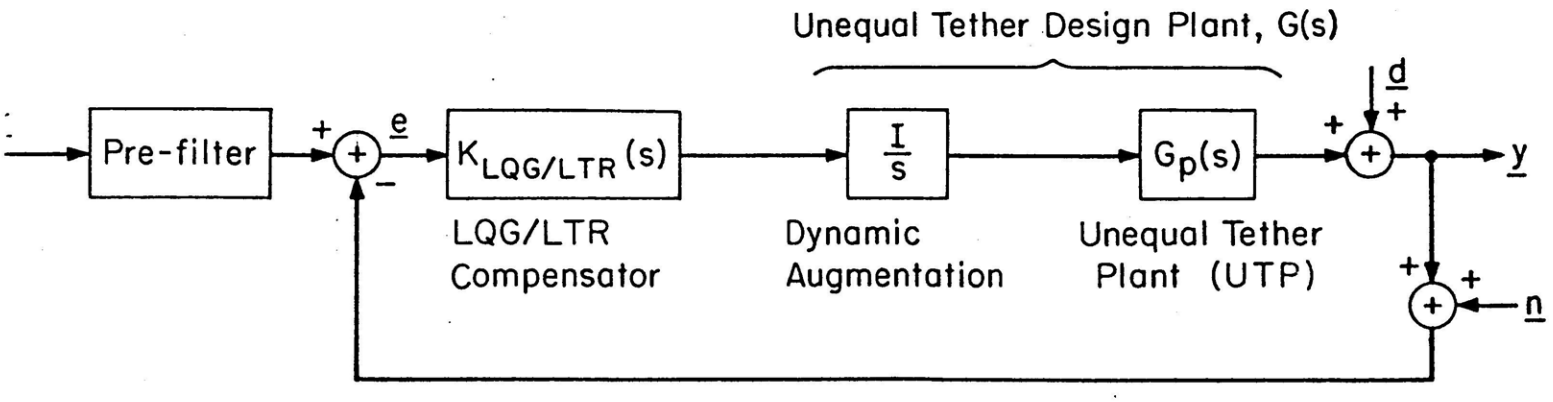

Fig. 5.5.1.1: Structure of Unequal Tether AFCS.

As noted earlier, the Unequal Tether Plant, $G_p(s)$, consists of the (always decoupled) AVM and SASM Plants; i.e. $G_p(s) = \text{diag}(G_{p1}(s), G_{p23}(s))$.

The dynamic augmentation consists of four integrators (one per input channel). As in the Equal Tether Problem, their primary function is to guarantee zero steady state errors to step commands for $\Sigma\dot{z}$, Δx, x_L-Σx, and $\Sigma\dot{x}$. It should be emphasized that, in general, the dynamic augmentation can be any linear time invariant continuous system which is realizable and helps the designer meet the specifications.

The Unequal Tether Plant plus the dynamic augmentation (four integrators) shall be referred to as the Unequal Tether Design Plant. The Unequal Tether Design Plant consists of an AVM Design Plant and a SASM Design Plant. The AVM Design Plant, as in Chapters 3 and 4, shall be denoted by:

$$G_1(s) = C_1(sI - A_1)^{-1}B_1 \tag{5.26}$$

$$= G_{p1}(s) / s \tag{5.27}$$

The SASM Design Plant shall be denoted by:

$$G_{23}(s) = C_{23}(sI - A_{23})^{-1}B_{23} \tag{5.28}$$

$$= G_{p23}(s) / s \tag{5.29}$$

The state space representation for the Unequal Tether Design Plant is as follows:

$$\dot{\underline{x}} = A\,\underline{x} + B\,\underline{u} \qquad \underline{x} \in \mathbf{R^{16}};\ \underline{u} \in \mathbf{R^4} \tag{5.30}$$

$$\underline{y} = C\,\underline{x} + \underline{d} \qquad \underline{y} \in \mathbf{R^4};\ \underline{d} \in \mathbf{R^4} \tag{5.31}$$

where

$$\underline{u} = [u_1 \ \ u_2 \ \ u_3 \ \ u_4]^T \tag{5.32}$$

$$= [\Sigma\dot{\Theta}_c \ \ \Delta\dot{B}_{lc} \ \ \Delta\dot{\Theta}_c \ \ \Sigma\dot{B}_{lc}]^T \tag{5.33}$$

$$\underline{x} = [\underline{x}_p{}^T \ \ \underline{u}_p{}^T]^T \tag{5.34}$$

$$\underline{x}_p = [\Sigma\dot{z} \,\|\, \Delta x \ \ \Delta\theta \ \ \Delta\dot{x} \ \ \Delta\dot{\theta} \ \ \Sigma\theta \ \ \Delta z \ \ x_L' \ \ \Sigma\dot{x} \ \ \Sigma\dot{\theta} \ \ \Delta\dot{z} \ \ \dot{x}_L']^T \tag{5.35}$$

$$\underline{u}_p = [\Sigma\Theta_c \,\|\, \Delta B_{lc} \ \ \Delta\Theta_c \ \ \Sigma B_{lc}]^T \tag{5.36}$$

$$\underline{y} = [\Sigma\dot{z} \,\|\, \Delta x \ \ x_L\text{-}\Sigma x \ \ \Sigma\dot{x}]^T + \underline{d} \tag{5.37}$$

and $\underline{d}$ is a four dimensional signal vector which contains output disturbances on $\Sigma\dot{z}$, Δx, x_L-Σx, and $\Sigma\dot{x}$, respectively. The relationship between (A, B, C) and (A_{p1}, B_{p1}, C_{p1}) and (A_{p23}, B_{p23}, C_{p23}) is as follows:

$$A = \begin{bmatrix} A_p & B_p \\ 0 & 0 \end{bmatrix} \tag{5.39}$$

$$B = [0 \quad I]^T \tag{5.40}$$

$$C = [C_p \quad 0]. \tag{5.41}$$

where $A_p \equiv (\text{diag}(A_{p1}, A_{p23})$, $B_p \equiv \text{diag}(B_{p1}, B_{p23})$, and $C_p \equiv \text{diag}(C_{p1}, C_{p23})$.

The Unequal Tether Design Plant tfm is given by:

$$G(s) = C(sI - A)^{-1}B \, . \tag{5.42}$$

The Unequal Tether LQG/LTR compensator consists of two compensators (one for each of the Unequal Tether Design Plants). It can be denoted as follows:

$$K_{LQG/LTR}(s) = \text{diag}\,\{K^1_{LQG/LTR}(s), K^{23}_{LQG/LTR}(s)\} \tag{5.43}$$

where $K^1_{LQG/LTR}(s)$ and $K^{23}_{LQG/LTR}(s)$ denote the AVM and SASM LQG/LTR compensators, respectively. The order of the Unequal Tether LQG/LTR compensator is 16; the order of the Unequal Tether Design Plant (Unequal Tether Plant plus dynamic augmentation).

Since the total compensation consists of the dynamic augmentation plus the LQG/LTR compensator, it makes sense to define the compensator, K(s), as follows:

$$K(s) \equiv K_{LQG/LTR}(s) \, / \, s \tag{5.44}$$

$$= \text{diag}\,\{K_1(s), K_{23}(s)\} \tag{5.45}$$

where $K_1(s)$ and $K_{23}(s)$ denote the AVM and SASM compensators, respectively.

The pre-filter consists of three Butterworth filters; one for each reference command input to the SASM AFCS. As in the Equal Tether Problem, their introduction is essential in order to bandlimit reference commands so that the pitch rates, control rates, and other internal variable rates are

tolerable. It should be emphasized though that typically Δx and x_L - Σx will be commanded to zero.

As for the Equal Tether Problem, we define the Unequal Tether Loop, Sensitivity, and Closed Loop tfm's as follows:

Loop:
$$G_L(s) = G_p(s)\, K(s) \tag{5.46}$$
$$= \text{diag}(\, G_{L1}(s), G_{L23}(s)\,) \tag{5.47}$$

$$G_{L1}(s) = G_{p1}(s)\, K_1(s) \tag{5.48}$$
$$G_{L23}(s) = G_{p23}(s)\, K_{23}(s) \tag{5.49}$$

Sensitivity:
$$S(s) = [\, I + G_L(s)\,]^{-1} \tag{5.50}$$
$$= \text{diag}(\, S_1(s)\, S_{23}(s)\,) \tag{5.51}$$

$$S_1(s) = [\, I + G_{L1}(s)\,]^{-1} \tag{5.52}$$
$$S_{23}(s) = [\, I + G_{L23}(s)\,]^{-1} \tag{5.53}$$

Closed Loop:
$$T(s) = [\, I + G_L(s)\,]^{-1}\, G_L(s) \tag{5.54}$$
$$= \text{diag}(\, T_1(s)\, T_{23}(s)\,) \tag{5.55}$$

$$T_1(s) = [\, I + G_{L1}(s)\,]^{-1}\, G_{L1}(s) \tag{5.56}$$
$$T_{23}(s) = [\, I + G_{L23}(s)\,]^{-1}\, G_{L23}(s) \tag{5.57}$$

where the subscript "1" refers to the AVM AFCS and the subscript "23" refers to the SASM AFCS.

As in the Equal Tether Control Problem, the prime objectives of the Unequal Tether AFCS, in addition to guaranteeing nominal stability, can be listed as follows:

1. Low frequency command following;
2. Low frequency disturbance rejection;
3. Insensitivity to low frequency modeling errors;
4. High frequency sensor noise attenuation;
5. Robustness to high frequency unmodeled dynamics.

To assure the first three, we require that the Unequal Tether Sensitivity tfm, S(s), be "small" at "low" frequencies where reference commands, disturbaces, and "unintentional" modeling errors have their greatest spectral content. To assure the last two, we require that the Unequal Tether Closed Loop tfm, T(s), be "small" at high frequencies where sensor noises and "intentionally" unmodeled dynamics have their greatest spectral content.

In addition to the above five desirable feedback properties, the Unequal Tether AFCS must be designed so that the closed loop system exhibits "good" internal performance. This means that the pitch rates of the helicopters, as well as their vertical and horizontal acceleration characteristics, must be "passenger friendly". It also implies that the amplitude and/or spectral content of references, as well as the closed loop bandwidth must be resticted so that the control transients do not exceed the control limits. This saturation issue is particularly important to Twin Lift engineers because of the inherent open loop instabilities associated with the Unequal Tether Configuration. The presence of these instabilities imply that the closed loop system will have a finite "downward gain margin". Consequently, if the controls are permitted to saturate an effective loop gain reduction will occur and the system may become highly oscillatory and possibly go unstable.

The sections which follow shall present performance and stability robustness specifications for the final Unequal Tether AFCS. These design specifications shall be pesented in terms of the final AVM and SASM loop, sensitivity, and closed loop functions. These specifications will primarily be based on TLHS capabilities, as reflected in the linear model. Before presenting the specifications it is important to put our goals into proper perspective.

In chapter 4 we showed that a trade-off must be made between performance and stability robustness when designing an Equal Tether AFCS. It was also shown that this trade-off is particularly pronounced when a high performance (high bandwidth) design is sought. In the remaining sections of this chapter we present design specifications which are comparable to those presented for the Equal Tether AFCS. In the next chapter we apply the LQG/LTR procedure to the Unequal Tether Design Plant in order to meet the specifications and ascertain whether the performance/robustness trade-off is less pronounced when the tether lengths are unequal.

5.5.2 Design Specifications for Unequal Tether (SASM) AFCS

For simplicity, the AVM AFCS used for the Equal Tether AFCS shall also be used for the Unequal Tether AFCS. It thus suffices to give specifications for the SASM AFCS.

The structure of the final SASM AFCS is shown in Fig. 5.5.2.1.

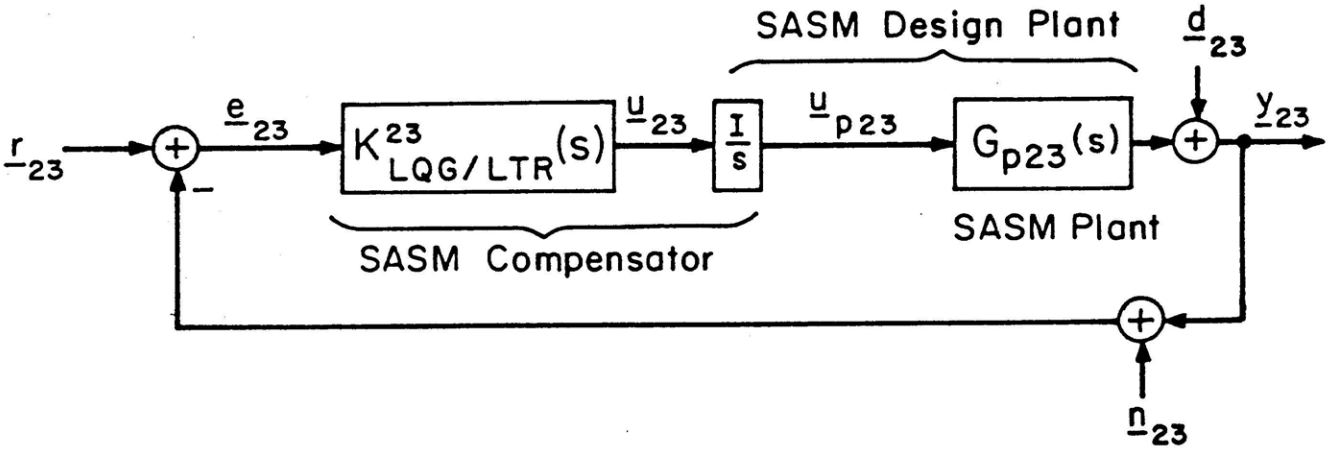

Fig. 5.5.2.1: Structure of SASM AFCS.

Since the SASM Plant, $G_{p23}(s)$, does not contain any natural integrators, it has been augmented with three (one per input channel) so that we are guaranteed zero steady state error to step reference commands, r_{23}, for Δx, x_L-Σx, and Σx. The integrators will also guarantee zero steady state error to step output disturbances, d_{23}. The combined SASM Plant and integrators, as stated earlier, shall be referred to as the SASM Design Plant and shall be denoted by the tfm $G_{23}(s)$, where

$$G_{23}(s) = G_{p23}(s) / s \tag{5.58}$$

$$= C_{23}(sI - A_{23})^{-1} B_{23} \tag{5.59}$$

In Chapter 6, the SASM LQG/LTR compensator, $K^{23}{}_{LQG/LTR}(s)$, and the SASM pre-filter shall be developed. Since a high performance design is desired, the specifications for the final SASM AFCS were selected as follows:

SASM AFCS Design Specifications

Performance:

1. Zero steady state error to step commands and step output disturbances in all directions. To guarantee this the SASM Plant was augmented with three integrators (one per channel) at the plant input.

2. Less than 10% steady state error ($\|\underline{e}_{23}\|_2 \leq 0.1 \|\underline{d}_{23}\|_2$) to sinusoidal commands and output disturbances with spectral content at or below 0.06 rad/sec. This requires that the final SASM sensitivity tfm satisfy

$$\sigma_{max}[S_{23}(j\omega)] \leq -20 \text{ db} \qquad \text{for all } \omega \leq 0.06 \text{ rad/sec}$$

3. Low frequency errors on the unit circle are of equal importance. This implies that the final SASM sensitivity tfm should satisfy:

$$\sigma_{max}[S_{23}(j\omega)] \approx \sigma_{min}[S_{23}(j\omega)] \quad \text{(at each } \omega)$$

at low frequencies; i.e. the loop singular values should be matched at low frequencies.

4. Gain crossover frequencies: $0.5 \text{ rad/sec} \leq \omega_{g23} \leq 2 \text{ rad/sec}$.

5. Noise attenuation: $\sigma_{max}[T_{23}(j\omega)] \leq -20$ db for all $\omega \geq 20$ rad/sec.

Robustness

1. Robustness to low frequency uncertainty and high frequency unmodeled rotor dynamics (ω_r = 27 rad/sec).

   To ensure this we require that the final SASM sensitivity tfm satisfy:

$$\sigma_{max}[S_{23}(j\omega)] \leq \beta_{23} = 1.93 \text{ (5.72 db) for all } \omega \geq 0.$$

   It can be shown that this translates into the following MIMO stability margins:

$$\text{Gain Margins: } \downarrow GM_{23} \geq \beta_{23} / (\beta_{23} + 1) = 0.66 \text{ (-3.6 db)}$$

$$\uparrow GM_{23} \geq \beta_{23} / (\beta_{23} - 1) = 2.08 \text{ (6.3 db)}$$

$$\text{Phase Margins: } | PM_{23} | \geq 2\sin^{-1}(1 / 2\beta_{23}) = \underline{30^\circ}$$

2. Closed loop gain crossover frequencies (bandwidth): $\omega_{CL23} \leq 3$ rad/sec.

The SASM pre-filters shall be selected so that references are appropriately bandlimited. Butterworth filters shall be used since they are maximally flat in the pass band. The order of the filters, as well as their cut-off frequencies, will be selected from the final reference to control singular values since these show clearly what reference frequencies are amplified by the AFCS.

We point out, once again, the similarity between the above method of posing specifications and the classical Bode method. It should also be noted that the specifications have been expressed in terrms of the loop, sensitivity, and closed loop tfm's associated with the plant output (or error signal); i.e. the specifications have been presented at the plant output. We make this point because, in general, a designer may also want to satisfy design specifications "at the plant input". Such specifications would be presented in terms of the singular values of the loop tfm obtained by breaking the loop at the plant input.

In order to assess the ease/difficulty in meeting the design specifications we refer to Fig. 5.5.2.2 which shows the singular values of the Equal and Unequal Tether Design Plants (AVM Design Plant omitted). Upon comparison of these singular values we see relatively little difference. It thus follows that the trade-off between performance and robustness exhibited in Chapter 4 for the Equal Tether Design Problem is not only expected to be present for the Unequal Tether Design Plant, but it is expected to be just as pronounced. This also follows from the fact that Equal and Unequal Tether Design Plants have very similar pole-zero structures.

5.6 Summary

In this chapter the TLHS Unequal Tether Configuration ($H_s = 2H_m$; $H_m = H$) was analyzed and compared with the Equal Tether Configuration. The primary reason fior studying the Unequal Tether Configuration in this thesis was to see whether or not having unequal tether lengths lessons the trade-off between performance and stability robustness when a high performance (high bandwidth) design is desired. Because of the great similarities between the Equal and Unequal Tether Plants, it was concluded that the above trade-off would not only be present for the Unequal

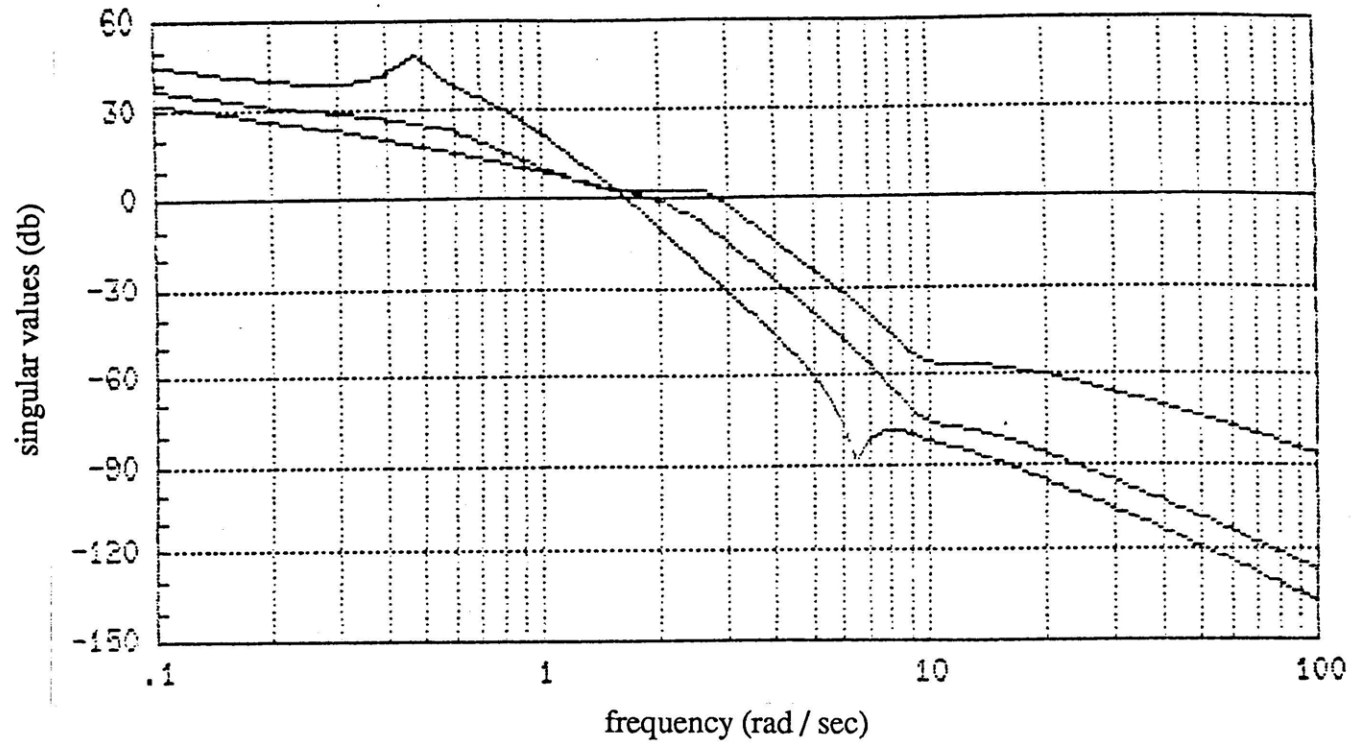

a) SM and ASM Design Plants

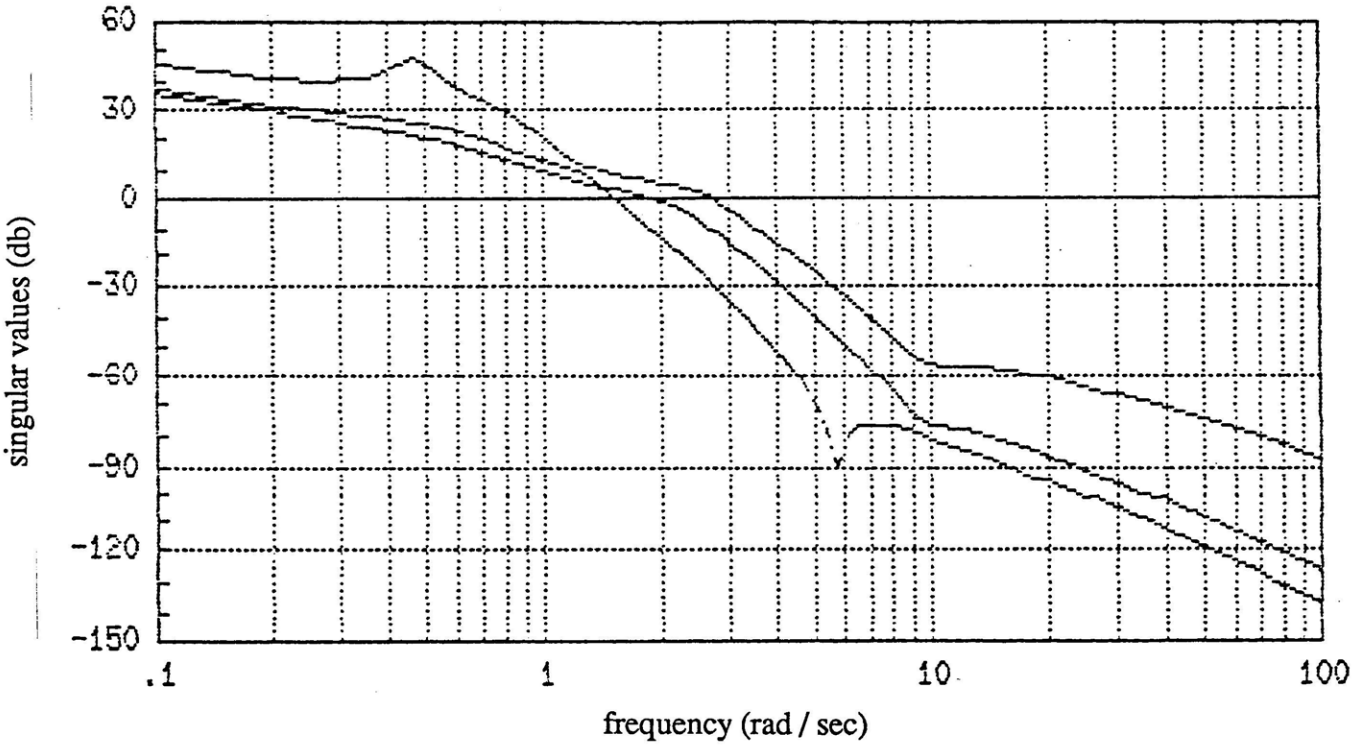

b) SASM Design Plant

Fig. 5.5.2.2: Singular Values of Equal and Unequal Tether Design Plants

(AVM Design Plant omitted).

Tether Problem, but would be just as pronounced as for the Equal Tether Problem. This shall be confirmed in Chapter 6.

In this chapter it was shown that when the tether lengths are unequal the Symmetric and Anti-Symmetric Motions (SM and ASM) becomes coupled. The combined SM and ASM was named "the SASM".

The natural modes of the Unequal Tether Configuration were identified, discussed, and compared to those of the Equal Tether Configuration. The Unequal Tether Plant was then defined in terms of an AVM Plant and a SASM Plant. The transmission zeros and frequency responses of the Equal and Unequal Tether Plants were discussed and compared. The comparisons indicated only small differences between the designs.

Finally, the chapter concluded with a description of the Unequal Tether AFCS and design specifications to be met. To help meet the performance specifications the Unequal Tether Plant was augmented giving us the Unequal Tether Design Plant.

In the next chapter we shall use the LQG/LTR design methodology and simple filtering techniques to develop an AFCS for the Unequal Tether Configuration. The AFCS shall satisfy the specifications presented in subsection 5.5.2.

CHAPTER 6: AFCS DESIGN FOR UNEQUAL TETHER CONFIGURATION

6.1 Introduction

In Chapter 4 a high bandwidth AFCS, with modest robustness properties, was developed for the Equal Tether Configuration. It was shown that in designing an Equal Tether AFCS, a designer must trade-off performance versus stability robustness. It was also shown that this trade-off becomes particularly pronounced when a high performance (high bandwidth) design is the objective.

In this chapter the LQG/LTR design methodology is applied to the Unequal Tether Design Plant, discussed in Chapter 5. The chapter shows how the methodology, coupled with singular value ideas, can be used to systematically develop and AFCS for the Unequal Tether Configuration. A design satisfying the specifications presented in Chapter 5 is obtained and evaluated. Comparisons are made between the Equal and Unequal Tether AFCS's. From the comparison several conclusions are drawn. First, having unequal tether lengths does not lessen the performance-robustness trade-off encountered in the design of the Equal Tether AFCS. Secondly, a high bandwidth AFCS design for either configuration is feasible only when model uncertainty is sufficiently low. If model uncertainty is high then the designs become unfeasible. This is because, in such a case, the large robustness requirement forces the helicopters to undergo substantial pitching and oscillations in the vertical plane in order to regulate the horizontal separation and load motion when horizontal and vertical velocities are commanded. More specifically, if model uncertainty is high then only low bandwidth Equal and Unequal Tether AFCS designs become feasible. Finally, it is also concluded that there are no major dynamic advantages or disadvantages between Equal and Unequal Tethered flight. The latter, of course, is preferred because it offers greater tip-to-tip main rotor clearance.

6.2 Design and Evaluation of Unequal Tether AFCS

6.2.1 Introduction

In this section the LQG/LTR design methodology, described in section 4.2, shall be applied to the Unequal Tether Design Plant, $G(s) = G_p(s) / s = C(sI - A)^{-1}B$ discussed in Chapter 5. A compensator satisfying the performance and robustness specifications presented in Chapter 5 is

obtained. The Unequal Tether Design Plant consists of the Unequal Tether Plant, $G_p(s) = C(_p\, sI - A_p)^{-1}B_p$, preceded by four integrators. We recall that the Unequal Tether Plant has four controls: $\Sigma\Theta_c$, ΔB_{lc}, $\Delta\Theta_c$, ΣB_{lc} which are assumed to be measured in degs, and four outputs: $\Sigma\dot{z}$, Δx, $x_L - \Sigma x$, $\Sigma\dot{x}$ which are assumed to be measured in ft/sec, ft, ft, and ft/sec, respectuvely.

6.2.2 Design of Unequal Tether AFCS

To obtain the target loop dynamics, $G_{KF}(s) = C(sI - A)^{-1}H_\mu$, we solved the following FARE:

$$0 = A\Sigma_\mu + \Sigma_\mu A + LL^T - \Sigma_\mu C^T (1/\mu) C \Sigma_\mu \tag{6.1}$$

$$H_\mu = \Sigma_\mu C^T (1/\mu). \tag{6.2}$$

$$L = B\ [C_p(-A_p)^{-1}B_p]^{-1} \tag{6.3}$$

and

$$\mu = 1. \tag{6.4}$$

Eq. (6.3) guarantees that the target loop singular values will be matched at low frequencies. To "recover" the target loop dynamics we solved the following CARE:

$$0 = -K_\rho A - A^T K_\rho - C^T C + K_\rho B R^{-1} B^T K_\rho, \tag{6.5}$$

$$G_\rho = R^{-1} B^T K_\rho. \tag{6.6}$$

with

$$R = \mathrm{diag}(\rho_1,\ \rho_2,\ \rho_3,\ \rho_3) \tag{6.7}$$

where

$$\rho_1 = \rho_2 = 0.1\ \rho_3 = 10^{-6} \tag{6.8}$$

The recovered Unequal Tether LQG/LTR compensator is then given by:

$$K_{LQG/LTR}(s) = G_\rho\ (sI - A + BG_\rho + H_\mu C)^{-1}\ H_\mu \tag{6.9}$$

where the filter and control gain matrices, H_μ and G_ρ, are given in Table 6.2.2.1. The filter and control matrices for the Equal Tether AFCS are also given in the table.

Table 6.2.2.1: Filter and Control Gain Matrices For Equal and Unequal Tether AFCS's

Equal Tether AFCS:

$H_\mu =$

0.0582	-0.0000	0.0000	-0.0000
-0.0000	0.2194	0.0000	-0.0000
0.0000	-0.0000	0.1201	0.0605
0.0000	-0.0000	-0.0239	0.0477
0.4921	-0.0000	-0.0000	-0.0000
-0.0000	2.2063	0.0000	-0.0000
0.0000	-4.9246	-0.0000	0.0000
-0.0000	2.4339	0.0000	-0.0000
0.0000	-4.5237	-0.0000	0.0000
-0.0000	0.0000	0.3605	-1.0979
0.0000	-0.0000	1.6237	0.3121
0.0000	-0.0000	0.0017	0.0117
0.0000	-0.0000	-0.1552	1.0734
-0.0000	-0.0000	0.2494	0.0244
0.0000	0.0000	0.6729	-0.2014
-0.0000	0.0000	0.0250	-0.0129

$G_\rho =$

COLUMNS 1 THRU 8							
90.2992	-0.0000	0.	0.	994.7484	0.0000	-0.0000	0.0000
-0.0000	22.7950	0.	0.	-0.0000	955.4616	-36.4496	282.7296
-0.0000	0.0000	13.0342	-1.1653	-0.0000	-0.0000	0.0000	-0.0000
0.0000	0.0000	-1.1653	23.5920	0.0000	0.0000	-0.0000	0.0000

COLUMNS 9 THRU 16							
0.0000	0.	0.	0.	0.	0.	0.	0.
-2.6378	0.	0.	0.	0.	0.	0.	0.
-0.0000	43.7344	138.3322	156.5858	149.8413	45.5383	87.6480	153.4790
-0.0000	-63.2715	-74.8953	-79.9454	275.6631	-17.1355	-27.2046	-49.3773

Unequal Tether AFCS:

$H_\mu =$

0.0582	-0.0000	0.0000	-0.0000
0.0000	0.1504	0.0060	0.0019
0.0000	0.0155	0.1186	0.0649
0.0000	0.0004	-0.0255	0.0468
0.4921	0.0000	-0.0000	0.0000
0.0000	1.9954	0.1050	0.1125
-0.0000	-3.4602	-0.0580	-0.5435
0.0000	2.0035	0.1097	0.2149
-0.0000	-2.7217	0.0032	-0.3350
-0.0000	-0.3285	0.3523	-1.0808
0.0000	-0.0313	1.6057	0.4537
0.0000	0.2932	-0.0384	0.1879
0.0000	0.1195	-0.1530	1.0522
-0.0000	-0.1433	0.2579	-0.0022
0.0000	-0.0983	0.6341	-0.2005
0.0000	0.3056	0.0155	0.0095

$G_\rho =$

COLUMNS 1 THRU 8							
90.2992	-0.0000	0.0000	-0.0000	994.7484	-0.0000	0.0000	-0.0000
0.0000	22.7266	0.0186	0.3255	0.0000	966.7645	-35.8927	284.2341
0.0000	0.0019	12.2572	-1.0652	0.	15.0265	0.1072	4.2872
-0.0000	0.0326	-1.0652	23.5113	0.0000	-12.4205	-0.3739	-2.0392

COLUMNS 9 THRU 16							
0.0000	-0.0000	-0.0000	-0.0000	0.0000	-0.0000	-0.0000	-0.0000
-2.5897	6.5393	-1.7077	16.4405	11.1940	2.7003	1.9341	5.3352
0.0354	95.8351	137.3841	176.2613	153.5281	85.8231	90.3329	162.7604
-0.0363	-91.3561	-76.7285	-99.8125	273.6375	-30.7654	-28.6615	-53.7143

Note: It is assumed here that the Equal Tether Design Plant states are arranged in the same order as the Unequal Tether Design Plant states (Chapter 5);

i.e. $\underline{x}_p = [\ \Sigma\dot{z} \parallel \Delta x\ \ \Delta\theta\ \ \Delta\dot{x}\ \ \Delta\dot{\theta} \parallel \Sigma\theta\ \ \Delta z\ \ x_L'\ \ \Sigma\dot{x}\ \ \Sigma\dot{\theta}\ \ \Delta\dot{z}\ \ \dot{x}_L'\ ]^T$

6.2.3 Frequency Domain Evaluation of Unequal Tether (SASM) AFCS

In this section we evaluate the loop, sensitivity, closed loop, LQG/LTR compensator, and reference to control singular values for the Equal and Unequal Tether AFCS's. Since the AVM AFCS is common to both, we shall focus on the singular values associated with the combined SM and ASM AFCS's and those associated with the SASM AFCS. The combined SM and ASM AFCS's form a three-input three-output system. The SASM AFCS is also a three-input three-output system.

Fig. 6.2.3.1 shows the target and recovered loop singular values for the Equal and Unequal Tether AFCS's. The target loop singular values for each configuration look almost identical. The recovered loop singular values differ a little.

Fig. 6.2.3.2 shows the sensitivity and closed loop singular values for the Equal and Unequal Tether AFCS's. The sensitivities for each configuration are seen to be nearly identical. The same is true for the closed loop singular values for each configuration.

Fig. 6.2.3.3 shows the LQG/LTR compensator and reference to control singular values for the Equal and Unequal Tether AFCS's. In this figure we see the biggest differences, but even they are small.

Based on the Unequal Tether reference to control singular values we shall use 3rd order Butterworth filters:

$$H(s) = \omega_0^3 / [s^3 + 2\omega_0 s^2 + 2\omega_0^2 s + \omega_0^3] \qquad (6.10)$$

with $\omega_0 = 4$ rad/sec to pre-filter Δx, $x_L - \Sigma x$, and $\Sigma \dot{x}$ reference commands. This is what we used for the Equal Tether AFCS.

6.2.4 Unequal Tether AFCS Poles and Zeros

Table 6.2.4.1 contains the target open loop poles and zeros for the Equal and Unequal Tether AFCS's. Table 6.2.4.2 contains the recovered open loop poles and zeros.

Table 6.2.4.3 contains the target closed loop poles and zeros for the Equal and Unequal Tether AFCS's. Table 6.2.4.4 contains the recovered closed loop poles and zeros.

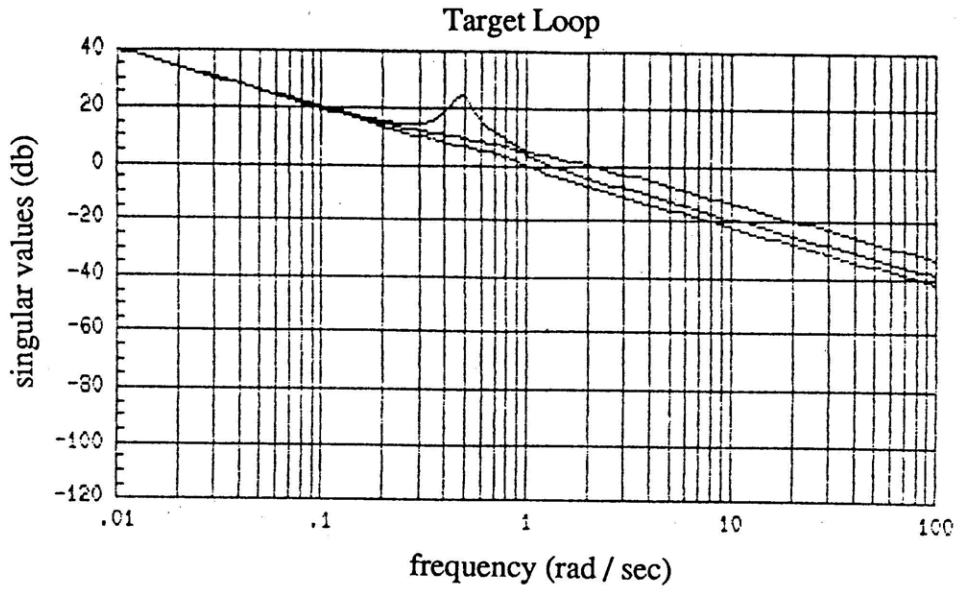

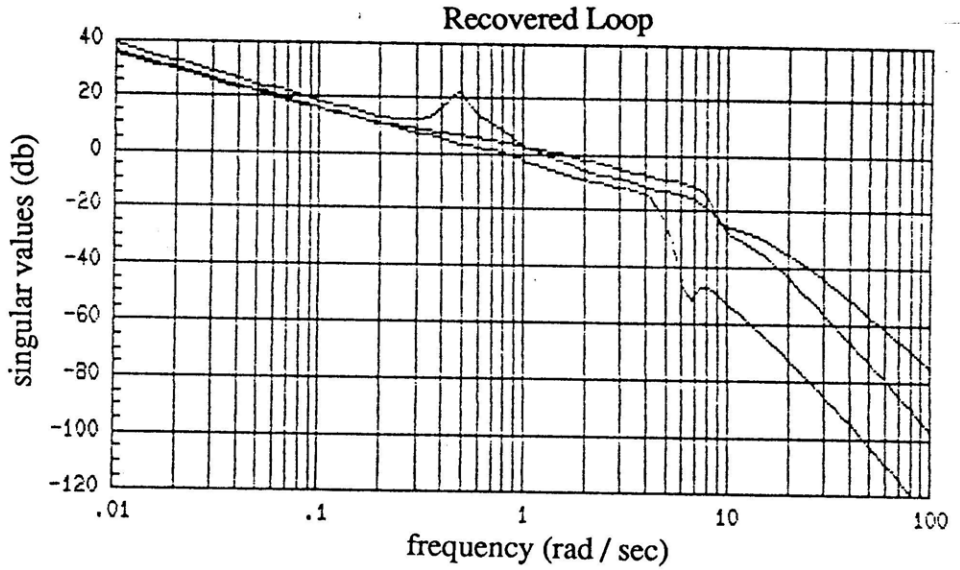

a) Equal Tether (SM and ASM) AFCS

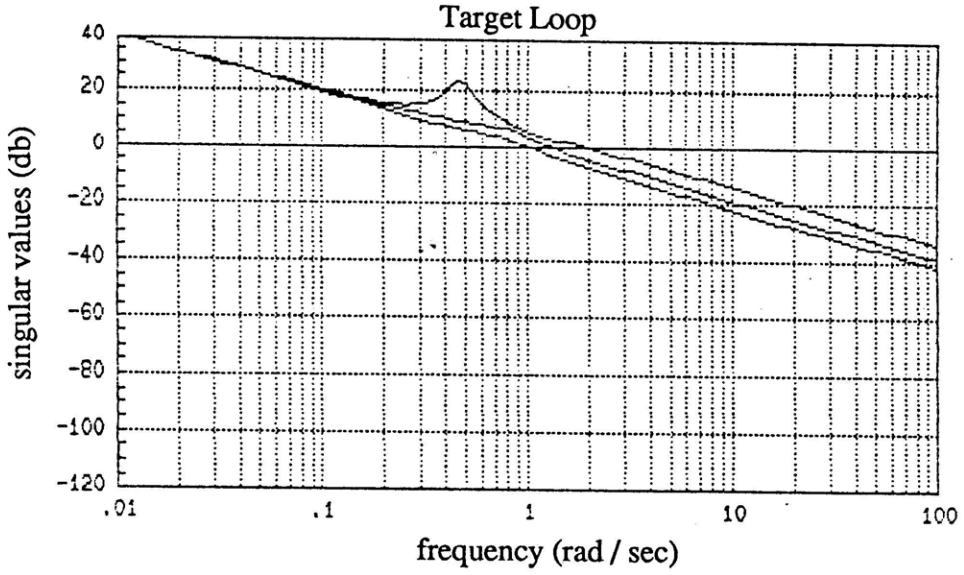

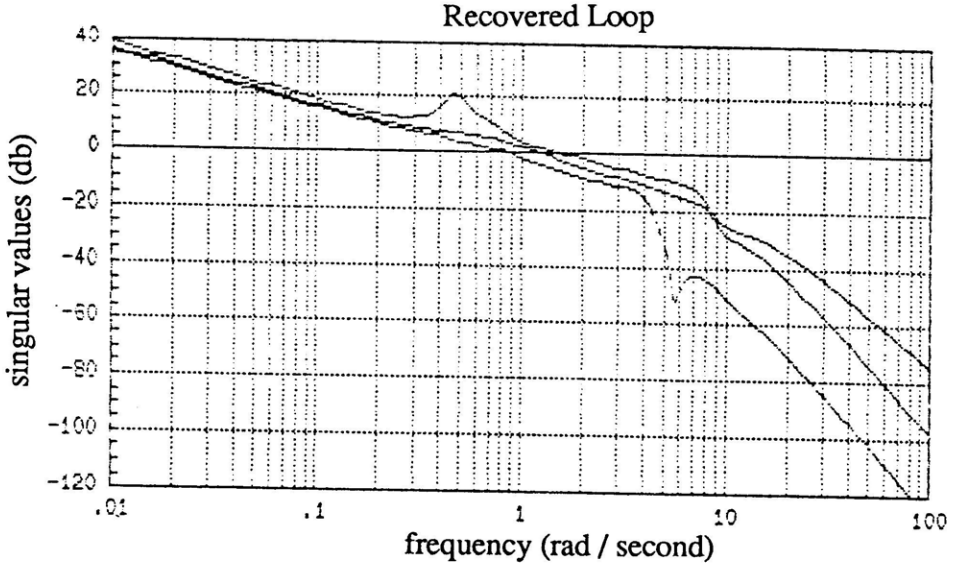

b) Unequal Tether (SASM) AFCS

Fig. 6.2.3.1: Recovery of Open Loop Singular Values For Equal and Unequal Tether AFCS's (excluding AVM AFCS).

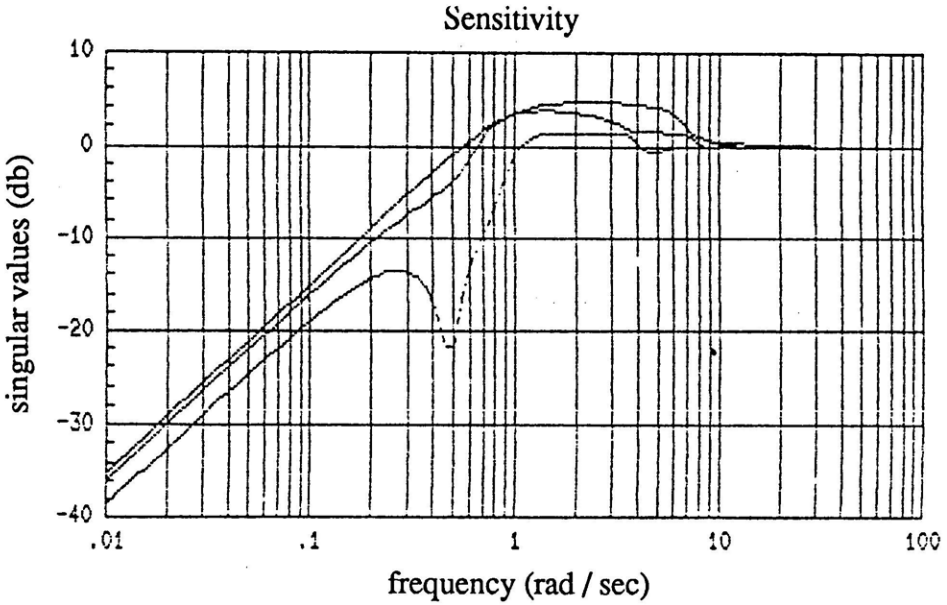

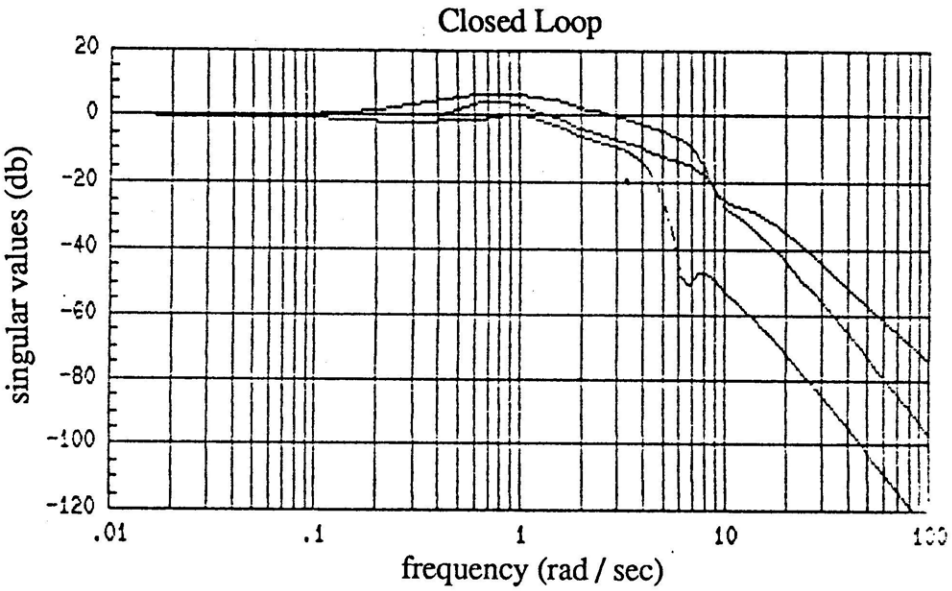

a) Equal Tether (SM and ASM) AFCS

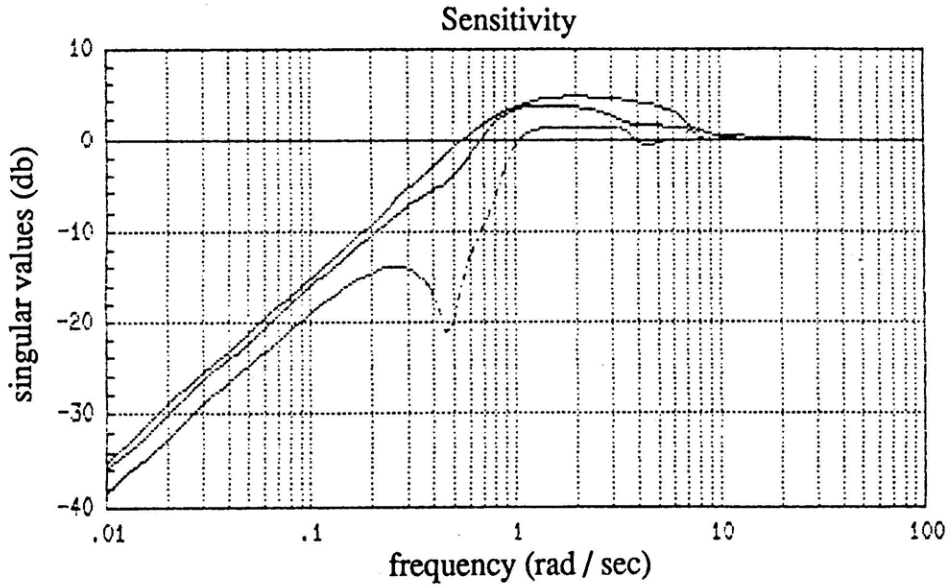

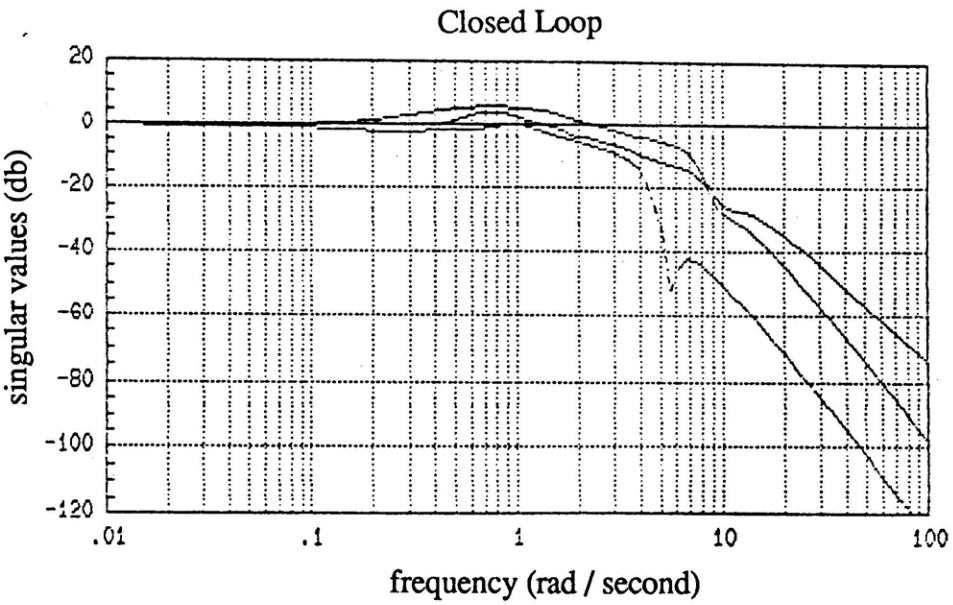

b) Unequal Tether (SASM) AFCS

Fig. 6.2.3.2: Sensitivity and Closed Loop Singular Values For Equal and Unequal Tether AFCS's (excluding AVM AFCS).

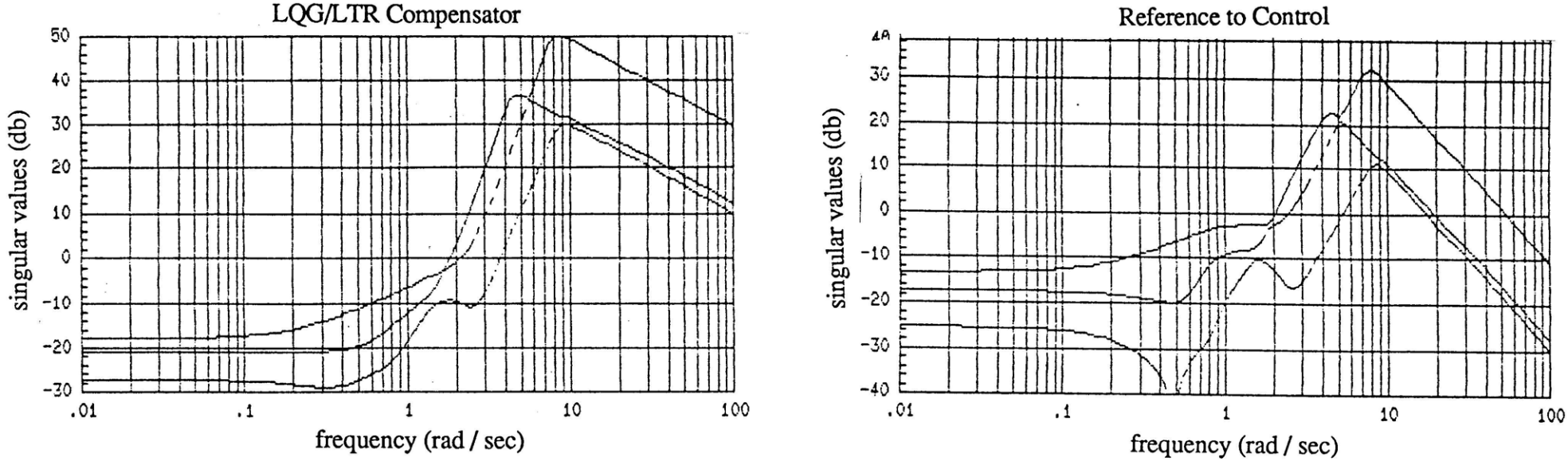

a) Equal Tether (SM and ASM) AFCS

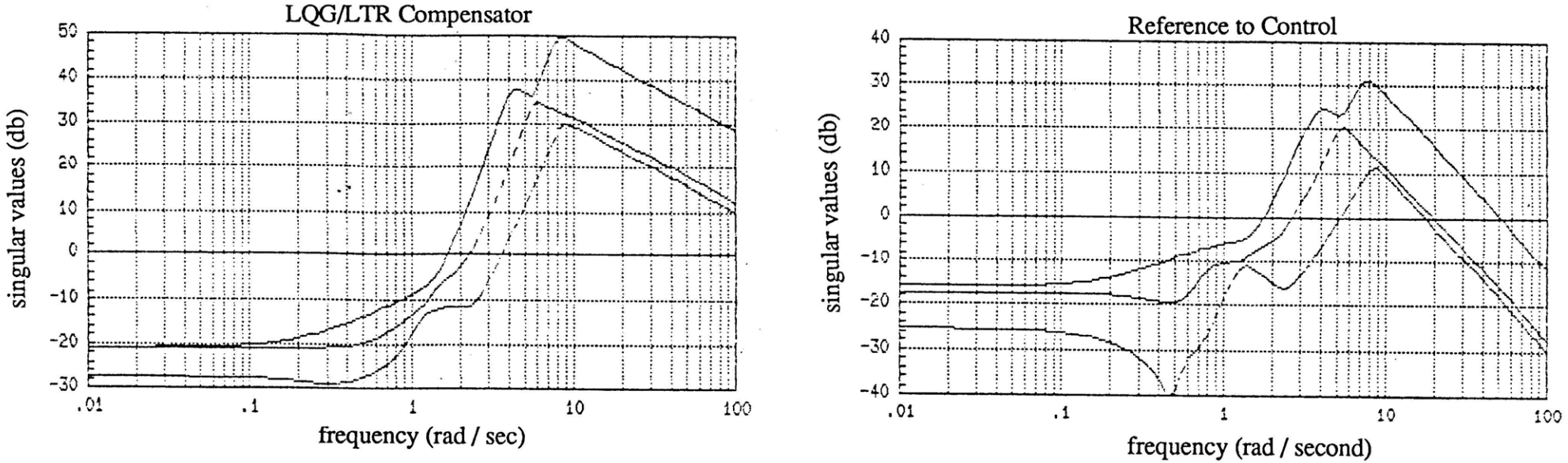

b) Unequal Tether (SASM) AFCS

Fig. 6.2.3.3: LQG/LTR Compensator and Reference to Control Singular Values For Equal and Unequal Tether AFCS's (excluding AVM AFCS).

Table 6.2.4.1: Target Open Loop Poles and Zeros For Equal and Unequal Tether AFCS's (excluding AVM AFCS)

a) Equal Tether AFCS

	Poles: $\lambda_i(A_2)$	Zeros: $C_2(sI - A_2)^{-1}H_{\mu 2}$
SM:	s = 0	
	s = 0.7561	s = - 0.34183
	s = - 0.8122 ± j 2.2228	s = - 0.8175 ± j 2.2269
	s = - 2.2919	s = - 2.2286
ASM:	Poles: $\lambda_i(A_3)$	Zeros: $C_3(sI - A_3)^{-1}H_{\mu 3}$
	s = 0, 0	
	s = 0.0402 ± j 0.4785	s = - 0.3754 ± j 0.71707
	s = - 0.1976 ± j 0.7364	s = - 0.2724 ± j 0.735
	s = - 2.119	s = - 2.127
	s = - 0.5313 ± j 2.624	s = - 0.5349 ± j 2.622

b) Unequal Tether AFCS

	Poles: $\lambda_i(A_{23})$	Zeros: $C_{23}(sI - A_{23})^{-1}H_{\mu 23}$
SASM:	s = 0	
	s = 0.6604	s = - 0.329
	s = - 0.7883 ± j 1.8885	s = - 0.7949 ± j 1.8927
	s = - 2.227	s = - 2.2249
	s = 0, 0	
	s = 0.0478 ± j 0.4698	s = - 0.3551 ± j 0.7081
	s = - 0.1897 ± j 0.7291	s = - 0.277 ± j 0.3639
	s = - 0.6119 ± j 2.4381	s = - 2.013
	s = - 2.0053	s = - 0.6167 ± j 2.4366

Table 6.2.4.2: Recovered Open Loop Poles and Zeros For Equal and Unequal Tether AFCS's (excluding AVM AFCS)

a) Equal Tether AFCS

	Design Plant Poles	LQG/LTR Compensator Poles
SM:	s = 0	s = - 1.4266 ± j 7.6892
	s = 0.7561	s = - 6.6325 ± j 7.7966
	s = - 0.8122 ± j 2.2228	s = - 12.043
	s = - 2.2919	
ASM:	s = 0, 0	
	s = 0.0422 ± j 0.4785	s = - 1.887 ± j 8.578
	s = - 1976 ± j 0.7364	s = - 0.8031 ± j 4.311
	s = - 2.119	s = - 3.635 ± j 3.942
	s = - 0.5313 ± j 2.624	s = - 5.974
		s = - 11.75 ± j 8.402
	Design Plant Zeros	LQG/LTR Compensator Zeros
SM:	s = - 1.55 ± j 9.4906	s = - 0.2525
		s = - 0.816 ± j 2.2228
		s = - 2.2898
ASM:	s = - 0.1786 ± j 6.413	s = - 0.2272 ± j 0.344
	s = - 1.3371 ± j 9.807	s = - 0.3391 ± j 0.6977
		s = - 2.124
		s = - 0.5319 ± j 2.621

b) Unequal Tether AFCS

	Design Plant Poles	LQG/LTR Compensator Poles
SASM:	s = 0	s = - 1.4413 ± j 7.591
	s = 0.6604	s = - 6.5793 ± j 7.6486
	s = - 0.7883 ± j 1.8885	s = - 11.8387
	s = - 2.227	s = - 1.8707 ± j 8.4977
	s = 0, 0	s = - 0.7128 ± j 4.0387
	s = 0.0478 ± j 0.4698	s = - 3.4453 ± j 3.8351
	s = - 0.1896 ± j 0.7291	s = - 5.8125
	s = - 0.6119 ± j 2.4381	s = - 11.6993 ± j 8.3816
	s = - 2.0053	
	Design Plant Zeros	LQG/LTR Compensator Zeros
	s = - 1.5437 ± j 9.3034	s = - 0.2499
	s = - 0.0912 ± j 5.6677	s = - 0.7931 ± j 1.8883
	s = - 1.4649 ± j 9.6454	s = - 2.2264
		s = - 0.3217 ± j 0.6964
		s = - 0.2267 ± j 0.3334
		s = - 2.011
		s = - 0.6138 ± j 2.4352

Table 6.2.4.3: Target Closed Loop Poles and Zeros For Equal and Unequal Tether AFCS's (excluding AVM AFCS)

a) Equal Tether AFCS

	Poles: $\lambda_i(A - H_\mu C)$	Zeros: $C(sI - A)^{-1}H_\mu$
SM:	s = - 0.7245 ± j 0.47483	s = - 0.3412
	s = - 0.8084 ± j 2.2288	s = - 0.8175 ± j 2.2269
	s = - 2.3006	s = - -2.2864
ASM:	s = - 0.5423	
	s = - 0.5748	
	s = - 0.2907 ± j 0.6241	s = - 0.2724 ± j 0.375
	s = - 0.3062 ± j 0.9024	s = - 0.3754 ± j 0.7107
	s = - 2.113	s = - 2.127
	s = - 0.5323 ± j 2.626	s = - 0.5349 ± j 2.676

b) Unequal Tether AFCS

	Poles: $\lambda_i(A - H_\mu C)$	Zeros: $C(sI - A)^{-1}H_\mu$
SASM:	s = - 0.6625 ± j 0.461	s = - 0.329
	s = - 0.7824 ± j 1.8954	s = - 0.7949 ± j 1.8927
	s = - 2.2309	s = - 2.2249
	s = - 0.556 ± j 0.0297	
	s = - 0.3041 ± j 0.6153	s = - 0.3551 ± j 0.7081
	s = - 0.2924 ± j 0.8876	s = - 0.277 ± j 0.3639
	s = - 2.0019	s = - 2.013
	s = - 0.6127 ± j 2.4401	s = - 0.6167 ± j 2.4366

Table 6.2.4.4: Recovered Closed Loop Poles and Zeros For Equal and Unequal Tether AFCS's (excluding AVM AFCS)

a) Equal Tether AFCS

	Poles:	Zeros:
SM:	$\lambda_i(A_2 - H_{\mu 2}C_2)$	SM LQG/LTR Compensator
	s = - 0.72449 ± j 0.47483	s = - 0.25254
	s = - 0.80839 ± j 2.2288	s = - 0.81602 ± j 2.2228
	s = - 2.3006	s = - 2.2898
	$\lambda_i(A_2 - B_2G_{\rho 2})$	SM Design Plant
	s = - 1.6909 ± j 7.3321	s = - 1.55 ± j 9.4906
	s = - 6.4223 ± j 6.2478	
	s = - 9.77284	
ASM:	$\lambda_i(A_3 - H_{\mu 3}C_3)$	ASM LQG/LTR Compensator
	s = - 0.5423	
	s = - 0.5748	
	s = - 0.2907 ± j 0.6241	s = - 0.2272 ± j 0.344
	s = - 0.3062 ± j 0.9024	s = - 0.3391 ± j 0.6977
	s = - 2.113	s = - 2.124
	s = - 0.5323 ± j 2.626	s = - 0.5319 ± j 2.621
	$\lambda_i(A_2 - B_2G_{\rho 2})$	ASM Design Plant
	s = - 1.005 ± j 4.177	s = - 0.1786 ± j 6.413
	s = - 3.463 ± j 3.199	s = - 1.371 ± j 9.807
	s = - 4.907	
	s = - 1.891 ± j 8.47	
	s = - 11.25 ± j 7.797	

b) Unequal Tether AFCS

SASM:	$\lambda_i(A_{23} - H_{\mu 23}C_{23})$	SASM LQG/LTR Compensator
	s = - 0.6625 ± j 0.461	s = - 0.2499
	s = - 0.7824 ± j 1.8954	s = - 0.7931 ± j 1.8883
	s = - 2.2309	s = - 2.2264
	s = - 0.556 ± j 0.0297	
	s = - 0.3041 ± j 0.6153	s = - 0.3217 ± j 0.6964
	s = - 0.2924 ± j 0.8876	s = - 0.2267 ± j 0.3334
	s = - 2.0019	s = - 2.011
	s = - 0.6127 ± j 2.4401	s = - 0.6138 ± j 2.4352
	$\lambda_i(A_{23} - B_{23}G_{\rho 23})$	SASM Design Plant
	s = - 1.6798 ± j 7.2744	s = - 1.5437 ± j 9.3034
	s = - 6.4006 ± j 6.2306	
	s = - 9.7147	
	s = - 0.9036 ± j 3.8984	s = - 0.0912 ± j 5.6677
	s = - 3.2745 ± j 3.0896	s = - 1.4649 ± j 9.6454
	s = - 4.7358	
	s = - 1.8764 ± j 8.3887	
	s = - 11.2155 ± j 7.7916	

Upon comparing table 6.2.4.1 with 6.2.4.2, and table 6.2.4.3 with 6.2.4.4, we see that the strategies of the Equal and Unequal Tether Compensators are quite similar. Zeros have been placed at appropriate locations to stabilize the configurations and provide damping (derivative action). The recovery process has placed poles at "high" frequencies to make the compensators realizable and limit the reference to control bandwidth.

6.2.5 Time Domain Evaluation of Unequal Tether AFCS

Figs. 6.2.5.1 - 6.2.5.5 show the response of the Equal and Unequal Tethered AFCS's to filtered $\Sigma\dot{x} = 1$ ft/sec step commands. A third order Butterworth filter with cut-off frequency at $\omega_0 = 4$ rad/sec was used to generate the commands.

The figures show that the Equal and Unequal Tether AFCS's respond quite similarly. The main difference between the responses are seen in Fig. 6.2.5.3 which shows the degree of coupling due to the unequal tether lengths. The figure shows that this effect is quite small. Moreover, we see that besides providing a greater tip-to-tip clearance, unequal tethered flight offers no major advantages over equal tethered flight.

Figs. 6.2.5.6 - 6.2.5.7 show the response of the Equal and Unequal Tether AFCS's for the following command/initial condition scenario:

$\Sigma\dot{z} = 5$ ft/sec unfiltered step response,

$\Delta x = 1$ ft initial condition,

$x_L - \Sigma x = -1$ ft initial condition,

$\Sigma\dot{x} = 5$ ft/sec filtered step command.

Again, 3rd order Butterworth filter with cut-off at $\omega_0 = 4$ rad/sec was used to generate the commands.

The figures show clearly that even for the modest robustness specifications presented in Chapters 3 and 5, the helicopters have to pitch and oscillate substantially in the vertical plane in order to regulate the horizontal separation and load motion when horizontal and vertical velocities are commanded. Moreover, we see that this is true whether the tether lengths are equal or unequal. If more stringent robustness specifications were given we would be forced to improveour recovery. This, however, would result in even more pitching and oscillations in the vertical plane.

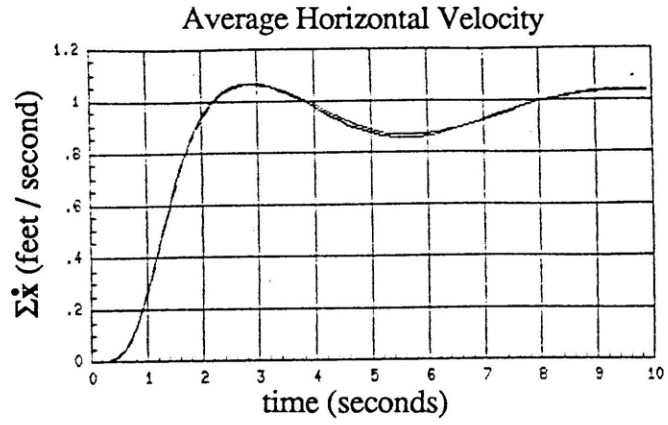

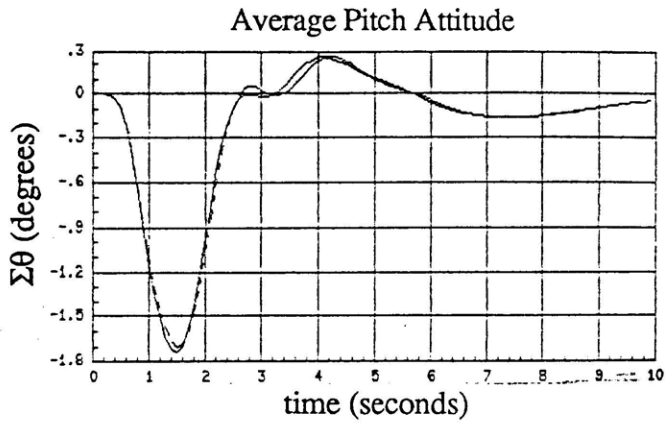

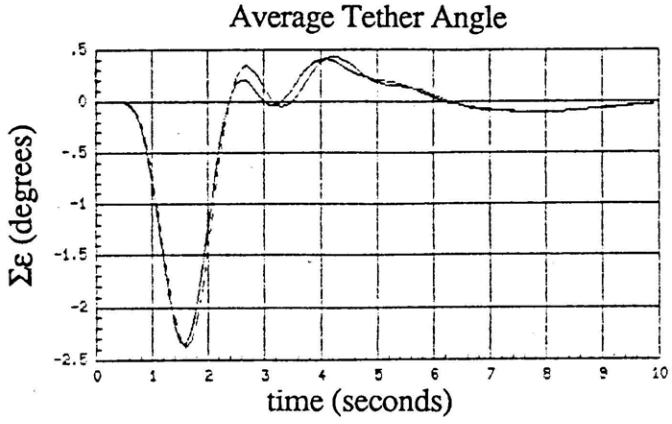

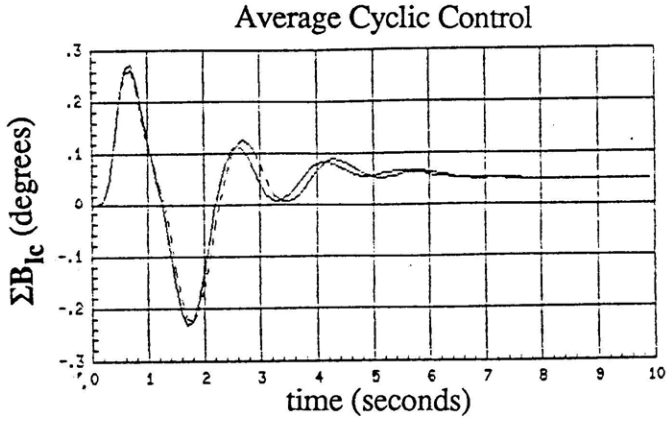

Fig. 6.2.5.1: $\Sigma\dot{x}$ = 1 ft/sec Filtered Step Response For Equal and Unequal Tether AFCS's.

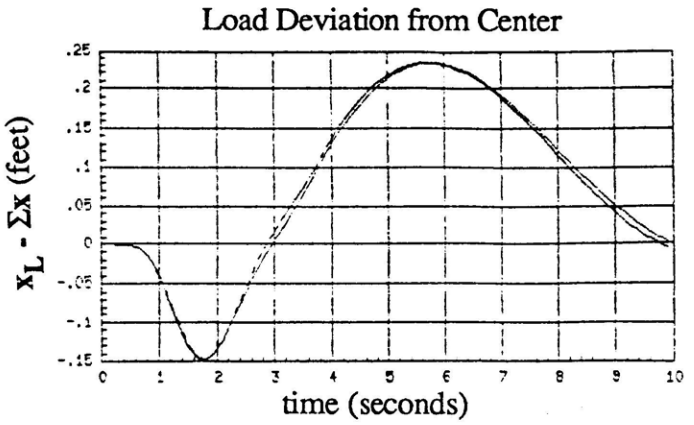

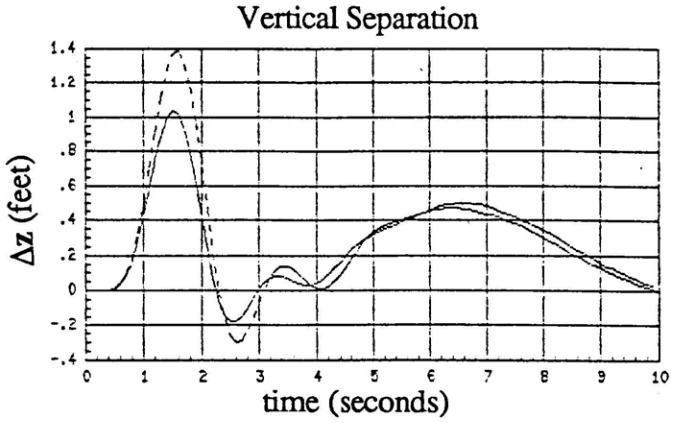

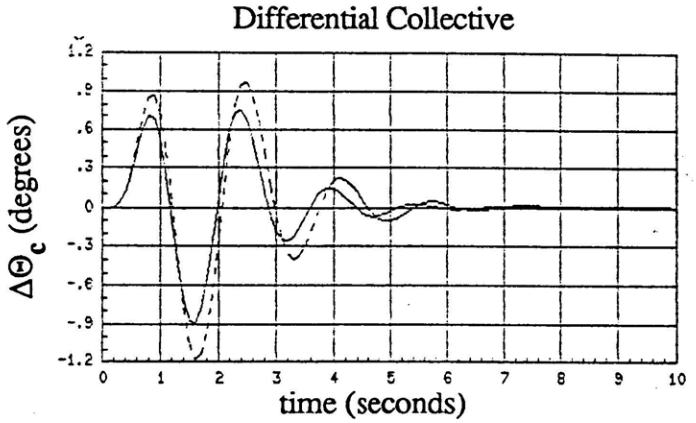

Fig. 6.2.5.2: $\Sigma\dot{x}$ = 1 ft/sec Filtered Step Response For Equal and Unequal Tether AFCS's.

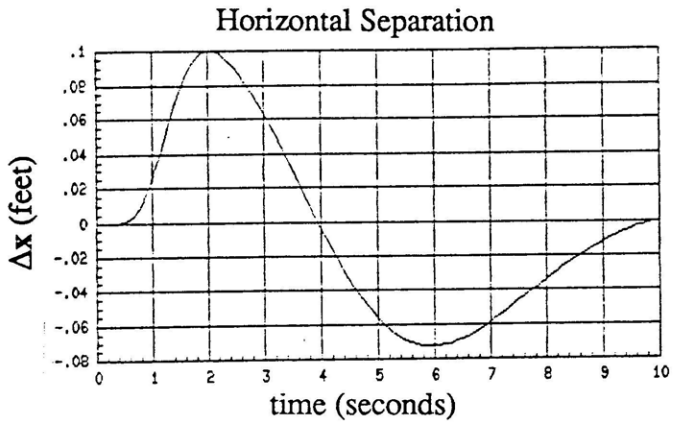

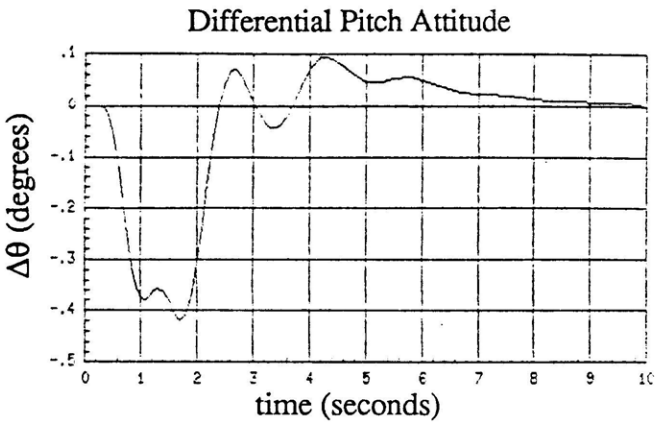

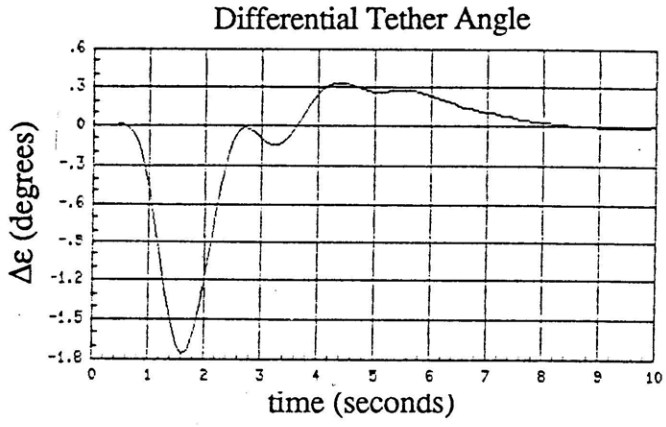

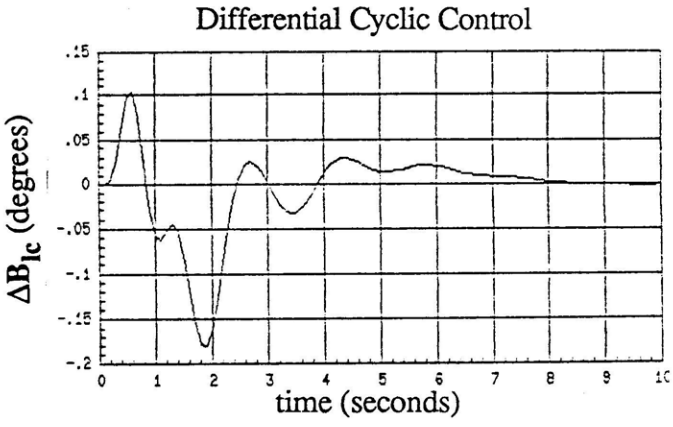

Fig. 6.2.5.3: $\Sigma\dot{x}$ = 1 ft/sec Filtered Step Response For Equal and Unequal Tether AFCS's.

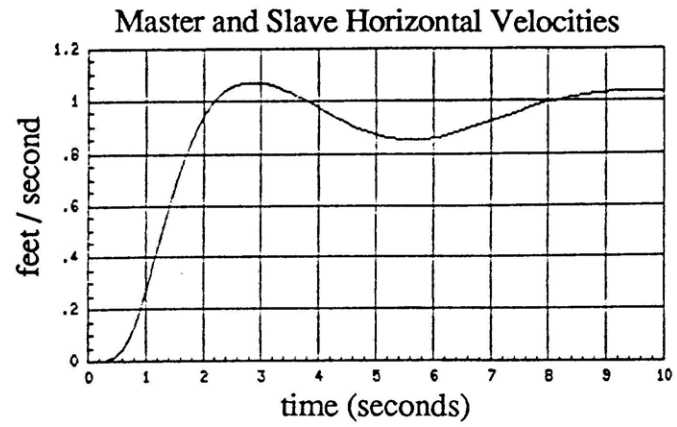

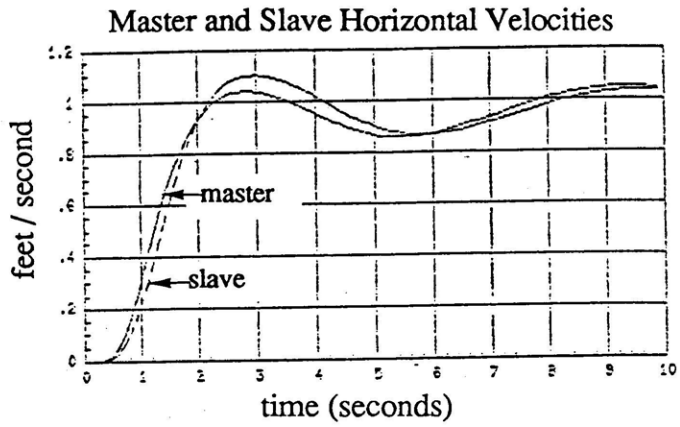

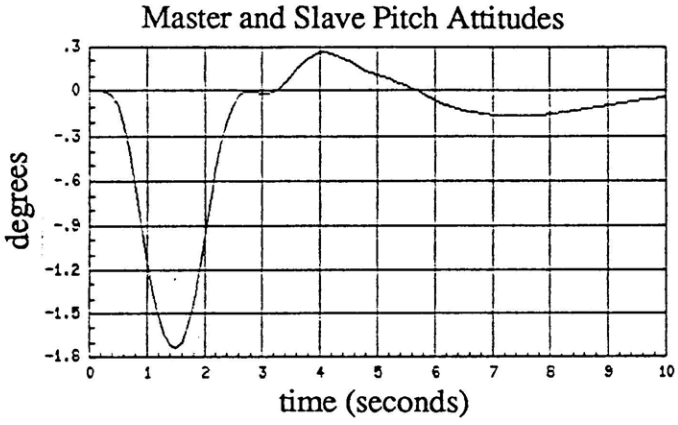

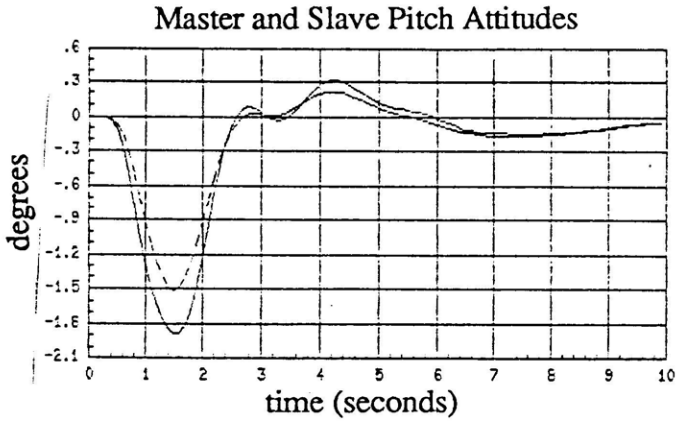

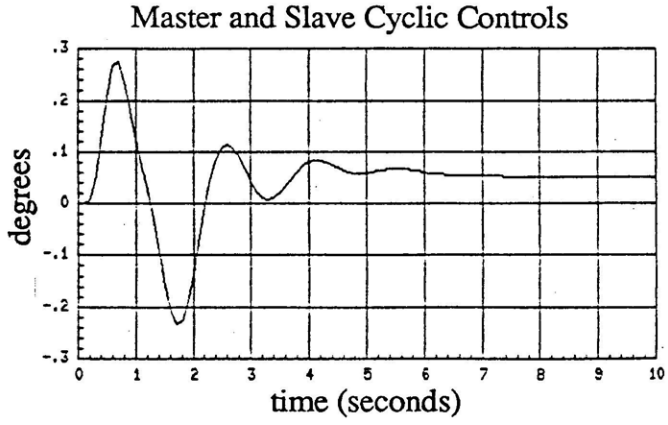

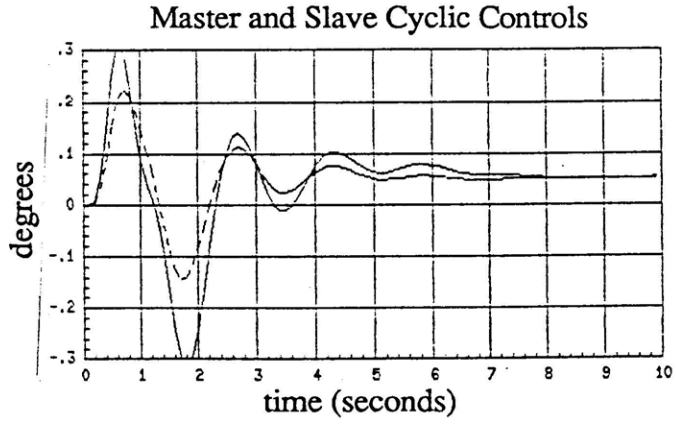

a) Equal Tether AFCS

b) Unequal Tether AFCS

Fig. 6.2.5.4: $\Sigma\dot{x}$ = 1 ft/sec Filtered Step Response For Equal and Unequal Tether AFCS's.

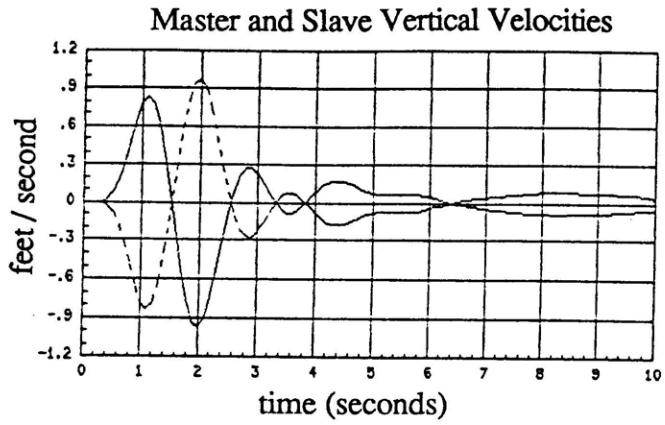

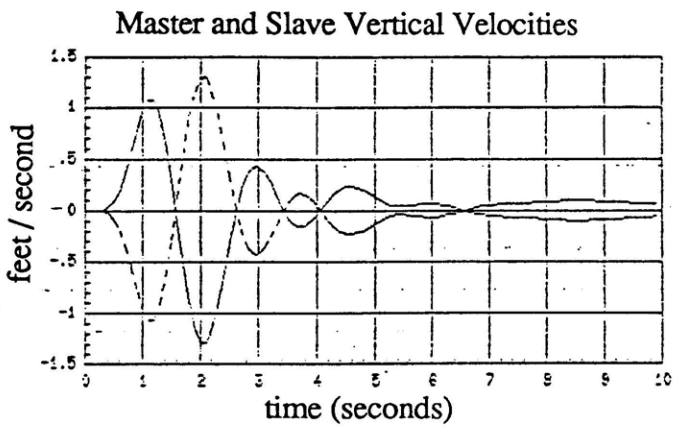

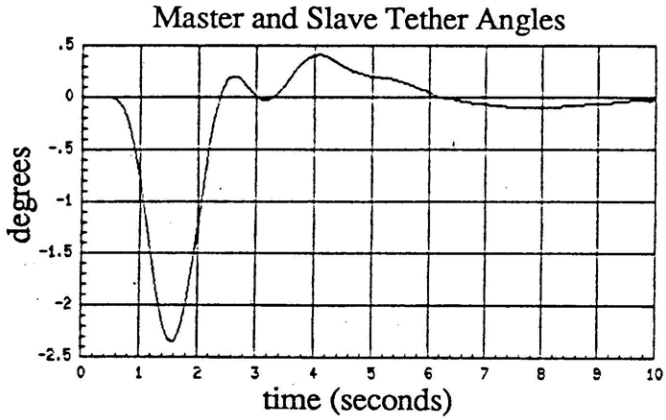

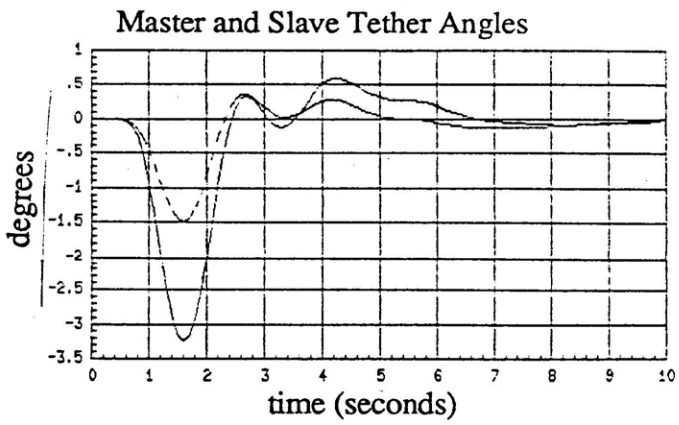

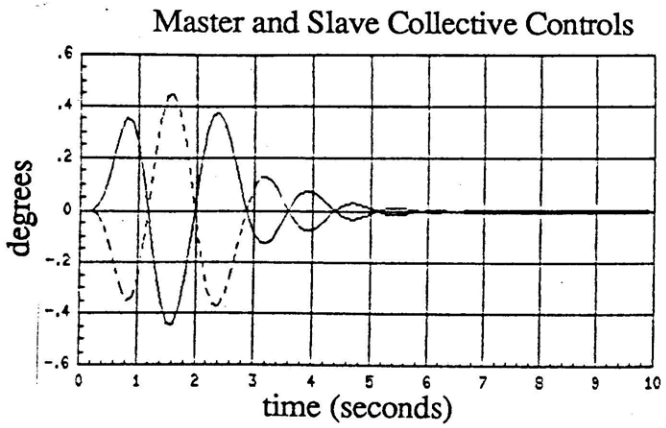

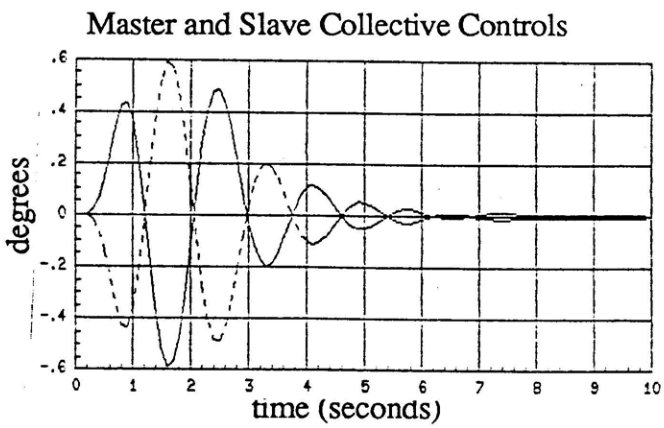

a) Equal Tether AFCS

b) Unequal Tether AFCS

Fig. 6.2.5.5: $\Sigma\dot{x}$ = 1 ft/sec Filtered Step Response For Equal and Unequal Tether AFCS's.

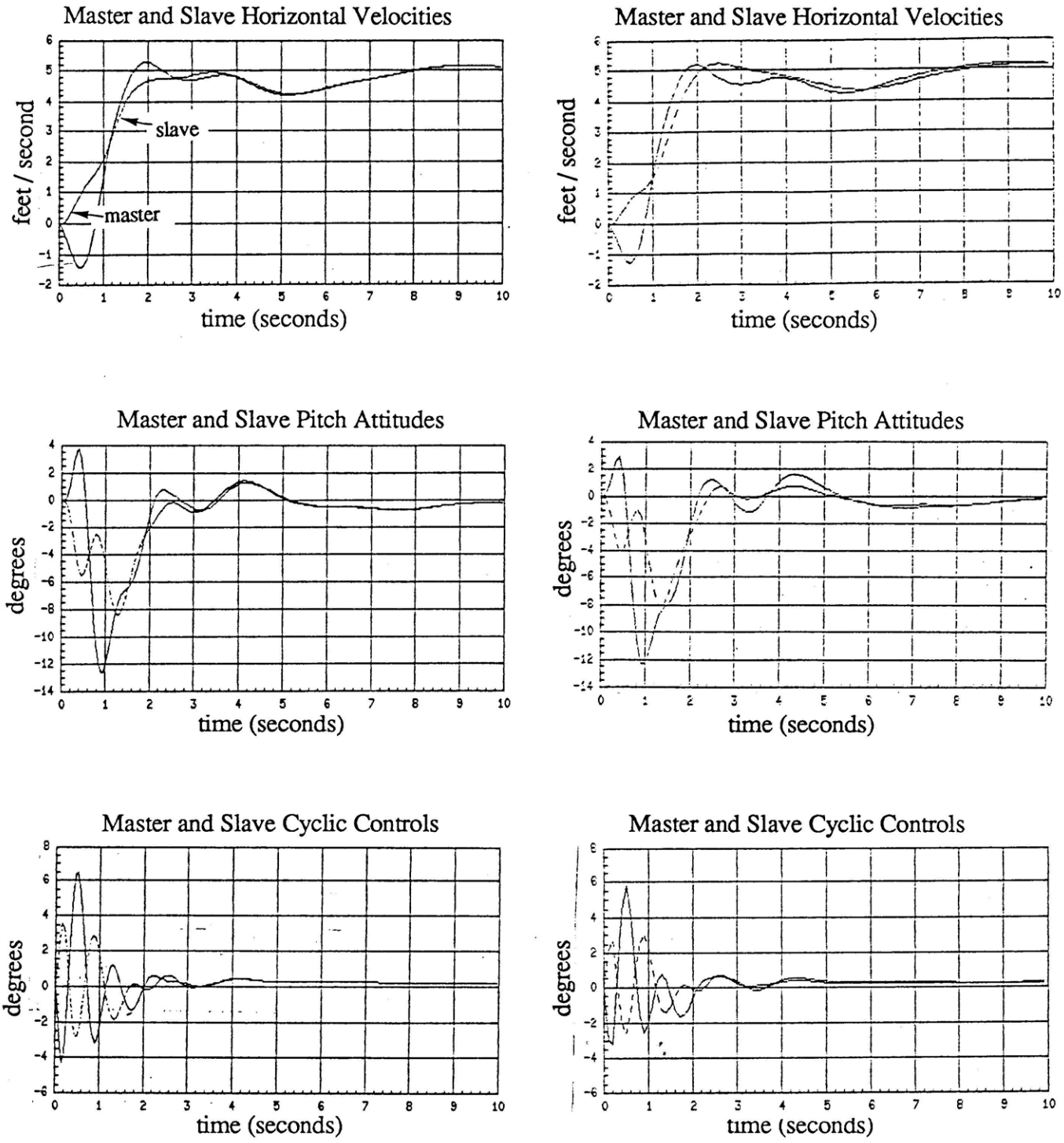

a) Equal Tether AFCS

b) Unequal Tether AFCS

Fig. 6.2.5.6: Overall Evaluation of Equal and Unequal Tether AFCS's.

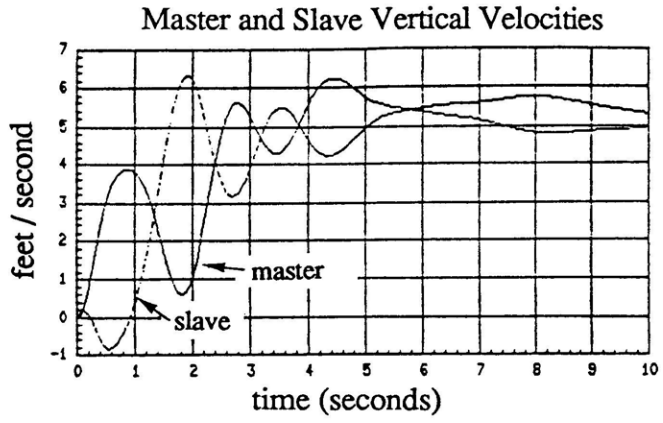

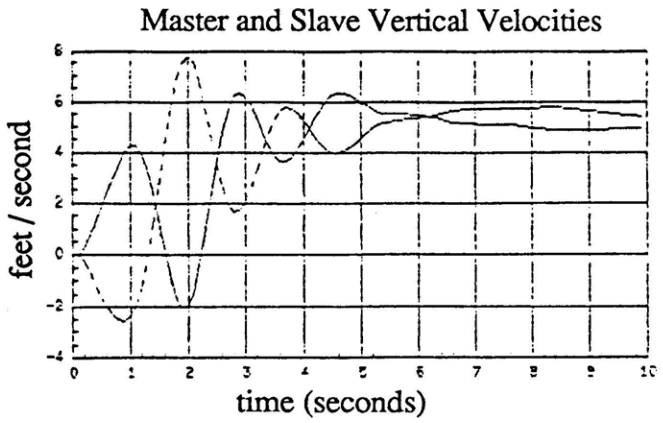

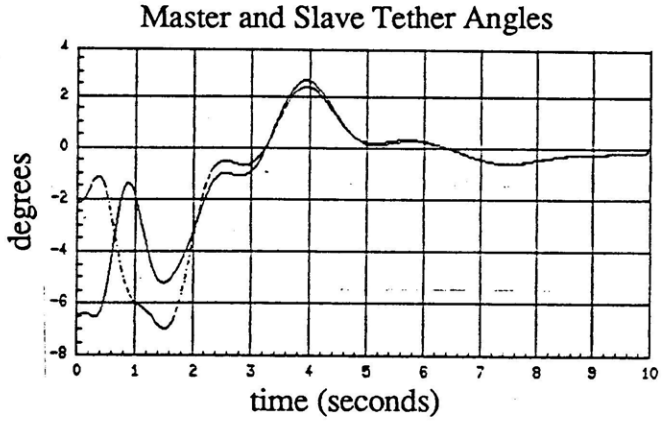

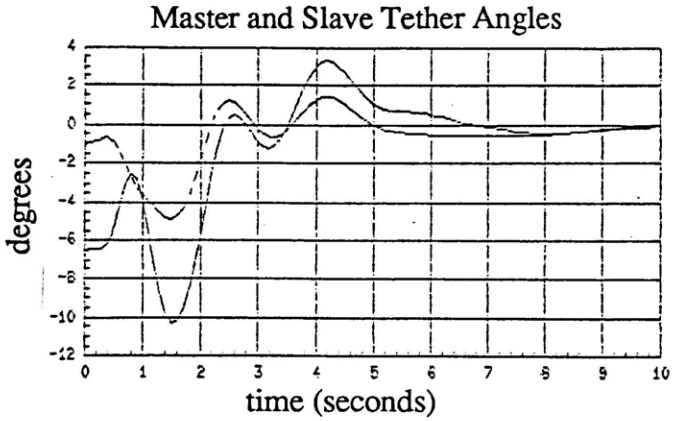

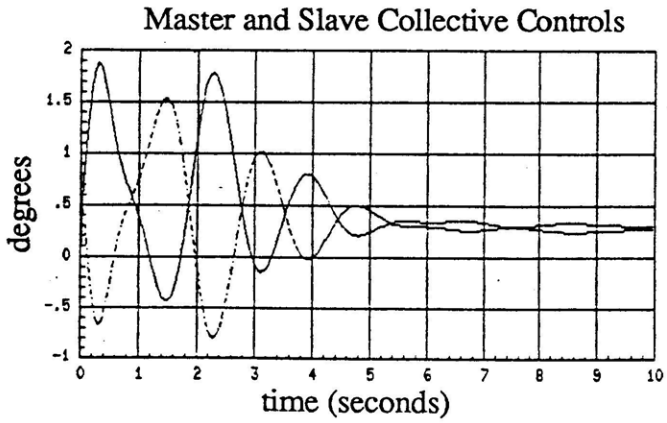

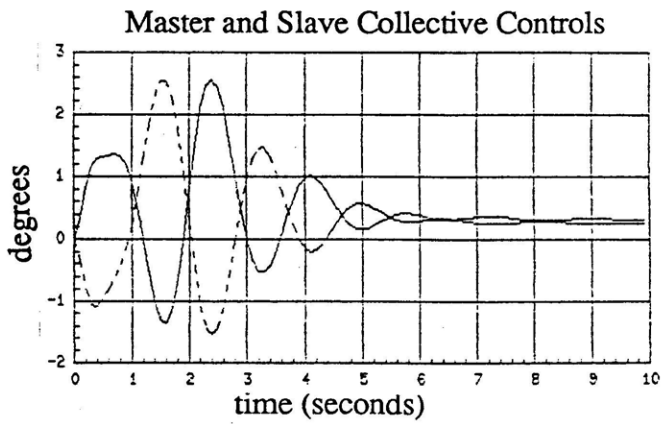

a) Equal Tether AFCS

b) Unequal Tether AFCS

Fig. 6.2.5.7: Overall Evaluation of Equal and Unequal Tether AFCS's.

If less stringent robustness specifications were given we would recover less. This would reduce the pitching and oscillations in the vertical plane. Consequently, we conclude that high performance (high bandwidth) Equal and Unequal Tether AFCS's are feasible only if model uncertainty is sufficiently low. Moreover, if model uncertainty is high then only low bandwidth designs become feasible.

The figures, combined with the singular values in sub-section 6.2.3, also indicates that having unequal tether lengths does not reduce the extent to which we must trade-off performance and stability robustness when a high bandwidth design is the objective. Physically, this is associated with the high bandwidth specification and the fact that the payload is very heavy. To reduce the trade-off it is thus necessary to lower the bandwidth or restrict Twin Lift transport operations to lighter payloads. The latter option is not acceptable since it defeats the fundamental purpose of Twin Lift; i.e. to transport payloads which existing heavy lift helicopters cannot. It thus follows that to lower the performance-robustness trade-off, the desired AFCS bandwidth must be reduced. To further help reduce the trade-off one could replace the integrators with first order lags with appropriate dc gains. Doing so would reduce the amount of lead needed to have nice stability margins. It should also be recalled that attaching the tethers directly to the helicopter c.g.'s (i.e. making h = 0) would result in the unstable Tethered Helicopter Mode moving toward the origin thus giving us a natural integrator in the Δx channel. This would allow us to remove the augmentation in the Δx channel all together.

6.3 Summary of Unequal Tether AFCS Design

In this chapter the LQG/LTR design methodology was applied to the Unequal Tether Design Plant discussed in Chapter 5. The method was used to systematically develop an Unequal Tether AFCS satisfying the performance and robustness specifications presented in Chapter 5. The Unequal Tether AFCS, consisting of an AVM AFCS and a SASM AFCS was evaluated in the frequency and time domains. The Equal and Unequal Tether AFCS designs were compared. The comparison showed little differences between the designs. In summary, the chapter showed that besides providing a larger tip-to-tip rotor clearance, Unequal Tethered flight does not offer any significant dynamic advantages over Equal Tethered flight.

CHAPTER 7: SUMMARY, CONCLUSIONS, AND DIRECTIONS FOR FURTHER RESEARCH

7.1 Summary and Conclusions

Because of the inherent coupling in TLHS's, SISO design techniques can not easily be used to systematically develop a MIMO AFCS for TLHS's. In this thesis systematic guidelines for designing a MIMO AFCS were presented. These guidelines combine state space methods and singular value ideas with the well established LQG/LTR design methodology.

Two configurations were considered. One with equal tether lengths (Equal Tether Configuration) and the other with unequal tether lengths (Unequal Tether Configuration). The configurations were analyzed and design specifications were presented for each in the frequency domain using singular value concepts. The specifications called for high performance (high bandwidth) AFCS designs with modest robustness properties. The designs were obtained, evaluated, and compared.

It was concluded that high performance AFCS designs for either configuration are feasibile only if model uncertainty is sufficiently low. If model uncertainty is high then the designs become unfeasible. This is because, in such a case, the large robustness requirement forces the helicopters to undergo substantial pitching and oscillations in the vertical plane in order to regulate the horizontal separation and load motion when horizontal and vertical velocities are commanded. Moreover, if model uncertainty is high then only low bandwidth designs become feasible. This is due to the fact that a trade-off must be made between performance and stability robustness and that this trade-off is exacerbated by the high bandwidth objective.

It was also concluded that besides providing a larger tip-to-tip rotor clearance, unequal tethered flight offers no significant dynamic advantages over equal tethered flight.

7.2 Directions for Further Research

It was shown in the thesis that whether the tether lengths are equal or unequal, Twin Lift controlengineers must trade-off performance versus stability robustness. Moreover, this trade-off is exacerbated when the objective is high performance (high bandwidth) designs. To reduce this trade-off several options should be considered.

One option is to lower the desired bandwidth. This would certainly reduce the amount of

pitching and oscillations that the helicopters must undergo in order to regulate the horizontal separation and load motion when horizontal and vertical velocities are commanded. Before pursuing this option, however, several alternatives should be considered.

One alternative to consider is to completely drop the integrators augmented at the plant input or to replace them with first order lags with appropriate dc gains. Doing so would reduce the amount of lead needed to obtain nice stability margins thus lowering the performance-robustness trade-off. Attaching the tethers to the helicopter c.g.'s ($h = 0$) should also be considered since it would result in a natural integrator in the Δx channel. Doing so should significantly reduce helicopter pitching.

To reduce the oscillations in the vertival plane the parameters Z and L should be appropriately selected. Z represents the distance that the load hangs below the spreader bar c.g. and L is the spreader bar length. More specifically, Z and L should be selected so that the Vertical Spring Mode has desirable characteristics. Decreasing the ratio $\hat{Z} = Z / L$, for example, results in a larger damping ratio. Another option which may help is to employ a control strategy which varies the tether legngths in real time. By doing so we introduce another degree of freedom in the controls. This new control could be used to further dampen the vertical oscillations and load motion.

After pursuing the above geometric considerations with the 7 degree of freedom TLHS model used throughout the thesis, designs based on a 16 degree of freedom model (incorporating 6 degrees of freedom for each helicopter and 4 for the load-bar assembly) should be conducted. In addition, actuator, sensor, and unmodeled rotor dynamics as well as disturbance, noise, and pilot models should also be considered. Full nonlinear simulations should also be conducted.

Finally, realistic design specifications should be formulated in terms of singular value and singular vector information at both natural loop breaking points; i.e. i.e. at the plant input and at the plant output (error signal). To help formulate the specifications, the results of Freudenberg and Looze [20] should prove helpful. Given specifications at each loop breaking point which are "dynamically consistent", the ideas of LQG/LTR [5-9], formal loop shaping [5-9], H^{∞} optimization [22], and structured singular values [10] should be integrated to obtain a methodology to meet both sets of specifications. Such a methodology does not currently exist.

APPENDIX 1: Glossary for TLHS Variables and Parameters; Contains Nominal Parameter Values

Notes: 1. Whether a variable in this thesis is an "incremental" (small signal) quantity or a true quantity should be determined by the context in which it appears.

2. Equilibrium (large signal) quantities are always denoted by using zero subscripts.

Ex:
$$\underset{\text{true quantity}}{v} = \underset{\text{equilibrium quantity}}{v_o} + \underset{\text{incremental quantity}}{\delta v} \qquad \text{(A1.1)}$$

3. Throughout the thesis, the symbol v is often used although δv is the quantity actually being addressed. In this example v can be, for example, the actual separation between the helicopters:

$\Delta x = \Delta x_o + \delta\Delta x = L + \delta\Delta x$ where $L \equiv$ spreader bar length.

Throughout the thesis, the symbol Δx is often used although $\delta\Delta x$ is the quantity being addressed.

Basic Motion Variables

x_m, x_s - Horizontal displacement of master and slave helicopter c.g.s.

z_m, z_s - Vertical displacement of master and slave helicopter c.g.s.

θ_m, θ_s - Pitch attitude of master and slave helicopters.

x_L, z_L - Horizontal and vertical displacement of load c.g.

x_B, z_B - Horizontal and vertical displacement of spreader bar c.g.

$\varepsilon_m, \varepsilon_s$ - Angle of master and slave tethers with respect to vertical.

ε_B - Angle of spreader bar with respect to horizontal.

Equilibrium values: $\dot{x}_{mo} = \dot{x}_{so} = 0$ (A1.2)

$$z_{mo} = z_{so} = 0 \quad \text{(A1.3)}$$

$$\theta_{mo} = \theta_{so} = \dot{\theta}_{mo} = \dot{\theta}_{so} = 0 \quad \text{(A1.4)}$$

$$\dot{x}_{Lo} = \dot{z}_{Lo} = 0 \quad \text{(A1.5)}$$

$$\dot{x}_{Bo} = \dot{z}_{Bo} = 0 \quad \text{(A1.6)}$$

$$\varepsilon_{mo} = \varepsilon_{so} = \dot{\varepsilon}_{mo} = \dot{\varepsilon}_{so} = 0 \quad \text{(A1.7)}$$

$$\varepsilon_{Bo} = \dot{\varepsilon}_{Bo} = 0 \quad \text{(A1.8)}$$

i.e. At equilibrium the helicopters are motionless with the tethers vertical and the spreader bar horizontal.

Average Motion Variables

$\Sigma\dot{x} \equiv \frac{1}{2}[\dot{x}_m+\dot{x}_s]$ - Average horizontal velocity of helicopters. (A1.9)

$\Sigma\dot{z} \equiv \frac{1}{2}[\dot{z}_m+\dot{z}_s]$ - Average vertical velocity of helicopters. (A1.10)

$\Sigma\theta \equiv \frac{1}{2}[\theta_m+\theta_s]$ - Average pitch attitude of helicopters. (A1.11)

$\Sigma\varepsilon \equiv \frac{1}{2}[\varepsilon_m+\varepsilon_s]$ - Average tether angle with respect to vertical. (A1.12)

Difference Motion Variables

$\Delta x \equiv x_m - x_s$ - Horizontal separation between helicopters. (A1.13)

$\Delta z \equiv z_m - z_s$ - Vertical separation between helicopters. (A1.14)

$\Delta\varepsilon \equiv \varepsilon_m - \varepsilon_s$ - Difference in tether angles. (A1.15)

Generalized Load Coordinate

$$x_L' \equiv x_L - \Sigma x - (h+H_s)\Sigma\theta - \frac{Z}{L}\Delta z \quad \text{(A1.16)}$$

$$= \frac{1}{2}[H_s(\varepsilon_s-\theta_s)+H_m(\varepsilon_m-\theta_m)] + \frac{1}{2}[H_m-H_s]\theta_m \quad \text{(A1.17)}$$

For equal tether problem $H_s = H_m = H$ and $x_L' = H[\Sigma\varepsilon-\Sigma\theta]$.

Helicopter Controls

Θ_{cm}, Θ_{cs} - Collective pitch control on master and slave helicopters.
- Controls vertical (up/down) translation of helicopters.
- Positive values of collective cause upward motion.

B_{1cm}, B_{1cs} - Cyclic pitch control on master and slave helicopters.
- Controls horizontal (fore/aft) translation and pitching of helicopters.
- Positive values of cyclic cause downward pitching and forward motion.

$\Theta_{cmo}, \Theta_{cso}$ - Equilibrium (large signal) components of collective for master and slave helicopters. These provide the vertical aerodynamic forces, Z_{mo} and Z_{so} (to be defined subsequently), which maintain vertical equilibrium.

B_{1cmo}, B_{1cso} - Equilibrium (large signal) components of cyclic for master and slave helicopters. These generate the aerodynamic forces and moments, X_{mo}, X_{so}, M_{mo}, and M_{so} (to be defined subsequently). Both B_{1cmo} and B_{1cso} are zero since $X_{mo}=X_{so}=M_{mo}=M_{so}=0$.

Incremental Control limitations:

It is assumed throughout the thesis that the incremental control limitations are as follows:

$$|\Theta_c| \leq 10 \text{ degrees for the collectives} \tag{A1.18}$$

$$|B_{1c}| \leq 15 \text{ degrees for the cyclics.} \tag{A1.19}$$

Average Controls

$$\Sigma\Theta_c \equiv \frac{1}{2}[\Theta_{cm}+\Theta_{cs}] \text{ - Average collective pitch control.} \tag{A1.20}$$

$$\Sigma B_{1c} \equiv \frac{1}{2}[B_{1cm}+B_{1cs}] \text{ - Average cyclic pitch control.} \tag{A1.21}$$

Differential Controls

$\Delta\Theta_c \equiv \Theta_{cm} - \Theta_{cs}$ - Differential collective pitch control. (A1.22)

$\Delta B_{1c} \equiv B_{1cm} - B_{1cs}$ - Differential cyclic pitch control. (A1.23)

UH-60A Blackhawk Helicopter Characteristics

W_H = 14000 pounds - Helicopter weight.

M_H = 434.78 slugs - Helicopter mass.

I_y = 5700 slugft^2 - Helicopter moment of inertia about pitch axis.

ω_r = 27 rad/sec(258RPM) - First harmonic of main rotor.

h = 3.6 feet - Distance from helicopter c.g. to helicopter-tether attachment point.

UH-60A Control Derivatives Near Hover

$X_{\Theta c}$ =0 ft/rad sec^2 - Horizontal acceleration per radian of collective pitch.

X_{B1c}=27.4 ft/rad sec^2 - Horizontal acceleration per radian of cyclic pitch.

$Z_{\Theta c}$=340.9 ft/rad sec^2 - Vertical acceleration per radian of collective pitch.

Z_{B1c}=0 ft/rad sec^2 - Vertical acceleration per radian of cyclic pitch.

$M_{\Theta c}$=0 rad/rad sec^2 - Angular acceleration per radian of collective pitch.

M_{B1c}=-47.24 rad/rad sec^2 - Angular acceleration per radian of cyclic pitch.

UH-60A Aerodynamic Derivatives Near Hover

X_u = -0.06 $\frac{\text{ft/sec}^2}{\text{ft/sec}}$ - Used to characterize horizontal drag forces due to horizontal motion.

X_w = 0 " - Used to characterize horizontal drag forces due to vertical motion.

X_q = 0 $\frac{\text{ft/sec}^2}{\text{rad/sec}}$ - Used to characterize horizontal drag forces due to pitching.

$Z_u = 0$ $\frac{ft/sec^2}{ft/sec}$ - Used to characterize vertical drag forces due to horizontal motion; results in decoupling of helicopter vertical and longitudinal dynamics.

$Z_w = -0.346$ " - Used to characterize vertical drag forces due to vertical motion.

$Z_q = 0$ $\frac{ft/sec^2}{rad/sec}$ - Used to characterize vertical drag forces due to pitching.

$M_u = 0.041$ $\frac{rad/sec^2}{ft/sec}$ - Used to characterize pitching moments due to forward motion.

$M_w = 0$ " - Used to characterize pitching moments due to vertical motion.

$M_q = -3.1$ $\frac{rad/sec^2}{rad/sec}$ - Used to characterize rotational damping due to pitching.

Aerodynamic Forces and Moments Acting on Helicopters

X_m, X_s - Horizontal aerodynamic forces acting on master and slave helicopter c.g.s.

Z_m, Z_s - Vertical aerodynamic forces acting on master and slave helicopter c.g.s.

M_m, M_s - Aerodynamic moments about master and slave helicopter pitch axes.

Equilibrium values:

$$X_{mo} = X_{so} = 0 \tag{A1.24}$$

$$Z_{mo} = Z_{so} = W_H + \frac{1}{2}[W_B + W_L] = 20322 \text{ lbs.} \tag{A1.25}$$

$$M_{mo} = M_{so} = 0 \tag{A1.26}$$

Tether Parameters

H_m, H_s - Master and slave tether lengths

$$H_A \equiv \frac{2H_s H_m}{H_s + H_m} \tag{A1.27}$$

$$\hat{H}_A \equiv \frac{H_A}{L} \tag{A1.28}$$

$$S \equiv \frac{H_m - H_s}{H_s + H_m} \tag{A1.29}$$

$$w_A \equiv \sqrt{\frac{g}{H_A}} \tag{A1.30}$$

For Equal Tether Problem: $H_s=H_m=H=13.25$ft.

$H_A=H=13.25$ft.

$\hat{H}_A=0.19$

$S=0$

$W_A=1.559$ rad/sec

For Unequal Tether Problem: $H_m=H=13.25$ft.

$H_s=2H_m=26.5$ft.

$H_A=\frac{4}{3}H=17.67$ft.

$\hat{H}_A=0.256$

$S=-\frac{1}{3}$

$w_A=1.35$rad/sec

Spreader Bar, Load, and Load-Bar Assembly Parameters

$L = 69$ft. - Spreader bar length.

$W_B = 644$lbs. - " " weight.

$M_B = 20$slugs - " " mass.

$I_B = \frac{1}{12} M_B L^2 = 7935$slug ft^2 - " " moment of inertia about its cg. (A1.31)

$e_b \equiv \frac{2I_B}{M_H L^2} = \frac{M_B}{6M_H} = 0.0077$ (A1.32)

$Z = 34.5$ft. - Distance that load is suspended below spreader bar c.g. during unperturbed hover. (A1.33)

$\hat{Z} = \frac{Z}{L} = 0.5$ (A1.34)

$W_L = 12000$lbs. - Weight of load.

$M_L = 372.67$slugs - Mass " "

$\mu \equiv \frac{M_L+M_B}{2M_H} = 0.4516$ - Load-bar to helicopter mass ratio. (A1.35)

$$\delta_L \equiv \frac{M_L}{M_L+M_B} = 0.9491 \quad \text{- Load to load-bar mass ratio.} \tag{A1.36}$$

$$\varepsilon \equiv \frac{M_H h}{I_y} = 0.2746 \text{ft}^{-1} \tag{A1.37}$$

$g = 32.2$ ft/sec^2 - Acceleration due to gravity

$$\Psi \equiv 1+e_b + 4\mu\hat{Z}^2\delta_L(1-\delta_L) = 1.0295 \tag{A1.38}$$

$$D \equiv -w_A^2 \left[1+\mu+(h+H_s)\mu\varepsilon + \frac{4T\delta_L\hat{Z}}{\omega_A^2}\right] \tag{A1.39}$$

$$E \equiv -[X_u+M_u(h+H_s)] \tag{A1.40}$$

$$F \equiv (h+H_s)\varepsilon\mu w_A^2 SH_s - w_A^2 H_s - 4T\delta_L\hat{Z}H_s \tag{A1.41}$$

$$J \equiv [\mu\delta_L\hat{Z}w_A^2]^{-1} \tag{A1.42}$$

$$T \equiv \mu\delta_L\hat{Z}w_A^2/\psi \tag{A1.43}$$

$$V \equiv 1+(h+H_s)\ \varepsilon+\frac{1}{\mu}+\frac{4\delta_L^2\hat{Z}^2}{\Psi} \tag{A1.44}$$

APPENDIX 2: Derivation of Linear Model for Longitudinal Dynamics of TLHS Near Hover

In this appendix a seven degree of freedom linear model is derived for the longitudinal dynamics of the TLHS near hover. Fig. A2.1 shows the initial seven degrees of freedom chosen, the aerodynamic forces and moments acting on the helicopters, and the key Twin Lift parameters.

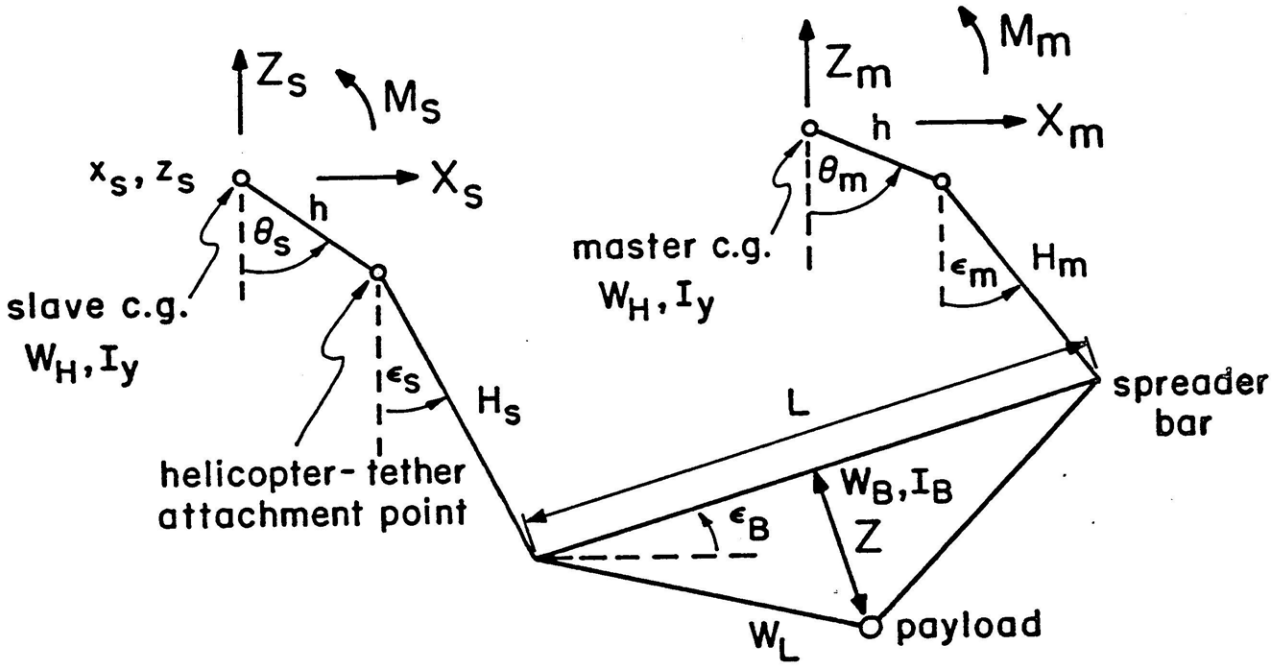

Fig. A2.1: TLHS; Longitudinal Configuration Initial Seven Degrees of Freedom; Aerodynamics Forces and Moments.

The initial seven degrees of freedom chosen were

x_s, z_s - Horizontal and vertical coordinates of slave helicopter c.g.'s.
θ_s, θ_m - Pitch attitude of slave and master helicopters.
$\varepsilon_s, \varepsilon_m$ - Angle that slave and master tethers make with respect to vertical.
ε_B - Angle that spreader bar makes with respect to horizontal.

The aerodynamic forces and moments acting on the helicopters are as follows:

X_m, X_s - Horizontal aerodynamic forces acting on master and slave helicopter c.g.'s.

Z_m, Z_s - Vertical aerodynamic forces acting on master and slave helicopter c.g.'s.

M_m, M_s - Aerodynamic moments about master and slave helicopter pitch axes.

The Twin Lift parameters which appear in Fig. A2.1 are defined in Appendix 1.

Using the aforementioned seven degrees of freedom, aerodynamic forces and moments, and the Twin Lift parameters shown in Fig. A2.1, a linear model can be developed using the Lagrangian method [1]. An outline of this procedure shall now be given.

Derivation of Linear Model

(1) Use $x_s, z_s, \theta_s, \theta_m, \varepsilon_s, \varepsilon_m, \varepsilon_B$ as your initial 7 degrees of freedom.

(2) Compute $(x_B, z_B), (x_L, z_L)$, and (x_m, z_m) and the corresponding velocities and accelerations in terms of the above 7 degrees of freedom.

(3) Compute the kinetic energy of the system, E_k. The master, slave, and bar have rotational as well as translational kinetic energy. The load, however, only has translational kinetic energy since it's being modelled as a point mass.

(4) Compute the potential energy of the system, E_p.

(5) Form the Lagrangian energy function $E_L \equiv E_k - E_p$.

(6) The 7 nonlinear ordinary differential equations describing the longitudinal planar dynamics of the TLHS are then given by

$$\frac{d}{dt}\left[\frac{\partial E_L}{\partial \dot{q}_i}\right] - \frac{\partial E_L}{\partial q_i} = Q_{qi} \equiv \frac{\partial W_v}{\partial q_i} \qquad \text{(A2.1)}$$

where $q_i \equiv \{x_s, z_s, \theta_s, \theta_m, \varepsilon_s, \varepsilon_m, \varepsilon_B\}$ and the Q_{qi} are generalized forces to be computed (Appendix 2.1).

(7) The generalized forces are found by using the $x_m, z_m, \theta_m, x_s, z_s \theta_s$ eqs. of (2) and the following virtual work function:

$$W = [X_m \delta x_m + Z_m \delta z_m + M_m \delta \theta_m] + [X_s, \delta x_s + Z_s \delta z_s + M_s \delta \theta_s] \quad \text{(A2.2)}$$

The aerodynamic forces and moments acting on the spreader bar and load have been assumed negligible in comparison to those acting on the master and slave helicopters (Appendix 2.2).

(8) Assume that the TLHS is nominally at rest with the tethers parallel and the spreader bar horizontal:

$$\dot{x}_{so} = \dot{x}_{mo} = \dot{x}_{Bo} = \dot{x}_{Lo} = 0 \quad \text{(A2.3)}$$

$$\dot{z}_{so} = \dot{z}_{mo} = \dot{z}_{Bo} = \dot{z}_{Lo} = 0 \quad \text{(A2.4)}$$

$$\varepsilon_{so} = \varepsilon_{mo} = \dot{\varepsilon}_{so} = \dot{\varepsilon}_{mo} = 0 \quad \text{(A2.5)}$$

$$\dot{\theta}_{so} = \dot{\theta}_{mo} = 0 \quad \text{(A2.6)}$$

Also assume that the helicopter c.g.'s* lie on the helicopter shafts so that $\theta_{mo} = \theta_{so} = 0$.

(9) Obtain the equilibrium values of the aerodynamic forces and moments:

$$X_{m_o} = X_{s_o} = 0 \quad \text{(master and slave swashplates horizontal)} \quad \text{(A2.7)}$$

$$Z_{m_o} = Z_{s_o} = W_H + \frac{1}{2}[W_B + W_L] \quad \text{(A2.8)}$$

$$M_{m_o} = M_{s_o} = 0$$

(10) Use the equilibrium values of [8] and [9] with the equations found in [6] and [7]. Each variable should be expressed as a sum of a large signal component (equilibrium value) and a small signal (incremental) component (deviation of true value from the equilibrium value).

---

* The c.g. position, which is of great importance in the stability of fixed-wing aircraft, has no effect on the stability of the hovering helicopter.

Ex: $X_m = X_{m_o} + \Delta X_m$ (for forces) (A2.10)

$\dot{x}_m = \dot{x}_{m_o} + \delta\dot{x}_m$ (for position and angular variables) (A2.11)

i.e. True value = Equilibrium value + incremental value.

(11) Assume that the variable perturbations δv are small. Neglecting products and squares of variables gives us a set of 7 linear ordinary differential equations in terms of the small signal (incremental) aerodynamic forces and moments acting on the system; namely $(\Delta X_m, \Delta Z_m, \Delta M_m)$ and $(\Delta X_s, \Delta Z_s, \Delta M_s)$. For notational economy drop the δ's on the motion variables (Appendix 2.3).

(12) Introduce $\mu \equiv \frac{M_L + M_B}{2M_H}$, $\varepsilon \equiv \frac{h' M_H}{I_y}$, $\delta_L \equiv \frac{M_L}{M_L + M_B}$ (A2.12)

$$\varepsilon_b \equiv \frac{2I_B}{M_H L^2}, \quad I_B \equiv \frac{1}{12} M_B L^2 \quad \text{(Appendix 2.4).} \tag{A2.13}$$

(13) Next we introduce variables which exploit the symmetry of the TLHS [1].

3 Average Variables

$$\Sigma x \equiv \frac{1}{2}[x_m + x_s] \quad \Sigma z \equiv \frac{1}{2}[z_m + z_s] \quad \Sigma\theta \equiv \frac{1}{2}[\theta_m + \theta_s] \tag{A2.14}$$

3 Difference Variables

$$\Delta x \equiv x_m - x_s \quad \Delta z \equiv z_m - z_s \quad \Delta\theta \equiv \theta_m - \theta_s \tag{A2.15}$$

Generalized Load Coordinate

$$x'_L \equiv x_L - \Sigma x - (h + H_s)\,\Sigma\theta - \frac{Z}{L}\Delta z \quad \text{(Discussed in Appendix 2.5)} \tag{A2.16}$$

where all variables above represent small perturbations of true quantities from the equilibrium quantities.

(14) Introduce $H_A \equiv \frac{2H_sH_m}{H_s+H_m}$, $S \equiv \frac{H-H_s}{H_s+H_m}$, $w_A^2 \equiv \frac{g}{H_A}$ (Appendix 2.6) (A2.17)

(15) After the equations are manipulated a little, we develop the aerodynamic forces and moments on the helicopters in terms of control and aerodynamic derivatives which shall be briefly discussed (Appendix 2.7).

(15a) What are control derivatives?

They are constants of proportionality that allow us to introduce the four controls $\theta_{cm}, \theta_{cs}, B_{1cm}, B_{1cs}$ into the linear differential equations.

(15b) What are aerodynamic derivatives?

They are constants of proportionality that allow us to characterize the drag forces which act on the system as it moves.

Ex: $$\frac{\Delta X_m + \Delta X_s}{M_H} = -g(1+\mu)\Sigma\dot{\theta} + X_q\dot{\Sigma\theta} + X_u\Sigma\dot{x} + X_w\Sigma\dot{z} + X_{B1c}\Sigma B_{1c} + X_{\Theta_c}\Sigma\theta_c \quad \text{(A2.18)}$$

(16) Conventionally, helicopter aerodynamic forces are expressed in terms of body axis forces and body axis motion variables. To use the control and aerodynamic derivatives one must be careful to use the appropriate rotation to get the needed space fixed axis quantities from the body fixed axis quantities.

(17) Substituting in the aerodynamic forces and moments developed in 15-16 gives us the final seven linear ordinary differential equations describing the longitudinal (planar) dynamics of the TLHS near hovering trim (Appendix 2.8).

Note: For hovering flight the following control and aerodynamic derivaties can be neglected:

$$X_w = X_q = X_{\Theta_c} = Z_u = Z_q = Z_{B1c} = M_w = M_{\Theta_c} = 0 \quad \text{(A2.19)}$$

(18) The final seven linear ordinary differential equations may then be written in matrix form as

$$M\dot{\underline{z}} + N\dot{\underline{z}} + P\underline{z} = R\underline{u} \tag{A2.20}$$

where

$$\underline{z} \equiv [\Sigma z \quad |\Delta x \ \Delta\theta| \ \Sigma x \ \Sigma\theta \ \Delta z \ x_L']^T \tag{A2.21}$$

$$\underline{u} \equiv [\Sigma\theta_c \ |\Delta B_{1c}| \ \Delta\theta_c \Sigma B_{1c}]^T \tag{A2.22}$$

For details contact Professor Curtiss of Princeton Universtiy [1].

(19) The above model in (18) can be expressed in state space form as

$$\dot{\underline{\lambda}} = \hat{A}\underline{\lambda} + \hat{B}\underline{u} \qquad \hat{\underline{A}} = \begin{bmatrix} 0 & I \\ -M^{-1}N & -M'P \end{bmatrix} \quad \hat{B} = \begin{bmatrix} 0 \\ M^{-1}R \end{bmatrix} \tag{A2.23}$$

$$\underline{\lambda} \equiv \begin{bmatrix} \underline{z} \\ \dot{\underline{z}} \end{bmatrix} \tag{A2.24}$$

(20) The model to be used throughout the thesis (Table 2.4.1) does not include Σz and Σx.

$$\dot{\underline{x}}_p = A_p \underline{x}_p + B_p \underline{u}_p \qquad \underline{x}_p \in R^{12}; \quad \underline{u}_p \in R^4 \tag{A2.25}$$

$$\underline{x}_p = [\Sigma\dot{z} \ |\Delta x \ \Delta\theta \ \Delta\dot{x} \ \Delta\dot{\theta}| \ \Sigma\theta \ \Delta z \ x_L' \ \Sigma\dot{x} \ \dot{\Sigma}\theta \ \dot{\Delta}z \ \dot{x}_L']^T \tag{A2.26}$$

$$\underline{u}_p = [\Sigma\theta_c \ |\Delta B_{1c}| \ \Delta\theta_c \Sigma B_{1c}]^T \ . \tag{A2.27}$$

APPENDIX 2.1: Seven Nonlinear Ordinary Differential Equations for Longitudinal Dynamics of TLHS Near Hover; Written in terms of True Variables and Generalized Forces.

1. $$M_H\ddot{x}_s + M_L\ddot{x}_L + M_B\ddot{x}_B + M_H\ddot{x}_B = Q_{x_s} \tag{A2.1.1}$$

2. $$M_H\ddot{z}_s + M_L\ddot{z}_L + M_B\ddot{z}_B + M_H\ddot{z}_m + [2W_H+W_B+W_L] = Q_{z_s} \tag{A2.1.2}$$

3. $$h\cos\theta_s\,[M_B\ddot{x}_B + M_L\ddot{x}_L + M_H\ddot{x}_m] + h\sin\theta_s\,[M_B\ddot{z}_B + M_L\ddot{z}_L + M_H\ddot{z}_m] + I_y\ddot{\theta}_s + h\sin\theta_s\,[W_H+W_B+W_L] = Q_{\theta_s} \tag{A2.1.3}$$

4. $$H_s\cos\varepsilon_s\,[M_L\ddot{x}_L + M_B\ddot{x}_B + M_H\ddot{x}_m] + H_s\sin\varepsilon_B[M_L\ddot{z}_L + M_B\ddot{z}_B + M_H\ddot{z}_m] + H_s\sin\varepsilon_s\,[W_H+W_B+W_L] = Q_{\varepsilon_s} \tag{A2.1.4}$$

5. $$\cos\varepsilon_B\,[M_LZ\ddot{x}_L + M_B\tfrac{L}{2}\ddot{z}_B + M_L\tfrac{L}{2}\ddot{z}_L + M_HL\ddot{z}_m] + I_B\ddot{\varepsilon}_B + \sin\varepsilon_B\,[M_LZ\ddot{z}_L - M_B\tfrac{L}{2}\ddot{x}_B - M_HL\ddot{x}_m - M_L\tfrac{L}{2}\ddot{x}_L] + L\cos\varepsilon_B\,[W_H + \frac{W_B+W_L}{2}] + W_LZ\sin\varepsilon_B = Q_{\varepsilon_B} \tag{A2.1.5}$$

6. $$-M_HH_m\,[\ddot{x}_m\cos\varepsilon_m+\ddot{z}_m\sin\varepsilon_m] - W_HH_m\sin\varepsilon_m = Q_{\varepsilon_m} \tag{A2.1.6}$$

7. $$-M_Hh\,[\ddot{x}_m\cos\theta_m+\ddot{z}_m\sin\theta_m] + I_y\ddot{\theta}_m - W_Hh\sin\theta_m = Q_{\theta_m} \tag{A2.1.7}$$

The generalized forces are Q_{q_i} where $q_i = [x_s, z_s, \theta_s, \varepsilon_s, \varepsilon_B, \varepsilon_m, \theta_m]$.

APPENDIX 2.2: Seven Generalized Forces; Written in terms of True Aerodynamic Forces and Moments Acting on Helicopters

$$\begin{aligned}\delta W \equiv & [X_m \delta x_m + Z_m \delta z_m + M_m \delta\theta_m] + [X_s \delta x_s + Z_s \delta z_s + M_s \delta\theta_s] \\ = & [X_s + X_m]\delta x_s + [Z_m + Z_s]\delta z_s + [M_s + X_m h\cos\theta_s + Z_m h\sin\theta_s]\delta\theta_s \\ & + [X_m H_s \cos\varepsilon_B + Z_m H_s \sin\varepsilon_s]\delta\varepsilon_s + [-X_m L\sin\varepsilon_B + Z_m L\cos\varepsilon_B]\delta\varepsilon_B \\ & + [-X_m H_m \cos\varepsilon_m - Z_m H_m \sin\varepsilon_m]\delta\varepsilon_m + [M_m - x_m h\cos\theta_n - Z_m h\sin\theta_m]\delta\theta_m \end{aligned} \quad \text{(A2.2.1)}$$

Note: The aerodynamic forces and moments on the load and bar have been as assumed to be neglible in comparison with the aerodynamic forces and moments on the master and slave.

From this virtual work function we get the seven generalized forces:

1. $Qx_s = X_m + X_s$ (A2.2.2)

2. $Qz_s = Z_m + Z_s$ (A2.2.3)

3. $Q\theta_s = M_s + h\cos\theta_s + Z_m h\sin\theta_s$ (A2.2.4)

4. $Q\varepsilon_s = X_m H_s \cos\varepsilon_s + Z_m H_s \sin\varepsilon_s$ (A2.2.5)

5. $Q\varepsilon_B = -X_m L\sin\varepsilon_B + Z_m L\cos\varepsilon_B$ (A2.2.6)

6. $Q\varepsilon_m = -X_m H_m \cos\varepsilon_m - Z_m H_m \sin\varepsilon_m$ (A2.2.7)

7. $Q\theta_m = M_m - X_m h\cos\theta_m - Z_m h\sin\theta_m$ (A2.2.8)

where X_m, Z_m, M_m and X_s, Z_s, M_s are the aerodynamic forces and moments acting on the helicopters (Figure A2.1.).

APPENDIX 2.3: Seven Linear Ordinary Differential Equations for the Longitudinal Dynamics of TLHS Near Hover; Written in terms of Incremental Variables and Incremental Aerodynamic Forces and Moments Acting on Helicopters

Inserting the equilibrium relationships into the equations of motion and assuming that the angular perturbations are small and neglecting products and squares of the motion variables, the following linearized equations of motion are obtained:

1. $$M_H\ddot{x}_s + M_H\ddot{x}_m + [M_L+M_B]\ddot{x}_L - M_B Z\ddot{\varepsilon}_B = \Delta X_s + \Delta X_m \qquad (A2.3.1)$$

2. $$M_H\ddot{z}_s + M_L[\ddot{z}_s + \frac{L}{2}\ddot{\varepsilon}_B] + M_B[\ddot{z}_s + \frac{L}{2}\ddot{\varepsilon}_B] + M_H[\ddot{z}_s + L\ddot{\varepsilon}_B] = \Delta Z_m + \Delta Z_s \qquad (A2.3.2)$$

3. $$I_y\ddot{\theta}_s - h[M_H\ddot{x}_m + (M_L+M_B)\ddot{x}_L - M_B Z\ddot{\varepsilon}_B + \frac{g}{2}(M_L+M_B)\theta_s] = \Delta M_s + h\Delta X_m \qquad (A2.3.3)$$

4. $$H_s[M_H\ddot{x}_m + (M_L+M_B)\ddot{x}_L - M_B Z\ddot{\varepsilon}_B + \frac{g}{2}(M_L+M_B)\varepsilon_s] = H_s\Delta X_m \qquad (A2.3.4)$$

5. $$I_B\ddot{\varepsilon}_B + M_L Z[\ddot{x}_s + h\ddot{\theta}_s + H_s\ddot{\varepsilon}_s + Z\ddot{\varepsilon}_B] + M_B\frac{L}{2}[\ddot{z}_s + \frac{L}{2}\ddot{\varepsilon}_B] + M_H L[\ddot{z}_s + L\ddot{\varepsilon}_B] + M_L\frac{L}{2}[\ddot{z}_s + \frac{L}{2}\ddot{\varepsilon}_B] + M_L gZ\varepsilon_B = \Delta Z_m L \qquad (A2.3.5)$$

6. $$-H_m[M_H\ddot{x}_m - \frac{g}{2}(M_L+M_B)\varepsilon_m] = -H_m\Delta X_m \qquad (A2.3.6)$$

7. $$I_y\ddot{\theta}_m - h[M_H\ddot{x}_m - \frac{g}{2}(M_B+M_L)\theta_m] = \Delta M_m - h\Delta X_m \qquad (A2.3.7)$$

where all the variables now represent small perturbations from the equilibrium values. These equations of motion can now be combined in various ways to obtain a more convenient set of equations.

APPENDIX 2.4: Seven Linear Ordinary Differential Equations After Rearranging Terms and Introducing Parameters

2 Horizontal Force Equations:

$$\ddot{x}_s - \mu g \varepsilon_s = \frac{\Delta X_s}{M_H} \qquad \mu \equiv \frac{M_L + M_B}{2M_H} \qquad \text{(A2.4.1)}$$

$$\ddot{x}_m - \mu g \varepsilon_m = \frac{\Delta X_m}{M_H} \qquad \text{(A2.4.2)}$$

2 Pitching Moment Equations:

$$\ddot{\theta}_s + \varepsilon\mu g(\theta_s - \varepsilon_s) = \frac{\Delta M_s}{I_y} \qquad \varepsilon \equiv \frac{M_H h}{I_y} = \frac{h}{K_y^2} \qquad \text{(A2.4.3)}$$

$$\ddot{\theta}_m + \varepsilon\mu g(\theta_m - \varepsilon_m) = \frac{\Delta M_m}{I_y} \qquad \text{(A2.4.4)}$$

1 Load Equation:

$$\ddot{x}_L - (1-\delta_L) Z \ddot{\varepsilon}_B + \frac{g}{2}(\varepsilon_s + \varepsilon_m) = 0 \qquad \delta_L \equiv \frac{M_L}{M_L + M_B} \qquad \text{(A2.4.5)}$$

2 Vertical Force Equations of Helicopters, coupled by the tethers, spreader bar, and load:

$$(1+\mu)\ddot{z}_m + (e_b - \mu)\frac{L}{2}\ddot{\varepsilon}_B + 2\mu\delta_L \hat{Z}(\ddot{x}_L + g\varepsilon_B) = \frac{\Delta Z_m}{M_H} \qquad \varepsilon_b \equiv \frac{2I_B}{M_H L^2} \qquad \text{(A2.4.6)}$$

$$(1+\mu)\ddot{z}_s - (e_b - \mu)\frac{L}{2}\ddot{\varepsilon}_B - 2\mu\delta_L \hat{Z}(\ddot{x}_L + g\varepsilon_B) = \frac{\Delta Z_s}{M_H} \qquad I_B = \frac{1}{12} M_B L^2 \qquad \text{(A2.4.7)}$$

$$\hat{Z} \equiv \frac{Z}{L}$$

Notes:

1. The forces ΔX_s, ΔX_m, ΔZ_s, ΔZ_m and the moments ΔM_s, ΔM_m denote incremental aerodynamic forces and moments.

2. The variables x_s, ε_s, x_m, ε_m, θ_s, θ_m, x_L, ε_B, z_m, and z_s denote incremental (small signal) quantities, i.e. small perturbations about their equilibrium (large signal) counterparts.

APPENDIX 2.5: A Generalized Load Coordinate

The absolute position of the load can be approximated by

$$x_L = x_s + h\theta_s + H_s\varepsilon_s + \frac{L}{2} + Z\varepsilon_B \qquad \text{(A2.5.1)}$$

$$= x_m + h\theta_m + H_m\varepsilon_m - \frac{L}{2} + Z\varepsilon_B \qquad \text{(A2.5.2)}$$

Taking the average of these gives us

$$x_L = \Sigma x + h\Sigma\theta + \frac{1}{2}(H_s\varepsilon_s + H_m\varepsilon_m) + Z\varepsilon_B \qquad \text{(A2.5.3)}$$

Using the fact that $\varepsilon_B \cong \frac{\Delta z}{L}$ gives us the following

$$x_L = \Sigma x + h\Sigma\theta + \frac{1}{2}(H_s\varepsilon_s + H_m\varepsilon_m) + \frac{Z}{L}\Delta z \qquad \text{(A2.5.4)}$$

or

$$x_L - \Sigma x - h\Sigma\theta - \frac{Z}{L}\Delta z = \frac{1}{2}(H_s\varepsilon_s + H_m\varepsilon_m) \qquad \text{(A2.5.5)}$$

Subtracting $H_s\Sigma\theta$ from both sides gives us the desired generalized load coordinate:

$$x_L' \equiv x_L - \Sigma x - (h + H_s)\Sigma\theta - \frac{Z}{L}\Delta z \qquad \text{(A2.5.6)}$$

$$= \frac{1}{2}(H_s\varepsilon_s + H_m\varepsilon_m) - H_s\Sigma\theta \qquad \text{(A2.5.7)}$$

$$= \frac{1}{2}[H_s(\varepsilon_s-\theta_s) + H_m(\varepsilon_m-\theta_m)] + \frac{1}{2}[H_m-H_s]\theta_m \qquad \text{(A2.5.8)}$$

If $H_s=H_m$ then $x_L' = \frac{H}{2}[(\varepsilon_s-\theta_s)+(\varepsilon_m-\theta_m)] = H[\Sigma\varepsilon-\Sigma\theta]$ is exactly the average displacement of the spreader bar end points from the helicopter-tether attachment points measured parallel to the helicopters.

It should also be noted that using eqs. (A2.5.1-A2.5.2) one gets

$$\Delta x = x_m - x_s = -[h\Delta\theta + H_m\varepsilon_m - H_s\varepsilon_s] - L$$

To get the incremental (small signal) form of this eq. all we need to do is set L=0.

APPENDIX 2.6: Seven Linear Ordinary Differential Equations for Longitudinal Dynamics of TLHS Near Hover; Written in Terms of Incremental Variables and Incremental Aerodynamic Forces and Moments Acting on Helicopters

2 Horizontal Force Equations

$$1.\quad \Sigma\ddot{x} - \mu g\left[\frac{1}{H_A}(x_L' + H_s\Sigma\theta) + \frac{S}{2H_A}(\Delta x + h\Delta\theta)\right] = \frac{\Delta X_m + \Delta X_s}{2M_H} \qquad (A2.6.1)$$

$$2.\quad \Delta\ddot{x} - \mu g\left[-\frac{2S}{H_A}(x_L' + H_s\Sigma\theta) - \frac{1}{H_A}(\Delta x + h\Delta\theta)\right] = \frac{\Delta X_m - \Delta X_s}{2M_H} \qquad (A2.6.2)$$

2 Pitching Moment Equations

$$3.\quad \Sigma\ddot{\theta} + \varepsilon\mu g\Sigma\theta - \varepsilon\mu g\left[\frac{1}{H_A}(x_L' - H_s\Sigma\theta) + \frac{S}{2H_A}(\Delta x + h\Delta\theta)\right] = \frac{\Delta M_m + \Delta M_s}{2I_y} \qquad (A2.6.3)$$

$$4.\quad \Delta\ddot{\theta} + \varepsilon\mu g\Delta\theta - \varepsilon\mu g\left[-\frac{2S}{H_A}(x_L' + H_s\Sigma\theta) - \frac{1}{H_A}(\Delta x - h\Delta\theta)\right] = \frac{\Delta M_m - \Delta M_s}{I_y} \qquad (A2.6.4)$$

1 Load Equation

$$5.\quad \ddot{x}_L' + w_A^2 x_L' + \hat{\Sigma}\dot{x} + (h+H_s)\hat{\Sigma}\dot{\theta} + w_A^2 H_s\Sigma\theta + \frac{1}{2}w_A^2 S\Delta x + \frac{1}{2}w_A^2 Sh\Delta\theta + \delta_L\hat{Z}\Delta\ddot{z} \qquad (A2.6.5)$$

2 Vertical Force Equations

$$6.\quad (1+\mu)\Sigma\ddot{z} = \frac{\Delta Z_m + \Delta Z_s}{2M_H} \qquad (A2.6.6)$$

$$7.\quad \left[1+e_b+4\mu\delta_L(1-\delta_L)\hat{Z}^2\right]\Delta\ddot{z} + 4\mu\delta_L\hat{Z}w_A^2\hat{H}_A\Delta\ddot{z} - 4\mu\delta_L\hat{Z}w_A^2(x_L'+H_s\Sigma\theta) - 2\mu\delta_L\hat{Z}w_A^2 S(\Delta x+h\Delta\theta) = \frac{\Delta Z_m - \Delta Z_s}{M_H} \qquad (A2.6.7)$$

where

$$H_A \equiv \frac{2H_sH_m}{H_s+H_m},\quad S \equiv \frac{H_m-H_s}{H_s+H_m},\quad H_A \equiv \frac{H_A}{L},\quad w_A^2 \equiv \frac{g}{H_A}, \qquad (A2.6.8)$$

and

$$H_s = \frac{H_A}{1+S},\quad H_m = \frac{H_A}{1-S},\quad S = \frac{H_A-H_s}{H_s}$$

APPENDIX 2.7: Incremental Aerodynamic Forces and Moments Written in Terms of Final Incremental Variables

$$\frac{\Delta X_m + \Delta X_s}{2M_H} = -g(1+\mu)\Sigma\theta + X_u\Sigma\dot{x} + X_w\Sigma\dot{z} + X_q\Sigma\dot{\theta} + X_{B1c}\Sigma B_{1c} + X_{\theta c}\Sigma\theta_c \qquad \text{(A2.7.1)}$$

$$\frac{\Delta X_m - \Delta X_s}{M_H} = -g(1+\mu)\Delta\theta + X_u\Delta\dot{x} + X_w\Delta\dot{z} + X_q\Delta\dot{\theta} + X_{B1c}\Delta B_{1c} + X_{\theta c}\Delta\theta_c \qquad \text{(A2.7.2)}$$

$$\frac{\Delta M_m + \Delta M_s}{2I_y} = M_u\Sigma\dot{x} + M_w\Sigma\dot{z} + M_q\Sigma\dot{\theta} + M_{B1c}\Sigma B_{1c} + M_{\theta c}\Sigma\theta_c \qquad \text{(A2.7.3)}$$

$$\frac{\Delta M_m - \Delta M_s}{I_y} = M_u\Delta\dot{x} + M_w\Delta\dot{z} + M_q\Delta\dot{\theta} + M_{B1c}\Sigma B_{1c} + M_{\theta c}\Delta\theta_c \qquad \text{(A2.7.4)}$$

$$\frac{\Delta Z_m + \Delta Z_s}{2M_H} = Z_u\Sigma\dot{x} + Z_w\Sigma\dot{z} + Z_q\Sigma\dot{\theta} + Z_{B1c}\Sigma B_{1c} + Z_{\theta c}\Sigma\theta_c \qquad \text{(A2.7.5)}$$

$$\frac{\Delta Z_m - \Delta Z_s}{M_H} = Z_u\Delta\dot{x} + Z_w\Delta\dot{z} + Z_q\Delta\dot{\theta} + Z_{B1c}\Delta B_{1c} + Z_{\theta c}\Delta\theta_c \qquad \text{(A2.7.6)}$$

Note: For flight conditions near hover $X_w = X_q = X_{\theta_c} = Z_u = Z_q = Z_{B_{1c}} = M_w = M_{\theta_c} = 0$.

APPENDIX 2.8: Linear Model for Longitudinal Dynamics of TLHS Near Hover (Symbolic)

2 Horizontal Force Equations

$$1.\quad \Sigma\ddot{x}-X_u\Sigma\dot{x}+g\left[1+\mu S\frac{H_s}{H_A}\right]\Sigma\theta-\frac{1}{2}\mu S w_A^2 h\Delta\theta - \frac{1}{2}\mu S w_A^2\Delta x - \mu w_A^2 x_L' = X_{B1c}\Sigma B_{1c} \qquad (A2.8.1)$$

$$2.\quad \Delta\ddot{x}-X_u\Delta\dot{x}+\mu w_A^2\Delta x + [g(1+\mu)+\mu w_A^2 h]\Delta\theta + 2\mu w_A^2 H_s S\Sigma\theta + 2\mu w_A^2 S x_L' = X_{B1c}\Delta B_{1c} \qquad (A2.8.2)$$

2 Pitching Moment Equations

$$3.\quad \Sigma\ddot{\theta}-M_q\Sigma\dot{\theta}+\varepsilon\mu w_A^2 S H_s\Sigma\theta - M_u\Sigma\dot{x} - \frac{1}{2}\varepsilon\mu w_A^2 S\Delta x - \frac{1}{2}\varepsilon\mu w_A^2 Sh\Delta\theta - \varepsilon\mu w_A^2 x_L' = M_{B1c}\Sigma B_{1c} \qquad (A2.8.3)$$

$$4.\quad \Delta\ddot{\theta}-M_q\Delta\dot{\theta}+\varepsilon\mu w_A^2 (H_A+h)\Delta\theta + 2\varepsilon\mu w_A^2 S H_s\Sigma\theta - M_u\Delta\dot{x} + \varepsilon\mu w_A^2\Delta x + 2\varepsilon\mu w_A^2 S x_L' = M_{B1c}\Delta B_{1c} \qquad (A2.8.4)$$

1 Load Equation

$$5.\quad \ddot{x}_L'+w_A^2 x_L' + \Sigma\ddot{x} + (h+H_s)\Sigma\ddot{\theta} + w_A^2 H_s\Sigma\theta + \frac{1}{2}w_A^2 S\Delta x + \frac{1}{2}w_A^2 Sh\Delta\theta + \delta_L\hat{Z}\Delta\ddot{z}=0 \qquad (A2.8.5)$$

2 Vertical Force Equation

$$6.\quad (1+\mu)\Sigma\ddot{z} - Z_w\Sigma\dot{z} = Z_{\theta c}\Sigma\theta_c \qquad (A2.8.6)$$

$$7.\quad [1+e_b+4\mu\delta_L(1-\delta_L)\hat{Z}^2]\Delta\ddot{z} - Z_w\Delta\dot{z} + 4\mu\delta_L\hat{Z}w_A^2\hat{H}_A\Delta z - 4\mu\delta_L\hat{Z}w_A^2 x_L' - 4\mu\delta_L\hat{Z}w_A^2 H_s\Sigma\theta - 2\mu\delta_L\hat{Z}w_A^2 S\Delta x - 2\mu\delta_L\hat{Z}w_A^2 Sh\Delta\theta = Z_{\theta_c}\Delta\theta_c \qquad (A2.8.7)$$

All variables above represent small perturbations from the equilibrium values.

The above seven linear ordinary differential equations may be concisely written in state space form (Table 2.4.1) to obtain the 12th order model (Σz and Σx not included*) to be used throughout the thesis.

*Σz and Σx are needed only if "exact load positioning" is critical.

APPENDIX 3: Linear Model for a Single Helicopter Near Hover*

Vertical Dynamics

$$\ddot{z} = Z_w \dot{z} + Z_{\theta c}\, \theta_c \tag{A3.1}$$

$$\frac{\dot{z}}{\theta_c} = \frac{Z_{\theta c}}{s - Z_w} \tag{A3.2}$$

pole: $s = Z_w = -0.346$ (A3.3)

dc gain = $\dfrac{Z_{\theta c}}{-Z_w} = 17.2$ ft/deg sec (A3.4)

Horizontal/Pitching Dynamics

$$\begin{bmatrix} \dot{\theta} \\ \ddot{\theta} \\ \ddot{x} \end{bmatrix} = \begin{bmatrix} 0 & 1 & 0 \\ 0 & M_q & M_u \\ -g & 0 & X_u \end{bmatrix} \begin{bmatrix} \theta \\ \dot{\theta} \\ \dot{x} \end{bmatrix} + \begin{bmatrix} 0 \\ M_{Blc} \\ X_{Blc} \end{bmatrix} B_{lc} \tag{A3.5}$$

$$\frac{\theta}{B_{lc}} = M_{Blc} \left[\frac{s + \dfrac{X_{Blc} M_u}{M_{Blc}} - X_u}{s^3 - (X_u + M_q) s^2 + M_q X_u s + g M_u} \right] \tag{A3.6}$$

poles: $s = 0.034] \pm j0.6366$; $\zeta = -0.053$; $\omega_n = 0.64$ (A3.7)

$s = -3.229$

zeros: $s = -0.03622$ (A3.8)

dc gain = $\dfrac{1}{g} \left[X_{Blc} - \dfrac{g M_{Blc}}{X_{Blc}} \right] = -1.296$ deg/deg (A3.9)

$$\frac{\dot{x}}{B_{lc}} = X_{Blc} \left[\frac{s^2 - M_q s - \dfrac{g M_{Blc}}{X_{Blc}}}{s^3 - (X_u + M_q) s^2 + M_q X_u s + g M_u} \right] \tag{A3.10}$$

zeros: $s = -1.55 \pm j7.288$; $\zeta = 0.21$; $\omega_n = 7.29$ (A3.11)

dc gain = $-\dfrac{M_{Blc}}{M_u} = 20.11$ ft/deg (A3.12)

$g = 3.2283$ ft sec^{-2}/deg $\quad X_u = -0.06$ ft sec^{-2}/sec^{-1}

$M_q = -3.1$ deg sec^{-2}/deg sec^{-1} $\quad X_{Blc} = 0.478$ ft sec^{-2}/deg

$M_u = 2.3493$ deg sec^{-2}/ft sec^{-1}, $\quad M_{Blc} = -47.24$ deg sec^{-2}/deg

---

* Parameter values are given in Appendix 1.

REFERENCES

[1] H.C. Curtiss, Jr., and F.W. Warburton, "Stability and Control of the Twin Lift Helicopter System," Presented at 40th annual forum of AHS, Arlington, Va., May 16-18, 1984.

[2] L. Kaufman, and E.R. Schultz, "The Stability and Control of Tethered Helicopters", JAHS, Vol. 7, No.4, October 1962.

[3] A.R.S. Bramwell, Helicopter Dynamics, John Wiley and Sons, New York, 1976.

[4] T.A. Dukes, "Maneuvering Heavy Sling Loads Near Hover", JAHS, "Part1: Damping the Pendulous Motion,", April 1973, "Part 2: Some Elementary Maneuvers", July 1973.

[5] J.C. Doyle, and G. Stein, "Multivariable Feedback Design: Concepts for a Classical/Modern Synthesis", IEEE Trans. on Auto. Control, Vol. AC-26, No. 1, pp. 4-15, February 1981.

[6] G. Stein and M. Athans, "The LQG/LTR Procedure for Multivariable Feedback Control Design", Tech. Paper, MIT LIDS-P-1384, May 1984.

[7] M. Athans, 6.232 class notes, MIT, Spring 1985.

[8] N.A. Lehtomaki, N.R. Sandell, and M. Athans, "Robustness Results in LQG Based Multivariable Control Designs", IEEE Trans. on Auto. Control, Vol. AC-26, No.1, pp. 75-93, February 1981.

[9] N.A. Lehtomaki, Practical Robustness Measures in Multivariable Control System Analysis, Ph.D. thesis, MIT LIDS-TH-1093, May 1981.

[10] J. Doyle, "Analysis of Feedback Systems with Structured Uncertainties", IEE PROC, Vol. 129, Pt. D, No. 6, November 1982.

[11] T. Kailaith, "Linear Systems", Prentice-Hall, New Jersey, 1980.

[12] G. Strang, "Linear Algebra and its Applications", 2nd Edition, Academic Press, 1980.

[13] V.C. Klema, and A.J. Laub, "The Singular Value Decomposition: Its Computation and Some Applications", IEEE Trans. on Auto. Control, Vol. AC-25, No. 2, pp.164-176, April 1980.

[14] K. Ogata, "Modern Control Engineering", Prentice-Hall, New Jersey, 1970.

[15] H. Kwakernaak, and R. Sivan, "Linear Optimal Control Systems", John Wiley and Sons, New York, 1972.

[16] NASA Contractor Report 3579.

[18] P. Kapasouris, A Design Methodology for Plants with Saturating Actuators, Ph.D. thesis, December 1987.

[19] M. Athans and P. Falb, "Optimal Control", McGraw Hill, 1966.

[20] J. S. Freudenberg and D.P. Looze, "Relations Between Properties of Multivariable Feedback Systems at Different Loop-Breaking Points: Part 1", 1985 CDC. " : Part 2", 1986 ACC.

[21] M.G. Safonov, and M. Athans, "Gain and Phase Margin For Multi-Loop LQG Regulators", IEEE Trans. on Auto. Control", Vol AC-22, No. 2, pp.173-179, 1977

[22] B.A. Francis, "A Course in H_∞ Control Theory", Springer-Verlag, New York, 1987